

Modelling and Simulation in Engineering

Structural Modelling at the Micro-, Meso-, and Nanoscales

Guest Editors: Angelo Marcello Tarantino, Julius Kaplunov,
Raimondo Luciano, Carmelo Majorana, Theodoros C. Rousakis,
and Kasper Willam





Structural Modelling at the Micro-, Meso-, and Nanoscales

Structural Modelling at the Micro-, Meso-, and Nanoscales

Guest Editors: Angelo Marcello Tarantino, Julius Kaplunov,
Raimondo Luciano, Carmelo Majorana, Theodoros C. Rousakis,
and Kasper Willam



Copyright © 2017 Hindawi Publishing Corporation. All rights reserved.

This is a special issue published in “Modelling and Simulation in Engineering.” All articles are open access articles distributed under the Creative Commons Attribution License, which permits unrestricted use, distribution, and reproduction in any medium, provided the original work is properly cited.

Editorial Board

Khalid Al-Begain, UK
Adel Alimi, Tunisia
Zeki Ayag, Turkey
José M. Balthazar, Brazil
Sergio Baragetti, Italy
Andrzej Bargiela, UK
Joaquim Barros, Portugal
Salim Belouettar, Luxembourg
Jean-Michel Bergheau, France
Tianshu Bi, China
Agostino Bruzzone, Italy
Jinn Kuen Chen, USA
Elio Chiodo, Italy
Min-Chie Chiu, Taiwan
Weizhong Dai, USA
Ming-Cong Deng, Japan
Tadashi Dohi, Japan
Dimitris Drikakis, UK
Andrzej Dzielinski, Poland
Abdelali El Aroudi, Spain
Enmin Feng, China

Huijun Gao, China
Dariusz J. Gawin, Poland
Chung-Souk Han, USA
Shinsuke Hara, Japan
Jing-song Hong, China
Qinglei Hu, China
Bassam A. Izzuddin, UK
MuDer Jeng, Taiwan
Chia-Feng Juang, Taiwan
Stavros Kotsopoulos, Greece
Nikos D. Lagaros, Greece
Hak-Keung Lam, UK
Hongyi Li, China
Dimitrios E. Manolakos, Greece
Shengwei Mei, China
Laurent Mevel, France
Azah Mohamed, Malaysia
Carlos A. Mota Soares, Portugal
Antonio Munjiza, UK
Javier Murillo, Spain
Petr Musilek, Canada

Tomoharu Nakashima, Japan
Gaby Neumann, Germany
Javier Otamendi, Spain
Anna Pandolfi, Italy
Bei Peng, China
Ricardo Perera, Spain
Zhiping Qiu, China
Luis Carlos Rabelo, USA
Franco Ramírez, Spain
Rubens Sampaio, Brazil
Aiguo Song, China
Soib Taib, Malaysia
Mohamed B. Trabia, USA
Giuseppe A. Trunfio, Italy
Joseph Virgone, France
Ligang Wu, China
Feng Xiao, China
Farouk Yalaoui, France
Shigeru Yamada, Japan
ShengKai Yu, Singapore

Contents

Structural Modelling at the Micro-, Meso-, and Nanoscales

Angelo Marcello Tarantino, Julius Kaplunov, Raimondo Luciano, Carmelo Majorana, Theodoros C. Rousakis, and Kasper Willam

Volume 2017, Article ID 3504949, 3 pages

On Torsion of Functionally Graded Elastic Beams

Marina Diaco

Volume 2016, Article ID 8464205, 7 pages

A Note on Torsion of Nonlocal Composite Nanobeams

Luciano Feo and Rosa Penna

Volume 2016, Article ID 5934814, 5 pages

On Bending of Bernoulli-Euler Nanobeams for Nonlocal Composite Materials

Luciano Feo and Rosa Penna

Volume 2016, Article ID 6369029, 5 pages

Finite Thin Cover on an Orthotropic Elastic Half Plane

Federico Oyedeji Falope and Enrico Radi

Volume 2016, Article ID 5393621, 11 pages

Modelling of Creep and Stress Relaxation Test of a Polypropylene Microfibre by Using Fraction-Exponential Kernel

Andrea Sorzia

Volume 2016, Article ID 3823047, 7 pages

Numerical Investigation of Pull-In Instability in a Micro-Switch MEMS Device through the Pseudo-Spectral Method

P. Di Maida and G. Bianchi

Volume 2016, Article ID 8543616, 6 pages

Floquet Theory for Discontinuously Supported Waveguides

A. Sorzia

Volume 2016, Article ID 2651953, 7 pages

Euler-Bernoulli Nanobeam Welded to a Compressible Semi-Infinite Substrate

Pietro Di Maida and Federico Oyedeji Falope

Volume 2016, Article ID 8574129, 9 pages

Initiation of Failure for Masonry Subject to In-Plane Loads through Micromechanics

V. P. Berardi

Volume 2016, Article ID 2959038, 6 pages

Modelling a Coupled Thermoelctromechanical Behaviour of Contact Elements via Fractal Surfaces

G. Mazzucco, F. Moro, and M. Guarnieri

Volume 2016, Article ID 5219876, 15 pages

Fire Spalling Prevention via Polypropylene Fibres: A Meso- and Macroscale Approach

G. Mazzucco and G. Xotta

Volume 2016, Article ID 8639545, 11 pages



A Review on Radiation Damage in Concrete for Nuclear Facilities: From Experiments to Modeling

Beatrice Pomaro

Volume 2016, Article ID 4165746, 10 pages

Some Aspects of Structural Modeling of Damage Accumulation and Fracture Processes in Metal Structures at Low Temperature

Valeriy Lepov, Albert Grigoriev, Valentina Achikasova, and Kyunna Lepova

Volume 2016, Article ID 7178028, 6 pages

Editorial

Structural Modelling at the Micro-, Meso-, and Nanoscales

**Angelo Marcello Tarantino,¹ Julius Kaplunov,² Raimondo Luciano,³ Carmelo Majorana,⁴
Theodoros C. Rousakis,⁵ and Kasper Willam⁶**

¹University of Modena and Reggio Emilia, Modena, Italy

²Keele University, Staffordshire, UK

³University of Cassino, Cassino, Italy

⁴University of Padova, Padova, Italy

⁵University of Thrace, Komotini, Greece

⁶University of Colorado, Boulder, CO, USA

Correspondence should be addressed to Angelo Marcello Tarantino; angelomarcello.tarantino@unimore.it

Received 24 October 2016; Accepted 24 October 2016; Published 10 January 2017

Copyright © 2017 Angelo Marcello Tarantino et al. This is an open access article distributed under the Creative Commons Attribution License, which permits unrestricted use, distribution, and reproduction in any medium, provided the original work is properly cited.

An important target in industry is that of developing new technologies for microelectromechanical systems (MEMS) and nanoelectromechanical systems (NEMS), designed for a multitude of applications in many technical fields. For example, carbon nanotubes are currently considered very prominent materials owing to their excellent electric, thermal, and mechanical properties. These new materials are employed also for purely mechanical purposes. In fact, carbon nanotubes are often used as reinforcement of traditional construction materials, because their application can improve significantly the tensile strength.

Micro-, meso-, and nanostructures need a structural and constitutive modelling consistent with their actual geometrical dimensions. In this regard, it is necessary to develop suitable models that lead to reliable results, since in the literature they are often not available. This special issue is dedicated to theoretical, numerical, and experimental investigations of the behaviour of structures at micro-, meso-, and nanoscale. The purpose is to collect and compare the contributions of a research field very timely and of great scientific interest.

The papers in this special issue cover the following topics: (i) static analysis, buckling, and vibration of micro-, meso-, and nanostructures; (ii) nanobeams, nanoshells, and nanoplates; (iii) micro-, meso-, and nanostructural

effects; (iv) size effects; (v) microelectromechanical systems (MEMS); (vi) nanoelectromechanical systems (NEMS); (vii) nonlocal theory applied to micro-, meso-, and nanoscales; (viii) nanocomposite materials; (ix) carbon nanotubes; (x) micro- and mesomechanics of concrete; (xi) functionally graded materials; (xii) piezo and magnetic elastic materials; (xiii) homogenization techniques.

The contributions offered by each paper are detailed in the following.

V. Lepov et al. study the problem of brittle fracture of structures at low-temperature conditions connected to damage accumulation and ductile-brittle transition in metals. The internal friction method is applied to revealing the mechanism of dislocation microstructure changes during the low-temperature ductile-brittle transition. It has been shown for the first time that transition is not connected to interatomic interactions but it is stipulated by thermofluctuation on nucleus such as microcracks and by their further growth and coalescence. The proposed mechanism would be used for theoretical and numerical modelling of damage accumulation and fracture in materials.

B. Pomaro considers the radiation damage process in concrete and proposes a unified approach to the practical and predictive assessment of irradiated concrete, which combines both physics and structural mechanics issues. Her paper

provides a collection of the most distinguished contributions on this topic in the past 50 years up to present, which shows a remarkable renewed interest on the subject.

G. Mazzucco and G. Xotta examine structural elements in concrete exposed to high and rapidly rising temperatures. To reduce the risk of spalling of a concrete material under fire condition, the inclusion of a low dosage of polypropylene fibres in the mix design of concrete is largely recognized. PP fibres in fact evaporate above certain temperatures, thus increasing the porosity and reducing the internal pressure in the material by an increase of the voids connectivity in the cement paste. In their work the contribution of polypropylene fibres on concrete behaviour has been numerically investigated using a coupled hygro-thermal-mechanical finite element formulation at the macro- and mesoscale levels.

G. Mazzucco et al. propose a three-dimensional coupled thermoelectromechanical model for electrical connectors to evaluate local stress and temperature distributions around the contact area of electric connectors. A micromechanical numerical model has been developed by merging together the contact theory approach, which makes use of the so-called roughness parameters obtained from experimental measurements on real contact surfaces, with the topology description of the rough surface via the theory of fractal geometry. In particular, the variation of asperities has been evaluated via the Weierstrass-Mandelbrot function. In this way the micromechanical model allowed for an upgraded contact algorithm in terms of effective contact area and thermal and electrical contact conductivities. A comparison between numerical and analytical results shows that the adopted procedure is suitable to simulate the transient thermoelectromechanical response of electric connectors.

L. Feo and R. Penna employ the Eringen elastic constitutive relation to assess small-scale effects in nanobeams. Structural behaviour is studied for functionally graded materials in the cross-sectional plane and torsional loading conditions. Torsional rotations and equilibrated moments are evaluated by solving a first-order differential equation of elastic equilibrium with boundary conditions of kinematic-type. Benchmark examples are briefly discussed, thus enlightening the effectiveness of the proposed methodology.

P. Di Maida and G. Bianchi perform a pseudospectral approximation to solve the problem of pull-in instability in a cantilever microswitch. A numerical comparison is presented between a pseudospectral and a finite element (FE) approximation of the problem. It is shown that the pseudospectral method appears more effective in accurately approximating the behaviour of the cantilever near its tip. This fact is crucial to capturing the threshold voltage on the verge of pull-in. Conversely, the FE approximation presents rapid successions of attracting/repulsing regions along the cantilever, which are not restricted to the near pull-in regime.

M. Diaco analyses orthotropic Saint-Venant beams under torsion, for which a skillful solution method has been recently proposed by Ecsedi considering a class of inhomogeneous beams with shear moduli defined in terms of Prandtl's stress function of corresponding homogeneous beams. Using this approach, orthotropic functionally graded beams with shear moduli tensors defined in terms of the stress function

are studied. A result of invariance on twist centre is also achieved. Examples of functionally graded elliptic cross-sections of orthotropic beams are developed, thus detecting new benchmarks for computational mechanics.

V. P. Berardi presents a micromechanical procedure to evaluate the initiation of damage and failure of masonry with in-plane loads. Masonry material is viewed as a composite with periodic microstructure and, therefore, a unit cell with suitable boundary conditions is assumed as a representative volume element of the masonry. The finite element method is used to determine the average stress on the unit cell corresponding to a given average strain prescribed on the unit cell. Finally, critical curves representing the initiation of damage and failure in both clay brick masonry and adobe masonry are provided.

P. Di Maida and F. O. Falope investigate the contact problem of an Euler-Bernoulli nanobeam of finite length bonded to a homogeneous elastic half plane. The analysis is performed under plane strain condition. Owing to the bending stiffness of the beam, shear and peeling stresses arise at the interface between the beam and the substrate within the contact region. The investigation allows evaluating the role played by the Poisson ratio of the half plane (and, in turn, its compressibility) on the beam-substrate mechanical interaction. Different symmetric as well as skew-symmetric loading conditions for the beam are considered, with particular emphasis on concentrated transversal and horizontal forces and couples acting at its edges. It is found that the Poisson ratio of the half plane affects the behaviour of the interfacial stress field, particularly at the beam edges, where the shear and peel stresses are singular.

F. O. Falope and E. Radi study the mechanical behaviour of thin films bonded to a homogeneous elastic orthotropic half plane under plane strain condition. Both the film and semi-infinite substrate display linear elastic orthotropic behaviour. By assuming perfect adhesion between film and half plane together with membrane behaviour of the film, the compatibility condition between the coating and substrate leads to a singular integral equation with Cauchy kernel. Such an equation is straightforwardly solved by expanding the unknown interfacial stress in series of Chebyshev polynomials displaying square-root singularity at the film edges. This approach allows handling the singular behaviour of the shear stress and, in turn, reducing the problem to a linear algebraic system of infinite terms. Results are found for two loading cases, with particular reference to concentrated axial forces acting at the edges of the film. The corresponding mode II stress intensity factor has been assessed, thus providing the stress concentrations at both ends of the covering. Possible applications of the results here obtained range from MEMS, NEMS, and solar silicon cell for energy harvesting to welded joint and building foundation.

A. Sorzia carries out creep and relaxation tensile tests until breakage of polypropylene fibres. Creep and stress relaxation curves are obtained and fit by a model adopting a fraction-exponential kernel in the viscoelastic operator. Taking into account the fact that the addition of polypropylene fibres greatly improves the tensile strength of composite materials with concrete matrix, the proposed analytical

model is used for simulating the mechanical behaviour of composite materials with embedded viscoelastic fibres.

L. Feo and R. Penna evaluate size effects in functionally graded elastic nanobeams by making recourse to the nonlocal continuum mechanics. The Bernoulli-Euler kinematic assumption and the Eringen nonlocal constitutive law are assumed in the formulation of the elastic equilibrium problem. An innovative methodology, characterized by a lowering in the order of governing differential equation, is adopted to solve the boundary value problem of a nanobeam under flexure. Unlike standard treatments, a second-order differential equation of nonlocal equilibrium elastic is integrated in terms of transverse displacements and equilibrated bending moments. Benchmark examples are developed, thus providing the nonlocality effect in nanocantilever and clamped-simply supported nanobeams for selected values of the Eringen scale parameter.

A. Sorzia applies the Floquet theory of periodic coefficient second-order ODEs to an elastic waveguide. The waveguide is modelled as a uniform elastic string periodically supported by a discontinuous Winkler elastic foundation and, as a result, a Hill equation is found. The fundamental solutions, the stability regions, and the dispersion curves are determined. An asymptotic approximation to the dispersion curve is also provided. It is further shown that the end points of the band gap structure correspond to periodic and semiperiodic solutions of the Hill equation.

The scope of the works presented in this special issue offers a real insight into the progress made across a wide range of theoretical and technical topics related to structural modelling at the micro-, meso-, and nanoscales. We hope that this special issue will stimulate further research interests.

Acknowledgments

On behalf of the guest editors, we would like to acknowledge all the editorial members, contributed authors, and dedicated referees for their invaluable time, great contributions, and assistance to this volume. Without such efforts we would not be able to accomplish this very interesting and informative special issue.

*Angelo Marcello Tarantino
Julius Kaplunov
Raimondo Luciano
Carmelo Majorana
Theodoros C. Rousakis
Kasper Willam*

Research Article

On Torsion of Functionally Graded Elastic Beams

Marina Diaco

Department of Structures for Engineering and Architecture, University of Naples Federico II, via Claudio 21, 80125 Naples, Italy

Correspondence should be addressed to Marina Diaco; diaco@unina.it

Received 14 December 2015; Accepted 5 October 2016

Academic Editor: Theodoros C. Rousakis

Copyright © 2016 Marina Diaco. This is an open access article distributed under the Creative Commons Attribution License, which permits unrestricted use, distribution, and reproduction in any medium, provided the original work is properly cited.

The evaluation of tangential stress fields in linearly elastic orthotropic Saint-Venant beams under torsion is based on the solution of Neumann and Dirichlet boundary value problems for the cross-sectional warping and for Prandtl stress function, respectively. A skillful solution method has been recently proposed by Ecsedi for a class of inhomogeneous beams with shear moduli defined in terms of Prandtl stress function of corresponding homogeneous beams. An alternative reasoning is followed in the present paper for orthotropic functionally graded beams with shear moduli tensors defined in terms of the stress function and of the elasticity of reference inhomogeneous beams. An innovative result of invariance on twist centre is also contributed. Examples of functionally graded elliptic cross sections of orthotropic beams are developed, detecting thus new benchmarks for computational mechanics.

1. Introduction

Analyses of composite media are a well-investigated research field in structural mechanics. Theoretical noteworthy results also in the nonlinear range have recently contributed to several engineering applications, such as beam and plate theories [1–3], fracture mechanics [4–8], hyperelastic media [9–11], concrete systems [12–16], nonlocal models [17–19], homogenization [20–22], thermoelasticity [23–25], nanostructures [26–30], and limit analysis [31–33]. In the context of the classical theory of elasticity, an innovative methodology for the analysis of beams was proposed by Saint-Venant [34, 35], with the assumption that the normal interactions between longitudinal fibres vanish [36]. Basic results about this model are collected in classical treatments [37–44] with a coordinate approach. Coordinate-free investigations can be found in [45–48]. Nevertheless, analytical solutions of beams subjected to torsion can be obtained only for special cross-sectional geometries and shear moduli distributions. Exact solutions of functionally graded structures can be found in [49]. However, finite element strategies are often adopted in order to get effective numerical results when exact solutions are not available; see, for example, [50–53]. Alternatively, experimental methods are employed; see, for example, [54]. Recently Ecsedi showed that, for functionally graded cross sections under torsion, with shear modulus

defined by a positive function of the Prandtl stress function of a corresponding homogeneous cross-section, the warping is invariant and the stress function is expressed in terms of the one associated with the reference homogeneous cross section [55, 56]. Ecsedi's treatment is based on an integral transformation proposed by Kirchhoff in nonlinear heat conduction [57]. An intrinsic reasoning is illustrated in the present paper, by performing a direct discussion of Neumann and Dirichlet boundary value problems for the cross-sectional warping and for the stress function of orthotropic composite beams under torsion. An invariance condition for the Cicala-Hodges centre is also assessed (see Section 3). Finally, new analytical solutions of functionally graded elliptic cross sections are constructed in Section 4. Basic results of Saint-Venant theory of linearly elastic orthotropic beams are collected in the next section.

2. Composite Saint-Venant Beams under Torsion

Let Ω be the simply or multiply connected cross section of an orthotropic and linearly elastic Saint-Venant composite beam under torsion. Position of a point in Ω , with respect to the centre \mathbf{G} of the Young moduli $E : \Omega \mapsto \mathcal{R}$ of beam's longitudinal fibers, is denoted by \mathbf{r} . The tensor \mathbf{R} is the rotation by $\pi/2$ counterclockwise in the cross-sectional plane

π_Ω . Hence $\mathbf{R}^T = \mathbf{R}^{-1} = -\mathbf{R}$ and $\mathbf{R}\mathbf{R} = -\mathbf{I}$. Tangential stresses can be expressed in terms of the warping function [34] $\phi : \Omega \mapsto \mathcal{R}$ or of the stress function [58] $\Psi : \Omega \mapsto \mathcal{R}$ by the coordinate-free formulae [59]

$$\begin{aligned} \boldsymbol{\tau}(\boldsymbol{\alpha}, \mathbf{r}) &= \boldsymbol{\Lambda}(\mathbf{r}) \boldsymbol{\gamma}(\mathbf{r}) = \alpha \boldsymbol{\Lambda}(\mathbf{r}) (\mathbf{R}\mathbf{r} + \nabla\phi(\mathbf{r})) \\ &= -\alpha \mathbf{R}\nabla\Psi(\mathbf{r}), \end{aligned} \quad (1)$$

where the scalar α is the twist, $\boldsymbol{\gamma} : \Omega \mapsto V$ is the elastic tangential strain, and $\boldsymbol{\Lambda} : \Omega \mapsto L(V; V)$ is the positive definite symmetric Lamé tensor field, V being the two-dimensional linear space of translations in π_Ω . The warping field is the solution of the following Neumann-like problem [60]:

$$\begin{aligned} \operatorname{div}(\boldsymbol{\Lambda}(\mathbf{r}) \nabla\phi(\mathbf{r})) &= -\operatorname{div}(\boldsymbol{\Lambda}(\mathbf{r}) \mathbf{R}\mathbf{r}), \quad \mathbf{r} \in \Omega, \\ (\boldsymbol{\Lambda}(\mathbf{r}) \nabla\phi(\mathbf{r})) \cdot \mathbf{n}(\mathbf{r}) &= -(\boldsymbol{\Lambda}(\mathbf{r}) \mathbf{R}\mathbf{r}) \cdot \mathbf{n}(\mathbf{r}), \quad \mathbf{r} \in \partial\Omega, \end{aligned} \quad (2)$$

where \mathbf{n} is the unit outward normal to the domain Ω . Prandtl stress function is the solution of the Dirichlet problem

$$\begin{aligned} \operatorname{div}(\mathbf{R}\boldsymbol{\Lambda}^{-1}\mathbf{R}\nabla\Psi)(\mathbf{r}) &= 2 \quad \text{on } \Omega, \\ \Psi(\mathbf{r}) &= 0 \quad \text{on } \partial\Omega_o, \\ \Psi(\mathbf{r}) &= c_i \\ &\text{on } \partial\Omega_i, \quad c_i \in \mathcal{R}, \quad i = 1, 2, \dots, n, \end{aligned} \quad (3)$$

where Ω is a multiply connected cross-section, with $\partial\Omega_o$ exterior boundary and $\partial\Omega_i$ boundary of the i th hole, being $i = 1, \dots, n$ and $n \geq 0$. The procedure for the evaluation of integration constants c_i is illustrated in [59]. Note that the warping function $\phi : \Omega \mapsto \mathcal{R}$ has been introduced above by assuming tacitly that the cross section undergoes a rotation about the pole \mathbf{G} . Denoting by $\phi_C : \Omega \mapsto \mathcal{R}$ the warping function corresponding to a cross-sectional rotation with respect to a point $\mathbf{C} \in \pi_\Omega$, we get the formula

$$\phi_C = \phi(\mathbf{r}) + (\mathbf{R}\mathbf{r}_C) \cdot \mathbf{r} - c, \quad (4)$$

with \mathbf{r}_C position vector of \mathbf{C} and $c \in \mathcal{R}$. Tangential stress fields are independent of the rotation centre [40]. The twist centre \mathbf{C}^{tw} and a particular value of the constant c were introduced in [61] by requiring that zeroth and first elastic moments of the scalar field $\phi_C : \Omega \mapsto \mathcal{R}$ are zero

$$\begin{aligned} \int_{\Omega} E(\mathbf{r}) (\phi(\mathbf{r}) - c) dA &= 0, \\ \int_{\Omega} E(\mathbf{r}) (\phi(\mathbf{r}) + (\mathbf{R}\mathbf{r}_C) \cdot \mathbf{r}) \mathbf{r} dA &= \mathbf{o}. \end{aligned} \quad (5)$$

The position of the twist centre is given by the formula

$$\mathbf{r}_{\mathbf{C}^{\text{tw}}} = \mathbf{R}\mathbf{J}_{\mathbf{G}}(E)^{-1} \int_{\Omega} E(\mathbf{r}) \phi(\mathbf{r}) \mathbf{r} dA, \quad (6)$$

with $\mathbf{J}_{\mathbf{G}}(E) := \int_{\Omega} E(\mathbf{r}) \mathbf{r} \otimes \mathbf{r} dA$ bending stiffness and \otimes tensor product. An equivalent definition of twist centre was proposed by Trefftz [62] in energetic terms. In [59] it was shown that the twist centre \mathbf{C}^{tw} coincides with the shear centre $\mathbf{C}_{\text{timo}}^{\text{sh}}$ of Timoshenko beams [63], evaluated by the composite and orthotropic Saint-Venant beam theory. Hereafter, the point $\mathbf{C} := \mathbf{C}^{\text{tw}} \equiv \mathbf{C}_{\text{timo}}^{\text{sh}}$ will be named the Cicala-Hodges centre. The next section provides a family of composite beams, generated by a Lamé tensor field $\boldsymbol{\Lambda} : \Omega \mapsto L(V; V)$, for which the warping field and the Cicala-Hodges centre are invariant.

3. Invariances

Let us consider a sequence of tensor fields $\{\boldsymbol{\Lambda}_1, \boldsymbol{\Lambda}_2, \dots, \boldsymbol{\Lambda}_n\}$ generated by a Lamé tensor field $\boldsymbol{\Lambda}_1 : \Omega \mapsto L(V; V)$ and by a sequence of positive scalar functions $\{h_1, h_2, \dots, h_n\}$; that is, $h_i : \mathcal{X}_i \subseteq \mathcal{R} \mapsto]0, +\infty[$, according to the rule:

$$\boldsymbol{\Lambda}_n = (h_{n-1} \circ \Psi_{n-1}) \boldsymbol{\Lambda}_{n-1}, \quad n \geq 2, \quad (7)$$

with $\Psi_{n-1} : \Omega \mapsto \mathcal{R}$ Prandtl stress function associated with the torsion tangential stress field involving Lamé tensor field $\boldsymbol{\Lambda}_{n-1} : \Omega \mapsto L(V; V)$. The sequence of Lamé fields $\{\boldsymbol{\Lambda}_1, \boldsymbol{\Lambda}_2, \dots, \boldsymbol{\Lambda}_n\}$ induces a sequence of Neumann-like PDE problems $\{\mathcal{P}_1, \mathcal{P}_2, \dots, \mathcal{P}_n\}$ for the warping field, defined by

$$\mathcal{P}_{n-1} \left\{ \begin{array}{ll} \operatorname{div}(\boldsymbol{\Lambda}_{n-1} \boldsymbol{\gamma}_{n-1})(\mathbf{r}) = 0, & \text{in } \Omega, \\ (\boldsymbol{\Lambda}_{n-1}(\mathbf{r}) \boldsymbol{\gamma}_{n-1}(\mathbf{r})) \cdot \mathbf{n}(\mathbf{r}) = 0, & \text{on } \partial\Omega, \end{array} \right. \quad (8)$$

with $\boldsymbol{\gamma}_{n-1}(\mathbf{r}) = \boldsymbol{\Lambda}_{n-1}^{-1}(\mathbf{r}) \boldsymbol{\tau}_{n-1}(\mathbf{r}) = \alpha(\mathbf{R}\mathbf{r} + \nabla\phi_{n-1}(\mathbf{r}))$. The following results hold true.

Proposition 1. *Neumann-like PDE problems $\{\mathcal{P}_1, \mathcal{P}_2, \dots, \mathcal{P}_n\}$ provide, to within an additive constant, the same solution $\phi : \Omega \mapsto \mathcal{R}$.*

Proof. Let ϕ_{n-1} be the solution, to within a constant, of the problem \mathcal{P}_{n-1} . Since $\boldsymbol{\Lambda}_n = (h_{n-1} \circ \Psi_{n-1}) \boldsymbol{\Lambda}_{n-1}$, problem \mathcal{P}_n takes the form:

$$\mathcal{P}_n \left\{ \begin{array}{ll} \operatorname{div}((h_{n-1} \circ \Psi_{n-1}) \boldsymbol{\Lambda}_{n-1} \boldsymbol{\gamma}_n)(\mathbf{r}) = 0, & \text{in } \Omega, \\ (\boldsymbol{\Lambda}_{n-1}(\mathbf{r}) \boldsymbol{\gamma}_n(\mathbf{r})) \cdot \mathbf{n}(\mathbf{r}) = 0, & \text{on } \partial\Omega. \end{array} \right. \quad (9)$$

Resorting to the formula

$$\begin{aligned} \operatorname{div}((h_{n-1} \circ \Psi_{n-1}) \boldsymbol{\Lambda}_{n-1} \boldsymbol{\gamma}_n)(\mathbf{r}) &= (h_{n-1} \circ \Psi_{n-1})(\mathbf{r}) \operatorname{div}(\boldsymbol{\Lambda}_{n-1} \boldsymbol{\gamma}_n)(\mathbf{r}) \\ &\quad + dh(\Psi_{n-1}(\mathbf{r})) \nabla\Psi_{n-1}(\mathbf{r}) \cdot (\boldsymbol{\Lambda}_{n-1} \boldsymbol{\gamma}_n(\mathbf{r})) \end{aligned} \quad (10)$$

and setting $\phi_n(\mathbf{r}) = \phi_{n-1}(\mathbf{r}) + c$ with $c \in \mathcal{R}$, we get $\boldsymbol{\gamma}_n = \boldsymbol{\gamma}_{n-1}$, so that the problem \mathcal{P}_n may be rewritten as

$$\mathcal{P}_n \left\{ \begin{array}{l} (h_{n-1} \circ \Psi_{n-1})(\mathbf{r}) \operatorname{div}(\Lambda_{n-1} \boldsymbol{\gamma}_{n-1})(\mathbf{r}) + dh(\Psi_{n-1})(\mathbf{r}) \nabla \Psi_{n-1}(\mathbf{r}) \cdot (\Lambda_{n-1} \boldsymbol{\gamma}_{n-1})(\mathbf{r}) = 0, \quad \text{in } \Omega, \\ (\Lambda_{n-1}(\mathbf{r}) \boldsymbol{\gamma}_{n-1}(\mathbf{r})) \cdot \mathbf{n}(\mathbf{r}) = 0, \quad \text{on } \partial\Omega. \end{array} \right. \quad (11)$$

Recalling the relation $\boldsymbol{\tau}_{n-1}(\alpha, \mathbf{r}) = \Lambda_{n-1}(\mathbf{r}) \boldsymbol{\gamma}_{n-1}(\mathbf{r}) = -\alpha \mathbf{R} \nabla \Psi_{n-1}(\mathbf{r})$, we infer that $\nabla \Psi_{n-1}(\mathbf{r}) \cdot (\Lambda_{n-1} \boldsymbol{\gamma}_{n-1})(\mathbf{r}) = 0$ and the problem \mathcal{P}_n collapses into the one \mathcal{P}_{n-1} . The result follows. \square

Proposition 2. *The relationship between Prandtl stress functions corresponding to Lamé tensor fields Λ_{n-1} and $\Lambda_n = (h_{n-1} \circ \Psi_{n-1}) \Lambda_{n-1}$ is expressed by the formula $\Psi_n = H_{n-1} \circ \Psi_{n-1}$, with H_{n-1} antiderivative of h_{n-1} such that Ψ_n is identically zero on the cross-sectional exterior boundary $\partial\Omega_o$.*

Proof. Resorting to Proposition 1 we get $\boldsymbol{\gamma}_{n-1} = \boldsymbol{\gamma}_n$. Then the equivalences hold

$$\begin{aligned} \Lambda_{n-1}^{-1} \boldsymbol{\tau}_{n-1} &= \Lambda_n^{-1} \boldsymbol{\tau}_n \iff \\ \Lambda_{n-1}^{-1} (-\alpha \mathbf{R} \nabla \Psi_{n-1}) &= \Lambda_n^{-1} (-\alpha \mathbf{R} \nabla \Psi_n), \quad (12) \\ &= ((h_{n-1} \circ \Psi_{n-1}) \Lambda_{n-1})^{-1} (-\alpha \mathbf{R} \nabla \Psi_n), \end{aligned}$$

whence $(h_{n-1} \circ \Psi_{n-1}) \nabla \Psi_{n-1} = \nabla (H_{n-1} \circ \Psi_{n-1}) = \nabla \Psi_n$ which gives $\Psi_n = H_{n-1} \circ \Psi_{n-1}$, with H_{n-1} antiderivative of h_{n-1} such that Ψ_n is identically zero on the cross-sectional exterior boundary $\partial\Omega_o$. \square

Proposition 3. *Let $E : \Omega \mapsto]0, +\infty[$ be the Euler moduli scalar field of orthotropic and composite beams whose Lamé fields are described by the sequence $\{\Lambda_1, \Lambda_2, \dots, \Lambda_n\} = \{\Lambda_1, (h_1 \circ \Psi_1) \Lambda_1, \dots, (h_{n-1} \circ \Psi_{n-1}) \Lambda_{n-1}\}$. For these beams, the location of the Cicala-Hodges centre is invariant.*

Proof. The result follows by the formula providing the twist centre position $\mathbf{r}_{C^{tw}} = \mathbf{R} \mathbf{J}_G(E)^{-1} \int_{\Omega} E(\mathbf{r}) \phi(\mathbf{r}) \mathbf{r} dA$ and by Proposition 1. \square

4. Examples

Let us provide some analytical solutions of functionally graded orthotropic beams under torsion with elliptic cross sections. Inertia principal axes $\{x, y\}$ with origin in the centre \mathbf{G} of the Euler moduli field $E : \Omega \mapsto \mathcal{R}$ will be adopted in the sequel. Position vector \mathbf{r} and rotation \mathbf{R} are written as

$$\begin{aligned} \mathbf{r} &= \begin{bmatrix} x \\ y \end{bmatrix}, \\ \mathbf{R} &= \begin{bmatrix} 0 & -1 \\ 1 & 0 \end{bmatrix}, \end{aligned} \quad (13)$$

whence $\mathbf{R}\mathbf{r} = [-y, x]^T$. Torsional warping of elliptic composite beams with Lamé tensor field,

$$\begin{aligned} \Lambda_1(x, y) &= \begin{bmatrix} \mu_x & \mu_{xy} \\ \mu_{xy} & \mu_y \end{bmatrix} \\ &= \left(-k_1 k_2 \frac{a^2 y^2 + b^2 x^2 - a^2 b^2}{a^2 k_2 + b^2 k_1} + k_3 \right) \begin{bmatrix} k_1 & 0 \\ 0 & k_2 \end{bmatrix}, \end{aligned} \quad (14)$$

is provided by the formula [40] $\phi(x, y) = -((a^2 k_2 - b^2 k_1)/(a^2 k_2 + b^2 k_1))xy + c$, with $c \in \mathcal{R}$, $k_1, k_2, k_3 \in]0, +\infty[$ and a, b lengths of the ellipse semidiameters. Plots of the shear modulus μ_x and of the warping ϕ are provided in Figures 1 and 2.

Cartesian components of the tangential strain field $\boldsymbol{\gamma}$ and stress function Ψ_1 are given by the formulae

$$\begin{aligned} \boldsymbol{\gamma}(\alpha, x, y) &= \begin{bmatrix} \gamma_{xz} \\ \gamma_{yz} \end{bmatrix} = \alpha (\mathbf{R}\mathbf{r} + \nabla \phi(\mathbf{r})) = \frac{2\alpha}{a^2 k_2 + b^2 k_1} \\ &\cdot \begin{bmatrix} -a^2 k_2 y \\ b^2 k_1 x \end{bmatrix}, \\ \Psi_1(x, y) &= k_1 k_2 \\ &\cdot \frac{a^2 y^2 + b^2 x^2 - a^2 b^2}{a^2 k_2 + b^2 k_1} \left(\frac{1}{2} k_1 k_2 \frac{a^2 y^2 + b^2 x^2 - a^2 b^2}{a^2 k_2 + b^2 k_1} \right. \\ &\left. - k_3 \right), \end{aligned} \quad (15)$$

as depicted in Figures 3 and 4. As shown in Section 3, Lamé tensor field Λ_1 generates a sequence of composite beams under torsion for which warping function and Cicala-Hodges centre are invariant, and the relevant stress functions are given by Proposition 2. Analytical solutions of the following composite elliptic beams under torsion are discussed. The former is characterized by Lamé shear moduli described by the tensor field $\Lambda_2 = (\Psi_1 + k) \Lambda_1$, with $k \in]0, +\infty[$. The corresponding stress function is given by the formula $\Psi_2 = (1/2) \Psi_1^2 + k \Psi_1$, as assessed in Proposition 2. The latter is characterized by Lamé shear moduli described by the tensor field $\Lambda_3 = (\exp \circ \Psi_2) \Lambda_2$, where \exp denotes the exponential function. The corresponding stress function is given by the formula $\Psi_3 = (\exp \circ \Psi_2) - 1$, as assessed in Proposition 2. Stress functions and tangential stresses are depicted in Figures 5, 6, 7, and 8.

It is worth noting that if the Euler moduli scalar field E is assumed to be the same in the examples discussed above, then

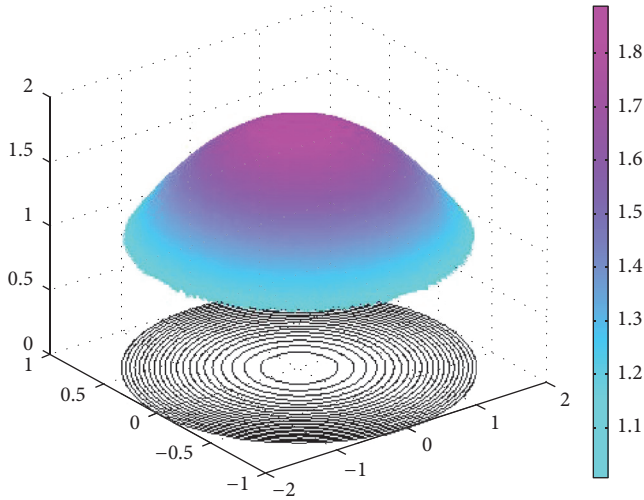


FIGURE 1: Shear modulus μ_x ; $a = 2, b = 1; k_1 = k_3 = 1, k_2 = 2$. Color spectrum: μ_x .

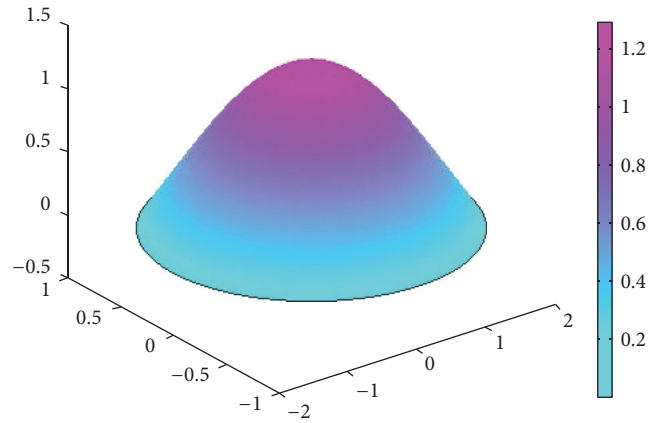


FIGURE 4: Stress function Ψ_1 ; $a = 2, b = 1; k_1 = k_3 = 1, k_2 = c = 2$. Color spectrum: Ψ_1 .

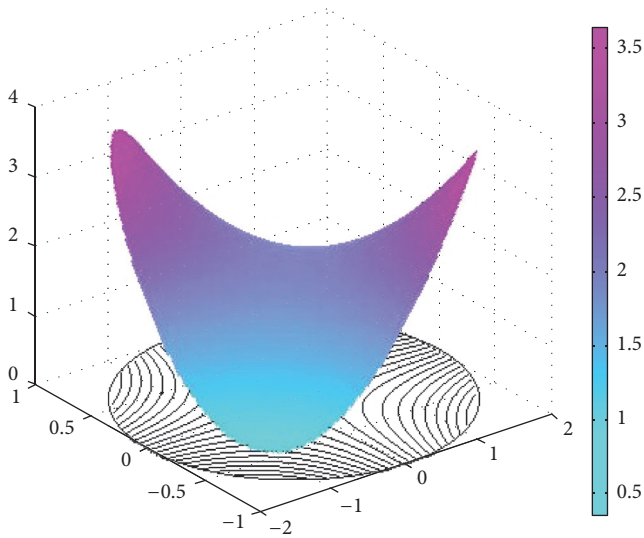


FIGURE 2: Cross-sectional torsional warping ϕ ; $a = 2, b = 1; k_1 = 1, k_2 = c = 2$. Color spectrum: ϕ .

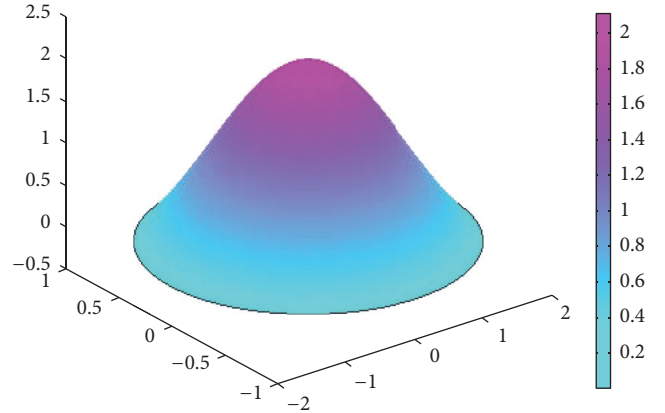


FIGURE 5: Stress function Ψ_2 ; $a = 2, b = 1; k_1 = k_3 = 1, k_2 = c = 2$. Color spectrum: Ψ_2 .

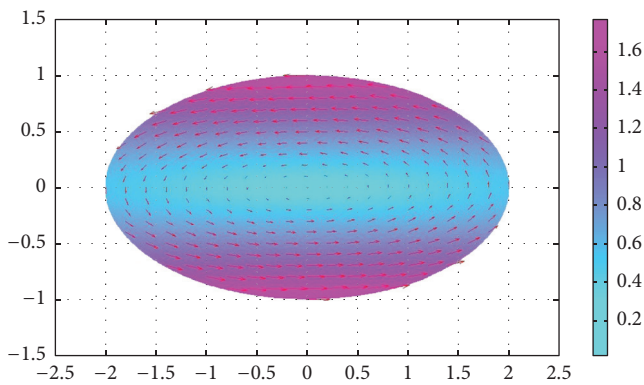


FIGURE 3: Tangential strain field per unit twist γ/α ; $a = 2, b = 1; k_1 = k_3 = 1, k_2 = 2$. Color spectrum: $\|\gamma(x, y)\| := [\gamma_{xz}^2(x, y) + \gamma_{yz}^2(x, y)]^{1/2}$ for $\alpha = 1$.

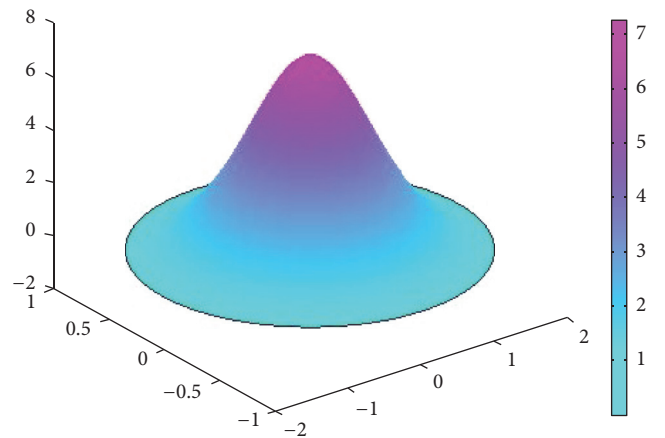


FIGURE 6: Stress function Ψ_3 ; $a = 2, b = 1; k_1 = k_3 = 1, k_2 = c = 2$. Color spectrum: Ψ_3 .

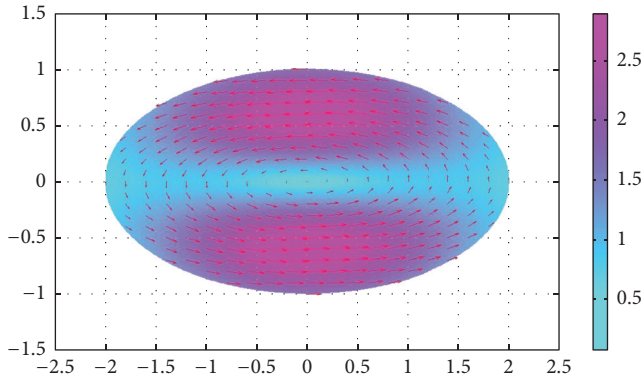


FIGURE 7: Tangential stress field per unit twist τ_2/α ; $a = 2$, $b = 1$; $k_1 = k_3 = 1$, $k_2 = 2$. Color spectrum: $\|\tau_2(x, y)\|$ for $\alpha = 1$.

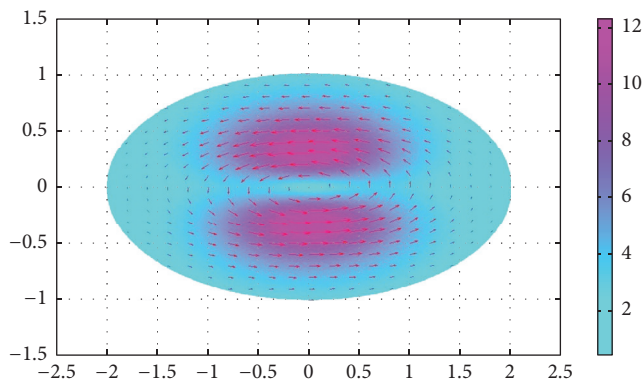


FIGURE 8: Tangential stress field per unit twist τ_3/α ; $a = 2$, $b = 1$; $k_1 = k_3 = 1$, $k_2 = 2$. Color spectrum: $\|\tau_3(x, y)\|$ for $\alpha = 1$.

warping functions and Cicala-Hodges centres are invariant, as prescribed by Propositions 1 and 3.

5. Conclusions

The outcomes of the present paper may be summarized as follows.

- (i) Neumann and Dirichlet boundary value problems for the cross-sectional warping and for Prandtl stress function of linearly elastic, orthotropic composite beams under torsion have been examined.
- (ii) Invariance conditions for the warping and for the Cicala-Hodges shear centre of simply and multiply connected cross sections have been established.
- (iii) The relationship between Prandtl stress functions of orthotropic composite beams with invariant warping has been assessed.
- (iv) Examples have been developed for orthotropic composite beams with elliptic cross section, providing thus also new benchmarks for numerical analyses.

Competing Interests

The author declares no competing interests.

References

- [1] D. H. Hodges, *Nonlinear Composite Beam Theory*, AIAA, Reston, Va, USA, 2006.
- [2] F. Marmo and L. Rosati, “Analytical integration of elasto-plastic uniaxial constitutive laws over arbitrary sections,” *International Journal for Numerical Methods in Engineering*, vol. 91, no. 9, pp. 990–1022, 2012.
- [3] F. Marmo and L. Rosati, “The fiber-free approach in the evaluation of the tangent stiffness matrix for elastoplastic uniaxial constitutive laws,” *International Journal for Numerical Methods in Engineering*, vol. 94, no. 9, pp. 868–894, 2013.
- [4] A. M. Tarantino, “Nonlinear fracture mechanics for an elastic Bell material,” *The Quarterly Journal of Mechanics and Applied Mathematics*, vol. 50, no. 3, pp. 435–456, 1997.
- [5] A. M. Tarantino, “The singular equilibrium field at the notch-tip of a compressible material in finite elastostatics,” *Journal of Applied Mathematics and Physics*, vol. 48, no. 3, pp. 370–388, 1997.
- [6] A. M. Tarantino, “On extreme thinning at the notch tip of a neo-Hookean sheet,” *The Quarterly Journal of Mechanics and Applied Mathematics*, vol. 51, no. 2, pp. 179–190, 1998.
- [7] A. M. Tarantino, “On the finite motions generated by a mode I propagating crack,” *Journal of Elasticity*, vol. 57, no. 2, pp. 85–103, 1999.
- [8] A. M. Tarantino, “Crack propagation in finite elastodynamics,” *Mathematics and Mechanics of Solids*, vol. 10, no. 6, pp. 577–601, 2005.
- [9] A. M. Tarantino, “Asymmetric equilibrium configurations of symmetrically loaded isotropic square membranes,” *Journal of Elasticity*, vol. 69, no. 1–3, pp. 73–97, 2002.
- [10] A. M. Tarantino, “Homogeneous equilibrium configurations of a hyperelastic compressible cube under equitriaxial dead-load tractions,” *Journal of Elasticity*, vol. 92, no. 3, pp. 227–254, 2008.
- [11] F. Marmo and L. Rosati, “A general approach to the solution of Boussinesq’s problem for polynomial pressures acting over polygonal domains,” *Journal of Elasticity*, vol. 122, no. 1, pp. 75–112, 2016.
- [12] G. Dinelli, G. Belz, C. E. Majorana, and B. A. Schrefler, “Experimental investigation on the use of fly ash for lightweight precast structural elements,” *Materials and Structures*, vol. 29, no. 194, pp. 632–638, 1996.
- [13] V. A. Salomoni, C. E. Majorana, G. M. Giannuzzi, and A. Miliozzi, “Thermal-fluid flow within innovative heat storage concrete systems for solar power plants,” *International Journal of Numerical Methods for Heat and Fluid Flow*, vol. 18, no. 7–8, pp. 969–999, 2008.
- [14] V. A. Salomoni, G. Mazzucco, C. Pellegrino, and C. E. Majorana, “Three-dimensional modelling of bond behaviour between concrete and FRP reinforcement,” *Engineering Computations*, vol. 28, no. 1, pp. 5–29, 2011.
- [15] V. A. Salomoni, C. E. Majorana, B. Pomaro, G. Xotta, and F. Gramigna, “Macroscale and mesoscale analysis of concrete as a multiphase material for biological shields against nuclear radiation,” *International Journal for Numerical and Analytical Methods in Geomechanics*, vol. 38, no. 5, pp. 518–535, 2014.

- [16] G. Xotta, G. Mazzucco, V. A. Salomoni, C. E. Majorana, and K. J. Willam, "Composite behavior of concrete materials under high temperatures," *International Journal of Solids and Structures*, vol. 64, pp. 86–99, 2015.
- [17] F. Marotti de Sciarra, "A general theory for nonlocal softening plasticity of integral-type," *International Journal of Plasticity*, vol. 24, no. 8, pp. 1411–1439, 2008.
- [18] F. Marotti de Sciarra, "Variational formulations and a consistent finite-element procedure for a class of nonlocal elastic continua," *International Journal of Solids and Structures*, vol. 45, no. 14-15, pp. 4184–4202, 2008.
- [19] F. Marotti de Sciarra, "Variational formulations, convergence and stability properties in nonlocal elastoplasticity," *International Journal of Solids and Structures*, vol. 45, no. 7-8, pp. 2322–2354, 2008.
- [20] F. Greco and R. Luciano, "A theoretical and numerical stability analysis for composite micro-structures by using homogenization theory," *Composites Part B: Engineering*, vol. 42, no. 3, pp. 382–401, 2011.
- [21] A. Caporale, L. Feo, R. Luciano, and R. Penna, "Numerical collapse load of multi-span masonry arch structures with FRP reinforcement," *Composites Part B: Engineering*, vol. 54, no. 1, pp. 71–84, 2013.
- [22] A. Caporale, L. Feo, and R. Luciano, "Damage mechanics of cement concrete modeled as a four-phase composite," *Composites Part B: Engineering*, vol. 65, pp. 124–130, 2014.
- [23] F. Marotti de Sciarra and M. Salerno, "On thermodynamic functions in thermoelasticity without energy dissipation," *European Journal of Mechanics—A/Solids*, vol. 46, pp. 84–95, 2014.
- [24] L. Rosati and F. Marmo, "Closed-form expressions of the thermo-mechanical fields induced by a uniform heat source acting over an isotropic half-space," *International Journal of Heat and Mass Transfer*, vol. 75, pp. 272–283, 2014.
- [25] M. Čanadija, R. Barretta, and F. Marotti de Sciarra, "A gradient elasticity model of Bernoulli-Euler nanobeams in non-isothermal environments," *European Journal of Mechanics—A/Solids*, vol. 55, pp. 243–255, 2016.
- [26] F. Marotti de Sciarra and R. Barretta, "A new nonlocal bending model for Euler-Bernoulli nanobeams," *Mechanics Research Communications*, vol. 62, no. 1, pp. 25–30, 2014.
- [27] F. Marotti de Sciarra, M. Čanadija, and R. Barretta, "A gradient model for torsion of nanobeams," *Comptes Rendus—Mecanique*, vol. 343, no. 4, pp. 289–300, 2015.
- [28] R. Barretta, R. Luciano, and F. Marotti De Sciarra, "A fully gradient model for euler-bernoulli nanobeams," *Mathematical Problems in Engineering*, vol. 2015, Article ID 495095, 8 pages, 2015.
- [29] R. Barretta, L. Feo, R. Luciano, F. Marotti de Sciarra, and R. Penna, "Functionally graded Timoshenko nanobeams: a novel nonlocal gradient formulation," *Composites B*, vol. 100, pp. 208–219, 2016.
- [30] R. Barretta, L. Feo, R. Luciano, and F. Marotti de Sciarra, "Application of an enhanced version of the Eringen differential model to nanotechnology," *Composites B*, vol. 96, pp. 274–280, 2016.
- [31] A. Caporale, R. Luciano, and L. Rosati, "Limit analysis of masonry arches with externally bonded FRP reinforcements," *Computer Methods in Applied Mechanics and Engineering*, vol. 196, no. 1–3, pp. 247–260, 2006.
- [32] A. Caporale and R. Luciano, "Limit analysis of masonry arches with finite compressive strength and externally bonded reinforcement," *Composites Part B: Engineering*, vol. 43, no. 8, pp. 3131–3145, 2012.
- [33] A. Caporale, L. Feo, D. Hui, and R. Luciano, "Debonding of FRP in multi-span masonry arch structures via limit analysis," *Composite Structures*, vol. 108, no. 1, pp. 856–865, 2014.
- [34] A. J. C. B. de Saint-Venant, "Mémoire sur la torsion des prismes," *Mémoires de l'Académie Royale des Sciences de Paris, Savants Étrangers*, vol. 14, pp. 233–560, 1855.
- [35] A. J. C. B. de Saint-Venant, "Mémoire sur la exion des prismes," *Journal de Mathématiques Pures et Appliquées*, vol. 1, no. 2, pp. 89–189, 1856.
- [36] A. Clebsh, *Theorie der Elasticität Fester Körper*, B.G. Teubner, Leipzig, Germany, 1862.
- [37] A. E. H. Love, *A Treatise on the Mathematical Theory of Elasticity*, Dover, New York, NY, USA, 1944.
- [38] N. I. Muskhelishvili, *Some Basic Problems of the Mathematical Theory of Elasticity*, Leningrad, Moscow, Russia, 3rd edition, 1953, Translated from the russian by J. R. M. Radok, P. Noordhoff, Holland, Groningen, Netherlands.
- [39] S. Timoshenko and J. N. Goodier, *Theory of Elasticity*, McGraw-Hill, New York, NY, USA, 1951.
- [40] I. S. Sokolnikoff, *Mathematical Theory of Elasticity*, McGraw-Hill, New York, NY, USA, 1956.
- [41] V. V. Novozhilov, *Theory of Elasticity*, Pergamon, London, UK, 1961.
- [42] S. G. Lekhnitskii, *Theory of Elasticity of an Anisotropic Elastic Body*, Holden-Day, San Francisco, Calif, USA, 1963.
- [43] L. Solomon, *Élasticité Lineaire*, Masson, Paris, France, 1968.
- [44] A. I. Lurje, *Theory of Elasticity*, Izd. Nauka, Moscow, Russia, 1970 (Russian).
- [45] R. Barretta and A. Barretta, "Shear stresses in elastic beams: an intrinsic approach," *European Journal of Mechanics, A/Solids*, vol. 29, no. 3, pp. 400–409, 2010.
- [46] G. Romano, A. Barretta, and R. Barretta, "On torsion and shear of Saint-Venant beams," *European Journal of Mechanics—A/Solids*, vol. 35, pp. 47–60, 2012.
- [47] R. Barretta, "On stress function in Saint-Venant beams," *Meccanica*, vol. 48, no. 7, pp. 1811–1816, 2013.
- [48] R. Barretta, "Analogies between Kirchhoff plates and Saint-Venant beams under torsion," *Acta Mechanica*, vol. 224, no. 12, pp. 2955–2964, 2013.
- [49] R. Barretta, "Analogies between Kirchhoff plates and Saint-Venant beams under flexure," *Acta Mechanica*, vol. 225, no. 7, pp. 2075–2083, 2014.
- [50] R. Luciano and J. R. Willis, "Bounds on non-local effective relations for random composites loaded by configuration-dependent body force," *Journal of the Mechanics and Physics of Solids*, vol. 48, no. 9, pp. 1827–1849, 2000.
- [51] R. Luciano and J. R. Willis, "Boundary-layer corrections for stress and strain fields in randomly heterogeneous materials," *Journal of the Mechanics and Physics of Solids*, vol. 51, no. 6, pp. 1075–1088, 2003.
- [52] R. Luciano and J. R. Willis, "Hashin-Shtrikman based FE analysis of the elastic behaviour of finite random composite bodies," *International Journal of Fracture*, vol. 137, no. 1–4, pp. 261–273, 2006.
- [53] F. Marotti de Sciarra, "Finite element modelling of nonlocal beams," *Physica E: Low-Dimensional Systems and Nanostructures*, vol. 59, pp. 144–149, 2014.

- [54] A. Patti, R. Barretta, F. Marotti de Sciarra, G. Mensitieri, C. Menna, and P. Russo, "Flexural properties of multi-wall carbon nanotube/polypropylene composites: experimental investigation and nonlocal modeling," *Composite Structures*, vol. 131, pp. 282–289, 2015.
- [55] I. Ecsedi, "Some analytical solutions for Saint-Venant torsion of non-homogeneous cylindrical bars," *European Journal of Mechanics—A/Solids*, vol. 28, no. 5, pp. 985–990, 2009.
- [56] I. Ecsedi, "Some analytical solutions for Saint-Venant torsion of non-homogeneous anisotropic cylindrical bars," *Mechanics Research Communications*, vol. 52, pp. 95–100, 2013.
- [57] H. S. Carslaw and J. C. Jager, *Conduction of Heat in Solids*, Clarendon Press, Oxford, UK, 1959.
- [58] L. Prandtl, "Zur torsion von prismatischen staben," *Physikalische Zeitschrift*, vol. 4, pp. 758–770, 1903.
- [59] R. Barretta, "On the relative position of twist and shear centres in the orthotropic and fiberwise homogeneous Saint-Venant beam theory," *International Journal of Solids and Structures*, vol. 49, no. 21, pp. 3038–3046, 2012.
- [60] R. Barretta, "Cesàro-Volterra method in orthotropic Saint-Venant beam," *Journal of Elasticity*, vol. 112, no. 2, pp. 233–253, 2013.
- [61] P. Cicala, "Il centro di taglio nei solidi cilindrici," *Atti Accademia delle Scienze di Torino (serie Fisica)*, vol. 70, pp. 356–371, 1935.
- [62] E. Trefftz, "Über den Schubmittelpunkt in einem durch eine Einzellast gebogenen Balken," *Zeitschrift für Angewandte Mathematik und Mechanik*, vol. 15, no. 4, pp. 220–225, 1935.
- [63] W. Yu, D. H. Hodges, V. Volovoi, and C. E. S. Cesnik, "On Timoshenko-like modeling of initially curved and twisted composite beams," *International Journal of Solids and Structures*, vol. 39, no. 19, pp. 5101–5121, 2002.

Research Article

A Note on Torsion of Nonlocal Composite Nanobeams

Luciano Feo and Rosa Penna

Department of Civil Engineering, University of Salerno, Via Ponte don Melillo, 84084 Fisciano, Italy

Correspondence should be addressed to Luciano Feo; l.feo@unisa.it

Received 4 December 2015; Accepted 5 October 2016

Academic Editor: Theodoros C. Rousakis

Copyright © 2016 L. Feo and R. Penna. This is an open access article distributed under the Creative Commons Attribution License, which permits unrestricted use, distribution, and reproduction in any medium, provided the original work is properly cited.

The ERINGEN elastic constitutive relation is used in this paper in order to assess small-scale effects in nanobeams. Structural behavior is studied for functionally graded materials in the cross-sectional plane and torsional loading conditions. The governing boundary value problem has been formulated in a mixed framework. Torsional rotations and equilibrated moments are evaluated by solving a first-order differential equation of elastic equilibrium with boundary conditions of kinematic-type. Benchmark examples are briefly discussed, enlightening thus effectiveness of the proposed methodology.

1. Introduction

Assessments of stress and displacement fields in continuous media are a subject of special interest in the theory of structures. Numerous case studies have been examined in the current literature with reference to beams [1–6], half-spaces [7, 8], thin plates [9, 10], compressible cubes [11], and concrete [12, 13]. Several methodologies of analysis have been developed in the research field of geometric continuum mechanics [14, 15], limit analysis [16–19], homogenization [20], elastodynamics [21–25], thermal problems [26–28], random composites [29–32], and nonlocal and gradient formulations [33–38]. A comprehensive analysis of classical and generalized models of elastic structures, with special emphasis on rods, can be found in the interesting book by IËŞAN [39]. In particular, IËŞAN [40–42] formulated a method for the solution of SAINT-VENANT problems in micropolar beams with arbitrary cross-section. Detailed solution of the torsion problem for an isotropic micropolar beam with circular cross-section is given in [43, 44]. Experimental investigations are required for the evaluation of the behavior of composite structures [45].

In the context of the present research, particular attention is devoted to the investigation of scale effects in nanostructures; see, for example, [46–55] and the reviews [56, 57]. Recent contributions on functionally graded materials have been developed for nanobeams under flexure [58, 59] and torsion [60].

Unlike previous treatments on torsion of gradient elastic bars (see, e.g., [61]) in which higher-order boundary conditions have to be enforced, this paper is concerned with the analysis of composite nanobeams with nonlocal constitutive behavior conceived by ERINGEN in [62]. Basic equations governing the ERINGEN model are preliminarily recalled in Section 2. The corresponding elastic equilibrium problem of torsion of an ERINGEN circular nanobeam is then formulated in Section 3. It is worth noting that only classical boundary conditions are involved in the present study. Small-scale effects are detected in Section 4 for two static schemes of applicative interest. Some concluding remarks are delineated in Section 5.

2. Eringen Nonlocal Elastic Model

Before formulating the elastostatic problem of a nonlocal nanobeam subjected to torsion, we shortly recall in the sequel some notions of nonlocal elasticity. To this end, let us consider a body \mathcal{B} made of a material, possibly composite, characterized by the following integral relation between the stress \mathbf{t}_{ij} at a point \mathbf{x} and the elastic strain field \mathbf{e}_{ij} in \mathcal{B} [62]:

$$\mathbf{t}_{ij}(\mathbf{x}) = \int_{\mathcal{B}} K(|\mathbf{x}' - \mathbf{x}|, \tau) \mathbb{E}_{ijhk}(\mathbf{x}') \mathbf{e}_{hk}(\mathbf{x}') dV. \quad (1)$$

The fourth-order tensor $\mathbb{E}_{ijhk}(\mathbf{x}')$, symmetric and positive definite, describes the material elastic stiffness at the point $\mathbf{x}' \in \mathcal{B}$.

The attenuation function K depends on the Euclidean distance $|\mathbf{x}' - \mathbf{x}|$ and on a nonlocal dimensionless parameter defined by

$$\tau = \frac{e_0 a}{l}, \quad (2)$$

where e_0 is a material constant, a is an internal characteristic length, and l stands for external characteristic length.

Assuming a suitable expression of the nonlocal modulus K in terms of a variant of the BESSEL function, we get the inverse differential relationship of (1) between the nonlocal stress and the elastic deformation

$$(1 - (e_0 a)^2 \nabla^2) \mathbf{t}_{ij} = \mathbb{E}_{ijhk} \mathbf{e}_{hk} \quad (3)$$

with ∇^2 the Laplacian. Note that (3) can be conveniently used in order to describe the law between the nonlocal shear stress field \mathbf{t}_i on the cross-section of a nanobeam and the elastic shear strain γ_i as follows:

$$\mathbf{t}_i - (e_0 a)^2 \frac{d^2 \mathbf{t}_i}{dx^2} = \mu \gamma_i, \quad (4)$$

where x is the axial direction and μ is the shear modulus.

3. Torsion of Nonlocal Circular Nanobeams

Let Ω be the cross-section of a circular nanobeam, of length L , subjected to the following loading conditions depicted in Figure 1:

$$\begin{aligned} m_t, & \\ \text{distributed couples per unit length in the interval } [0, L], & \\ \mathcal{M}_t, & \\ \text{concentrated couples at the end cross-sections } \{0, L\}. & \end{aligned} \quad (5)$$

The triplet (x, y, z) describes a set of Cartesian axes originating at the left cross-section centre \mathbf{O} .

Equilibrium equations are expressed by

$$\frac{dM_t}{dx} = -m_t, \quad \text{in } [0, L], \quad (6a)$$

$$M_t = \mathcal{M}_t, \quad \text{at } \{0, L\}, \quad (6b)$$

where M_t is the twisting moment.

Components of the displacement field, up to a rigid body motion, of a circular nanobeam under torsion write as

$$\begin{aligned} s_x(x, yz) &= 0, \\ s_y(x, yz) &= -\theta(x)z, \\ s_z(x, yz) &= \theta(x)y, \end{aligned} \quad (7)$$

where $\theta(x)$ is the torsional rotation of the cross-section at the abscissa x . Shear strains, compatible with the displacement field equation (7), are given by

$$\begin{aligned} \gamma_{yx}(x, y, z) &= -\frac{d\theta}{dx}xz, \\ \gamma_{zx}(x, y, z) &= \frac{d\theta}{dx}xy, \end{aligned} \quad (8)$$

where

$$\chi_t(x) = \frac{d\theta}{dx}(x) \quad (9)$$

is the twisting curvature. The shear modulus μ is assumed to be functionally graded only in the cross-sectional plane (y, z) .

The elastic twisting stiffness is provided by

$$k_t = \int_{\Omega} \mu (y^2 + z^2) dA, \quad (10)$$

where the symbol \cdot is the inner product between vectors.

The differential equation of nonlocal elastic equilibrium of a nanobeam under torsion is formulated as follows. Let us preliminarily multiply (4) by $\mathbf{Rr} := \{-z, y\}$ and integrate on Ω

$$\int_{\Omega} \mathbf{Rr} \cdot \mathbf{t} dA - (e_0 a)^2 \int_{\Omega} \mathbf{Rr} \cdot \frac{d\mathbf{t}}{dx^2} dA = \int_{\Omega} \mu \mathbf{Rr} \cdot \boldsymbol{\gamma} dA, \quad (11)$$

with the vector $\boldsymbol{\gamma} := \{\gamma_{yx}, \gamma_{zx}\}$ given by (8).

Enforcing (6a) and imposing the static equivalence condition

$$M_t = \int_{\Omega} (\tau_{zx}y - \tau_{yx}z) dA, \quad (12)$$

we get the relation

$$M_t(x) + (e_0 a)^2 \frac{dM_t}{dx}(x) = k_t \frac{d\theta}{dx}(x). \quad (13)$$

This equation can be interpreted as decomposition formula of the twisting curvature χ_t into elastic $(\chi_t)_{\text{EL}}$ and inelastic $(\chi_t)_{\text{IN}}$ parts

$$\chi_t = (\chi_t)_{\text{EL}} + (\chi_t)_{\text{IN}}, \quad (14)$$

with

$$(\chi_t)_{\text{EL}} = \frac{M_t}{k_t}, \quad (15a)$$

$$(\chi_t)_{\text{IN}} = \frac{(e_0 a)^2}{k_t} \frac{dM_t}{dx}. \quad (15b)$$

Accordingly, the scale effect exhibited by the torsional rotation function of a nonlocal nanobeam can be evaluated by solving a corresponding linearly elastic beam subjected to the twisting curvature distortion $(\chi_t)_{\text{IN}}$ (15b).

4. Benchmark Examples

Let us consider a nanocantilever and a fully clamped nanobeam of length L subjected to the following quadratic distribution of couples per unit length:

$$m_t = \frac{m}{L^2} x^2. \quad (16)$$

The cross-sectional torsional rotation is evaluated by following the methodology illustrated in the previous section.

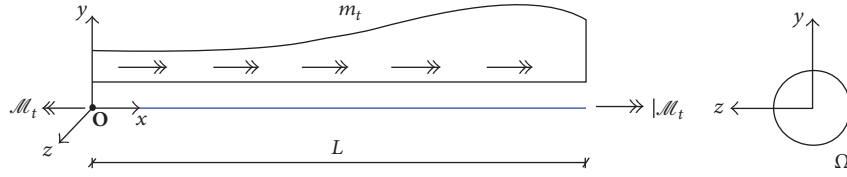
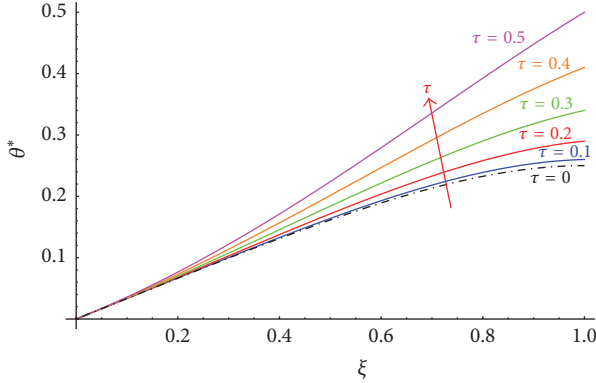
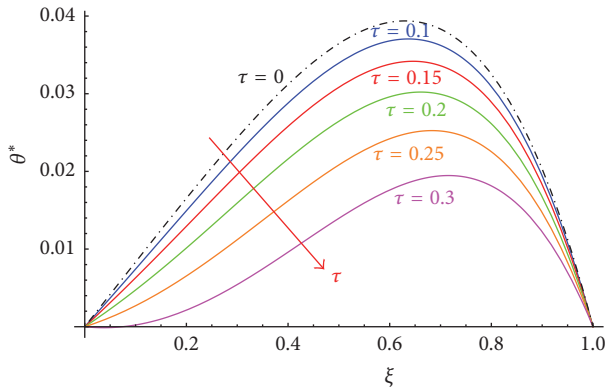


FIGURE 1: Sketch of a nanobeam under torsion.


 FIGURE 2: Torsional rotation θ^* for the nanocantilever versus ξ for increasing values of τ .

 FIGURE 3: Dimensionless torsional rotation θ^* for the fully clamped nanobeam versus ξ for increasing values of τ .

The nonlocality effect is assessed by prescribing the twisting curvature distortion equation (15b)

$$(\chi_t)_{IN} = \frac{(e_0 a)^2}{k_t} \frac{2m}{L^2} x \quad (17)$$

on corresponding (cantilever and fully clamped) local nanobeams. Let us set $\xi = x/L$ and $\theta^*(\xi) = k_t/(mL^2)\theta(\xi)$. Torsional rotations θ^* versus ξ of both the nanobeams are displayed in Figures 2 and 3 for selected values of the nonlocal parameter $\tau := e_0 a/L$.

5. Concluding Remarks

The basic outcomes contributed in the present paper are listed as follows:

- (1) Size-effects in nanobeams under torsion have been evaluated by resorting to the nonlocal theory of elasticity.
- (2) Exact torsional rotations solutions of cross-sections of functionally graded nanobeams have been established for nanocantilevers and fully clamped nanobeams under a quadratic distribution of couples per unit length.
- (3) It has been observed that the stiffness of a nanobeam under torsional loadings is affected by the scale parameter and depends on the boundary kinematic constraints. Indeed, as shown in Figures 2 and 3, contrary to the nanocantilever structural behavior, the fully clamped nanobeam becomes stiffer for increasing values of the nonlocal parameter.

Competing Interests

There is no conflict of interests related to this paper.

References

- [1] R. Barretta, "On Cesàro-Volterra method in orthotropic Saint-Venant beam," *Journal of Elasticity*, vol. 112, no. 2, pp. 233–253, 2013.
- [2] R. Barretta and M. Diaco, "On the shear centre in Saint-Venant beam theory," *Mechanics Research Communications*, vol. 52, pp. 52–56, 2013.
- [3] G. Romano, A. Barretta, and R. Barretta, "On torsion and shear of Saint-Venant beams," *European Journal of Mechanics. A. Solids*, vol. 35, pp. 47–60, 2012.
- [4] R. Barretta, "On stress function in Saint-Venant beams," *Meccanica*, vol. 48, no. 7, pp. 1811–1816, 2013.
- [5] F. Marmo and L. Rosati, "Analytical integration of elasto-plastic uniaxial constitutive laws over arbitrary sections," *International Journal for Numerical Methods in Engineering*, vol. 91, no. 9, pp. 990–1022, 2012.
- [6] F. Marmo and L. Rosati, "The fiber-free approach in the evaluation of the tangent stiffness matrix for elastoplastic uniaxial constitutive laws," *International Journal for Numerical Methods in Engineering*, vol. 94, no. 9, pp. 868–894, 2013.
- [7] L. Rosati and F. Marmo, "Closed-form expressions of the thermo-mechanical fields induced by a uniform heat source acting over an isotropic half-space," *International Journal of Heat and Mass Transfer*, vol. 75, pp. 272–283, 2014.
- [8] F. Marmo and L. Rosati, "A general approach to the solution of Boussinesq's problem for polynomial pressures acting over polygonal domains," *Journal of Elasticity*, vol. 122, no. 1, pp. 75–112, 2016.

- [9] R. Barretta, "Analogies between Kirchhoff plates and Saint-Venant beams under torsion," *Acta Mechanica*, vol. 224, no. 12, pp. 2955–2964, 2013.
- [10] R. Barretta, "Analogies between Kirchhoff plates and Saint-Venant beams under flexure," *Acta Mechanica*, vol. 225, no. 7, pp. 2075–2083, 2014.
- [11] A. M. Tarantino, "Homogeneous equilibrium configurations of a hyperelastic compressible cube under equitriaxial dead-load tractions," *Journal of Elasticity*, vol. 92, no. 3, pp. 227–254, 2008.
- [12] V. A. Salomoni, G. Mazzucco, C. Pellegrino, and C. E. Majorana, "Three-dimensional modelling of bond behaviour between concrete and FRP reinforcement," *Engineering Computations*, vol. 28, no. 1, pp. 5–29, 2011.
- [13] V. A. Salomoni, C. E. Majorana, B. Pomaro, G. Xotta, and F. Gramegna, "Macroscale and mesoscale analysis of concrete as a multiphase material for biological shields against nuclear radiation," *International Journal for Numerical and Analytical Methods in Geomechanics*, vol. 38, no. 5, pp. 518–535, 2014.
- [14] G. Romano, R. Barretta, and M. Diaco, "The geometry of nonlinear elasticity," *Acta Mechanica*, vol. 225, no. 11, pp. 3199–3235, 2014.
- [15] G. Romano, R. Barretta, and M. Diaco, "Geometric continuum mechanics," *Meccanica*, vol. 49, no. 1, pp. 111–133, 2014.
- [16] A. Caporale, R. Luciano, and L. Rosati, "Limit analysis of masonry arches with externally bonded FRP reinforcements," *Computer Methods in Applied Mechanics and Engineering*, vol. 196, no. 1–3, pp. 247–260, 2006.
- [17] A. Caporale and R. Luciano, "Limit analysis of masonry arches with finite compressive strength and externally bonded reinforcement," *Composites Part B: Engineering*, vol. 43, no. 8, pp. 3131–3145, 2012.
- [18] A. Caporale, L. Feo, R. Luciano, and R. Penna, "Numerical collapse load of multi-span masonry arch structures with FRP reinforcement," *Composites Part B: Engineering*, vol. 54, no. 1, pp. 71–84, 2013.
- [19] A. Caporale, L. Feo, D. Hui, and R. Luciano, "Debonding of FRP in multi-span masonry arch structures via limit analysis," *Composite Structures*, vol. 108, no. 1, pp. 856–865, 2014.
- [20] F. Greco and R. Luciano, "A theoretical and numerical stability analysis for composite micro-structures by using homogenization theory," *Composites Part B: Engineering*, vol. 42, no. 3, pp. 382–401, 2011.
- [21] A. M. Tarantino, "Nonlinear fracture mechanics for an elastic Bell material," *The Quarterly Journal of Mechanics and Applied Mathematics*, vol. 50, no. 3, pp. 435–456, 1997.
- [22] A. M. Tarantino, "The singular equilibrium field at the notch-tip of a compressible material in finite elastostatics," *Journal of Applied Mathematics and Physics*, vol. 48, no. 3, pp. 370–388, 1997.
- [23] A. M. Tarantino, "On extreme thinning at the notch tip of a neo-Hookean sheet," *The Quarterly Journal of Mechanics and Applied Mathematics*, vol. 51, no. 2, pp. 179–190, 1998.
- [24] A. M. Tarantino, "On the finite motions generated by a mode I propagating crack," *Journal of Elasticity*, vol. 57, no. 2, pp. 85–103, 1999.
- [25] A. M. Tarantino, "Crack propagation in finite elastodynamics," *Mathematics and Mechanics of Solids*, vol. 10, no. 6, pp. 577–601, 2005.
- [26] V. A. Salomoni, C. E. Majorana, G. M. Giannuzzi, and A. Miliozzi, "Thermal-fluid flow within innovative heat storage concrete systems for solar power plants," *International Journal of Numerical Methods for Heat and Fluid Flow*, vol. 18, no. 7-8, pp. 969–999, 2008.
- [27] F. Marotti de Sciarra and M. Salerno, "On thermodynamic functions in thermoelasticity without energy dissipation," *European Journal of Mechanics. A. Solids*, vol. 46, pp. 84–95, 2014.
- [28] G. Xotta, G. Mazzucco, V. A. Salomoni, C. E. Majorana, and K. J. Willam, "Composite behavior of concrete materials under high temperatures," *International Journal of Solids and Structures*, vol. 64, pp. 86–99, 2015.
- [29] R. Luciano and J. R. Willis, "Bounds on non-local effective relations for random composites loaded by configuration-dependent body force," *Journal of the Mechanics and Physics of Solids*, vol. 48, no. 9, pp. 1827–1849, 2000.
- [30] R. Luciano and J. R. Willis, "Non-local effective relations for fibre-reinforced composites loaded by configuration-dependent body forces," *Journal of the Mechanics and Physics of Solids*, vol. 49, no. 11, pp. 2705–2717, 2001.
- [31] R. Luciano and J. R. Willis, "Boundary-layer corrections for stress and strain fields in randomly heterogeneous materials," *Journal of the Mechanics and Physics of Solids*, vol. 51, no. 6, pp. 1075–1088, 2003.
- [32] R. Luciano and J. R. Willis, "Hashin-Shtrikman based FE analysis of the elastic behaviour of finite random composite bodies," *International Journal of Fracture*, vol. 137, no. 1–4, pp. 261–273, 2006.
- [33] R. De Borst and H.-B. Muehlhaus, "Gradient-dependent plasticity: formulation and algorithmic aspects," *International Journal for Numerical Methods in Engineering*, vol. 35, no. 3, pp. 521–539, 1992.
- [34] E. C. Aifantis, "Strain gradient interpretation of size effects," *International Journal of Fracture*, vol. 95, no. 1–4, pp. 299–314, 1999.
- [35] E. C. Aifantis, "Gradient deformation models at nano, micro, and macro scales," *Journal of Engineering Materials and Technology, Transactions of the ASME*, vol. 121, no. 2, pp. 189–202, 1999.
- [36] R. H. J. Peerlings, R. De Borst, W. A. M. Brekelmans, and J. H. P. De Vree, "Gradient enhanced damage for quasi-brittle materials," *International Journal for Numerical Methods in Engineering*, vol. 39, no. 19, pp. 3391–3403, 1996.
- [37] R. H. J. Peerlings, M. G. D. Geers, R. de Borst, and W. A. M. Brekelmans, "A critical comparison of nonlocal and gradient-enhanced softening continua," *International Journal of Solids and Structures*, vol. 38, no. 44–45, pp. 7723–7746, 2001.
- [38] H. Askes and E. C. Aifantis, "Gradient elasticity in statics and dynamics: an overview of formulations, length scale identification procedures, finite element implementations and new results," *International Journal of Solids and Structures*, vol. 48, no. 13, pp. 1962–1990, 2011.
- [39] D. Ieşan, "Classical and generalized models of elastic rods," in *Modern Mechanics and Mathematics*, D. Gao and R. W. Ogden, Eds., CRC Series, CRC Press, 2008.
- [40] D. Ieşan, "Saint-Venant's problem in micropolar elasticity," in *Mechanics of Micropolar Media*, O. Brulin and R. K. T. Hsieh, Eds., pp. 281–390, World Scientific, Singapore, 1982.
- [41] D. Ieşan, "Generalized twist for the torsion of micropolar cylinders," *Meccanica*, vol. 21, no. 2, pp. 94–96, 1986.
- [42] D. Ieşan, "Generalized torsion of elastic cylinders with microstructure," *Note di Matematica*, vol. 27, no. 2, pp. 121–130, 2007.

- [43] R. D. Gauthier and W. E. Jahsman, "Quest for micropolar elastic constants," *Journal of Applied Mechanics, Transactions ASME*, vol. 42, no. 2, pp. 369–374, 1975.
- [44] G. V. K. Reddy and N. K. Venkatasubramanian, "Saint-Venant's problem for a micropolar elastic circular cylinder," *International Journal of Engineering Science*, vol. 14, no. 11, pp. 1047–1057, 1976.
- [45] G. Dinelli, G. Belz, C. E. Majorana, and B. A. Schrefler, "Experimental investigation on the use of fly ash for lightweight precast structural elements," *Materials and Structures/Materiaux et Constructions*, vol. 29, no. 194, pp. 632–638, 1996.
- [46] J. Peddieson, G. R. Buchanan, and R. P. McNitt, "Application of nonlocal continuum models to nanotechnology," *International Journal of Engineering Science*, vol. 41, no. 3–5, pp. 305–312, 2003.
- [47] J. N. Reddy, "Nonlocal theories for bending, buckling and vibration of beams," *International Journal of Engineering Science*, vol. 45, no. 2–8, pp. 288–307, 2007.
- [48] Q. Wang and K. M. Liew, "Application of nonlocal continuum mechanics to static analysis of micro- and nano-structures," *Physics Letters, Section A: General, Atomic and Solid State Physics*, vol. 363, no. 3, pp. 236–242, 2007.
- [49] M. Aydogdu, "A general nonlocal beam theory: its application to nanobeam bending, buckling and vibration," *Physica E: Low-Dimensional Systems and Nanostructures*, vol. 41, no. 9, pp. 1651–1655, 2009.
- [50] O. Civalek and Ç. Demir, "Bending analysis of microtubules using nonlocal Euler-Bernoulli beam theory," *Applied Mathematical Modelling*, vol. 35, no. 5, pp. 2053–2067, 2011.
- [51] H.-T. Thai and T. P. Vo, "A nonlocal sinusoidal shear deformation beam theory with application to bending, buckling, and vibration of nanobeams," *International Journal of Engineering Science*, vol. 54, pp. 58–66, 2012.
- [52] R. Barretta and F. Marotti De Sciarra, "A nonlocal model for carbon nanotubes under axial loads," *Advances in Materials Science and Engineering*, vol. 2013, Article ID 360935, 6 pages, 2013.
- [53] F. Marotti de Sciarra and R. Barretta, "A gradient model for Timoshenko nanobeams," *Physica E: Low-Dimensional Systems and Nanostructures*, vol. 62, pp. 1–9, 2014.
- [54] R. Barretta, L. Feo, R. Luciano, and F. Marotti de Sciarra, "Application of an enhanced version of the Eringen differential model to nanotechnology," *Composites B*, vol. 96, pp. 274–280, 2016.
- [55] R. Barretta, L. Feo, R. Luciano, F. Marotti de Sciarra, and R. Penna, "Functionally graded Timoshenko nanobeams: a novel nonlocal gradient formulation," *Composites B*, vol. 100, pp. 208–219, 2016.
- [56] B. Arash and Q. Wang, "A review on the application of nonlocal elastic models in modeling of carbon nanotubes and graphenes," *Computational Materials Science*, vol. 51, no. 1, pp. 303–313, 2012.
- [57] R. Rafiee and R. M. Moghadam, "On the modeling of carbon nanotubes: a critical review," *Composites Part B: Engineering*, vol. 56, pp. 435–449, 2014.
- [58] R. Barretta, R. Luciano, and F. M. de Sciarra, "A fully gradient model for Euler-Bernoulli nanobeams," *Mathematical Problems in Engineering*, vol. 2015, Article ID 495095, 8 pages, 2015.
- [59] M. A. Eltaher, S. A. Emam, and F. F. Mahmoud, "Static and stability analysis of nonlocal functionally graded nanobeams," *Composite Structures*, vol. 96, pp. 82–88, 2013.
- [60] F. Marotti de Sciarra, M. Čanadija, and R. Barretta, "A gradient model for torsion of nanobeams," *Comptes Rendus—Mecanique*, vol. 343, no. 4, pp. 289–300, 2015.
- [61] K. A. Lazopoulos and A. K. Lazopoulos, "On the torsion problem of strain gradient elastic bars," *Mechanics Research Communications*, vol. 45, pp. 42–47, 2012.
- [62] A. C. Eringen, "On differential equations of nonlocal elasticity and solutions of screw dislocation and surface waves," *Journal of Applied Physics*, vol. 54, no. 9, pp. 4703–4710, 1983.

Research Article

On Bending of Bernoulli-Euler Nanobeams for Nonlocal Composite Materials

Luciano Feo and Rosa Penna

Department of Civil Engineering, University of Salerno, Via Giovanni Paolo II, 132, 84084 Fisciano, Italy

Correspondence should be addressed to Luciano Feo; l.feo@unisa.it

Received 4 December 2015; Accepted 24 April 2016

Academic Editor: Theodoros C. Rousakis

Copyright © 2016 L. Feo and R. Penna. This is an open access article distributed under the Creative Commons Attribution License, which permits unrestricted use, distribution, and reproduction in any medium, provided the original work is properly cited.

Evaluation of size effects in functionally graded elastic nanobeams is carried out by making recourse to the nonlocal continuum mechanics. The Bernoulli-Euler kinematic assumption and the Eringen nonlocal constitutive law are assumed in the formulation of the elastic equilibrium problem. An innovative methodology, characterized by a lowering in the order of governing differential equation, is adopted in the present manuscript in order to solve the boundary value problem of a nanobeam under flexure. Unlike standard treatments, a second-order differential equation of nonlocal equilibrium elastic is integrated in terms of transverse displacements and equilibrated bending moments. Benchmark examples are developed, thus providing the nonlocality effect in nanocantilever and clamped-simply supported nanobeams for selected values of the Eringen scale parameter.

1. Introduction

Analysis of nanodevices is a subject of special interest in the current literature. Particular attention is given to the static behavior of beam-like components of nanoelectromechanical systems (NEMS). Nonlocal constitutive behaviors are adequate in order to evaluate the size phenomenon in nanostructures; see, for example, [1–9]. Investigations on random elastic structures have been carried out in [10–13]. Many research efforts have been devoted to theoretical and computational advances about specific structural models [14–19]. Recent variational formulations of nonlocal continua have been developed in [20–22]. Noteworthy theoretical results on functionally graded nanobeams have been contributed in [23–25]. Nevertheless, exact solutions are not always available so that finite element strategies are needful; see, for example, [26]. Micromechanical approaches are broadly used in order to analyze the effective behavior of composite structures [27].

Innovative applications of engineering interest are proposed in [28–30]. Numerical and experimental methodologies for composite structures are developed in [31, 32]. Effective applications of tensionless models concerning crack propagation are reported in [33–37]. A skillful analysis of equilibrium configurations of hyperelastic cylindrical bodies and compressible cubes is carried out in [38].

The present paper deals with one-dimensional nanostructure by making recourse to the tools of nonlocal continuum mechanics. Small-scale effects exhibited by functionally graded nanobeams under flexure are analyzed in Section 2.

2. Nonlocal Elasticity

In local linear elasticity for isotropic materials, stress and strain at a point \mathbf{x} of a Cauchy continuum are functionally related by the following classical law:

$$\sigma_{ij}(\mathbf{x}) = 2\mu e_{ij}(\mathbf{x}) + \lambda e_{rr}(\mathbf{x}) \delta_{ij}, \quad (1)$$

with μ and λ LAMÉ constants.

Such a constitutive behavior is not adequate to evaluate size effects in nanostructures. An effective law able to capture scale phenomena was developed by Eringen in [39] who defined the following nonlocal integral operator:

$$\mathbf{t}_{ij}(\mathbf{x}) = \int_V K(|\mathbf{x}' - \mathbf{x}|, \tau) \sigma_{ij}(\mathbf{x}') dV, \quad (2)$$

where

(1) \mathbf{t}_{ij} is the nonlocal stress,

(2) σ_{ij} is the macroscopic stress given by (5),

- (3) K is the influence function,
 (4) $\tau = e_0 a / l$ a dimensionless nonlocal parameter defined in terms of the material constant e_0 and of the internal and external characteristic lengths a and l , respectively.

In agreement with the Eringen proposal in choosing the following influence function $1 - c^2 \nabla^2$, the nonlocal elastic law (2) rewrites as

$$(1 - (e_0 a)^2 \nabla^2) \mathbf{t}_{ij} = \boldsymbol{\sigma}_{ij}, \quad (3)$$

where ∇^2 denotes the Laplace operator. The differential form adopted for bending of nanobeams, analogous to (3), is provided by

$$\bar{\sigma} - c^2 \frac{d^2 \bar{\sigma}}{dx^2} = \sigma, \quad (4)$$

where $\bar{\sigma}$ is the nonlocal normal stress and σ is the macroscopic normal stress on cross sections. Note that the stress σ is expressed in terms of elastic axial strains by

$$\sigma = E \varepsilon, \quad (5)$$

with E Young modulus.

3. Bending of Nonlocal Nanobeams

Let us consider a bent nanobeam of length L , with Young modulus E functionally graded in the cross section Ω and uniform along the beam axis x . The cross-sectional elastic centre and the principal axes of elastic inertia, associated with the scalar field E , are, respectively, denoted by \mathbf{G} and by the pair (y, z) .

The nanobeam is assumed to be subjected in the plane (x, y) to the following loading conditions:

- q_t , distributed load per unit length in the interval $[0, L]$,
- \mathcal{F}_t , concentrated forces at the end cross sections $\{0, L\}$,
- \mathcal{M} , concentrated couples at the end cross sections $\{0, L\}$.

The bending stiffness is defined by

$$k_b := \int_{\Omega} E y^2 dA. \quad (6)$$

Differential and boundary conditions of equilibrium are expressed by

$$\begin{aligned} \frac{d^2 M_b}{dx^2} &= q_t, & \text{in } [0, L], \\ \frac{dM_b}{dx} &= \pm \mathcal{F}_t, & \text{at } \{0, L\}, \\ M_b &= \mp \mathcal{M}, & \text{at } \{0, L\}, \end{aligned} \quad (7)$$

where M_b is the bending moment.

The bending curvature, corresponding to the transverse displacement v , is given by

$$\chi(x) = \frac{d^2 v}{dx^2}(x). \quad (8)$$

The differential equation of nonlocal elastic equilibrium of a nanobeam under flexure is formulated as follows. Let us preliminarily multiply (4) by the coordinate y along the bending axis and integrate on the cross section Ω :

$$\int_{\Omega} \bar{\sigma} y dA - (e_0 a)^2 \int_{\Omega} \frac{d^2 \bar{\sigma}}{dx^2} y dA = \int_{\Omega} E \varepsilon y dA, \quad (9)$$

with the axial dilation provided by the known formula $\varepsilon(x) = -\chi(x)y$.

Enforcing (8) and (7)₁ and imposing the static equivalence condition

$$M_b = - \int_{\Omega} \sigma y dA, \quad (10)$$

we obtain the relation

$$M_b - (e_0 a)^2 q_t = k_b \frac{d^2 v}{dx^2}. \quad (11)$$

This equation can be interpreted as decomposition formula of the bending curvature $\chi_b = d^2 v / dx^2$ into elastic χ_{EL} and inelastic χ_{IN} parts

$$\chi_b = \chi_{EL} + \chi_{IN}, \quad (12)$$

with

$$\begin{aligned} \chi_{EL} &= \frac{M_b}{k_b}, \\ \chi_{IN} &= - \frac{(e_0 a)^2}{k_b} q_t. \end{aligned} \quad (13)$$

Accordingly, the scale effect exhibited by bending moments and displacements of a FG nonlocal nanobeam can be evaluated by solving a corresponding linearly elastic beam subjected to the bending curvature distortion χ_{IN} (13)₂.

4. Examples

The solution methodology of the nonlocal elastic equilibrium problem of a nanobeam enlightened in the previous section is here adopted in order to assess small-scale effects in nanocantilever and clamped-simply supported nanobeams under a uniformly distributed load q_t . The nonlocality effect on the transverse displacement is thus due to the uniform bending curvature distortion formulated in (13)₂. Graphical evidences of the elastic displacements are provided in Figures 1 and 2, in terms of the following dimensionless parameters $\xi = x/L$ and $v^*(\xi) = (100k_b)/(q_t L^4) v(\xi)$, for selected values of the nonlocal parameter $\tau := e_0 a / L$. Details of the calculations and some comments are reported below.

4.1. Cantilever Nanobeam. The bending moment is given by

$$M_b(x) = \frac{q_t}{2} x^2 - q_t L x + \frac{q_t L^2}{2}. \quad (14)$$

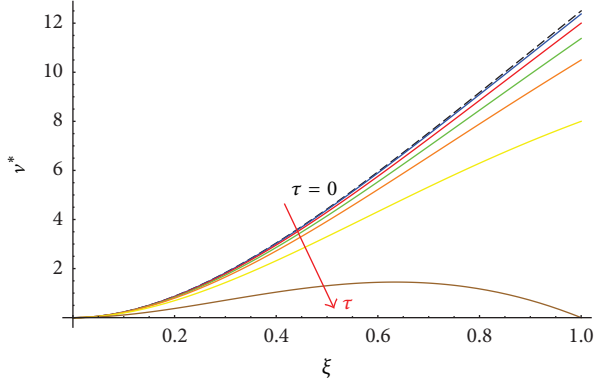


FIGURE 1: Dimensionless transverse displacements v^* for the nanocantilever versus ξ for $\tau \in \{0, 0.05, 0.1, 0.15, 0.2, 0.3, 0.5\}$.

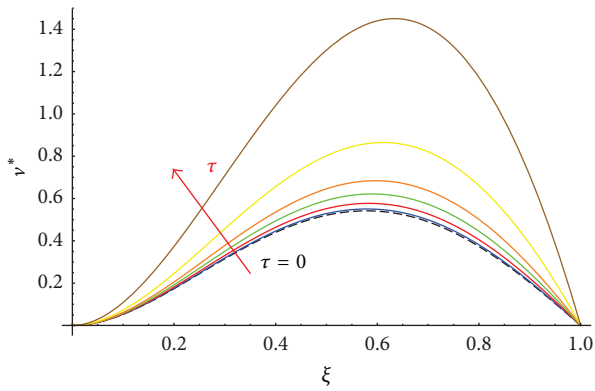


FIGURE 2: Dimensionless transverse displacement v^* for the clamped-simply supported nanobeam versus ξ for $\tau \in \{0, 0.05, 0.1, 0.15, 0.2, 0.3, 0.5\}$.

The l.h.s. of (11) is hence known, so that the differential condition of nonlocal elastic equilibrium to be integrated writes explicitly as

$$k_b \frac{d^2 v}{dx^2}(x) = M_b(x) - \tau^2 L^2 q_t. \quad (15)$$

The general integral of (15) takes the form

$$v(x) = ax + b + \bar{v}(x), \quad (16)$$

where

$$\bar{v}(x) = -\frac{q_t}{24k_b} x^4 + \frac{q_t L}{6k_b} x^3 - \frac{q_t L^2}{4} x^2 - \frac{\tau^2 L^2 q_t}{2k_b} x^2 \quad (17)$$

is a particular solution of (15). The evaluation of the integration constants a and b is carried out by prescribing the boundary conditions

$$\begin{aligned} v(0) &= 0, \\ \frac{dv}{dx}(0) &= 0. \end{aligned} \quad (18)$$

The transversal deflection follows by a direct computation

$$v(x) = \frac{q_t}{24k_b} x^4 - \frac{q_t L}{6k_b} x^3 + \frac{q_t L^2}{4k_b} x^2 - \frac{\tau^2 q_t L^2}{2k_b} x^2. \quad (19)$$

The maximum displacement is given by

$$v_m = v(L) = \left(\frac{1}{8} - \frac{\tau^2}{2} \right) \frac{q_t L^4}{k_b}. \quad (20)$$

Nanocantilever becomes stiffer with increasing the nonlocal parameter τ . Indeed, according to the analysis proposed in Section 3, the sign of the prescribed distortion χ_{IN} , describing the nonlocality effect, is opposite to the one of the elastic curvature χ_{EL} . In particular, the displacement of the free end vanishes if $\tau = 0.5$ (see Figure 1) according to (20).

It is worth noting that, with the structure being statically determinate, the bending moment (14) is not affected by the scale phenomenon.

4.2. *Clamped-Simply Supported Nanobeam.* Equilibrated bending moments are provided by the relation

$$M_b(x) = a_1(x-L) + \frac{q_t L^2}{2} - \frac{q_t}{2} x^2, \quad (21)$$

with $a_1 \in \mathcal{R}$ being an arbitrary constant. The differential condition of nonlocal elastic equilibrium (11) to be integrated takes thus the form

$$-k_b \frac{d^2 v}{dx^2}(x) = a_1(x-L) + \frac{q_t L^2}{2} - \frac{q_t}{2} x^2 + \tau^2 L^2 q_t. \quad (22)$$

Equation (22) is solved by imposing the following kinematic boundary conditions:

$$\begin{aligned} v(0) &= 0, \\ \frac{dv}{dx}(0) &= 0, \\ v(L) &= 0. \end{aligned} \quad (23)$$

A direct computation gives the transversal displacement field

$$v(x) = \frac{q_t}{24k_b} x^4 - \frac{5q_t L}{48k_b} x^3 + \frac{q_t L^2}{16k_b} x^2 + \frac{\tau^2 q_t L}{4k_b} x^2 (L-x) \quad (24)$$

and the bending moment

$$M_b(x) = \frac{q_t}{2} x^2 - \frac{q_t L}{2} \left(\frac{5}{4} + 3\tau^2 \right) x + \frac{q_t L^2}{2} \left(3\tau^2 + \frac{1}{4} \right). \quad (25)$$

The maximum displacement is given by

$$v_m = v(\bar{x}), \quad (26)$$

with $\bar{x} = 3L((3/2)(5/24 + \tau^2/2) - \sqrt{(9/16)\tau^4 + 11/768 + (13/96)\tau^2})$ solution of the equation (the known local maximum point $\bar{x} \approx 0.578L$ is recovered by setting $\tau = 0$) ($dv/dx(x) = 0$).

In agreement with the equivalence method exposed in Section 3, (24) and (25) provide the deflection and

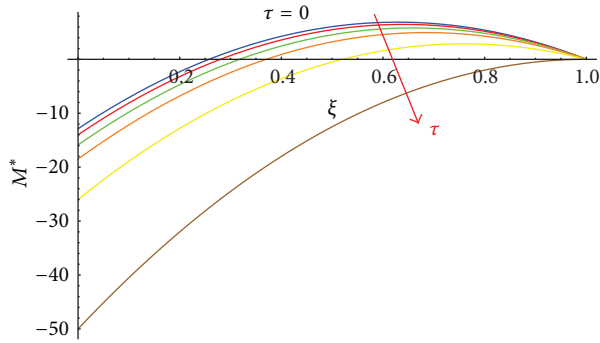


FIGURE 3: Dimensionless bending moment M^* versus dimensionless abscissa ξ of a clamped-simply supported nanobeam.

bending moment of a corresponding local nanobeam under the transversal load distribution q_t and the distortion χ_{IN} equivalent to the nonlocality effect.

A plot of the dimensionless bending moment $M^* = -(100/q_t L^2)M$ versus the dimensionless parameter $\xi = x/L$ is given in Figure 3 for increasing values of the nonlocal parameter τ .

5. Conclusion

The Eringen nonlocal law has been used in order to assess size effects in nanobeams formulated according to the Bernoulli-Euler kinematics. The treatment extends to functionally graded materials the analysis carried out in [24] under the special assumption of elastically homogeneous nanobeams. Transverse deflections of cantilever and clamped-simply supported nanobeams have been established for different values of the nonlocal parameter. Such analytical solutions could be conveniently adopted by other scholars as simple reference examples for numerical evaluations in nonlocal composite mechanics.

Competing Interests

The authors declare that they have no competing interests.

References

- [1] R. de Borst and H.-B. Muehlhaus, "Gradient-dependent plasticity: formulation and algorithmic aspects," *International Journal for Numerical Methods in Engineering*, vol. 35, no. 3, pp. 521–539, 1992.
- [2] E. C. Aifantis, "Gradient deformation models at nano, micro, and macro scales," *Journal of Engineering Materials and Technology*, vol. 121, pp. 189–202, 1999.
- [3] B. Arash and Q. Wang, "A review on the application of nonlocal elastic models in modeling of carbon nanotubes and graphenes," *Computational Materials Science*, vol. 51, no. 1, pp. 303–313, 2012.
- [4] R. Rafiee and R. M. Moghadam, "On the modeling of carbon nanotubes: a critical review," *Composites Part B: Engineering*, vol. 56, pp. 435–449, 2014.
- [5] J. N. Reddy, "Nonlocal theories for bending, buckling and vibration of beams," *International Journal of Engineering Science*, vol. 45, no. 2–8, pp. 288–307, 2007.
- [6] Ö. Civalek and Ç. Demir, "Bending analysis of microtubules using nonlocal Euler-Bernoulli beam theory," *Applied Mathematical Modelling*, vol. 35, no. 5, pp. 2053–2067, 2011.
- [7] H.-T. Thai and T. P. Vo, "A nonlocal sinusoidal shear deformation beam theory with application to bending, buckling, and vibration of nanobeams," *International Journal of Engineering Science*, vol. 54, pp. 58–66, 2012.
- [8] Q. Wang and K. M. Liew, "Application of nonlocal continuum mechanics to static analysis of micro- and nano-structures," *Physics Letters A*, vol. 363, no. 3, pp. 236–242, 2007.
- [9] R. Barretta, L. Feo, R. Luciano, and F. Marotti de Sciarra, "Application of an enhanced version of the Eringen differential model to nanotechnology," *Composites Part B: Engineering*, vol. 96, pp. 274–280, 2016.
- [10] R. Luciano and J. R. Willis, "Bounds on non-local effective relations for random composites loaded by configuration-dependent body force," *Journal of the Mechanics and Physics of Solids*, vol. 48, no. 9, pp. 1827–1849, 2000.
- [11] R. Luciano and J. R. Willis, "Non-local constitutive response of a random laminate subjected to configuration-dependent body force," *Journal of the Mechanics and Physics of Solids*, vol. 49, no. 2, pp. 431–444, 2001.
- [12] R. Luciano and J. R. Willis, "Boundary-layer corrections for stress and strain fields in randomly heterogeneous materials," *Journal of the Mechanics and Physics of Solids*, vol. 51, no. 6, pp. 1075–1088, 2003.
- [13] R. Luciano and J. R. Willis, "Hashin-Shtrikman based FE analysis of the elastic behaviour of finite random composite bodies," *International Journal of Fracture*, vol. 137, no. 1–4, pp. 261–273, 2006.
- [14] A. Caporale, R. Luciano, and L. Rosati, "Limit analysis of masonry arches with externally bonded FRP reinforcements," *Computer Methods in Applied Mechanics and Engineering*, vol. 196, no. 1–3, pp. 247–260, 2006.
- [15] F. Marmo and L. Rosati, "Analytical integration of elasto-plastic uniaxial constitutive laws over arbitrary sections," *International Journal for Numerical Methods in Engineering*, vol. 91, no. 9, pp. 990–1022, 2012.
- [16] F. Marmo and L. Rosati, "The fiber-free approach in the evaluation of the tangent stiffness matrix for elastoplastic uniaxial constitutive laws," *International Journal for Numerical Methods in Engineering*, vol. 94, no. 9, pp. 868–894, 2013.
- [17] R. Barretta, "Analogies between Kirchhoff plates and Saint-Venant beams under flexure," *Acta Mechanica*, vol. 225, no. 7, pp. 2075–2083, 2014.
- [18] L. Rosati and F. Marmo, "Closed-form expressions of the thermo-mechanical fields induced by a uniform heat source acting over an isotropic half-space," *International Journal of Heat and Mass Transfer*, vol. 75, pp. 272–283, 2014.
- [19] F. Marmo and L. Rosati, "A general approach to the solution of boussinesq's problem for polynomial pressures acting over polygonal domains," *Journal of Elasticity*, vol. 122, no. 1, pp. 75–112, 2016.
- [20] F. Marotti de Sciarra and M. Salerno, "On thermodynamic functions in thermoelasticity without energy dissipation," *European Journal of Mechanics—A/Solids*, vol. 46, pp. 84–95, 2014.
- [21] F. Marotti de Sciarra, "Finite element modelling of nonlocal beams," *Physica E*, vol. 59, pp. 144–149, 2014.

- [22] F. Marotti de Sciarra and R. Barretta, "A new nonlocal bending model for Euler-Bernoulli nanobeams," *Mechanics Research Communications*, vol. 62, no. 1, pp. 25–30, 2014.
- [23] R. Barretta, R. Luciano, and F. Marotti de Sciarra, "A fully gradient model for Euler-Bernoulli nanobeams," *Mathematical Problems in Engineering*, vol. 2015, Article ID 495095, 8 pages, 2015.
- [24] R. Barretta and F. Marotti de Sciarra, "Analogies between nonlocal and local Bernoulli-Euler nanobeams," *Archive of Applied Mechanics*, vol. 85, no. 1, pp. 89–99, 2015.
- [25] R. Barretta, L. Feo, R. Luciano, F. Marotti de Sciarra, and R. Penna, "Functionally graded Timoshenko nanobeams: a novel nonlocal gradient formulation," *Composites Part B: Engineering*, vol. 100, pp. 208–219, 2016.
- [26] F. Greco and R. Luciano, "A theoretical and numerical stability analysis for composite micro-structures by using homogenization theory," *Composites Part B: Engineering*, vol. 42, no. 3, pp. 382–401, 2011.
- [27] A. Caporale, L. Feo, D. Hui, and R. Luciano, "Debonding of FRP in multi-span masonry arch structures via limit analysis," *Composite Structures*, vol. 108, no. 1, pp. 856–865, 2014.
- [28] V. A. Salomoni, C. Majorana, G. M. Giannuzzi, and A. Miliuzzi, "Thermal-fluid flow within innovative heat storage concrete systems for solar power plants," *International Journal of Numerical Methods for Heat & Fluid Flow*, vol. 18, pp. 969–999, 2008.
- [29] V. A. Salomoni, G. Mazzucco, C. Pellegrino, and C. E. Majorana, "Three-dimensional modelling of bond behaviour between concrete and FRP reinforcement," *Engineering Computations*, vol. 28, no. 1, pp. 5–29, 2011.
- [30] V. A. Salomoni, C. E. Majorana, B. Pomaro, G. Xotta, and F. Gramegna, "Macroscale and mesoscale analysis of concrete as a multiphase material for biological shields against nuclear radiation," *International Journal for Numerical and Analytical Methods in Geomechanics*, vol. 38, no. 5, pp. 518–535, 2014.
- [31] G. Dinelli, G. Belz, C. E. Majorana, and B. A. Schrefler, "Experimental investigation on the use of fly ash for lightweight precast structural elements," *Materials and Structures*, vol. 29, no. 194, pp. 632–638, 1996.
- [32] G. Xotta, G. Mazzucco, V. A. Salomoni, C. E. Majorana, and K. J. Willam, "Composite behavior of concrete materials under high temperatures," *International Journal of Solids and Structures*, vol. 64, pp. 86–99, 2015.
- [33] A. M. Tarantino, "Nonlinear fracture mechanics for an elastic Bell material," *The Quarterly Journal of Mechanics & Applied Mathematics*, vol. 50, part 3, pp. 435–456, 1997.
- [34] A. M. Tarantino, "The singular equilibrium field at the notch-tip of a compressible material in finite elastostatics," *Journal of Applied Mathematics and Physics*, vol. 48, no. 3, pp. 370–388, 1997.
- [35] A. M. Tarantino, "On extreme thinning at the notch-tip of a neo-Hookean sheet," *The Quarterly Journal of Mechanics & Applied Mathematics*, vol. 51, part 2, pp. 179–190, 1998.
- [36] A. M. Tarantino, "On the finite motions generated by a mode I propagating crack," *Journal of Elasticity*, vol. 57, no. 2, pp. 85–103, 1999.
- [37] A. M. Tarantino, "Crack propagation in finite elastodynamics," *Mathematics and Mechanics of Solids*, vol. 10, no. 6, pp. 577–601, 2005.
- [38] A. M. Tarantino, "Homogeneous equilibrium configurations of a hyperelastic compressible cube under equitriaxial dead-load tractions," *Journal of Elasticity*, vol. 92, no. 3, pp. 227–254, 2008.
- [39] A. C. Eringen, "On differential equations of nonlocal elasticity and solutions of screw dislocation and surface waves," *Journal of Applied Physics*, vol. 54, no. 9, pp. 4703–4710, 1983.

Research Article

Finite Thin Cover on an Orthotropic Elastic Half Plane

Federico Oyedeji Falope¹ and Enrico Radi²

¹*DIEF, Department of Engineering Enzo Ferrari, University of Modena and Reggio Emilia, Via P. Vivarelli 10 Int. 27, 41125 Modena, Italy*

²*DISMI, Department of Sciences and Methods for Engineering, University of Modena and Reggio Emilia, Via Amendola 2, 42122 Reggio Emilia, Italy*

Correspondence should be addressed to Enrico Radi; eradi@unimore.it

Received 24 December 2015; Accepted 5 October 2016

Academic Editor: Julius Kaplunov

Copyright © 2016 F. O. Falope and E. Radi. This is an open access article distributed under the Creative Commons Attribution License, which permits unrestricted use, distribution, and reproduction in any medium, provided the original work is properly cited.

The present work deals with the mechanical behaviour of thin films bonded to a homogeneous elastic orthotropic half plane under plain strain condition and infinitesimal strain. Both the film and semi-infinite substrate display linear elastic orthotropic behaviour. By assuming perfect adhesion between film and half plane together with membrane behaviour of the film, the compatibility condition between the coating and substrate leads to a singular integral equation with Cauchy kernel. Such an equation is straightforwardly solved by expanding the unknown interfacial stress in series of Chebyshev polynomials displaying square-root singularity at the film edges. This approach allows handling the singular behaviour of the shear stress and, in turn, reducing the problem to a linear algebraic system of infinite terms. Results are found for two loading cases, with particular reference to concentrated axial forces acting at the edges of the film. The corresponding mode II stress intensity factor has been assessed, thus providing the stress concentrations at both ends of the covering. Possible applications of the results here obtained range from MEMS, NEMS, and solar Silicon cell for energy harvesting to welded joint and building foundation.

1. Introduction

A wide class of MEMS and NEMS are based on thin films and coatings technology and the most part of these microdevices involves film and substrate materials which exhibit anisotropic behaviour [1]. As an example, a crystalline undulator (CU) is a special kind of MEMS realized by properly patterning [2, 3], through a suitable photolithographic process, a coated ceramic substrate [4, 5] which generally consists of a silicon (Si) or germanium (Ge) crystalline plate. As shown in [4], based on the channeling phenomenon, a CU can be used as a compact source of intense and coherent electromagnetic waves, with particular reference to UV and hard X-rays.

Thin films and coatings are also widely used as thermal barriers and protective layers to shield compressors, internal combustion engines, and turbine engine components from gaseous and aqueous aggressive environments in order to prevent excessive wear and oxidation [6].

Thin films and coatings are usually employed for the realization of modern optical devices also, with particular reference to high-reflectance mirrors and lens in the interferometry and spectroscopy fields (optical filters, telescopes, binoculars, etc.).

In the field of civil engineering, sheets or fibre reinforced stiffeners are often modeled as thin membranes bonded to an elastic substrate simulating concrete [7–11] or rigid road pavement [12] (a viscoelastic analysis performed on variable structural systems can be found in [13, 14]). As a rough approximation, these problems have been modeled by considering beams resting on an elastic support (e.g., [15]).

Thin films and coatings bonded to an elastic substrate generate geometric discontinuities and, in turn, stress concentrations and strain localizations which can drive damaging phenomena like delamination and crack growth. These phenomena can be properly modeled in the framework of both infinitesimal [16, 17] and finite elastostatics [18–22]. In order to accurately evaluate the mechanical behaviour of this

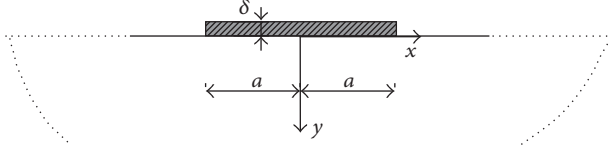


FIGURE 1: Half plane and film's geometry.

kind of micro- or nanosystems, the actual physical properties of the film and substrate materials must be taken into account and the accurate evaluation of the stress and strain fields, particularly along the interface, is mandatory (for nonhomogeneous graded films, nanobeams, and nanoplates, see, e.g., [23–26]).

The mechanical interaction between a thin film and an isotropic half plane has been widely investigated by many researchers through analytical models [5, 27–29] or via numerical analyses [30–32]. The present study investigates the mechanical interaction between a thin elastic film and an elastic orthotropic half plane under various loading conditions. In particular, the present work extends the results obtained in [5] by taking into account anisotropic behaviour of the substrate. The analysis has been performed by assuming plane strain conditions for both the film and the half plane. Moreover, the film is assumed very thin, thus allowing for neglecting its bending stiffness. The strain compatibility condition between the film and the underlying substrate leads to a singular integral equation with Cauchy kernel. By expanding the unknown interfacial shear stress in singular series of Chebyshev polynomials, the integral equation is reduced to an algebraic linear system of infinite terms which is solved for the coefficients of the series expansion. The shear stress intensity factors are then evaluated and compared for two different cases.

The paper is organized as follows: the formulation of the problem in terms of singular integral equation with the Cauchy kernel is presented in Section 2. In Section 3, effective values for material and geometric parameters governing the problem are quantified. The effect induced by the slenderness of the film with respect to the compliance of the half plane is discussed in Section 4 by studying two different loading cases γ . Finally, conclusions are drawn in Section 5.

2. Half Plane Covered by Thin Film

In the present section, the problem of an orthotropic elastic half plane covered by a thin film and subjected to two opposite or concordant axial loads (Figures 1 and 2) is treated. Perfect adhesion between the half plane and the film and negligible bending stiffness of the film have been assumed also. The present analysis could also be extended by assuming a proper constitutive law for the interface in order to simulate imperfect welding, detachment, and so on (e.g., [39]). Under these statements, only the tangential component of the interfacial stress arises within the contact

region (Figure 2). The strain fields along the contact region can be written in terms of the interface shear stress $\tau(x)$ by using Green's function for the elastic half plane and by the membrane constitutive equation:

$$\begin{aligned}\varepsilon_F &= K_F \int_x^a \tau(t) dt - \Delta\varepsilon, \\ \varepsilon_S &= \frac{K_S}{\pi} \int_{-a}^a \frac{\tau(t)}{y-t} dt.\end{aligned}\quad (1)$$

Then, the compatibility condition under perfect adhesion assumption leads to the following integral equation:

$$K_F \int_x^a \tau(t) dt - \Delta\varepsilon = \frac{K_S}{\pi} \int_{-a}^a \frac{\tau(t)}{x-t} dt, \quad (2)$$

where K_i ($i = F, S$ stands for “film” or “substrate,” resp.; see (A.3)) represents the compliance of the i component. The load term, $\Delta\varepsilon$, has been considered acting on the film only; namely,

$$\begin{aligned}\Delta\varepsilon &= -FK_F, \\ \Delta\varepsilon &= - \left[\left(1 + \frac{\alpha_{3F}}{\alpha_{1F}} \gamma_{31} \right) \alpha_S - \left(1 + \frac{\alpha_{3S}}{\alpha_{1F}} \right) \alpha_F \right] \Delta T,\end{aligned}\quad (3)$$

for the case of two opposite axial forces of magnitude F or thermal load variation ΔT , respectively (for a detailed study about the thermoelasticity without energy dissipation, see [40]). By using the Chebyshev polynomials of the first kind, $T_n(t)$, the following series expansion has been assumed for the shear stress:

$$\tau(x) = \frac{\sum_{n=0}^{\infty} C_n T_n(x/a)}{K_S \sqrt{1 - (x/a)^2}}, \quad \text{for } -a \leq x \leq a. \quad (4)$$

Introducing the series expansion (4) in (2) using the orthogonality properties of Chebyshev polynomials (Appendix B), multiplying by Chebyshev polynomials of second type $U_{m-1}(t)$ with $m = 0, 1, 2, \dots$, and integrating over $[-a, +a]$, the integral equation is transformed in a linear algebraic system for the unknown coefficient C_n . From (2) and (4), it follows that

$$\begin{aligned}\sum_{n=1}^{\infty} C_n \left[\frac{\pi\gamma}{2n} \delta_{nm} + B_{nm} \right] \\ = \Delta\varepsilon \left\{ \frac{1 - \cos(m\pi)}{m} + \frac{1 - \cos[(m+1)\pi]}{\gamma\pi} \right\}\end{aligned}\quad (5)$$

$$B_{nm} = \int_{-1}^{+1} U_{n-1}(\xi) U_{m-1}(\xi) d\xi, \quad \text{with } m = 1, 2, \dots, \quad (6)$$

where $\gamma = aK_F/K_S$ is a dimensionless parameter which governs the problem, whose role will be discussed in Section 4, and δ_{nm} is the Kronecker delta, respectively.

For the loading case sketched in Figure 2(b), the coefficient C_0 is provided by (4) together with the equilibrium condition of the film:

$$C_0 = \frac{\Delta\varepsilon}{\gamma\pi}. \quad (7)$$

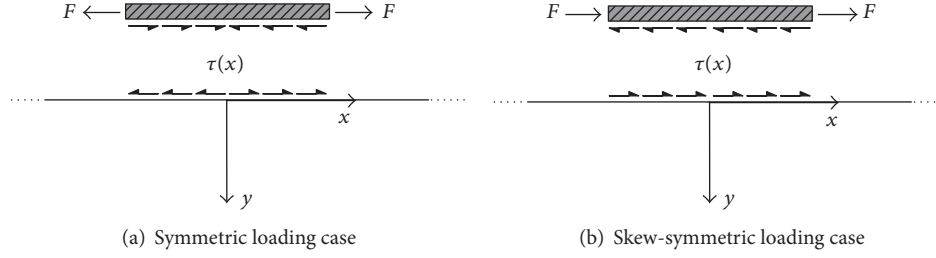


FIGURE 2: Loading cases.

By introducing the dimensionless variable $\xi = x/a$ over the contact domain, the solution of system (5) with respect to the series coefficient provides

$$\epsilon_x^S(\xi) = \sum_{n=1,2,3}^{\infty} C_n U_{n-1}(\xi), \quad (8)$$

$$\epsilon_x^F(\xi) = -\Delta\epsilon + \gamma \left[C_0 \arccos(\xi) + \sum_{n=1}^{\infty} C_n \frac{U_{n-1}(\xi)}{n} \sqrt{1-\xi^2} \right], \quad (9)$$

$$\tau(\xi) = \frac{1}{K_S \sqrt{1-\xi^2}} \sum_{n=0}^{\infty} C_n T_n(\xi), \quad (10)$$

$$\sigma_x^F(\xi) = \frac{\epsilon_y^F(\xi)}{\delta K_F}, \quad (11)$$

$$u^F(\xi) = a \left\{ -\Delta\epsilon\xi + \gamma \left[C_0 \left(1 - \sqrt{1-\xi^2} + \xi \arccos(\xi) \right) + C_1 \frac{\arccos(\xi) + \xi \sqrt{1-\xi^2}}{2} + \sum_{n=2}^{\infty} \frac{C_n n T_n(\xi) - \xi U_{n-1}(\xi)}{n^2 - 1} \right] \right\}, \quad (12)$$

with ϵ_x , τ , σ_x , and u being the longitudinal strain, shear stress, longitudinal stress, and longitudinal displacement, respectively. As a result of the assumption of perfect adhesion between the half plane and the film, expressions (8) and (9) must coincide.

3. Influence of the Parameter γ

The dimensionless parameter γ denotes the ratio between the substrate and film compliances. This factor governs the problem and affects the convergence of the Chebyshev series and the stress intensity factor K_{II} at the edges of the film.

Values of parameter γ , for different typical materials and film geometries involved in contact problems, can be found in Tables 1 and 2, respectively.

TABLE 1: Some materials involved in contact problems application.

Material	Ref	δK_F [$N^{-1}mm^2$]	K_S [$N^{-1}mm^2$]
Seabed soil	[33]	$9.97E-1$	1.27
Ice	[34]	$9.76E-3$	$9.82E-3$
Structural steel	[35]	$4.33E-5$	$8.67E-5$
Beech	[36]	$4.32E-5$	$8.44E-5$
Silicon nitride	[37]	$3.23E-5$	$6.47E-5$
Aluminium	[34]	$1.22E-5$	$2.44E-5$
Silicon	[38]	$5.15E-6$	$1.21E-5$
Spruce	[36]	$1.45E-6$	$4.88E-6$
Germanium	[34]	$8.89E-7$	$3.84E-6$

TABLE 2: Range of film length ratio in contact problems applications.

	Welded or bolted plates	Cu and silicon solar cells	Ice lenses	Slab foundations
$\frac{a}{\delta}$	10^1-10^2	10^3-10^4	10^2-10^3	10^2-10^3

The limit case occurring for high values of γ , ranging within $[10^{-1}, 10^2]$, is representative of contact problems met in MEMS and NEMS application. In this case, the half plane is stiffer than the film.

The other limit case concerns low values of γ , ranging within $[10^{-3}, 10^{-6}]$, occurring when the stiffness of the half plane is more compliant than the film or when the film has a squat geometry, typically involved in soil contact application.

4. Results and Discussion

Two different loading conditions, sketched in Figure 2, have been analysed. The Chebyshev coefficient index has been assumed odd or even including C_0 , for symmetric and skew-symmetric loading cases, respectively. The proper superposition of the two schemes provides the same results reported in [5], where an isotropic film subjected to a single axial force applied to a film end has been studied.

As reported in [27, 28, 41], both the high speed convergence of the coefficients C_n and the regularity of system (5) depend on the parameter γ . By truncating the Chebyshev series to $n = 40$ (20 terms in series expansion), Figure 3 and Table 3 show the convergence of the Chebyshev coefficients.

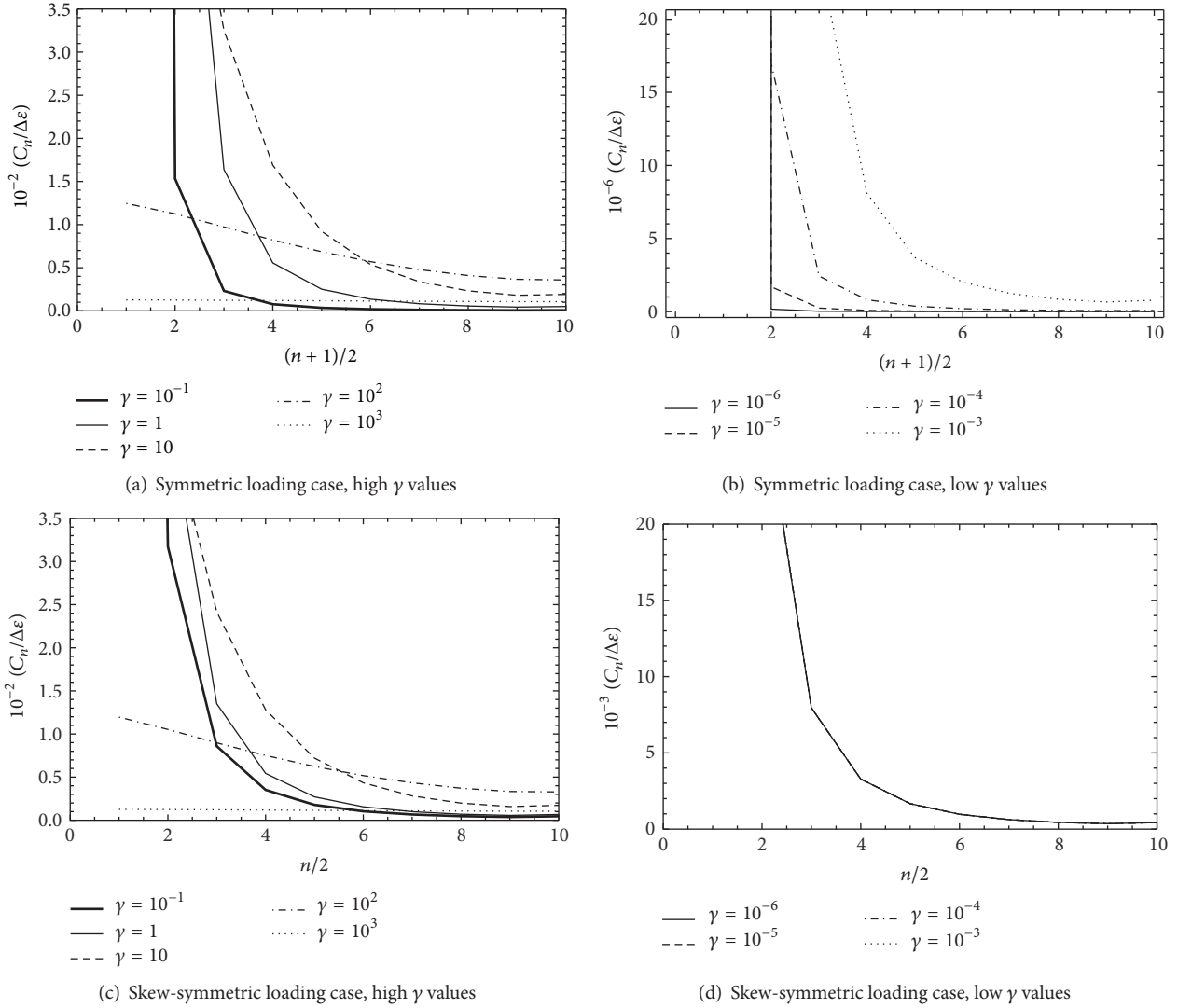


FIGURE 3: Convergence of Chebyshev coefficients.

TABLE 3: Sensibility of C_n with respect to γ .

γ	Symmetric load			Skew-symmetric load		
	$\frac{C_1}{\Delta\epsilon}$	$\frac{C_3}{\Delta\epsilon}$	$\frac{C_5}{\Delta\epsilon}$	$\frac{C_2}{\Delta\epsilon}$	$\frac{C_4}{\Delta\epsilon}$	$\frac{C_6}{\Delta\epsilon}$
10^{-3}	0.99	0.0161	0.0024	0.36	0.0288	0.00795
10^{-1}	0.92	0.0153	0.0023	0.34	0.0317	0.00859
10^0	0.54	0.0762	0.0163	0.27	0.0478	0.0135
10^1	0.10	0.0627	0.0325	0.08	0.0469	0.0241
10^2	0.012	0.0112	0.0097	0.01	0.010	0.00897

The convergence rate of the series decreases as γ increases. For $\gamma > 10$, the rate of convergence for the coefficients C_n becomes faster. The symmetric loading case exhibits higher convergence speed than the skew-symmetric case.

Under symmetric loading (Figure 2(a)), the longitudinal strain of the substrate (Figure 4) exhibits high sensitivity with respect to the governing parameter only for large value γ ; instead, for small value of γ , no significant impact on the

strain behaviour is detected. For $\gamma < 10^{-4}$, the film behaves like a rigid body. Similar to the strain field, the longitudinal displacement increases as the film's compliance increases with γ (Figure 5). For low values of γ , the film displacement varies linearly and attains a maximum value $a\Delta\epsilon$ at the film edges. For large values of γ , the axial stress of the film displays an oscillatory behaviour induced by the low convergence rate of the Chebyshev coefficient and by the high gradient of stress

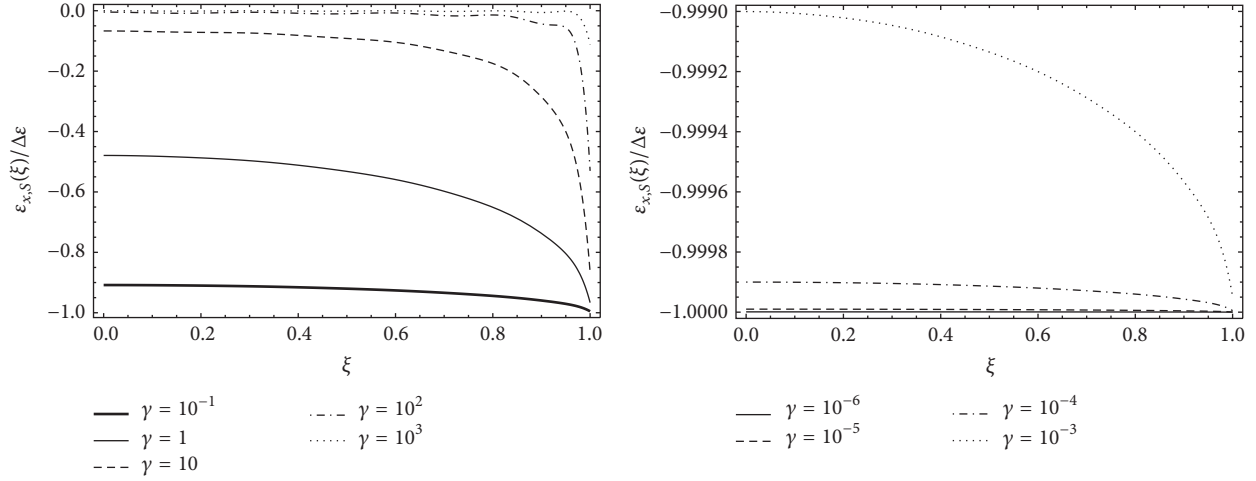


FIGURE 4: Longitudinal strain field for symmetric loading case.

field in the neighbourhood of the film's edges (Figure 5). As γ increases, the magnitude of shear stress field increases and its gradient decreases at the film edge (Figure 2(a)). This behaviour is explained by the stress intensity factor K_{II} at the films edge which monotonically decreases as γ increases (Figure 6).

For the symmetric loading case, the stress intensity factor is defined as proposed by [5]:

$$\begin{aligned} K_{II}(\pm 1) &= \lim_{\xi \rightarrow \pm 1} \tau(\xi) \sqrt{2\pi(\xi \mp 1)} \\ &= \sqrt{\pi} \sum_{n=1,3,\dots}^{\infty} \frac{C_n T_n(\xi)}{K_S}. \end{aligned} \quad (13)$$

In agreement with the asymptotic solution for isotropic materials in [28], for inextensible films, one finds

$$\lim_{\gamma \rightarrow 0} \sum_{n=1,3,\dots}^{\infty} \frac{C_n T_n}{\Delta \varepsilon} = \frac{C_1}{\Delta \varepsilon} = 1, \quad (14)$$

and the stress intensity factor then becomes

$$K_{II}(\xi = \pm 1) = \pm \sqrt{\pi} \frac{\Delta \varepsilon}{K_S} \quad (15)$$

in agreement with the value found in [5, 42] for isotopic constitutive law. By scaling, the term $\sqrt{2\pi}$ from the definition of the stress intensity factor (13) provides $K_{II}(\xi = \pm 1) = 0.707$, corresponding to the mode II stress intensity factor at crack tip, induced by the stress component $\tau(\xi = \pm 1)$ which may cause crack propagation along the $\pm\pi/4$ direction.

The same conclusion drawn about the stress and displacement fields under symmetric loading conditions could be extended to skew-symmetric loading condition (Figures 7 and 8) with the exception of the convergence rate and the stress intensity factor which are less sensible to the parameter γ .

Differently from the symmetric loading case, the singularity of the shear stress field is proportional by the Chebyshev

constant C_0 (7). The mode II of the stress intensity factor of the stress intensity factor assumes the following form:

$$\begin{aligned} K_{II}(\xi = \pm 1) &= \lim_{\xi \rightarrow \pm 1} \tau(\xi) \frac{\sqrt{2\pi(\xi \mp 1)}}{C_0} \\ &= \sqrt{\pi} \frac{\Delta \varepsilon}{K_S} \left(1 + \sum_{n=0}^{\infty} \frac{C_n T_n(\xi)}{C_0} \right). \end{aligned} \quad (16)$$

In the case of an inextensible film, namely, as $\gamma \rightarrow 0$, the sum in (16) becomes vanishing small. As a consequence for this asymptotic case, the stress intensity factor displays the same behaviour of the symmetric loading case (13) as reported in Figure 6.

5. Conclusions

The contact problem of a homogeneous orthotropic half plane covered by thin film has been analysed here (for the behaviours of nonhomogeneous nanobeams and nanoplates, see [43–45]). The interfacial singular shear stress has been approximated through a series expansion of Chebyshev polynomials. The governing singular integral equation derived from the compatibility condition between the half plane and thin film has been transformed into a linear algebraic system for the unknown coefficient C_n of the series. Once the Chebyshev coefficients have been calculated, the strain field, contact shear stress, and displacement field have been found in dimensionless form in terms of Chebyshev polynomials of the first and second kind.

The governing parameter γ assumes specific values for real applications. The rate of convergence of the proposed method displays high or low speed for low [10^{-6} , 10^{-3}] or high [10^{-1} , 10^3] values of γ , respectively. The relation between the parameter γ and the field of practical application (Table 2) suggests the appropriateness of the proposed method for geometries and material properties typically involved in MEMS or steel joints design.

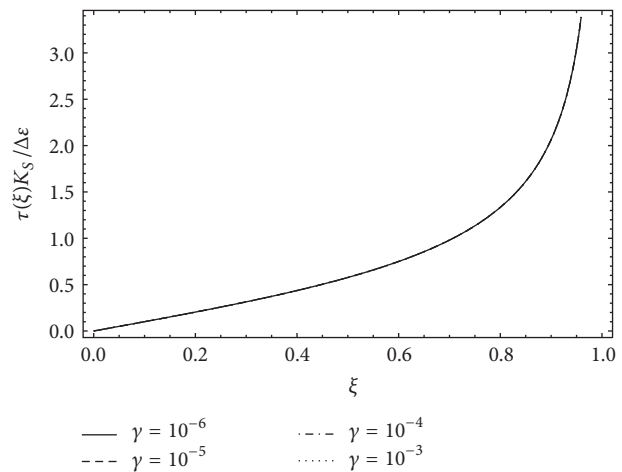
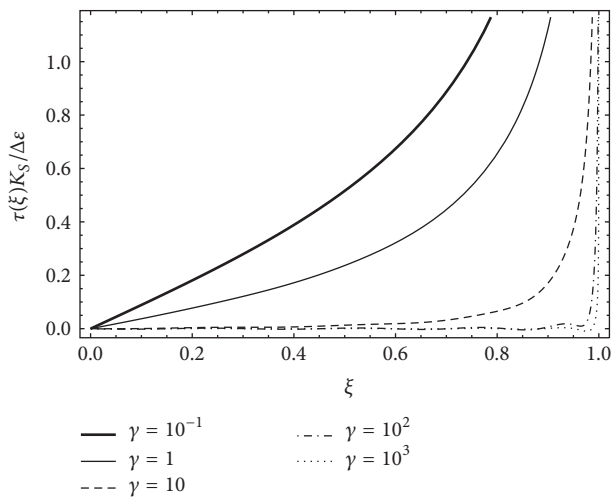
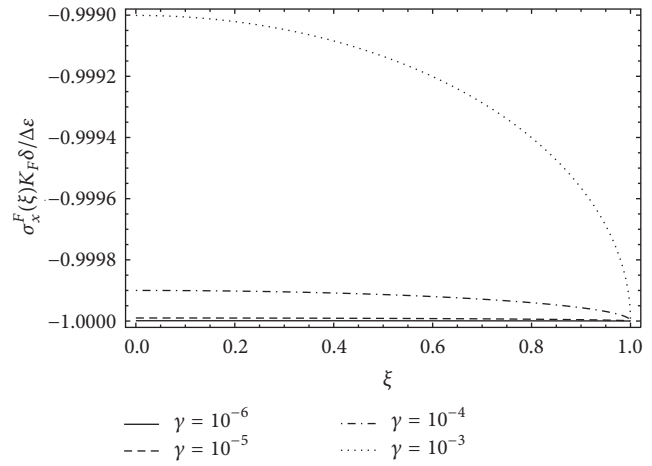
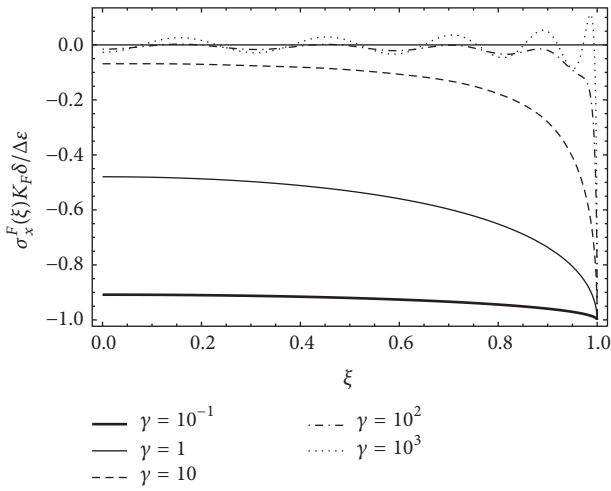
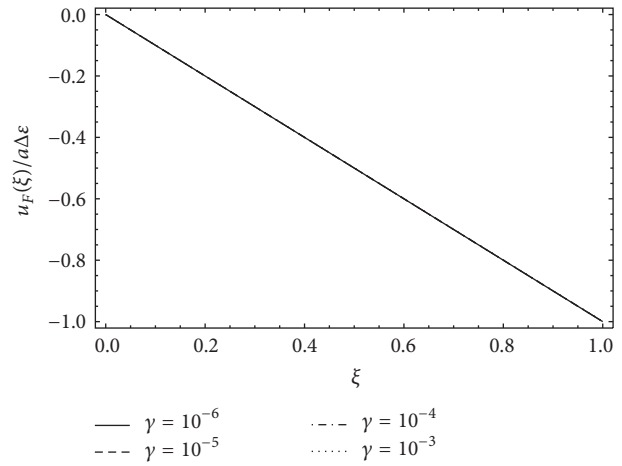
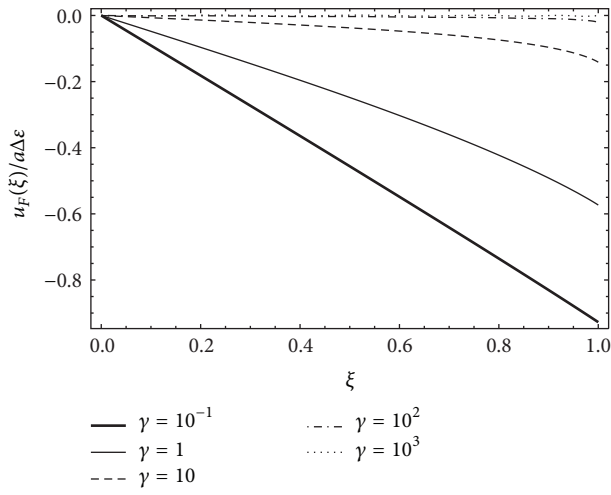


FIGURE 5: Longitudinal displacement, longitudinal stress, and shear stress field of symmetric loading case condition for high (left (a), (c), and (e)) and low (right (b), (d), and (f)) values of γ , respectively.

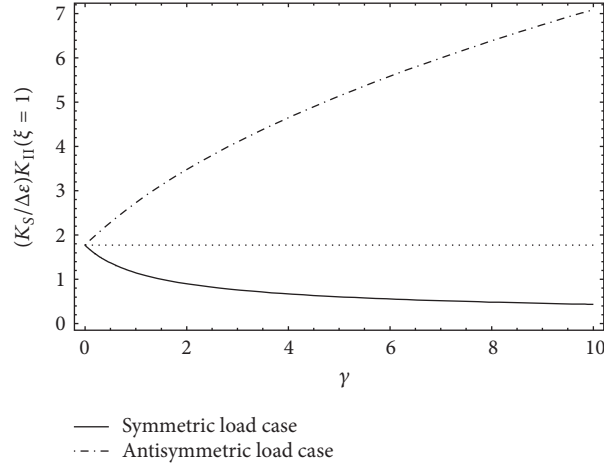


FIGURE 6: Stress intensity factor at film edge for symmetric loading case.

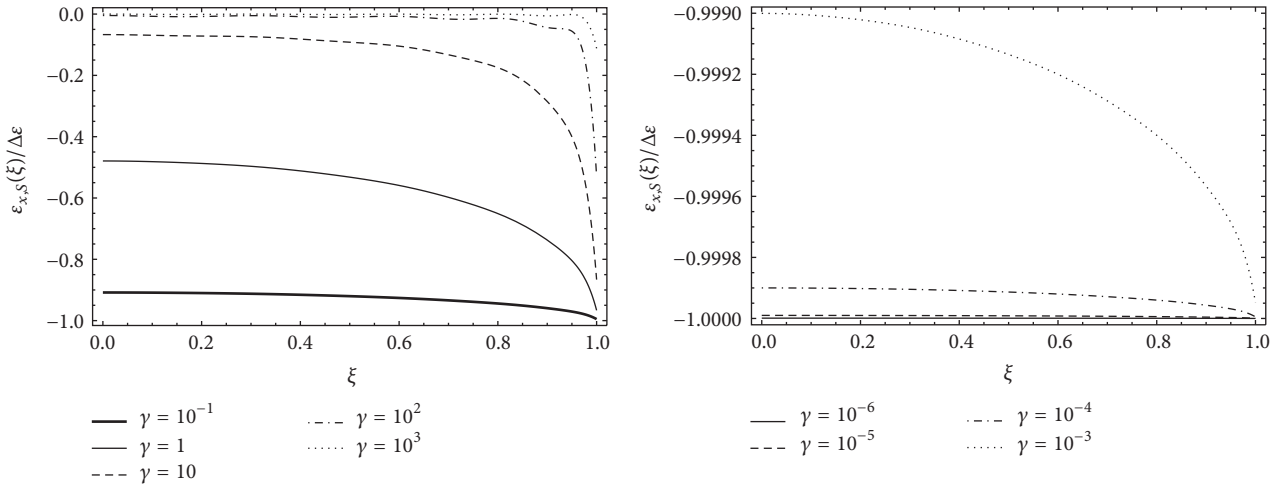


FIGURE 7: Longitudinal strain field for symmetric loading case.

Through the superposition of the two loading conditions here studied, it becomes possible to reproduce the case of a single force acting at the film edge. The stress intensity factors for both symmetric and skew-symmetric loading conditions exhibit opposite behaviour with respect to the dimensionless parameter γ . The results found here agree reasonably well with the solution reported in [5, 42] for the particular case of an isotropic half plane.

In order to take into account voids, defects, and inclusions that can occur during the deposition process of a film onto a substrate, the analysis will be extended to a nonhomogeneous half plane in a forthcoming paper (for a detailed study concerning nonhomogeneous bodies, see [46]).

Appendix

A. Elastic Parameters

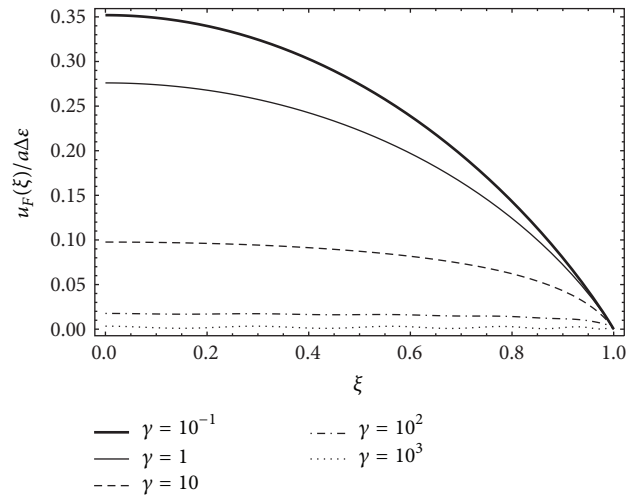
Denoting with c_{ij} the elastic stiffness coefficients, with E and ν being the Young modulus and the Poisson ratio, respectively,

from [16], the horizontal component of strain of the half plane surface is known in closed form:

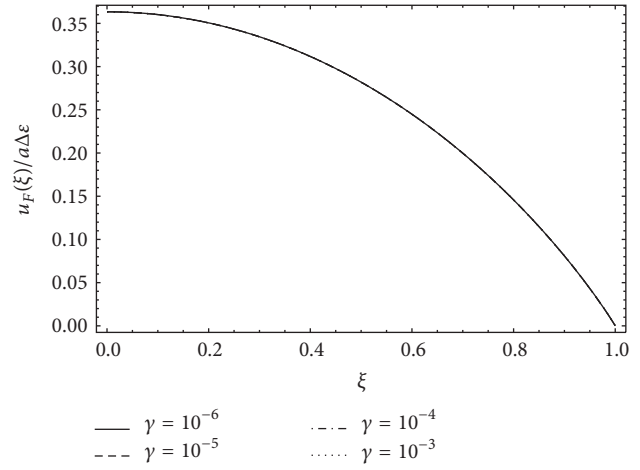
$$\varepsilon^S(y) = \frac{\beta_{22} \sqrt{C_h + 4}}{\lambda \pi} \int_{-a}^{+a} \frac{\tau(t)}{y-t} dt, \quad (\text{A.1})$$

where the elastic parameters read

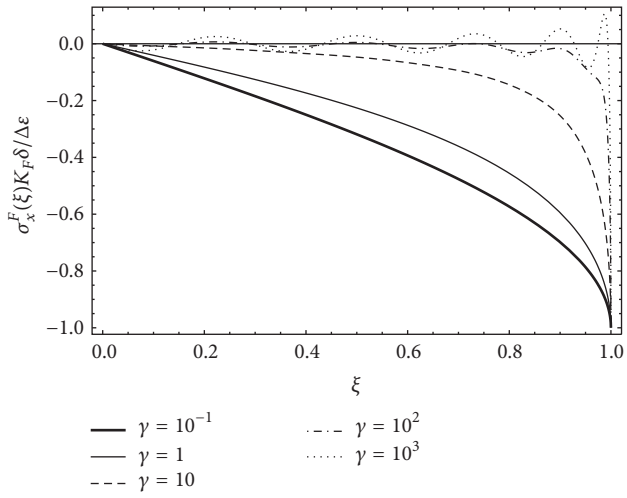
$$\begin{aligned} \beta_{22} &= \frac{c_{11}}{c_{11}c_{22} - c_{12}^2}, \\ \lambda &= \sqrt[4]{\frac{c_{11}}{c_{22}}}, \\ C_h &= \frac{(\tilde{c}_{12} + c_{12})(\tilde{c}_{12} - c_{12} - 2c_{66})}{\tilde{c}_{12}c_{66}}, \\ R &= \frac{(c_{12} - \lambda^2 c_{22})(c_{12} + c_{66})}{[\lambda^4 c_{22}^2 + \lambda^2 c_{12}c_{22}(C_h + 2) + c_{12}^2] c_{66}}, \\ \tilde{c}_{12} &= \sqrt{c_{11}c_{22}}, \end{aligned} \quad (\text{A.2})$$



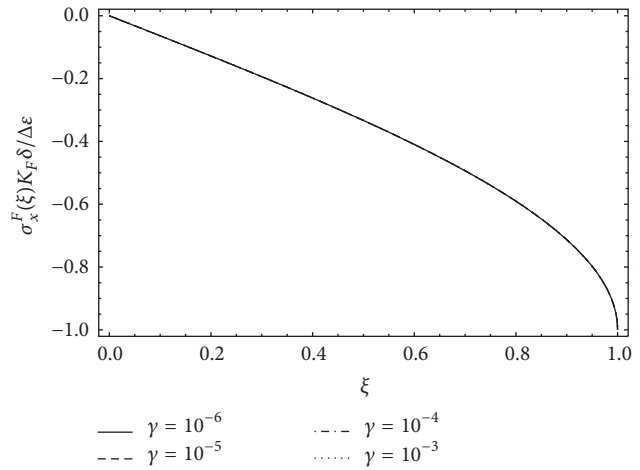
(a)



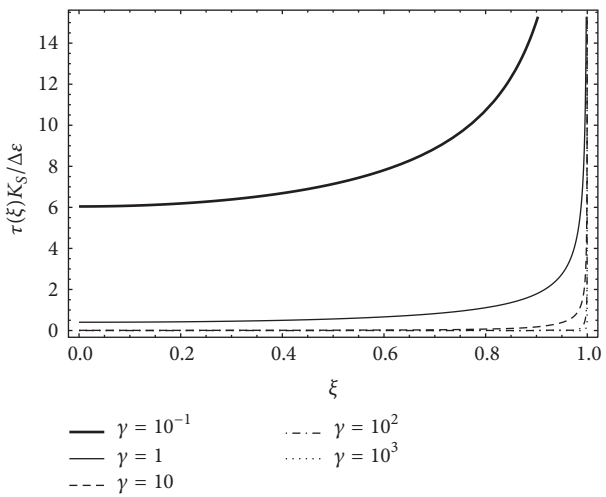
(b)



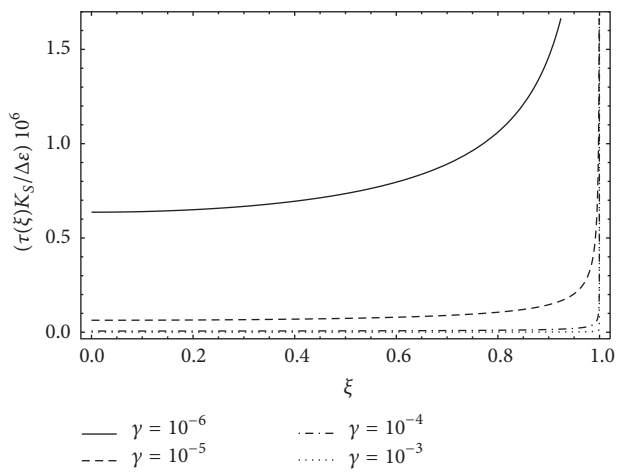
(c)



(d)



(e)



(f)

FIGURE 8: Longitudinal displacement, longitudinal stress, and shear stress field of skew-symmetric loading case condition for high (left (a), (c), and (e)) and low (right (b), (d), and (f)) values of γ , respectively.

and, in turn, the film and half plane compliances can be defined as

$$\begin{aligned} K_F &= \frac{\beta_{22,F}}{\delta}, \\ K_S &= \frac{\sqrt{C_h + 4}}{\lambda} \beta_{22,S}. \end{aligned} \quad (\text{A.3})$$

In case of isotropic half plane, the elastic parameters and compliances reduce to

$$\begin{aligned} \beta_{22} &= \frac{1 - \nu^2}{E}, \\ \lambda &= 1, \\ C_h &= 0, \\ R &= \frac{(1 - 2\nu)(1 + \nu)}{E}, \\ \bar{c}_{12} &= E, \\ K_S &= \frac{2(1 - \nu_S^2)}{E_S}, \\ K_F &= \frac{1 - \nu_F^2}{E_F \delta}, \end{aligned} \quad (\text{A.4})$$

and the half plane longitudinal strain reads [47]

$$\varepsilon^S(y) = \frac{(1 - \nu_S^2)}{E\pi} \int_{-a}^{+a} \frac{\tau(t)}{y - t} dt. \quad (\text{A.5})$$

B. Useful Integral Involving Chebyshev Polynomials

The Chebyshev polynomials of the first and second kind, $T_n(t)$ and $U_n(t)$, are defined as

$$\begin{aligned} T_n(\xi) &= \cos[n \arccos(\xi)], \\ U_n(\xi) &= \frac{\sin[(n+1) \arccos(\xi)]}{\sin[\arccos(\xi)]}. \end{aligned} \quad (\text{B.1})$$

In Section 2, the following identities have been used:

$$\begin{aligned} &\int_{-a}^a \frac{T_n(t)}{(t-x)\sqrt{1-t^2}} \\ &= \begin{cases} 0, & \text{if } n = 1, |x| < a \\ \pi U_{n-1}(x), & \text{if } n \neq 1, |x| < a \\ -\pi \frac{[x - \text{sign}(x)\sqrt{x^2-1}]^n}{\text{sign}(x)\sqrt{x^2-1}}, & \text{if } n \geq 0, |x| > 1 \end{cases} \end{aligned}$$

$$\int_x^1 \frac{T_n(t)}{\sqrt{1-t^2}} dt = \begin{cases} \frac{1}{n} U_{n-1}(x) \sqrt{1-x^2}, & \text{if } n \neq 0 \\ \arccos(x), & \text{if } n = 0 \end{cases}$$

$$\int_{-a}^{+a} U_{n-1}(t) U_{m-1}(t) \sqrt{1-t^2} dt = \frac{\pi}{2} \delta_{nm},$$

$$\int_{-a}^a U_{n-1}(t) dt = \begin{cases} \frac{2}{n}, & \text{if } n \text{ odd} \\ 0, & \text{if } n \text{ even} \end{cases}$$

$$\int_{-a}^{+a} \frac{T_n(t)}{\sqrt{1-t^2}} \ln \left| \frac{x}{a} - t \right| dt = \begin{cases} -\pi \ln(2), & \text{if } n = 0 \\ -\frac{\pi}{n} T_n(x), & \text{if } n > 0. \end{cases} \quad (\text{B.2})$$

Competing Interests

The authors declare that there are no competing interests regarding the publication of this paper.

References

- [1] L. B. Freund and S. Suresh, *Thin Film Materials. Stress, Defect Formation and Surface Evolution*, Cambridge University Press, 2003.
- [2] V. Guidi, L. Lanzoni, and A. Mazzolari, "Patterning and modeling of mechanically bent silicon plates deformed through coactive stresses," *Thin Solid Films*, vol. 520, no. 3, pp. 1074–1079, 2011.
- [3] L. Lanzoni and E. Radi, "Thermally induced deformations in a partially coated elastic layer," *International Journal of Solids and Structures*, vol. 46, no. 6, pp. 1402–1412, 2009.
- [4] V. Guidi, L. Lanzoni, A. Mazzolari, G. Martinelli, and A. Tralli, "Design of a crystalline undulator based on patterning by tensile Si3N4 strips on a Si crystal," *Applied Physics Letters*, vol. 90, no. 11, Article ID 114107, 2007.
- [5] L. Lanzoni, "Analysis of stress singularities in thin coatings bonded to a semi-infinite elastic substrate," *International Journal of Solids and Structures*, vol. 48, no. 13, pp. 1915–1926, 2011.
- [6] M. Ohring, *The Materials Science of Thin Films*, Academic Press, 1992.
- [7] A. Caporale, L. Feo, and R. Luciano, "Damage mechanics of cement concrete modeled as a four-phase composite," *Composites Part B: Engineering*, vol. 65, pp. 124–130, 2014.
- [8] G. Dinelli, G. Belz, C. E. Majorana, and B. A. Schrefler, "Experimental investigation on the use of fly ash for lightweight precast structural elements," *Materials and Structures*, vol. 29, no. 194, pp. 632–638, 1996.
- [9] V. A. Salomoni, C. E. Majorana, G. M. Giannuzzi, and A. Miliozzi, "Thermal-fluid flow within innovative heat storage concrete systems for solar power plants," *International Journal of Numerical Methods for Heat and Fluid Flow*, vol. 18, no. 7-8, pp. 969–999, 2008.
- [10] V. Salomoni, G. Mazzucco, C. Pellegrino, and C. Majorana, "Three-dimensional modelling of bond behaviour between concrete and FRP reinforcement," *Engineering Computations*, vol. 28, no. 1, pp. 5–29, 2011.
- [11] G. Xotta, G. Mazzucco, V. A. Salomoni, C. E. Majorana, and K. J. Willam, "Composite behavior of concrete materials under high

- temperatures," *International Journal of Solids and Structures*, vol. 64, pp. 86–99, 2015.
- [12] A. Nobili, L. Lanzoni, and A. M. Tarantino, "Experimental investigation and monitoring of a polypropylene-based fiber reinforced concrete road pavement," *Construction and Building Materials*, vol. 47, pp. 888–895, 2013.
- [13] L. Dezi, G. Menditto, and A. M. Tarantino, "Homogeneous structures subjected to repeated structural system changes," *Journal of Engineering Mechanics*, vol. 116, no. 8, pp. 1723–1732, 1990.
- [14] L. Dezi and A. Tarantino, "Time dependent analysis of concrete structures with variable structural system," *ACI Materials Journal*, vol. 88, no. 3, pp. 320–324, 1991.
- [15] A. Nobili, "Variational approach to beams resting on two-parameter tensionless elastic foundations," *Journal of Applied Mechanics, Transactions ASME*, vol. 79, no. 2, Article ID 021010, 2012.
- [16] R. Mahajan, F. Erdogan, and Y. T. Chou, "The crack problem for an orthotropic half-plane stiffened by elastic films," *International Journal of Engineering Science*, vol. 31, no. 3, pp. 403–424, 1993.
- [17] R. Mahajan, F. Erdogan, B. Kilic, and E. Madenci, "Cracking of an orthotropic substrate reinforced by an orthotropic plate," *International Journal of Solids and Structures*, vol. 40, no. 23, pp. 6389–6415, 2003.
- [18] A. M. Tarantino, "Nonlinear fracture mechanics for an elastic Bell material," *The Quarterly Journal of Mechanics and Applied Mathematics*, vol. 50, no. 3, pp. 435–456, 1997.
- [19] A. M. Tarantino, "The singular equilibrium field at the notch-tip of a compressible material in finite elastostatics," *Zeitschrift für Angewandte Mathematik und Physik*, vol. 48, no. 3, pp. 370–388, 1997.
- [20] A. M. Tarantino, "On extreme thinning at the notch tip of a neo-Hookean sheet," *The Quarterly Journal of Mechanics and Applied Mathematics*, vol. 51, no. 2, pp. 179–190, 1998.
- [21] A. M. Tarantino, "On the finite motions generated by a mode I propagating crack," *Journal of Elasticity*, vol. 57, no. 2, pp. 85–103, 1999.
- [22] A. M. Tarantino, "Crack propagation in finite elastodynamics," *Mathematics and Mechanics of Solids*, vol. 10, no. 6, pp. 577–601, 2005.
- [23] A. Apuzzo, R. Barretta, and R. Luciano, "Some analytical solutions of functionally graded Kirchhoff plates," *Composites Part B: Engineering*, vol. 68, pp. 266–269, 2015.
- [24] R. Barretta, L. Feo, and R. Luciano, "Some closed-form solutions of functionally graded beams undergoing nonuniform torsion," *Composite Structures*, vol. 123, pp. 132–136, 2015.
- [25] R. Barretta, L. Feo, and R. Luciano, "Torsion of functionally graded nonlocal viscoelastic circular nanobeams," *Composites Part B: Engineering*, vol. 72, pp. 217–222, 2015.
- [26] R. Luciano and J. R. Willis, "Non-local constitutive equations for functionally graded materials," *Mechanics of Materials*, vol. 36, no. 12, pp. 1195–1206, 2004.
- [27] K. N. H. Arutiunian, "Contact problem for half-plane with elastic reinforcement," *Journal of Applied Mathematics and Mechanics*, vol. 32, no. 4, pp. 632–646, 1968.
- [28] F. Erdogan and G. D. Gupta, "Problem of an elastic stiffener bonded to a half plane," *Journal of Applied Mechanics*, vol. 38, no. 4, pp. 937–941, 1971.
- [29] T. W. Shield and K. S. Kim, "Beam theory models for thin film segments cohesively bonded to an elastic half space," *International Journal of Solids and Structures*, vol. 29, no. 9, pp. 1085–1103, 1992.
- [30] H. Djabella and R. D. Arnell, "Two-dimensional finite-element analysis of elastic stresses in double-layer systems under combined surface normal and tangential loads," *Thin Solid Films*, vol. 226, no. 1, pp. 65–73, 1993.
- [31] J. F. Luo, Y. J. Liu, and E. J. Berger, "Analysis of two-dimensional thin structures (from micro- to nano-scales) using the boundary element method," *Computational Mechanics*, vol. 22, no. 5, pp. 404–412, 1998.
- [32] N. Tullini, A. Tralli, and L. Lanzoni, "Interfacial shear stress analysis of bar and thin film bonded to 2D elastic substrate using a coupled FE-BIE method," *Finite Elements in Analysis and Design*, vol. 55, pp. 42–51, 2012.
- [33] D. S. Jeng, "Tailoring of silicon crystals for relativistic-particle channeling," *Journal of Geotechnical and Geoenvironmental Engineering*, vol. 123, 1997.
- [34] H. B. Huntington, *The Elastic Constants of Crystals*, Academic Press, 2003.
- [35] EN-Standard, "European non-alloy structural steels," Technical Report, EN 10025-2, 2004.
- [36] D. Dinckal, "Analysis of elastic anisotropy of wood material for engineering applications," *Journal of Innovative Research in Engineering and Science*, vol. 2, no. 2, pp. 67–80, 2011.
- [37] O. Tabata, K. Kawahata, S. Sugiyama et al., "Mechanical property measurements of thin films using load-defection of composite rectangular membrane," in *Proceedings of the IEEE An Investigation of Micro Structures, Sensors, Actuators, Machines and Robots, Micro Electro Mechanical Systems*, vol. 56, pp. 152–156, February 1989.
- [38] M. A. Hopcroft, W. D. Nix, and T. W. Kenny, "What is the Young's modulus of Silicon?" *Journal of Microelectromechanical Systems*, vol. 19, no. 2, Article ID 5430873, pp. 229–238, 2010.
- [39] P. Bisegna and R. Luciano, "Bounds on the overall properties of composites with debonded frictionless interfaces," *Mechanics of Materials*, vol. 28, no. 1–4, pp. 23–32, 1998.
- [40] F. Marotti de Sciarra and M. Salerno, "On thermodynamic functions in thermoelasticity without energy dissipation," *European Journal of Mechanics. A. Solids*, vol. 46, pp. 84–95, 2014.
- [41] G. A. Morar and G. I. A. Popov, "On the contact problem for a half-plane with finite elastic reinforcement," *Percona Monitoring and Management*, vol. 34, no. 3, pp. 412–421, 1970.
- [42] W. T. Koiter, "On the diffusion of load from a stiffener into a sheet," *The Quarterly Journal of Mechanics and Applied Mathematics*, vol. 8, no. 2, pp. 164–178, 1955.
- [43] R. Barretta, L. Feo, R. Luciano, and F. Marotti de Sciarra, "A gradient Eringen model for functionally graded nanorods," *Composite Structures*, vol. 131, pp. 1124–1131, 2015.
- [44] R. Barretta, L. Feo, R. Luciano, and F. Marotti de Sciarra, "Variational formulations for functionally graded nonlocal Bernoulli-Euler nanobeams," *Composite Structures*, vol. 129, pp. 80–89, 2015.
- [45] R. Barretta, R. Luciano, and J. R. Willis, "On torsion of random composite beams," *Composite Structures*, vol. 132, pp. 915–922, 2015.
- [46] R. Luciano and J. R. Willis, "Hashin-Shtrikman based FE analysis of the elastic behaviour of finite random composite bodies," *International Journal of Fracture*, vol. 137, no. 1–4, pp. 261–273, 2006.
- [47] K. L. Johnson, *Contact Mechanics*, Cambridge University Press, London, UK, 1985.

Research Article

Modelling of Creep and Stress Relaxation Test of a Polypropylene Microfibre by Using Fraction-Exponential Kernel

Andrea Sorzia

Dipartimento di Scienze e Metodi dell'Ingegneria (DISMI), Università di Modena e Reggio Emilia, 42122 Reggio Emilia, Italy

Correspondence should be addressed to Andrea Sorzia; andrea.sorzia@unimore.it

Received 4 December 2015; Accepted 4 May 2016

Academic Editor: Julius Kaplunov

Copyright © 2016 Andrea Sorzia. This is an open access article distributed under the Creative Commons Attribution License, which permits unrestricted use, distribution, and reproduction in any medium, provided the original work is properly cited.

A tensile test until breakage and a creep and relaxation test on a polypropylene fibre are carried out and the resulting creep and stress relaxation curves are fit by a model adopting a fraction-exponential kernel in the viscoelastic operator. The models using fraction-exponential functions are simpler than the complex ones obtained from combination of dashpots and springs and, furthermore, are suitable for fitting experimental data with good approximation allowing, at the same time, obtaining inverse Laplace transform in closed form. Therefore, the viscoelastic response of polypropylene fibres can be modelled straightforwardly through analytical methods. Addition of polypropylene fibres greatly improves the tensile strength of composite materials with concrete matrix. The proposed analytical model can be employed for simulating the mechanical behaviour of composite materials with embedded viscoelastic fibres.

1. Introduction

Fibre-reinforced composite materials consist of fibres with high strength and elastic modulus embedded in a matrix to produce a combination of properties that cannot be achieved by single constituents. Usually, fibres are the principal load-carrying members, while the surrounding matrix keeps them in the desired location and orientation. The matrix acts as a load transfer medium between fibres and plays a number of useful functions, for example, protecting the fibres from environmental damage. Fibres may be made up of various materials, such as steel, polymer, glass, or carbon, whereas polymer, metal, or ceramic can be chosen for the matrix material.

Fibre-reinforced polymer composites are probably the most important and widespread fibre-reinforced materials used for commercial and industrial applications. This is due to the combination of their low density, strength-weight ratios, and modulus-weight ratios that make them more attractive than many traditional metallic materials [1].

A classic example of fibre-reinforced composite used in civil engineering is Fibre-Reinforced Concrete (FRC), widely adopted for industrial pavements, tunnel linings, marine structures, earthquake-resistant structures, and plate and slab

foundation [2]. In FRC composites, fibres are commonly added to concrete mixture in random disposition and short cuts in order to increase the cracking behaviour of concrete, thus transforming concrete from brittle into a ductile material [3]. However, there are composite materials in which fibres are aligned along particular directions, as it occurs in FRP frame elements (these composites can be studied by adopting, for instance, the approaches proposed in [4, 5]).

Recently, the use of macro synthetic fibres made of polymeric materials has been proposed for structural purposes [6, 7]. Experimental tests performed by Lanzoni et al. [8] show that the addition of polypropylene-based draw-wired fibres significantly improves crack resistance of the concrete mixture and enhances toughness and durability of FRC structural elements. Fibres could be found in interesting applications as an additive to improve concrete under aggressive environments (the mechanical behaviour has been studied under high thermal loads also [9, 10] and nuclear radiation [11]). However, particularly in such harsh conditions, a wide class of additives can be inserted at the mixing stage (like fly ash) to increase resistance of the concrete mixture [12].

Ductility and flexural strength of FRC are defined by energy-dissipation mechanisms during the pullout of the fibres that occurs in the opening propagating cracks [13, 14].

Pullout of the fibres begins after cracking the concrete matrix (for the stress and strain localizations at the crack tip, see, e.g., [14–17]) and ceases with the complete extraction of the fibres and its evolution depends on the bonding between fibre and matrix [18, 19]. Nevertheless due to their chemical inertness, polypropylene (PP) synthetic fibres have poor adhesion to the cement matrix with respect to other kinds of fibres. However, special surface nanotreatment can actually increase the adhesion properties between concrete and synthetic fibres, as shown by Di Maida et al. [3]. In this case, PP fibres may experience significant loading and consequently the viscous deformations of the composite material may considerably increase (for time-dependent effects in concrete structures see [20–22]). A single fibre can be studied as an embedded cylindrical body or a viscoelastic circular nanobeam in frictional contact with the cement matrix under axial tensile load (e.g., [23–25]).

Another application of synthetic fibres in civil engineering is the fibre-reinforced polymer (FRP) composites for reinforcement and retrofitting of concrete and masonry members, with applications in new buildings as well as for strengthening and/or rehabilitation of existing (prestressed as well as nonprestressed) structural members of both prefabricated and cast-in-place frames. FRP reinforcement consists in strengthening fibres applied to structural elements by a cementitious or polymeric-based layer. The mechanical performances of such systems can be assessed by solving the contact problem between two bounded layers [26–28] where the adhesive layer is a fibre-reinforced composite material [29] or, in a simpler way, as a fibre-reinforced Kirchhoff plate [30].

This work presents a creep and stress relaxation test performed over a PP synthetic fibre used for FRC. Creep is a time-dependent deformation of a viscoelastic material under the application of a constant stress at a constant temperature. Relaxation is the counterpart of creep, namely, a time-dependent stress of a viscoelastic material under the application of a constant deformation at a constant temperature. Both are complex phenomena for they depend on material properties (e.g., molecular orientation and crystallinity) and external conditions (e.g., applied stress, temperature, and moisture). Moreover, the viscoelastic behaviour of PP fibres embedded in an elastic matrix complicates the modelling of creep and stress relaxation response of the composite material, which depends on many additional parameters such as concentration, aspect ratio, orientation, and, obviously, mechanical properties of PP fibres.

Creep and stress relaxation tests best demonstrate the viscoelastic characteristics of a polymeric solid. In creep test, a constant stress is maintained on a specimen while its deformation is monitored as a function of time, and deformation increases with time. In stress relaxation test, a constant deformation is maintained while the stress on the specimen is monitored as a function of time, and stress decreases with time. Typical creep and stress relaxation diagrams exhibit an instantaneous elastic response followed by a delayed time-dependent response [1].

Over the experimental creep and stress relaxation tests performed, this paper proposes an analytical model to

fit these experimental curves. The model uses fraction-exponential kernel in the viscoelastic operator and was proposed, for the first time, by Scott Blair and Coppen [31, 32] and Rabotnov [33] independently.

The classical viscoelastic constitutive models represented by a combination of dashpots and springs are usually adopted for simulating creep behaviour of composite materials. However, the simplest ones (Maxwell and Kelvin-Voigt) are not sufficiently flexible to match experimental data for real materials. The more complex ones, obtained from combination of different Maxwell and Kelvin-Voigt models, require instead many parameters and do not allow obtaining inverse Fourier or Laplace transforms in closed form [34, 35]. Therefore, in the 50s of the last century, a viscoelastic stress-strain relation based on fractional derivative has been proposed. The fractional derivative model (FDM) is more flexible and requires a smaller number of parameters, so that their calibration is considerably simpler. The flexibility is due to the order of derivatives which can vary to obtain a constitutive law suitable for the considered material. In 1948 Rabotnov [33] suggested to use fraction-exponential operators that can describe experimental data of real materials with sufficient accuracy and allows one to obtain inverse Laplace transforms analytically [36]. Scott Blair and Coppen [31, 32] used fraction-exponential operators for description of viscoelastic properties of materials experimentally (see Rogosin and Mainardi [37]). Fraction-exponential functions in viscoelastic operators were used by many authors last decade. Detailed discussion can be found in the book of Podlubny [38]. Published broad surveys are, for example, [39–41].

The model developed in the present paper is able to describe the creep curve of a PP fibre carefully and it allows obtaining the creep and stress relaxation test response of a fibre composite material in closed form. Moreover, the adopted fraction-exponential operators can be efficiently employed for the homogenization of synthetic FRC by extending the Maxwell scheme developed for elastic composites to viscoelastic behaviour of the constituents (e.g., [34, 42]).

2. Materials and Methods

2.1. Material and Breaking Test. The fibre consists of PP monofilament with a diameter of 0.78 mm and length of 200 mm. Since the cross section of the fibre is not perfectly circular, the diameter is an average of six measurements: Two measurements in two orthogonal directions in three points of the fibre, namely, at the middle and at both ends. To evaluate elastic Young modulus and tensile strength, tensile tests were performed on four specimens of fibres until their breakage. Each fibre was clamped at its ends and pulled by an electromechanic traction machine under displacement control.

The load cell is a GALDABINI 514262 TYPE TCA, with OUTPUT sensitivity of 2 mV/V. The machine uses a 20-bit A/D converter to acquire the analogical quantities. The resolution of the load cell is 0.002 N over the entire field

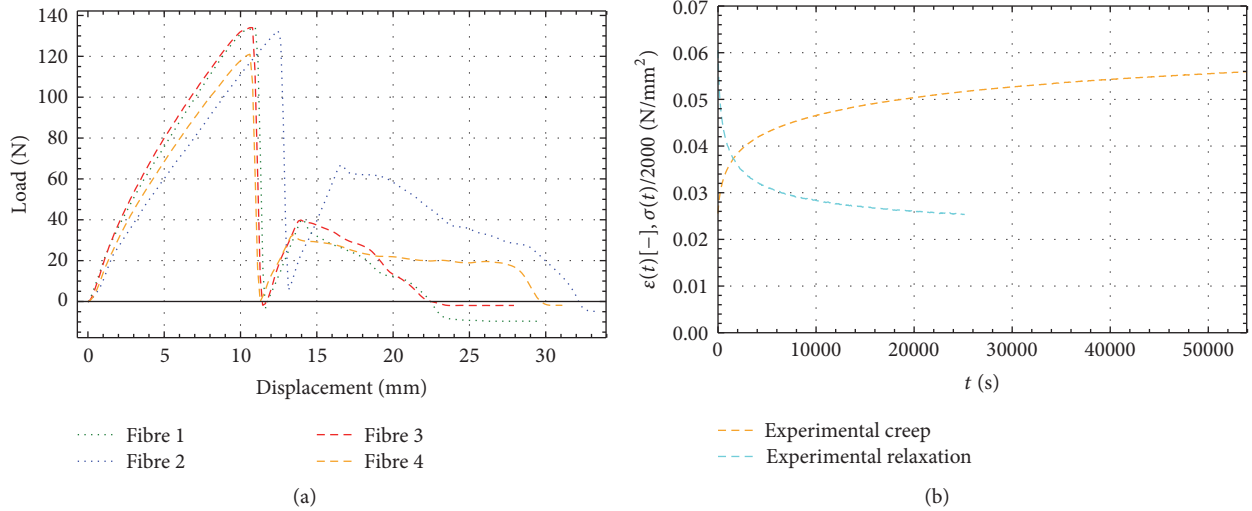


FIGURE 1: (a) Tensile tests until breakage on four specimens of fibre: load versus displacement. (b) Experimental curves: creep versus time (dashed orange curve) and stress relaxation versus time (dashed cyan curve: stress scaled by 1/2000).

TABLE 1: Properties of polypropylene fibre.

Diameter (mm)	0.78
Tensile strength (N/mm ²)	273.0
Elastic modulus E_0 at $t = 0$ (N/mm ²)	5.131×10^3
Elastic modulus E_∞ at $t \rightarrow \infty$ (N/mm ²)	1.959×10^3

of use, with a capacity of 250 N. The displacement control was performed by the actuator at a rate of 40 mm/min. The average value of the breakage tensile load is 130.5 N that occurs approximately at a displacement of 10 mm, namely, at 5% of strain.

The elastic Young modulus E_0 (Table 1) was determined from the ratio between stress and strain. The stresses and strains were calculated based on the early stage of the experimental load-displacement curve averaged on the four fibres.

The experiments were performed at 25°C. Since the glass transition temperature of the PP is approximately -20°C [43], at room temperature PP fibres exhibit a mechanical behaviour corresponding to that of a viscoelastic material in rubbery state, that is, a time-dependent response as shown in Figure 1(b).

Plots of breaking tests are reported in Figure 1(a). In particular, the first peak that can be observed in the curve is due to the breakage of the fibres that occurred on the clamped portion, at which followed a pullout stage until the complete detachment of the fibres. The properties adopted for PP fibre are listed in Table 1. The PP fibre was provided by the Italian company Fili&Forme® Ltd. and shown in Figure 3.

2.2. Creep and Relaxation Tests. The creep test was carried out on a sample of length 200 mm subject to a constant tensile force of 60 N by fixing between two clamps and measuring the displacement of the fibre over the time. The load cell is the same used for the breaking test (see Section 2.1) and the speed

to gain 60 N was performed at a rate of 40 mm/min. The total duration of the creep test was 15 hours needed for the fibre to achieve a (temporary) stationary value of the deformation (plateau region of the creep curve). However, it should be remarked that the deformation could further increase after 15 hours, since the maximum level of deformation is theoretically achieved at $t \rightarrow \infty$.

It is worth noting that at time longer than 20,000 s the strain exceeds 5% but the fibre does not break (Figure 1(b)). Conversely, the fibre under tensile test falls at a strain level equal to 5% (Figure 1(a)). This is due to the fact that the creep test was performed at a constant load of 60 N, less than one-half the ultimate tensile load of 130.5 N.

Similarly, the stress relaxation test was carried out on a sample of length 200 mm subject to a constant displacement of 5 mm and measuring the tensile force over the time. The speed to gain 5 mm was performed at a rate of 40 mm/min. The total duration time was 7 hours, until the force of the fibre was almost stationary. Plots of creep and stress relaxation tests are reported in Figure 1(b).

Both creep and relaxation tests were performed on a single specimen.

The elastic Young modulus E_∞ (Table 1) was assessed based on the final stage of the experimental creep and relaxation tests by knowing the imposed constant load and displacement values at which the tests were performed. The assumed values were the averages of the obtained experimental results.

3. Results and Discussion

3.1. Analytical Model for Creep and Stress Relaxation Curves. We wanted to fit experimental creep and stress relaxation curves with an analytical model by using fraction-exponential kernel that on one side fits carefully experimental data and, at the same time, allows analytical expression for inverse Laplace transform. Let us consider the Boltzmann

convolution integral that describes the creep strain $\varepsilon(t)$ of a material under a stress $\sigma(t)$ variable over time

$$\varepsilon(t) = \sigma_0 \psi(t) + \int_0^t \dot{\sigma}(\tau) \psi(t-\tau) d\tau, \quad (1)$$

where $\psi(t)$ is the creep function and $\sigma_0 = \sigma(0)$ the stress applied at $t = 0$. Note that the creep function $\psi(t)$ coincides with the axial strain produced by the constant stress $\sigma(t) = 1$. Integrating by parts (1) it follows

$$\varepsilon(t) = \sigma(t) \psi_0 - \int_0^t \sigma(\tau) \dot{\psi}(t-\tau) d\tau. \quad (2)$$

By following [34], we write (2) in the form

$$\varepsilon(t) = \frac{1}{E_0} \left[\sigma(t) - \lambda \int_0^t R_\alpha(\beta - \lambda, t - \tau) \sigma(\tau) d\tau \right], \quad (3)$$

where

$$\begin{aligned} R_\alpha(\beta - \lambda, t - \tau) &= (t - \tau)^\alpha \sum_{n=0}^{\infty} \frac{(\beta - \lambda)^n (t - \tau)^{n(1+\alpha)}}{\Gamma[(n+1)(1+\alpha)]}, \\ \psi_0 &= \frac{1}{E_0}, \\ \lambda &= \frac{E_0 - E_\infty}{E_0} \beta, \end{aligned} \quad (4)$$

where R_α is the Rabotnov function that allows using fraction-exponential kernel in viscoelastic operators, and E_0, E_∞ are the elastic Young modulus at $t = 0, t \rightarrow \infty$, respectively. A constant stress $\sigma(t) = \sigma_0$ is then assumed in order to simulate the creep test, so that

$$\begin{aligned} &\int_0^t R_\alpha(\beta - \lambda, t - \tau) \sigma(\tau) d\tau \\ &= \sigma_0 \sum_{n=0}^{\infty} \frac{(\beta - \lambda)^n}{\Gamma[(n+1)(1+\alpha)]} \int_0^t (t - \tau)^{n(1+\alpha)+\alpha} d\tau \\ &= \sigma_0 \sum_{n=0}^{\infty} \frac{(\beta - \lambda)^n (t - \tau)^{(n+1)(1+\alpha)}}{\Gamma[(n+1)(1+\alpha)+1]}, \end{aligned} \quad (5)$$

where the property of Euler gamma function $\Gamma(z+1) = z\Gamma(z)$ has been used.

By shifting the index $m = n + 1$, it follows

$$\begin{aligned} &\frac{\sigma_0}{\beta - \lambda} \sum_{n=0}^{\infty} \frac{(\beta - \lambda)^{n+1} t^{(n+1)(1+\alpha)}}{\Gamma[(n+1)(1+\alpha)+1]} \\ &= \frac{\sigma_0}{\beta - \lambda} \left\{ \sum_{m=0}^{\infty} \frac{(\beta - \lambda)^m t^{m(1+\alpha)}}{\Gamma[m(1+\alpha)+1]} - 1 \right\} \\ &= \frac{\sigma_0}{\beta - \lambda} \left\{ M_{1+\alpha} [(\beta - \lambda) t^{1+\alpha}] - 1 \right\}, \end{aligned} \quad (6)$$

where the Mittag-Leffler function,

$$M_a(z) = \sum_{m=0}^{\infty} \frac{z^m}{\Gamma[ma+1]}, \quad (7)$$

has been introduced. Therefore, (3) becomes

$$\varepsilon(t) = \frac{\sigma_0}{E_0} \left[1 - \frac{\lambda}{\beta - \lambda} \left\{ M_{1+\alpha} [(\beta - \lambda) t^{1+\alpha}] - 1 \right\} \right]. \quad (8)$$

By using the following properties of the Mittag-Leffler function

$$\begin{aligned} \lim_{t \rightarrow 0} M_{1+\alpha} [(\beta - \lambda) t^{1+\alpha}] &= 1, \\ \lim_{t \rightarrow \infty} M_{1+\alpha} [(\beta - \lambda) t^{1+\alpha}] &= 0, \end{aligned} \quad (9)$$

then, from (8) and (9), it follows

$$\begin{aligned} \varepsilon_0 &= \lim_{t \rightarrow 0} \varepsilon(t) = \frac{\sigma_0}{E_0}, \\ \varepsilon_\infty &= \lim_{t \rightarrow \infty} \varepsilon(t) = \frac{\sigma_0}{E_\infty}, \end{aligned} \quad (10)$$

where ε_0 and ε_∞ are the creep strains at $t = 0, t \rightarrow \infty$, respectively.

Again, let us consider the Boltzmann convolution integral that describes the relaxation stress $\sigma(t)$ of a material under a strain variable over time $\varepsilon(t)$.

$$\sigma(t) = \varepsilon_0 \phi(t) + \int_0^t \dot{\varepsilon}(\tau) \phi(t-\tau) d\tau, \quad (11)$$

where $\phi(t)$ is the relaxation function and $\varepsilon_0 = \varepsilon(0)$ the strain applied at $t = 0$. The relaxation function $\phi(t)$ coincides with the axial stress produced by the constant strain $\varepsilon(t) = 1$. Integrating by parts (11) it follows

$$\sigma(t) = \varepsilon(t) \phi_0 - \int_0^t \varepsilon(\tau) \dot{\phi}(t-\tau) d\tau. \quad (12)$$

By following [34], (12) can be written in the form

$$\begin{aligned} \sigma(t) &= E_0 \left[\varepsilon(t) + \lambda \int_0^t R_\alpha(\beta, t - \tau) \varepsilon(\tau) d\tau \right], \\ \phi_0 &= E_0. \end{aligned} \quad (13)$$

Assuming a constant strain $\varepsilon(t) = \varepsilon_0$ in order to simulate the stress relaxation test and following the way to find (8), (13) becomes

$$\sigma(t) = E_0 \varepsilon_0 \left\{ 1 + \frac{E_0 - E_\infty}{E_0} \left[M_{1+\alpha} (\beta t^{1+\alpha}) - 1 \right] \right\}. \quad (14)$$

For the properties of the Mittag-Leffler function, from (14) it follows

$$\begin{aligned} \sigma_0 &= \lim_{t \rightarrow 0} \sigma(t) = E_0 \varepsilon_0, \\ \sigma_\infty &= \lim_{t \rightarrow \infty} \sigma(t) = E_\infty \varepsilon_0, \end{aligned} \quad (15)$$

where σ_0 and σ_∞ are the stress relaxation at $t = 0, t \rightarrow \infty$, respectively.

The equations (8) and (14) represent the model by means of the fact that it was possible to fit accurately the experimental creep and stress relaxation tests for suitable values of parameters α and β . The plots of experimental and analytical creep and stress relaxation curves are reported in Figure 2(a) and the corresponding parameters α and β are reported in Table 2.

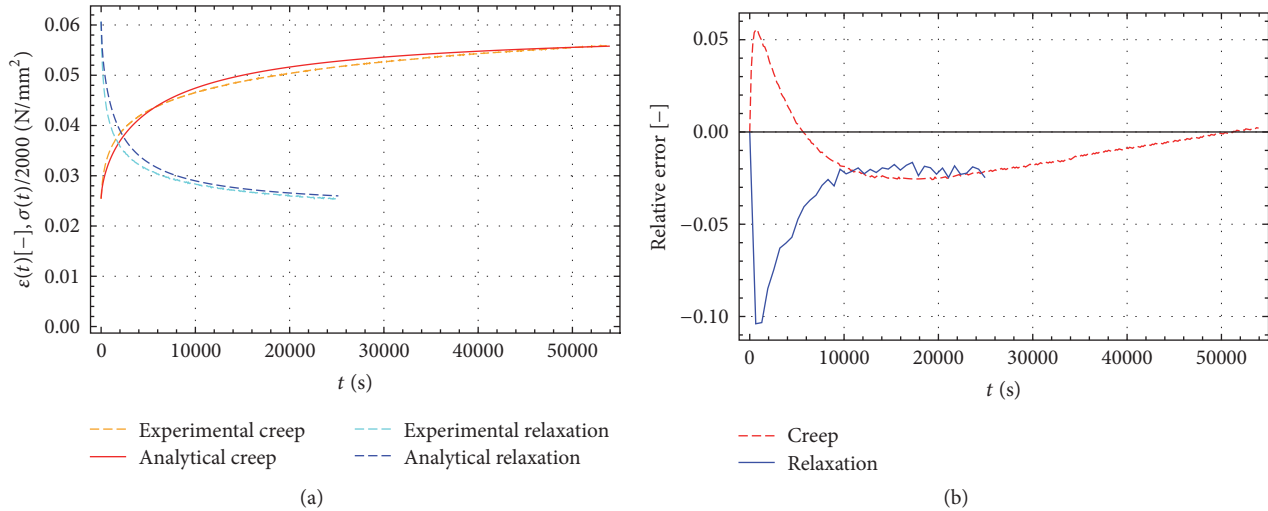


FIGURE 2: (a) Experimental creep curve (dashed orange curve) and analytical creep curve according to (8) (solid red curve). Experimental stress relaxation curve (dashed cyan curve) and analytical stress relaxation curve according to (14) (dashed blue curve) both scaled by 1/2000. (b) Relative error between experimental data on creep and relaxation and their model given by (8) and (14).

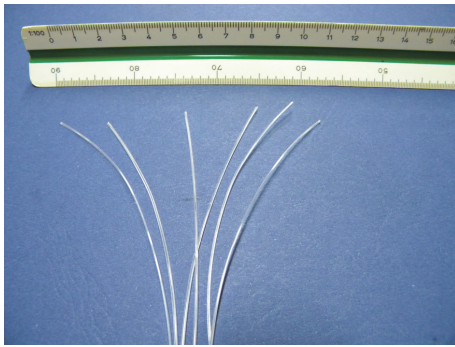


FIGURE 3: Polypropylene fibres used for tensile until breakage and creep and stress relaxation tests [3].

TABLE 2: Parameters α and β that fit experimental creep and relaxation curves using the model given by (8) and (14).

α (dimensionless)	$-1/3$
$\beta \text{ (s}^{-1+\alpha}\text{)}$	$-1/(100\sqrt{3})$

4. Conclusions

In the present paper we carried out a tensile test until breakage and a creep and stress relaxation test on a PP fibre and fitted these experimental tests by using a viscoelastic model based on fractional-exponential kernel. The curves plotted in Figure 2(a) show that the theoretical model closely fits the experimental results. The relative error, showing the deviation between the experimental data and the theoretical prediction, is plotted in Figure 2(b). It shows a maximum relative error of 5% and 10%, respectively, for creep and relaxation, occurring in a very small portion of the curves.

Conversely to complex viscoelastic models based on combinations of Maxwell and Kelvin-Voight schemes, the proposed model requires the calibration of only two parameters (α and β) to simulate creep and relaxation phenomena [35]. Moreover, for simple load or displacement histories, it allows calculating straightforwardly the stress and strain fields based on the calculation of the inverse Laplace transform in closed form. Note also that the Rabotnov function generally allows fitting the experimental data better than other conventional schemes based on the combination of springs and dashpots [34].

It has been proved that the model here adopted is able to match carefully experimental data obtained for PP fibres. In a forthcoming work, the present investigation will be extended in order to take into account the effects induced by thermal variations acting on FRC elements (for the thermodynamic aspects of thermoelasticity, see, e.g., [44]).

Competing Interests

The author declares that they have no competing interests.

References

- [1] P. K. Mallick, *Fiber Reinforced Composites—Materials, Manufacturing, and Design*, CRC Press, New York, NY, USA, 2008.
- [2] L. Lanzoni, A. Nobili, E. Radi, and A. Sorzia, “Axisymmetric loading of an elastic-plastic plate on a general two-parameter foundation,” *Journal of Mechanics of Materials and Structures*, vol. 10, no. 4, pp. 459–479, 2015.
- [3] P. Di Maida, E. Radi, C. Sciancalepore, and F. Bondioli, “Pullout behavior of polypropylene macro-synthetic fibers treated with nano-silica,” *Construction and Building Materials*, vol. 82, pp. 39–44, 2015.
- [4] R. Barretta, L. Feo, and R. Luciano, “Some closed-form solutions of functionally graded beams undergoing nonuniform torsion,” *Composite Structures*, vol. 123, pp. 132–136, 2015.

- [5] R. Luciano and J. R. Willis, "Hashin-Shtrikman based FE analysis of the elastic behaviour of finite random composite bodies," *International Journal of Fracture*, vol. 137, no. 1, pp. 261–273, 2006.
- [6] A. Nobili, L. Lanzoni, and A. M. Tarantino, "Experimental investigation and monitoring of a polypropylene-based fiber reinforced concrete road pavement," *Construction and Building Materials*, vol. 47, pp. 888–895, 2013.
- [7] E. S. Bernard, "Design of fibre reinforced shotcrete linings with macro-synthetic fibres," in *Proceedings of the 11th International Conference on Shotcrete for Underground Support*, F. Amberg and K. F. Garshol, Eds., vol. P11 of *Engineering Conferences International Symposium Series*, 2009, <http://dc.engconfintl.org/shotcrete/14>.
- [8] L. Lanzoni, A. Nobili, and A. M. Tarantino, "Performance evaluation of a polypropylene-based draw-wired fibre for concrete structures," *Construction and Building Materials*, vol. 28, no. 1, pp. 798–806, 2012.
- [9] G. Xotta, G. Mazzucco, V. A. Salomoni, C. E. Majorana, and K. J. Willam, "Composite behavior of concrete materials under high temperatures," *International Journal of Solids and Structures*, vol. 64–65, pp. 86–99, 2015.
- [10] V. A. Salomoni, C. E. Majorana, G. M. Giannuzzi, and A. Miliozzi, "Thermal-fluid flow within innovative heat storage concrete systems for solar power plants," *International Journal of Numerical Methods for Heat and Fluid Flow*, vol. 18, no. 7–8, pp. 969–999, 2008.
- [11] V. A. Salomoni, C. E. Majorana, B. Pomaro, G. Xotta, and F. Gramegna, "Macroscale and mesoscale analysis of concrete as a multiphase material for biological shields against nuclear radiation," *International Journal for Numerical and Analytical Methods in Geomechanics*, vol. 38, no. 5, pp. 518–535, 2014.
- [12] G. Dinelli, G. Belz, C. E. Majorana, and B. A. Schrefler, "Experimental investigation on the use of fly ash for lightweight precast structural elements," *Materials and Structures*, vol. 29, no. 194, pp. 632–638, 1996.
- [13] A. M. Tarantino, "On the finite motions generated by a mode I propagating crack," *Journal of Elasticity*, vol. 57, no. 2, pp. 85–103, 1999.
- [14] A. M. Tarantino, "Crack propagation in finite elastodynamics," *Mathematics and Mechanics of Solids*, vol. 10, no. 6, pp. 577–601, 2005.
- [15] A. M. Tarantino, "The singular equilibrium field at the notch-tip of a compressible material in finite elastostatics," *Zeitschrift für Angewandte Mathematik und Physik*, vol. 48, no. 3, pp. 370–388, 1997.
- [16] A. M. Tarantino, "On extreme thinning at the notch tip of a neo-Hookean sheet," *The Quarterly Journal of Mechanics and Applied Mathematics*, vol. 51, no. 2, pp. 179–190, 1998.
- [17] A. M. Tarantino, "Nonlinear fracture mechanics for an elastic Bell material," *The Quarterly Journal of Mechanics and Applied Mathematics*, vol. 50, no. 3, pp. 435–456, 1997.
- [18] M. Di Prisco, G. Plizzari, and L. Vandewalle, "Fibre reinforced concrete: new design perspectives," *Materials and Structures*, vol. 42, no. 9, pp. 1261–1281, 2009.
- [19] E. Radi and P. Di Maida, "Analytical solution for ductile and FRC plates on elastic ground loaded on a small circular area," *Journal of Mechanics of Materials and Structures*, vol. 9, no. 3, pp. 313–331, 2014.
- [20] L. Dezi and A. M. Tarantino, "Time dependent analysis of concrete structures with variable structural system," *ACI Materials Journal*, vol. 88, no. 3, pp. 320–324, 1991.
- [21] L. Dezi, G. Menditto, and A. M. Tarantino, "Viscoelastic heterogeneous structures with variable structural system," *Journal of Engineering Mechanics*, vol. 119, no. 2, pp. 238–250, 1993.
- [22] L. Dezi, G. Menditto, and A. M. Tarantino, "Homogeneous structures subjected to repeated structural system changes," *Journal of Engineering Mechanics*, vol. 116, no. 8, pp. 1723–1732, 1990.
- [23] R. Barretta, L. Feo, and R. Luciano, "Torsion of functionally graded nonlocal viscoelastic circular nanobeams," *Composites Part B: Engineering*, vol. 72, pp. 217–222, 2015.
- [24] R. Barretta, L. Feo, R. Luciano, and F. Marotti de Sciarra, "A gradient Eringen model for functionally graded nanorods," *Composite Structures*, vol. 131, pp. 1124–1131, 2015.
- [25] R. Barretta, L. Feo, R. Luciano, and F. Marotti de Sciarra, "Variational formulations for functionally graded nonlocal Bernoulli-Euler nanobeams," *Composite Structures*, vol. 129, pp. 80–89, 2015.
- [26] V. Salomoni, G. Mazzucco, C. Pellegrino, and C. Majorana, "Three-dimensional modelling of bond behaviour between concrete and FRP reinforcement," *Engineering Computations*, vol. 28, no. 1, pp. 5–29, 2011.
- [27] A. Caporale, L. Feo, R. Luciano, and R. Penna, "Numerical collapse load of multi-span masonry arch structures with FRP reinforcement," *Composites Part B: Engineering*, vol. 54, no. 1, pp. 71–84, 2013.
- [28] A. Caporale and R. Luciano, "Limit analysis of masonry arches with finite compressive strength and externally bonded reinforcement," *Composites Part B: Engineering*, vol. 43, no. 8, pp. 3131–3145, 2012.
- [29] P. Bisegna and R. Luciano, "Bounds on the overall properties of composites with debonded frictionless interfaces," *Mechanics of Materials*, vol. 28, no. 1–4, pp. 23–32, 1998.
- [30] A. Apuzzo, R. Barretta, and R. Luciano, "Some analytical solutions of functionally graded Kirchhoff plates," *Composites Part B: Engineering*, vol. 68, pp. 266–269, 2015.
- [31] G. W. Scott-Blair and F. M. V. Coppen, "The subjective judgement of the elastic and plastic properties of soft bodies; the 'differential thresholds' for viscosities and compression moduli," *Proceedings of the Royal Society B: Biological Sciences*, vol. 128, no. 850, pp. 109–125, 1939.
- [32] G. W. Scott Blair and F. M. V. Coppen, "The estimation of firmness in soft materials," *The American Journal of Psychology*, vol. 56, no. 2, pp. 234–246, 1943.
- [33] Yu. N. Rabotnov, "Equilibrium of an elastic medium with after-effect," *Journal of Applied Mathematics and Mechanics*, vol. 12, pp. 53–62, 1948 (Russian).
- [34] I. Sevostianov, V. Levin, and E. Radi, "Effective properties of linear viscoelastic microcracked materials: application of Maxwell homogenization scheme," *Mechanics of Materials*, vol. 84, pp. 28–43, 2015.
- [35] F. Di Paola and F. P. Pinnola, *Calcolo Frazionario & Viscoelasticità*, Dipartimento di Ingegneria Civile Ambientale e Aerospaziale, Università degli Studi di Palermo, Palermo, Italy, http://www1.unipa.it/fabio.bagarello/didattica/Di%20Paola%20e%20Pinnola_calcolo%20frazionario.pdf.
- [36] Yu. N. Rabotnov, *Elements of Hereditary Solid Mechanics*, Mir, Moscow, Russia, 1977.
- [37] S. Rogosin and F. Mainardi, "George William Scott Blair—the pioneer of fractional calculus in rheology," *Communications in Applied and Industrial Mathematics*, vol. 6, no. 1, article e-481, 2014.

- [38] I. Podlubny, *Fractional Differential Equations*, Academic Press, New York, NY, USA, 1998.
- [39] F. Mainardi, "Fractional calculus: some basic problems in continuum and statistical mechanics," in *Fractals and Fractional Calculus in Continuum Mechanics*, A. Carpinteri and F. Mainardi, Eds., Springer, Vienna, Austria, 1997.
- [40] F. Mainardi, "Applications of fractional calculus in mechanics," in *Transform Methods and Special Functions, Varna '96*, P. Rusev, I. Dimovski, and V. Kiryakova, Eds., SCT, Singapore, 1997.
- [41] Yu. A. Rossikhin and M. V. Shitikova, "Applications of fractional calculus to dynamic problems of linear and nonlinear hereditary mechanics of solids," *Applied Mechanics Reviews*, vol. 50, no. 1, pp. 15–67, 1997.
- [42] F. Greco and R. Luciano, "A theoretical and numerical stability analysis for composite micro-structures by using homogenization theory," *Composites Part B: Engineering*, vol. 42, no. 3, pp. 382–401, 2011.
- [43] B. Ellis and R. Smith, *Polymers A Property Database*, CRC Press, New York, NY, USA, 2nd edition, 2009.
- [44] F. Marotti de Sciarra and M. Salerno, "On thermodynamic functions in thermoelasticity without energy dissipation," *European Journal of Mechanics A: Solids*, vol. 46, pp. 84–95, 2014.

Research Article

Numerical Investigation of Pull-In Instability in a Micro-Switch MEMS Device through the Pseudo-Spectral Method

P. Di Maida and G. Bianchi

Dipartimento di Scienze e Metodi dell'Ingegneria (DISMI), Università degli Studi di Modena e Reggio Emilia, Via G. Amendola 2, 42122 Reggio Emilia, Italy

Correspondence should be addressed to P. Di Maida; pietro.dimaida@unimore.it

Received 4 December 2015; Revised 10 May 2016; Accepted 5 October 2016

Academic Editor: Julius Kaplunov

Copyright © 2016 P. Di Maida and G. Bianchi. This is an open access article distributed under the Creative Commons Attribution License, which permits unrestricted use, distribution, and reproduction in any medium, provided the original work is properly cited.

A pseudo-spectral approximation is presented to solve the problem of pull-in instability in a cantilever micro-switch. As well known, pull-in instability arises when the acting force reaches a critical threshold beyond which equilibrium is no longer possible. In particular, Coulomb electrostatic force is considered, although the method can be easily generalized to account for fringe as well as Casimir effects. A numerical comparison is presented between a pseudo-spectral and a Finite Element (FE) approximation of the problem, both methods employing the same number of degrees of freedom. It is shown that the pseudo-spectral method appears more effective in accurately approximating the behavior of the cantilever near its tip. This fact is crucial to capturing the threshold voltage on the verge of pull-in. Conversely, the FE approximation presents rapid successions of attracting/repulsing regions along the cantilever, which are not restricted to the near pull-in regime.

1. Introduction

Micro-Electro-Mechanical Systems (MEMS) form a rather diverse and inhomogeneous group of micro-devices aimed at sensing and actuating in a wide array of fields, ranging from mechanical or electronic engineering to chemistry or biology, from micro-mechanics to micro-machining [1–5]. The manufacturing technology is the common standground for such devices, which heavily relies on the different lithographic techniques borrowed from the technology of micro-electronics. Indeed, MEMS devices are mostly obtained from a silicon substrate. It is observed that MEMS are really “systems” in the sense that they are often made up of several functional parts joint together in the device (like piezo- and magneto-sensors [6]). Among MEMS, micro-switch forms a distinct set with great application potential, with special regard to phase shifters and Radio Frequency MEMS (RFMEMS). They are usually gathered in two groups, namely, capacitor and metal-air-metal switches. Besides, they are further divided according to the actuation method: electrostatic, electrothermal, magnetostatic, and piezoelectric among the

most common. A study of magnetoelastic actuated micro-switch is given in [7, 8] for the low-frequency asymptotic analysis of energy scavengers. In this paper, we focus attention on the pull-in instability of a capacitor micro-switch actuated by electrostatic Coulomb force. This particular application has received extensive attention in the literature, owing to the importance of pull-in induced failures in applications. A recent review on the subject can be found in [9]. A theoretical analysis of this problem within the static regime is provided in [10] and references therein. Pull-in voltage in cantilever MEMS have been considered in [11–14]. Failure mechanisms of MEMS include cracking [15–18], peeling of the cantilever [19–21], stiction to the substrate [22–24], and temperature [25, 26]. Besides, micropolar theories are often preferred when dealing with micro- and nanodevices to incorporate the scale effect [27, 28]. Spotlight is set on a pseudo-spectral approximation of the problem, which is compared with a Finite Element (FE) solution. Spectral methods belong to the family of Galerkin's (or Ritz's) methods [29]. Spectral methods are often divided into two groups, namely, *pseudo-spectral* or *interpolating*. The former group enforces the fulfillment of

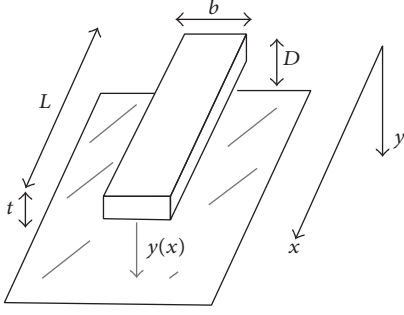


FIGURE 1: Micro-cantilever switch.

the differential operator at a set of points termed nodes (this is sometimes also named *orthogonal collocation*). For the latter group, wherein the Galerkin's method is properly placed, the expansion coefficients are obtained projecting the solution onto the basis set [30].

The paper is structured as follows: Section 2 sets forth the governing equations and the boundary condition for a cantilever. Section 3 introduces the pseudo-spectral method. A numerical comparison with the FE method is illustrated in Section 4. Finally, conclusions are drawn in Section 5.

2. Governing Equations

Let us consider a micro-cantilever switch device subjected to electrostatic attractive force (Figure 1). The micro-cantilever acts as one armor of a capacitor under the electric potential difference V . Let t denote the distance between the capacitor armors. We consider a plane problem and introduce the transverse displacement $y(x)$ for the cantilever. Let us introduce the dimensionless variables

$$\begin{aligned}\xi &= \frac{x}{L}, \\ u &= \frac{y}{t}.\end{aligned}\quad (1)$$

Then the governing equation for the cantilever reads

$$\frac{EIt}{L^4} \frac{d^4 u}{d\xi^4} = q_c + q_e, \quad (2)$$

where q_c and q_e are the Casimir and the electrostatic line-load, being

$$q_e = \alpha \epsilon_0 \frac{bV^2}{t^2(1-u)^2}. \quad (3)$$

Here, V stands for the electric potential difference acting between the capacitor armors (in the SI this is expressed in volt, i.e., $V = \text{N m/C}$ where N stands for newton, m for meter, and C for electric charge, expressed in Coulomb), b is the armors width, $\epsilon_0 = 8.854 \cdot 10^{-12} \text{ C}^2\text{N}^{-1}\text{m}^{-2}$ is the electric permittivity (in vacuum), and α is generally a function of u which takes into account the fringe effect. For the sake of illustrating the method, we neglect the Casimir force

contribution and assume α independent of u . Then, we can rewrite the governing equation (2) as

$$u^{(iv)} = \frac{A}{(1-u)^2}, \quad (4)$$

where prime denotes differentiation with respect to ξ and the following driving parameter is obtained:

$$A = \alpha \epsilon_0 \frac{bL^4}{t^3 EI} V^2 \geq 0. \quad (5)$$

Under the attractive electrostatic force, it is $0 \leq u(\xi) \leq u_{\max} \leq 1$ and the boundary conditions (BCs) for the cantilever read

$$u(0) = u'(0) = u''(1) = u'''(1) = 0. \quad (6)$$

Let us define $v(\xi) = 1 - u(\xi)$; thus (4) further reduces to

$$v^{(iv)} = -\frac{A}{v^2}, \quad (7)$$

with $0 \leq v_{\min} \leq v(\xi) \leq 1$ and the BCs

$$\begin{aligned}v(0) &= 1, \\ v'(0) &= v''(1) = v'''(1) = 0.\end{aligned}\quad (8)$$

It is observed that, integrating and making use of the last BC, it may be deduced that

$$v'''(\xi) = \int_{\xi}^1 \frac{A}{v^2(\tau)} d\tau, \quad (9)$$

which shows that the shearing force is generally positive and it is zero only at $\xi = 1$. The same argument may be applied to infer that v'' is generally negative, apart from the point $\xi = 1$ where it is zero, and that v' is generally negative, although it vanishes at $\xi = 0$. Consequently, v is a *monotonic decreasing* function of ξ and $v(1) = v_{\min}$. The nonlinear fourth order ODE (7) may be integrated once [31, §4.2.1] to give

$$2v'v''' - (v'')^2 = \frac{2A}{v} + \frac{4}{3}B. \quad (10)$$

It is observed that, in the case $B = 0$, (10) falls into the Emdem-Fowler class of nonlinear ODEs, which, in special cases, may admit closed form solutions [31, 32]. Evaluation at $\xi = 1$ and making use of the BCs (8) give

$$B = -\frac{3}{2} \frac{A}{v_{\min}}, \quad (11)$$

which shows that the situation $B = 0$ is not relevant in this problem. Besides, it follows

$$2v'v''' - (v'')^2 = 2A \left(\frac{1}{v} - \frac{1}{v_{\min}} \right) \leq 0, \quad (12)$$

and evaluation at $\xi = 0$ lends

$$[v''(0)]^2 = 2A \left(\frac{1}{v_{\min}} - 1 \right). \quad (13)$$

Consideration of the sign for v' and v''' yields the inequality

$$v'' \leq \sqrt{2A \left(\frac{1}{v_{\min}} - \frac{1}{v} \right)}. \quad (14)$$

3. Pseudo-Spectral Method

The governing equations (7) may be numerically solved through a pseudo-spectral approach [29, 33]. Accordingly, a n -degree polynomial function $p_n(\xi)$ is adopted to approximate the function $u(\xi)$ on the interval $[0, 1]$. Since a collocation method is adopted, the polynomial will be uniquely determined enforcing (7) at some $n + 1$ predetermined points (nodes). This procedure results in a system of nonlinear algebraic equations, which may be solved through standard methods, such as the iterative Newton method. The Jacobian of the system may be supplemented in closed form to the numerical equation solver.

Let $p_n(\xi) \in \mathcal{P}_n$ be the n -degree polynomial approximation of $v(\xi)$. The collocation set is defined through the first $n + 1$ Gauss-Lobatto points

$$\text{GL}_n = \{\eta_i \text{ such that } \eta_0 = -1, \eta_n = +1, p_n'(\eta_i) = 0, i = 1, \dots, n-1\}, \quad (15)$$

where p_n stands for the n th degree Legendre polynomial. Equation (7), evaluated at the interior nodes η_i , yields the system of $(n - 1)$ algebraic equations

$$p_n^2(\eta_i) p_n^{(iv)}(\eta_i) + A = 0, \quad i = 1, \dots, n-1, \quad (16)$$

which is then supplemented with the boundary conditions (8)

$$\begin{aligned} p_n(\eta_0) &= 1, \\ p_n'(\eta_0) &= p_n''(\eta_n) = p_n'''(\eta_n) = 0. \end{aligned} \quad (17)$$

The problem is now rewritten in matrix form. To this aim, let the unknown column vector, the vector of the square, and the vector of the m th derivative

$$\begin{aligned} \mathbf{x} &= [p_n(\eta_i)], \\ \mathbf{y} &= [p_n^2(\eta_i)], \\ \mathbf{x}^{(m)} &= [p_n^{(m)}(\eta_i)], \\ & i = 0, \dots, n, \quad m \in \mathbb{N}. \end{aligned} \quad (18)$$

Making use of the $(n + 1) \times (n + 1)$ derivative matrix \mathbf{D} (see [33, Chap.7]) we have

$$\begin{aligned} \mathbf{x}' &= \mathbf{D}\mathbf{x}, \\ \mathbf{x}'' &= \mathbf{D}\mathbf{D}\mathbf{x} = \mathbf{D}^2\mathbf{x}, \dots \end{aligned} \quad (19)$$

and (16) and (17) may be rewritten through the derivative matrix as

$$\mathbf{y}\widetilde{\mathbf{D}}^4\mathbf{x} + \mathbf{A}\text{Id} = \tilde{\mathbf{o}}, \quad (20)$$

where Id is the identity matrix. Here, $\widetilde{\mathbf{D}}^4$ is \mathbf{D}^4 supplemented with the BCs (8); that is, the first row is set to zero apart from the first entry that is set to 1; the second, the last-but-one and

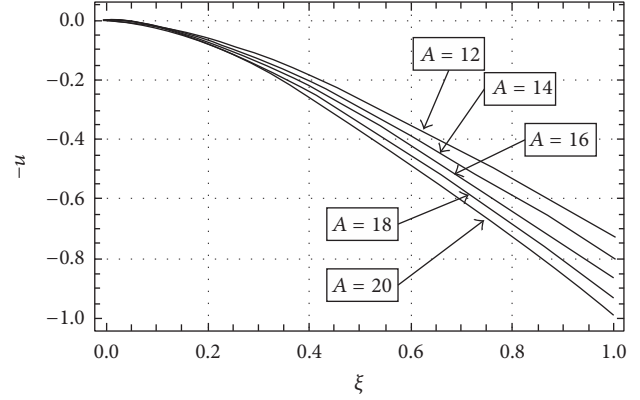


FIGURE 2: Displacement u at $A = 12, 14, 16, 18$ and $A = 20$.

the last rows are replaced by the first and the last rows of \mathbf{D} , \mathbf{D}^2 , and \mathbf{D}^3 , respectively. Then we have

$$\widetilde{\mathbf{D}}^4 = \begin{bmatrix} 1 & 0 & \dots & 0 \\ D_{0,0} & \dots & & D_{0,n} \\ D_{2,0}^4 & \dots & & D_{2,n}^4 \\ \vdots & \ddots & & \\ D_{n-2,0}^4 & \dots & & D_{n-2,n}^4 \\ D_{n-1,0}^2 & \dots & & D_{n-1,n}^2 \\ D_{n,0}^3 & D_{n,1}^3 & \dots & D_{n,n}^3 \end{bmatrix}. \quad (21)$$

At the RHS of system (20) we have the zero vector \mathbf{o} supplemented with the BCs, namely,

$$\tilde{\mathbf{o}} = \begin{bmatrix} 1 \\ 0 \\ \vdots \\ 0 \end{bmatrix}. \quad (22)$$

4. Numerical Solution

In this section, the pseudo-spectral approximation is compared with a Finite Element solution, both methods employing the same number of degrees of freedom, which corresponds to $n = 20$ for the order of the interpolating polynomial. For the FE solution, we introduce 10 nodes, each endowed with 2 degrees of freedom, that is, one translational and the other rotational. In Figure 2, the system of algebraic equations (20) is solved for different values of the driving parameter (voltage difference) A with the FE method. It clearly appears that, for $A = 20$, the cantilever dimensionless tip deflection is very close to 1; that is, the cantilever is at the verge of pull-in instability. Figure 3 shows the product $-v^{(iv)}v^2$, which should be constant along the cantilever and equal to A , for the FE approximation. It is evident that the quality of the numerical solution rapidly deteriorates near the cantilever tip, which is exactly where best accuracy

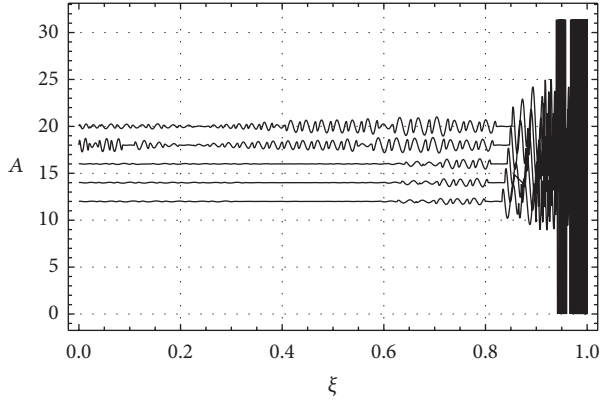


FIGURE 3: Plot of $-v^2 v^{(iv)}$ versus ξ according to the FE approximation: this product should return the constant A .

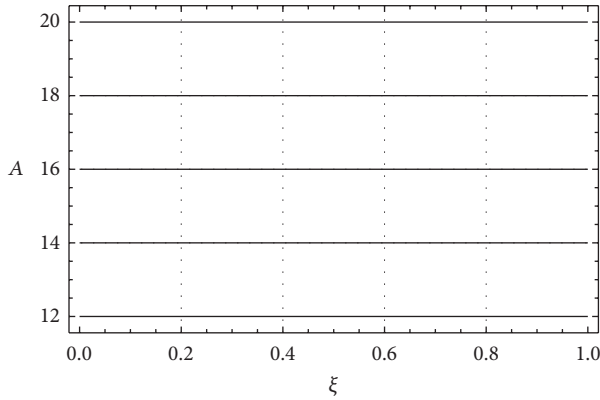


FIGURE 4: Plot of $-v^2 v^{(iv)}$ versus ξ according to the pseudo-spectral approximation: this product should return the constant A .

is demanded to effectively capture the pull-in threshold. Conversely, Figure 4 plots the product $-v^{(iv)}v^2$ for the pseudo-spectral approximation. The comparison between the two plots is a striking example of the effectiveness of this method in this kind of nonlinear problems. Figure 5 plots the slope, bending moment and shearing force along the cantilever beam, and it illustrates that BCs are well captured by the numerical solution, either FE or pseudo-spectral. The plot is obtained by successive differentiation of the displacement field and it is readily available for the spectral method, where polynomial functions are employed. Conversely, obtaining the corresponding curves for the FE approximation needs some extra care for curve fitting of the nodal displacement is first applied, which is then successively differentiated. Figure 6 plots the applied line load density $v^{(iv)}$ for the FE solution near pull-in, which corresponds to (the negative of) the electrostatic Coulomb force $-q_e$. It is remarkable that the electrostatic force appears highly oscillatory (note that curve-fitting is employed to get a continuous plot), and it attains unphysical negative values. As a comparison, Figure 7 describes the same behavior for $A = 12$, that is well below the threshold value for pull-in. It appears that the electrostatic force is rather poorly approximated by the

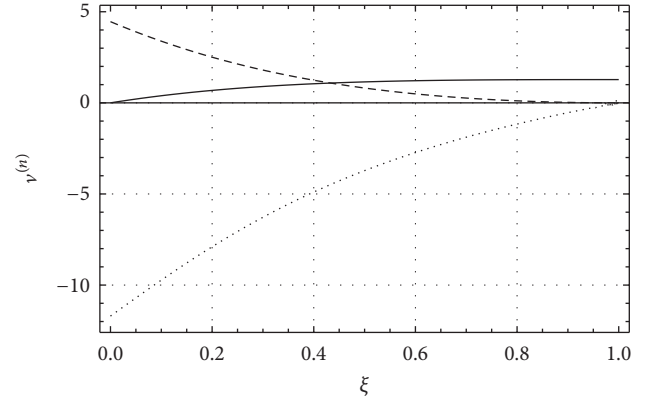


FIGURE 5: Slope (solid), bending moment (dashed), and shearing force (dotted) near pull-in. Graphs are indistinguishable between the pseudo-spectral and the FE solution.

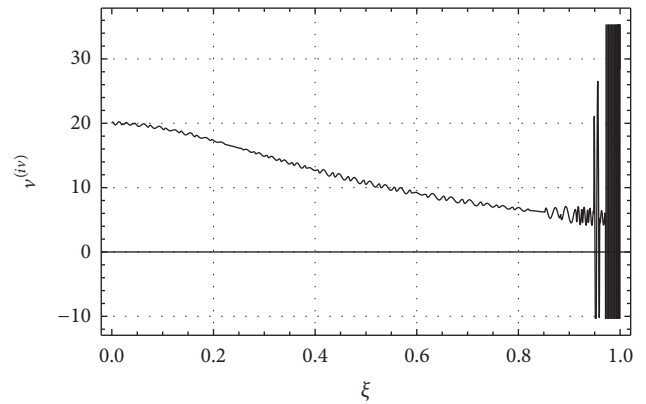


FIGURE 6: Line load density q_e on the cantilever beam near pull-in according to the FE approximation ($A = 20$).

method, even far from instability. On the contrary, Figures 8 and 9 illustrate the same graphs as obtained from the pseudo-spectral method. The smoothness of the solution is remarkable. The reason for the superior performance of the pseudo-spectral approximation seems to lie in the fact that it is more robust in dealing with little deviations of the cantilever tip displacement on the verge of contact. Indeed, it is well known that pseudo-spectral approximation guarantees high precision and exponential convergence (under suitable assumptions, see [29]), and this feature proves important in smoothly approximating the highly nonlinear behavior of the electrostatic force.

5. Conclusions

In this paper, the pseudo-spectral method is adopted to numerically solve the problem of pull-in instability in a cantilever beam. The beam constitutes one armor of a capacitor, the other armor being represented by a grounded flat surface. Although only Coulomb electrostatic force is considered, the method is easily extended to deal with the fringe effect and

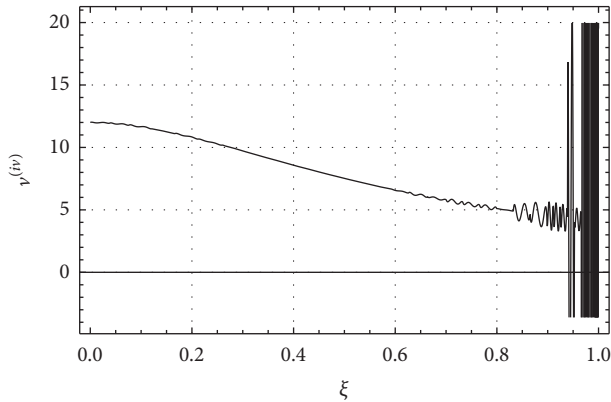


FIGURE 7: Line load density q_e on the cantilever beam near pull-in according to the FE approximation ($A = 12$).

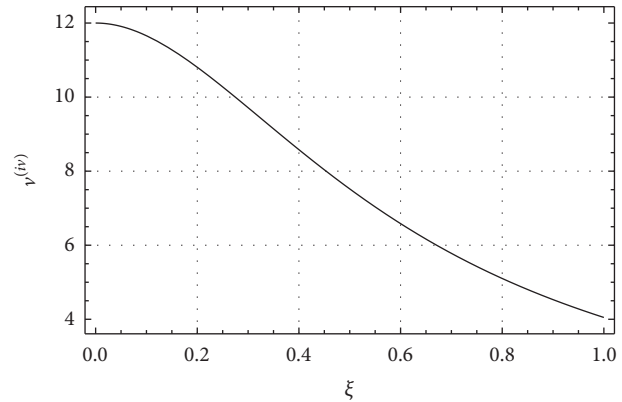


FIGURE 9: Line load density q_e on the cantilever beam near pull-in according to the pseudo-spectral approximation ($A = 12$).

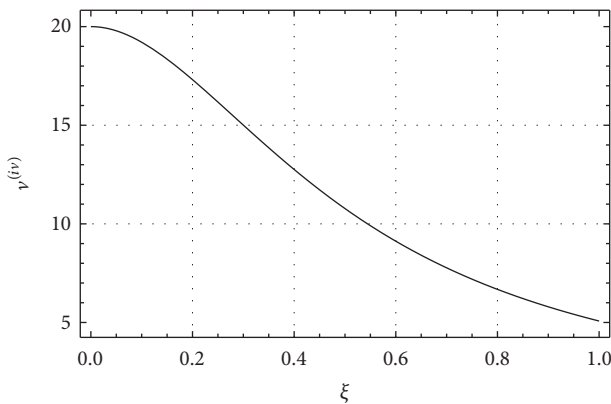


FIGURE 8: Line load density q_e on the cantilever beam near pull-in according to the pseudo-spectral approximation ($A = 20$).

the Casimir force. Results may be especially relevant for cantilever micro-switches in MEMS. It is shown that the pseudo-spectral method compares very favorably with an equivalent Finite Element approximation, equivalency being constituted by an equal number of degrees of freedom in the methods. In particular, good approximation for the cantilever deflection near its tip is crucial to capturing the threshold voltage on the verge of pull-in. Indeed, poor approximation leads to very unphysical oscillatory attraction/repulsion forces along the cantilever. It is further shown that the oscillatory behavior is not restricted to the near pull-in regime. Finally, it is emphasized that both methods exactly satisfy the boundary conditions (BCs). It is remarked that the present analysis can be extended to incorporate functionally graded cantilevers [34–36] and beam-plates [37, 38] or to include viscoelastic effects [39–42].

Competing Interests

The authors declare that they have no competing interests.

References

- [1] V. A. Salomoni, C. E. Majorana, G. M. Giannuzzi, and A. Miliozzi, “Thermal-fluid flow within innovative heat storage concrete systems for solar power plants,” *International Journal of Numerical Methods for Heat and Fluid Flow*, vol. 18, no. 7-8, pp. 969–999, 2008.
- [2] A. Nobili, L. Lanzoni, and A. M. Tarantino, “Experimental investigation and monitoring of a polypropylene-based fiber reinforced concrete road pavement,” *Construction and Building Materials*, vol. 47, pp. 888–895, 2013.
- [3] V. A. Salomoni, C. E. Majorana, B. Pomaro, G. Xotta, and F. Gramegna, “Macroscale and mesoscale analysis of concrete as a multiphase material for biological shields against nuclear radiation,” *International Journal for Numerical and Analytical Methods in Geomechanics*, vol. 38, no. 5, pp. 518–535, 2014.
- [4] G. Dinelli, G. Belz, C. E. Majorana, and B. A. Schrefler, “Experimental investigation on the use of fly ash for lightweight precast structural elements,” *Materials and Structures*, vol. 29, no. 194, pp. 632–638, 1996.
- [5] P. Bisegna and R. Luciano, “Bounds on the overall properties of composites with debonded frictionless interfaces,” *Mechanics of Materials*, vol. 28, no. 1–4, pp. 23–32, 1998.
- [6] A. Nobili and A. M. Tarantino, “Magnetostriction of a hard ferromagnetic and elastic thin-film structure,” *Mathematics and Mechanics of Solids*, vol. 13, no. 2, pp. 95–123, 2008.
- [7] A. Kudaibergenov, A. Nobili, and L. Prikazchikova, “On low-frequency vibrations of a composite string with contrast properties for energy scavenging fabric devices,” *Journal of Mechanics of Materials and Structures*, vol. 11, no. 3, pp. 231–243, 2016.
- [8] J. Kaplunov and A. Nobili, “Multi-parametric analysis of strongly inhomogeneous periodic waveguides with internal cut-off frequencies,” *Mathematical Methods in the Applied Sciences*, 2016.
- [9] W.-M. Zhang, H. Yan, Z.-K. Peng, and G. Meng, “Electrostatic pull-in instability in MEMS/NEMS: a review,” *Sensors and Actuators A: Physical*, vol. 214, pp. 187–218, 2014.
- [10] Y. Zhang and Y.-P. Zhao, “Static study of cantilever beam stiction under electrostatic force influence,” *Acta Mechanica Sinica*, vol. 17, no. 2, pp. 104–112, 2004.
- [11] L. C. Wei, A. B. Mohammad, and N. M. Kassim, “Analytical modeling for determination of pull-in voltage for an electrostatic actuated MEMS cantilever beam,” in *Proceedings of the*

- 5th IEEE International Conference on Semiconductor Electronics (ICSE '02), pp. 233–238, IEEE, Penang, Malaysia, December 2002.
- [12] S. Chowdhury, M. Ahmadi, and W. C. Miller, “A closed-form model for the pull-in voltage of electrostatically actuated cantilever beams,” *Journal of Micromechanics and Microengineering*, vol. 15, no. 4, pp. 756–763, 2005.
- [13] H. Sadeghian, G. Rezazadeh, and P. M. Osterberg, “Application of the generalized differential quadrature method to the study of pull-in phenomena of MEMS switches,” *Journal of Microelectromechanical Systems*, vol. 16, no. 6, pp. 1334–1340, 2007.
- [14] A. Ramezani, A. Alasty, and J. Akbari, “Closed-form solutions of the pull-in instability in nano-cantilevers under electrostatic and intermolecular surface forces,” *International Journal of Solids and Structures*, vol. 44, no. 14–15, pp. 4925–4941, 2007.
- [15] A. M. Tarantino, “On the finite motions generated by a mode I propagating crack,” *Journal of Elasticity*, vol. 57, no. 2, pp. 85–103, 1999.
- [16] A. M. Tarantino, “Nonlinear fracture mechanics for an elastic Bell material,” *The Quarterly Journal of Mechanics and Applied Mathematics*, vol. 50, no. 3, pp. 435–456, 1997.
- [17] R. Luciano and J. R. Willis, “Hashin-Shtrikman based FE analysis of the elastic behaviour of finite random composite bodies,” *International Journal of Fracture*, vol. 137, no. 1–4, pp. 261–273, 2006.
- [18] A. Nobili, E. Radi, and L. Lanzoni, “A cracked infinite Kirchhoff plate supported by a two-parameter elastic foundation,” *Journal of the European Ceramic Society*, vol. 34, no. 11, pp. 2737–2744, 2014.
- [19] L. Lanzoni and E. Radi, “Thermally induced deformations in a partially coated elastic layer,” *International Journal of Solids and Structures*, vol. 46, no. 6, pp. 1402–1412, 2009.
- [20] V. Guidi, L. Lanzoni, and A. Mazzolari, “Patterning and modeling of mechanically bent silicon plates deformed through coactive stresses,” *Thin Solid Films*, vol. 520, no. 3, pp. 1074–1079, 2011.
- [21] N. Tullini, A. Tralli, and L. Lanzoni, “Interfacial shear stress analysis of bar and thin film bonded to 2D elastic substrate using a coupled FE-BIE method,” *Finite Elements in Analysis and Design*, vol. 55, pp. 42–51, 2012.
- [22] C. H. Mastrangelo, *Suppression of Stiction in MEMS*, vol. 605 of *MRS Proceedings*, Cambridge University Press, Cambridge, UK, 1999.
- [23] W. Merlijn Van Spengen, R. Puers, and I. De Wolf, “A physical model to predict stiction in MEMS,” *Journal of Micromechanics and Microengineering*, vol. 12, no. 5, pp. 702–713, 2002.
- [24] Z. Yapu, “Stiction and anti-stiction in MEMS and NEMS,” *Acta Mechanica Sinica*, vol. 19, no. 1, pp. 1–10, 2003.
- [25] G. Xotta, G. Mazzucco, V. A. Salomoni, C. E. Majorana, and K. J. Willam, “Composite behavior of concrete materials under high temperatures,” *International Journal of Solids and Structures*, vol. 64, pp. 86–99, 2015.
- [26] F. Marotti de Sciarra and M. Salerno, “On thermodynamic functions in thermoelasticity without energy dissipation,” *European Journal of Mechanics—A: Solids*, vol. 46, pp. 84–95, 2014.
- [27] A. Nobili, “On the generalization of the Timoshenko beam model based on the micropolar linear theory: static case,” *Mathematical Problems in Engineering*, vol. 2015, Article ID 914357, 8 pages, 2015.
- [28] G. Napoli and A. Nobili, “Mechanically induced Helfrich-Hurault effect in lamellar systems,” *Physical Review E*, vol. 80, no. 3, Article ID 031710, 2009.
- [29] J. P. Boyd, *Chebyshev and Fourier Spectral Methods*, Dover Publications, 2nd edition, 2000.
- [30] F. Greco and R. Luciano, “A theoretical and numerical stability analysis for composite micro-structures by using homogenization theory,” *Composites—Part B: Engineering*, vol. 42, no. 3, pp. 382–401, 2011.
- [31] A. D. Polyanin and V. F. Zaitsev, *Handbook of Exact Solutions for Ordinary Differential Equations*, CRC Press, Boca Raton, Fla, USA, 1st edition, 1995.
- [32] P. L. Sachdev, *Nonlinear Ordinary Differential Equations and Their Applications*, Marcel Dekker, 1991.
- [33] D. Funaro, *Polynomial Approximation of Differential Equations*, vol. 8 of *Lecture Notes in Physics*, Springer, 1992.
- [34] R. Barretta, L. Feo, R. Luciano, and F. Marotti de Sciarra, “Variational formulations for functionally graded nonlocal Bernoulli-Euler nanobeams,” *Composite Structures*, vol. 129, pp. 80–89, 2015.
- [35] R. Barretta, L. Feo, R. Luciano, and F. Marotti de Sciarra, “A gradient Eringen model for functionally graded nanorods,” *Composite Structures*, vol. 131, pp. 1124–1131, 2015.
- [36] R. Barretta, L. Feo, and R. Luciano, “Some closed-form solutions of functionally graded beams undergoing nonuniform torsion,” *Composite Structures*, vol. 123, pp. 132–136, 2015.
- [37] R. Barretta and R. Luciano, “Exact solutions of isotropic viscoelastic functionally graded Kirchhoff plates,” *Composite Structures*, vol. 118, no. 1, pp. 448–454, 2014.
- [38] A. Apuzzo, R. Barretta, and R. Luciano, “Some analytical solutions of functionally graded Kirchhoff plates,” *Composites Part B: Engineering*, vol. 68, pp. 266–269, 2015.
- [39] L. Dezi, G. Menditto, and A. M. Tarantino, “Homogeneous structures subjected to repeated structural system changes,” *Journal of Engineering Mechanics*, vol. 116, no. 8, pp. 1723–1732, 1990.
- [40] L. Dezi and A. M. Tarantino, “Time-dependent analysis of concrete structures with a variable structural system,” *ACI Materials Journal*, vol. 88, no. 3, pp. 320–324, 1991.
- [41] L. Dezi, G. Menditto, and A. M. Tarantino, “Viscoelastic heterogeneous structures with variable structural system,” *Journal of Engineering Mechanics*, vol. 119, no. 2, pp. 238–250, 1993.
- [42] R. Barretta, L. Feo, and R. Luciano, “Torsion of functionally graded nonlocal viscoelastic circular nanobeams,” *Composites Part B: Engineering*, vol. 72, pp. 217–222, 2015.

Research Article

Floquet Theory for Discontinuously Supported Waveguides

A. Sorzia

Dipartimento di Scienze e Metodi dell'Ingegneria (DISMI), Università degli Studi di Modena e Reggio Emilia, Via G. Amendola 2, 42122 Reggio Emilia, Italy

Correspondence should be addressed to A. Sorzia; andrea.sorzia@unimore.it

Received 24 December 2015; Accepted 5 May 2016

Academic Editor: Julius Kaplunov

Copyright © 2016 A. Sorzia. This is an open access article distributed under the Creative Commons Attribution License, which permits unrestricted use, distribution, and reproduction in any medium, provided the original work is properly cited.

We apply Floquet theory of periodic coefficient second-order ODEs to an elastic waveguide. The waveguide is modeled as a uniform elastic string periodically supported by a discontinuous Winkler elastic foundation and, as a result, a Hill equation is found. The fundamental solutions, the stability regions, and the dispersion curves are determined and then plotted. An asymptotic approximation to the dispersion curve is also given. It is further shown that the end points of the band gap structure correspond to periodic and semiperiodic solutions of the Hill equation.

1. Introduction

Periodic structures often appear in several mechanical systems, ranging from strings and beams [1, 2] to phononic crystals [3–5] to name just a few. Such systems exhibit a typical pass/block band structure when wave propagation is considered. Indeed, periodic structures are especially relevant when employed as waveguides [6, 7] or energy scavenging devices [8]. The analysis of the transmission property of waveguides is best carried out through Floquet theory of periodic coefficient ODEs, although this fact is seldom neglected in favor of a more direct approach by means of the Floquet-Bloch boundary conditions. In this paper, an analysis of the mechanical problem of a uniform string periodically supported on a Winkler foundation is presented from the standpoint of the stability theory of Hill's equation [9]. Besides, a high-frequency asymptotic homogenization procedure is presented, following [10, 11]. The discontinuous character of the support may be due to crack propagation [12–15] or debonding in composite materials [16, 17]. It could also be due to the tensionless character of the substrate [18]. This study follows upon a very vast body of literature on elastic periodic structures [2, 19–24]. The situation of wave propagation through a thin coating layer [25–27] could also be considered. Applications in the realm of civil engineering are also possible [28–32]. The paper is structured as follows: Section 2 sets up the mechanical model and the governing

equations. Section 3 discusses stability of the solution of Hill's equation. The dispersion relation and its asymptotic approximation are presented in Section 4. Finally, conclusions are drawn in Section 5.

2. The Mechanical Model

Let us consider a homogeneous elastic string in uniform tension T , periodically supported on a Winkler elastic foundation (Figure 1). The governing equation for the transverse displacement $w(x, t)$ in the absence of loading is periodic with period L :

$$-T\partial_{xx}w + \rho A\partial_{tt}w + (1-H)\beta w = 0, \quad x \in (-L_1, L - L_1), \quad (1)$$

where ρA is the mass linear density of the string, assumed constant, β is the Winkler subgrade modulus (with physical dimension of stress), and H is Heaviside step function; that is,

$$H(x) = \begin{cases} 1, & x > 0, \\ 0, & x < 0. \end{cases} \quad (2)$$

This equation may be rewritten in dimensionless form

$$-\kappa^2 w'' + \ddot{w} + (1-H)w = 0, \quad x_1 \in (-\alpha, 1 - \alpha), \quad (3)$$

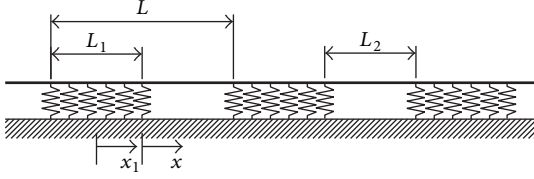


FIGURE 1: A homogeneous string periodically supported by an elastic foundation.

having introduced the dimensionless positive ratios:

$$\kappa = \sqrt{\frac{T}{\beta L^2}}, \quad (4)$$

$$\alpha = \frac{L_1}{L} \leq 1,$$

together with $x_1 = x/L \in [0, 1]$, the dimensionless axial coordinate, and $\tau = t/\sqrt{\rho A/\beta}$, the dimensionless time. Here, prime denotes differentiation with respect to x_1 and dot differentiation with respect to τ and $w(x_1, \tau)$ and $H(x_1)$ are assumed. We shall look for the harmonic behavior of w ; that is, $w(x_1, \tau) = u(x_1) \exp(i\Omega\tau)$, whence (3) becomes the constant coefficient ODE for $u(x_1)$:

$$-\kappa^2 u'' - \Omega^2 u + (1 - H)u = 0, \quad x_1 \in (-\alpha, 1 - \alpha). \quad (5)$$

We shift the unit period to range in the interval $(-\alpha/2, 1 - \alpha/2)$ in order to consider an even/odd problem; namely,

$$-\kappa^2 u'' - \Omega^2 u + \left[1 - H\left(x_1 - \frac{\alpha}{2}\right)\right]u = 0, \quad (6)$$

$$x_1 \in \left(-\frac{\alpha}{2}, 1 - \frac{\alpha}{2}\right).$$

The general harmonic solution of (3) in the supported region $x_1 \in (-\alpha/2, \alpha/2)$ is given by

$$u_s(x_1) = A_1 \exp\left(\frac{\sqrt{1 - \Omega^2}}{\kappa} x_1\right) + A_2 \exp\left(-\frac{\sqrt{1 - \Omega^2}}{\kappa} x_1\right), \quad (7)$$

while the solution in the free region $x_1 \in (\alpha/2, 1 - \alpha/2)$ is

$$u_f(x_1) = B_1 \sin\left(\frac{\Omega}{\kappa} x_1\right) + B_2 \cos\left(\frac{\Omega}{\kappa} x_1\right), \quad (8)$$

where A_1, A_2 and B_1, B_2 are integration constants to be determined through the boundary conditions (BCs). The BCs for the system require continuity at the supported/unsupported transition:

$$u_s(0) = u_f(0), \quad (9)$$

$$u'_s(0) = u'_f(0),$$

where prime stands for x_1 differentiation. Furthermore, consideration of the Floquet-Bloch waves lends the periodicity conditions

$$u_s\left(-\frac{\alpha}{2}\right) = u_f\left(1 - \frac{\alpha}{2}\right)\rho, \quad (10)$$

$$u'_s\left(-\frac{\alpha}{2}\right) = u'_f\left(1 - \frac{\alpha}{2}\right)\rho,$$

where $\rho \neq 0$ is the *characteristic multiplier*. For a second-order ODE, there are two nonnecessarily distinct characteristic multipliers, which are denoted by ρ_1 and ρ_2 . Besides, let $\rho_k = \exp(m_k)$ with $k \in \{1, 2\}$; then $m_k = iq$ is the *characteristic exponent*.

3. Boundedness and Periodicity of the Solution

Equation (5) is known as Hill's equation, after Hill who studied it in 1886 in the context of lunar dynamics [33]. For the sake of clarity, we shall write $(0, a)$ for the periodicity interval $(-\alpha/2, 1 - \alpha/2)$. It is easy to find a fundamental system of solutions $\phi_1(x_1), \phi_2(x_1)$ such that

$$\begin{aligned} \phi_1(0) &= 1, \\ \phi_1'(0) &= 0, \\ \phi_2(0) &= 0, \\ \phi_2'(0) &= 1. \end{aligned} \quad (11)$$

This is a set of two particular linearly independent solutions of the ODE (6); see [9] for further details. It is well known that, for any second-order ODE,

$$W(\phi_1(x_1), \phi_2(x_1)) = \det \begin{bmatrix} \phi_1(x_1) & \phi_2(x_1) \\ \phi_1'(x_1) & \phi_2'(x_1) \end{bmatrix} = \phi_1(x_1)\phi_2(x_1)' - \phi_2(x_1)\phi_1'(x_1) \equiv 1, \quad (12)$$

where W is the Wronskian of the fundamental solutions [34]. In light of the problem's symmetry, ϕ_1 is an *even* and ϕ_2 an *odd* function. Let us introduce the *discriminant*

$$D = \phi_1(a) + \phi_2'(a) = \rho_1 + \rho_2 = 2f(\Omega) \sin\left[\frac{(1 - \alpha)\Omega}{\kappa}\right] \sin\left(\frac{\alpha\sqrt{\Omega^2 - 1}}{\kappa}\right) + 2 \cos\left[\frac{(1 - \alpha)\Omega}{\kappa}\right] \cos\left(\frac{\alpha\sqrt{\Omega^2 - 1}}{\kappa}\right), \quad (13)$$

being

$$f(\Omega) = \frac{1 - 2\Omega^2}{2\Omega\sqrt{\Omega^2 - 1}} = -\frac{1 - 1/2\Omega^2}{\sqrt{1 - 1/\Omega^2}}. \quad (14)$$

Hill's equation is said to be *unstable* if all nontrivial solutions are unbounded in \mathbb{R} and *conditionally stable* if there is a

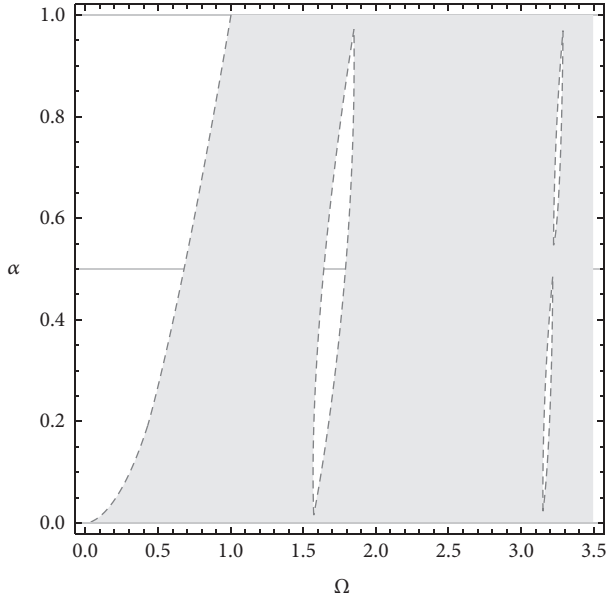


FIGURE 2: Stability regions (shaded in gray) for Hill's equation (5) at $\kappa = 0.5$. Solid and dashed curves represent the level lines $D = \pm 2$, respectively.

nontrivial solution bounded in \mathbb{R} and *stable* if all solutions are bounded in \mathbb{R} .

By Theorem 1.3.1 of [9], the solution is stable if $|D| < 2$ and unstable when $|D| > 2$ and special consideration is required for the case $|D| = 2$. Indeed, when $|D| < 2$, the characteristic multipliers ρ_1 and ρ_2 are complex conjugated and have unit modulus, whereupon the characteristic exponents are opposite; that is, $q_1 = -q_2$. Figure 2 plots the bounding curves $D = 2$ (dashed) and $D = -2$ (solid) as a function of Ω and α for $\kappa = 0.5$. Stable regions are shaded in gray. It is seen that Band Gaps (BGs) are bounded by dashed and solid curves in succession. When $D = \pm 2$ it is $\rho_1 = \rho_2 = \pm 1$, respectively.

It is also well known [9, Section 1.2] that the bounding curve $D = 2$ corresponds to solutions in the form

$$\begin{aligned} \psi_1(x_1) &= p_1(x_1), \\ \psi_2(x_1) &= p_2(x_1), \end{aligned} \quad (15)$$

where $p_1(x_1)$ and $p_2(x_1)$ are periodic functions with period 1, provided that the following condition which grants the availability of two eigenvectors for the repeated eigenvalue $\rho_{1,2} = 1$ holds

$$\phi_2(a) = \phi_1'(a) = 0. \quad (16)$$

Under the same condition, the bounding curve $D = -2$ corresponds to solutions in the form

$$\begin{aligned} \psi_1(x_1) &= P_1(x_1), \\ \psi_2(x_1) &= P_2(x_1), \end{aligned} \quad (17)$$

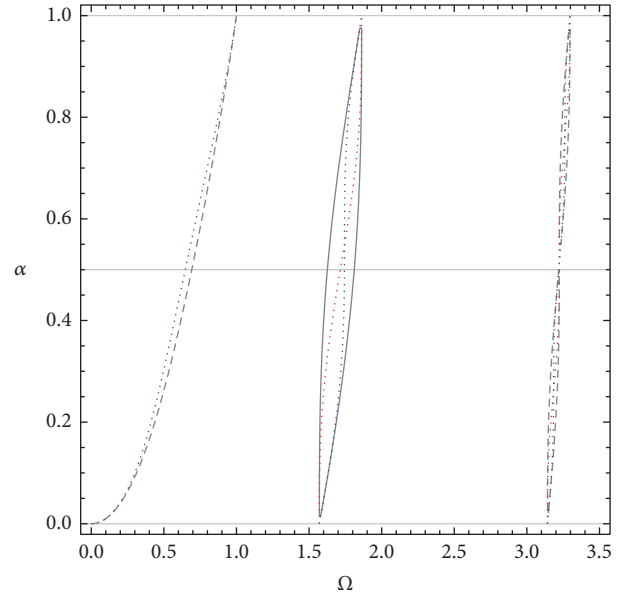


FIGURE 3: Periodic and semiperiodic solutions for Hill's equation (5) at $\kappa = 0.5$. The red and the blue dotted curves represent the solution of the first and the second of the conditions (16), respectively.

where $P_1(x_1)$ and $P_2(x_1)$ are *semiperiodic* function with period 1; that is,

$$P_i(x_1 + 1) = -P_i(x_1), \quad i = 1, 2. \quad (18)$$

In Figure 3, the solution curves for the first and the second of the conditions (16) are plotted in dotted line style and they partly overlie the conditionally stable curves $D = \pm 2$. However, it is observed that such conditions are satisfied only at some very special points. Indeed, we have

$$\begin{aligned} (1 - \Omega^2) \phi_2(a) - \kappa^2 \phi_1'(a) \\ = \frac{\kappa}{\Omega} \sin\left(\frac{(1 - \alpha)\Omega}{\kappa}\right) \cosh\left(\frac{\alpha\sqrt{1 - \Omega^2}}{\kappa}\right), \end{aligned} \quad (19)$$

whence crossing is possible either when

$$\Omega = n \frac{\kappa\pi}{1 - \alpha}, \quad n \in \{0, 1, 2, 3, \dots\} \quad (20)$$

or when $\alpha = 1$. The case $\alpha = 1$ relates to a fully supported string for which $\phi_1'(a)$ and $\phi_2(a)$ are both proportional to

$$\sqrt{\Omega^2 - 1} \sinh \frac{\sqrt{\Omega^2 - 1}}{\kappa}, \quad (21)$$

so that they vanish at the isolated points $\Omega = \sqrt{1 + n^2\kappa^2\pi^2}$, $n \in \{0, 1, 2, \dots\}$. The first point, $\Omega = 1$, corresponds to the pivotal frequency for the 0th BG. Conversely, the case $\alpha = 0$ corresponds to a free string, which is a nondispersive situation. Indeed, BGs collapse into single points which, according to (20), are located at $\Omega = n\kappa\pi$. Other (Ω, α, κ) combinations exist which satisfy $|D| = 2$ and (16), such as $(3.22313, 0.512649, 0.5)$. In all such points two periodic

(or semiperiodic) solutions exist and conditional stability is reverted to stability. However, in the general case, (16) never hold together and thus conditional stability remains. Indeed, the second of the conditions (15) is replaced by

$$\psi_2(x_1) = x_1 p_1(x_1) + p_2(x_1), \quad (22)$$

which is obviously unstable. By the same token, the second of the conditions (17) becomes

$$\psi_2(x_1) = x_1 P_1(x_1) + P_2(x_1). \quad (23)$$

Thus, the *coexistence problem* for period 1 is generally answered in the negative; that is, a single periodic (or semiperiodic) solution exists which is accompanied by a nonperiodic one. Besides, from a mechanical standpoint, it is observed that, in the general case, a periodic solution $p(x)$ is not acceptable on physical grounds, as it conveys a jump discontinuity at the boundary, unless

$$p(0) = p(a). \quad (24)$$

Likewise, a semiperiodic solution $P(x)$ is not acceptable unless

$$P(0) = -P(a). \quad (25)$$

We now prove that such conditions can always be met. To this aim we now take advantage of the problem's symmetry and recall that a nontrivial even solution exists if and only if

$$\begin{aligned} \phi_1' \left(\frac{a}{2} \right) &= 0 \\ \text{or } \phi_1 \left(\frac{a}{2} \right) &= 0, \end{aligned} \quad (26)$$

respectively, are periodic and semiperiodic, whereas an odd solution stands if and only if

$$\begin{aligned} \phi_2' \left(\frac{a}{2} \right) &= 0 \\ \text{or } \phi_2 \left(\frac{a}{2} \right) &= 0, \end{aligned} \quad (27)$$

again for periodic and semiperiodic [9, Theorem 1.3.4]. Now, when $D = 2$ we have the nontrivial periodic solution $p_1(x_1)$ and let us define

$$p_{1+}(x_1) = \frac{p_1(x_1) + p_1(a - x_1)}{p_1(0) + p_1(a)}. \quad (28)$$

By the periodicity of p_1 , clearly p_{1+} is proportional to the even part of p_1 and it is periodic. Besides,

$$\begin{aligned} p_{1+}(0) &= p_{1+}(a), \\ p_{1+}' \left(\frac{a}{2} \right) &= 0, \end{aligned} \quad (29)$$

which are, respectively, (24) and the first of the conditions (26). With the choice for the denominator in (28), it is also $p_{1+}(0) = 1$ by which we conclude that $p_{1+} \equiv \phi_1$ extended in

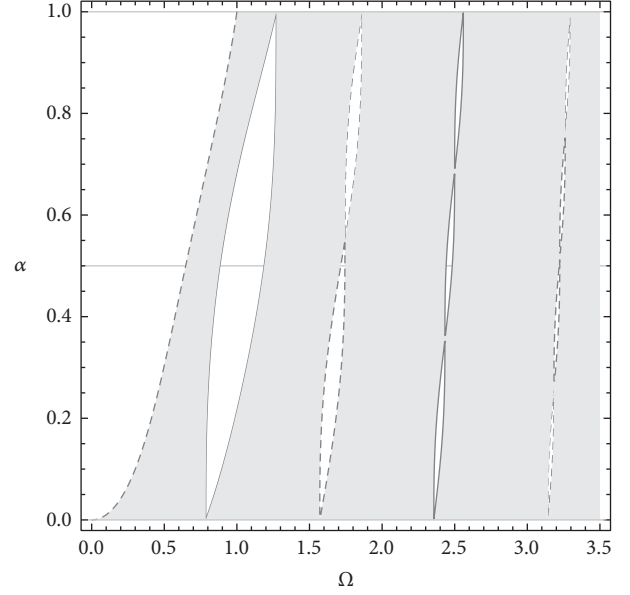


FIGURE 4: Stability regions (shaded in gray) for Hill's equation (5) at $\kappa = 0.25$.

periodic fashion (it is also easy to show that no slope jump discontinuity is admitted by Hill's equation. Then, one can prove that $\phi_1'(0) = \phi_1'(a) = 0$ and $\phi_2'(0) = \pm\phi_2'(a)$, where the sign is given in the periodic and semiperiodic situation, resp.). Likewise, when $D = -2$, we have the nontrivial semiperiodic solution $P_1(x_1)$ and let us define

$$P_{1-}(x_1) = \frac{P_1(x_1) - P_1(a - x_1)}{P_1(0) - P_1(a)}, \quad (30)$$

which, in light of P_1 being semiperiodic, is again proportional to the *even* part of P_1 . It is the sum of two semiperiodic functions; $P_{1-}(x)$ is semiperiodic; besides

$$\begin{aligned} P_{1-}(0) &= -P_{1-}(a), \\ P_{1-} \left(\frac{a}{2} \right) &= 0, \end{aligned} \quad (31)$$

which are, respectively, (25) and the second of the conditions (27). With the choice for the denominator in (30), it is $P_{1-}(0) = 1$ and we conclude that $P_{1-} \equiv \phi_1$ extended in semiperiodic fashion. Through the analogous definitions of p_{1-} and P_{1+} , one gets the odd function ϕ_2 extended in periodic and semiperiodic fashion, respectively.

The role of κ is illustrated comparing Figure 2 with Figure 4. It is seen that the frequency axis roughly scales with κ . Besides, reducing κ brings wider BGs which tilt and tend to cluster together. It is noticed that no symmetry exists about $\alpha = 0.5$.

4. Dispersion Relation

Imposing the BCs ((9), (10)) gives the dispersion relation:

$$\frac{1}{2}D - \cos q = 0. \quad (32)$$

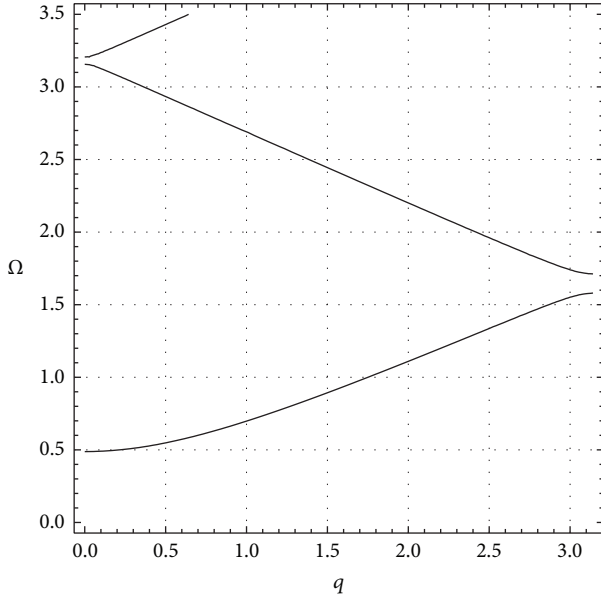


FIGURE 5: Dispersion relation for a string on a periodic support ($\kappa = 0.5$, $\alpha = 0.25$).

This relation can also be written as (see also [35])

$$\begin{aligned} & \frac{1}{2} [1 + f(\Omega)] \cos\left(\frac{(1-\alpha)\Omega - \alpha\sqrt{\Omega^2 - 1}}{\kappa}\right) \\ & + \frac{1}{2} (1 - f(\Omega)) \cos\left(\frac{(1-\alpha)\Omega + \alpha\sqrt{\Omega^2 - 1}}{\kappa}\right) \\ & - \cos q = 0 \end{aligned} \quad (33)$$

and it is plotted in Figure 5 for $\kappa = 0.5$ and $\alpha = 0.25$. Equation (32) conforms to the form of (4) in [19].

It is easy to prove that $f(\Omega)$ quickly asymptotes -1 from below for $\Omega > 1$, whence we can give a simple expression for the dispersion relation:

$$\frac{(1-\alpha)\Omega + \alpha\sqrt{\Omega^2 - 1}}{\kappa} = q + k\pi, \quad k \in \{0, 1, 2, \dots\}. \quad (34)$$

Such approximation is superposed onto the dispersion curves in Figure 8 whereupon it is seen that it is very effective already at Ω close to 1, although it is unable to capture the BGs.

The relevant bounding values for each band gap (BG) are obtained considering the periodic and the semiperiodic eigenvalue problems, for which two sets of BCs need to be considered, respectively:

- (1) the periodicity conditions $u(0) = u(a)$ and $u'(0) = u'(a)$;
- (2) the semiperiodicity conditions $u(0) = -u(a)$ and $u'(0) = -u'(a)$.

The relevant eigenfrequencies are denoted by $\lambda_0, \lambda_1, \dots$ and μ_0, μ_1, \dots , respectively, for the periodic and the semiperiodic eigenproblems. The eigenmode for the first periodic eigenfrequency λ_0 is shown in Figure 6 at $\kappa = 0.5$, $\alpha = 0.25$. Likewise,

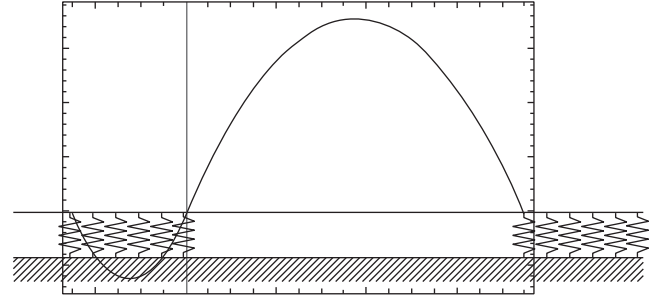


FIGURE 6: The first eigenmode, relative to the eigenfrequency $\lambda_0 = 0.488445$ at $\kappa = 0.5$, $\alpha = 0.25$, and $q = 0$, is a periodic function.

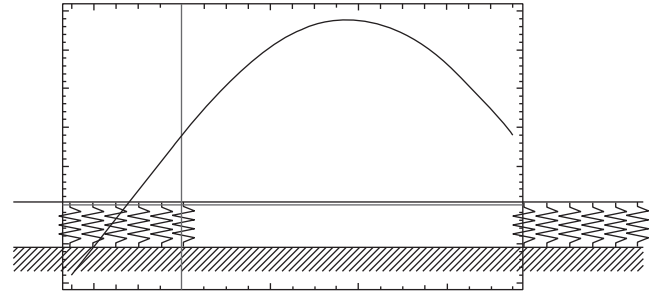


FIGURE 7: The eigenmode at the lower end of the first BG, relative to the eigenfrequency $\mu_0 = 1.57858$ at $\kappa = 0.5$, $\alpha = 0.25$, and $q = \pi$, is a semiperiodic function.

the eigenmode for the first semiperiodic eigenfrequency μ_0 is shown in Figure 7. Such eigenfrequency is the lower boundary of the system's first BG.

The dispersion curve intersection with the axis $q = 0$ is given by λ_m while the intersection with the axis $q = \pi$ is given by μ_m , where $m \in \mathbb{N}$. BGs' size is obtained by $\mu_{2m} - \mu_{2m+1}$ and $\lambda_{2m+1} - \lambda_{2m+2}$.

5. Conclusions

In this paper, the Floquet theory of periodic coefficient ODEs is applied to describe the behavior of a mechanical waveguide. A homogeneous elastic string periodically supported by an elastic Winkler foundation is considered and it is found that the governing equation is given by a second-order Hill equation. Floquet-Bloch periodic boundary conditions are enforced. The stability regions together with the dispersion relation are found in terms of the Floquet theory through the discriminant. An asymptotic approximation to the lowest cutoff frequency is given. The fundamental eigensolutions of the periodic and of the semiperiodic problem are also determined. It is remarked that the present methodology can be extended to tackle functionally graded beams [36–39] or plates [40, 41]. Applications in the realm of civil engineering are also possible [28–32, 42]. A nice extension of the present theory could be related to temperature [43, 44] or viscoelastic effects in the fiber [45–48].

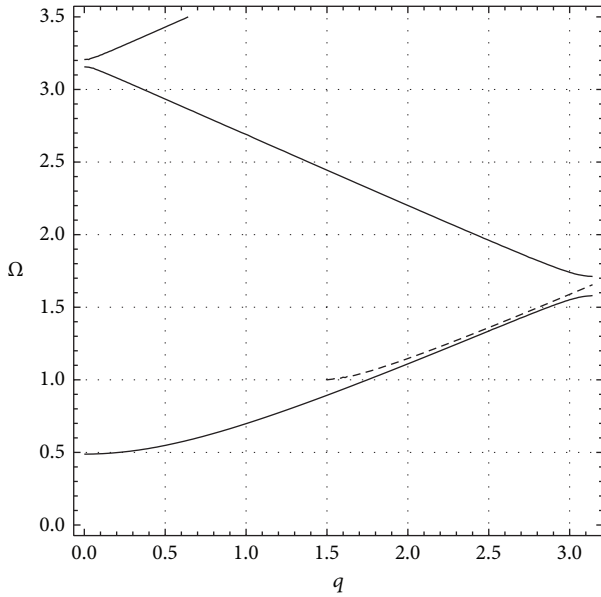


FIGURE 8: Dispersion relation (solid) superposed onto its first approximation (34) (dashed).

Competing Interests

The author declares that there are no competing interests.

References

- [1] D. J. Mead, “Wave propagation and natural modes in periodic systems: I. Mono-coupled systems,” *Journal of Sound and Vibration*, vol. 40, no. 1, pp. 1–18, 1975.
- [2] D. J. Mead, “Wave propagation in continuous periodic structures: research contributions from Southampton, 1964–1995,” *Journal of Sound and Vibration*, vol. 190, no. 3, pp. 495–524, 1996.
- [3] D. Yu, Y. Liu, H. Zhao, G. Wang, and J. Qiu, “Flexural vibration band gaps in Euler-Bernoulli beams with locally resonant structures with two degrees of freedom,” *Physical Review B*, vol. 73, no. 6, Article ID 064301, 2006.
- [4] Y. Zhang, L. Han, and L.-H. Jiang, “Transverse vibration bandgaps in phononic-crystal Euler beams on a Winkler foundation studied by a modified transfer matrix method,” *Physica Status Solidi (B)*, vol. 250, no. 7, pp. 1439–1444, 2013.
- [5] Y. Zhang, J. He, and L.-H. Jiang, “Flexural vibration band gaps characteristics in phononic crystal Euler beams on two-parameter foundation,” *Advances in Mechanical Engineering*, vol. 5, Article ID 935258, 2013.
- [6] J. Miklowitz, *The Theory of Elastic Waves and Waveguides*, Elsevier, New York, NY, USA, 2012.
- [7] A. B. Movchan and L. I. Slepyan, “Resonant waves in elastic structured media: dynamic homogenisation versus Green’s functions,” *International Journal of Solids and Structures*, vol. 51, no. 13, pp. 2254–2260, 2014.
- [8] A. Kudaibergenov, A. Nobili, and L. Prikazchikova, “On low-frequency vibrations of a composite string with contrast properties for energy scavenging fabric devices,” *Journal of Mechanics of Materials and Structures*, vol. 11, no. 3, pp. 231–243, 2016.
- [9] M. S. Eastham, *The Spectral Theory of Periodic Differential Equations*, Scottish Academic Press, Edinburgh, UK, 1973.
- [10] R. V. Craster, J. Kaplunov, and A. V. Pichugin, “High-frequency homogenization for periodic media,” *Proceedings of The Royal Society of London. Series A. Mathematical, Physical and Engineering Sciences*, vol. 466, no. 2120, pp. 2341–2362, 2010.
- [11] T. Antonakakis and R. V. Craster, “High-frequency asymptotics for microstructured thin elastic plates and platonics,” *Proceedings of the Royal Society A: Mathematical, Physical and Engineering Sciences*, vol. 468, no. 2141, pp. 1408–1427, 2012.
- [12] A. M. Tarantino, “On the finite motions generated by a mode I propagating crack,” *Journal of Elasticity*, vol. 57, no. 2, pp. 85–103, 1999.
- [13] A. M. Tarantino, “Crack propagation in finite elastodynamics,” *Mathematics and Mechanics of Solids*, vol. 10, no. 6, pp. 435–456, 2005.
- [14] R. Luciano and J. R. Willis, “Hashin-Shtrikman based FE analysis of the elastic behaviour of finite random composite bodies,” *International Journal of Fracture*, vol. 137, no. 1–4, pp. 261–273, 2006.
- [15] A. Nobili, E. Radi, and L. Lanzoni, “A cracked infinite Kirchhoff plate supported by a two-parameter elastic foundation,” *Journal of the European Ceramic Society*, vol. 34, no. 11, pp. 2737–2744, 2014.
- [16] A. Caporale and R. Luciano, “Limit analysis of masonry arches with finite compressive strength and externally bonded reinforcement,” *Composites Part B: Engineering*, vol. 43, no. 8, pp. 3131–3145, 2012.
- [17] V. Salomoni, G. Mazzucco, C. Pellegrino, and C. Majorana, “Three-dimensional modelling of bond behaviour between concrete and FRP reinforcement,” *Engineering Computations*, vol. 28, no. 1, pp. 5–29, 2011.
- [18] A. Nobili, “Superposition principle for the tensionless contact of a beam resting on a Winkler or a Pasternak foundation,” *Journal of Engineering Mechanics*, vol. 139, no. 10, pp. 1470–1478, 2013.
- [19] D. J. Mead, “Free wave propagation in periodically supported, infinite beams,” *Journal of Sound and Vibration*, vol. 11, no. 2, pp. 181–197, 1970.
- [20] M. Gei, A. B. Movchan, and D. Bigoni, “Band-gap shift and defect-induced annihilation in prestressed elastic structures,” *Journal of Applied Physics*, vol. 105, no. 6, Article ID 063507, 2009.
- [21] G. Napoli and A. Nobili, “Mechanically induced Helfrich-Hurault effect in lamellar systems,” *Physical Review E—Statistical, Nonlinear, and Soft Matter Physics*, vol. 80, no. 3, Article ID 031710, 2009.
- [22] S. Nemat-Nasser, J. R. Willis, A. Srivastava, and A. V. Amirkhizi, “Homogenization of periodic elastic composites and locally resonant sonic materials,” *Physical Review B*, vol. 83, no. 10, Article ID 104103, 2011.
- [23] R. V. Craster, J. Kaplunov, E. Nolde, and S. Guenneau, “Bloch dispersion and high frequency homogenization for separable doubly-periodic structures,” *Wave Motion*, vol. 49, no. 2, pp. 333–346, 2012.
- [24] J. Kaplunov and A. Nobili, “The edge waves on a Kirchhoff plate bilaterally supported by a two-parameter elastic foundation,” *Journal of Vibration and Control*, 2015.
- [25] A. Nobili and A. M. Tarantino, “Magnetostriction of a hard ferromagnetic and elastic thin-film structure,” *Mathematics and Mechanics of Solids*, vol. 13, no. 2, pp. 95–123, 2008.
- [26] V. Guidi, L. Lanzoni, and A. Mazzolari, “Patterning and modeling of mechanically bent silicon plates deformed through coactive stresses,” *Thin Solid Films*, vol. 520, no. 3, pp. 1074–1079, 2011.

- [27] N. Tullini, A. Tralli, and L. Lanzoni, "Interfacial shear stress analysis of bar and thin film bonded to 2D elastic substrate using a coupled FE-BIE method," *Finite Elements in Analysis and Design*, vol. 55, pp. 42–51, 2012.
- [28] A. M. Tarantino, "Homogeneous equilibrium configurations of a hyperelastic compressible cube under equitriaxial dead-load tractions," *Journal of Elasticity*, vol. 92, no. 3, pp. 227–254, 2008.
- [29] V. A. Salomoni, C. E. Majorana, G. M. Giannuzzi, and A. Miliozzi, "Thermal-fluid flow within innovative heat storage concrete systems for solar power plants," *International Journal of Numerical Methods for Heat and Fluid Flow*, vol. 18, no. 7-8, pp. 969–999, 2008.
- [30] V. A. Salomoni, C. E. Majorana, B. Pomaro, G. Xotta, and F. Gramegna, "Macroscale and mesoscale analysis of concrete as a multiphase material for biological shields against nuclear radiation," *International Journal for Numerical and Analytical Methods in Geomechanics*, vol. 38, no. 5, pp. 518–535, 2014.
- [31] G. Dinelli, G. Belz, C. E. Majorana, and B. A. Schrefler, "Experimental investigation on the use of fly ash for lightweight precast structural elements," *Materials and Structures*, vol. 29, no. 194, pp. 632–638, 1996.
- [32] P. Bisegna and R. Luciano, "Bounds on the overall properties of composites with debonded frictionless interfaces," *Mechanics of Materials*, vol. 28, no. 1–4, pp. 23–32, 1998.
- [33] G. W. Hill, "On the part of the motion of the lunar perigee which is a function of the mean motions of the sun and moon," *Acta Mathematica*, vol. 8, no. 1, pp. 1–36, 1886.
- [34] V. I. Smirnov, *A Course of Higher Mathematics: Volume 2, Advanced Calculus*, Pergamon Press, 1964.
- [35] J. Kaplunov and A. Nobili, "Multi-parametric analysis of strongly inhomogeneous periodic waveguides with internal cut-off frequencies," *Mathematical Methods in the Applied Sciences*, 2016.
- [36] R. Luciano and J. R. Willis, "Non-local constitutive equations for functionally graded materials," *Mechanics of Materials*, vol. 36, no. 12, pp. 1195–1206, 2004.
- [37] R. Barretta, L. Feo, and R. Luciano, "Some closed-form solutions of functionally graded beams undergoing nonuniform torsion," *Composite Structures*, vol. 123, pp. 132–136, 2015.
- [38] R. Barretta, L. Feo, R. Luciano, and F. Marotti de Sciarra, "A gradient Eringen model for functionally graded nanorods," *Composite Structures*, vol. 131, pp. 1124–1131, 2015.
- [39] R. Barretta, L. Feo, R. Luciano, and F. Marotti de Sciarra, "Variational formulations for functionally graded nonlocal Bernoulli-Euler nanobeams," *Composite Structures*, vol. 129, pp. 80–89, 2015.
- [40] R. Barretta and R. Luciano, "Exact solutions of isotropic viscoelastic functionally graded Kirchhoff plates," *Composite Structures*, vol. 118, no. 1, pp. 448–454, 2014.
- [41] A. Apuzzo, R. Barretta, and R. Luciano, "Some analytical solutions of functionally graded Kirchhoff plates," *Composites Part B: Engineering*, vol. 68, pp. 266–269, 2015.
- [42] A. M. Tarantino, "On extreme thinning at the notch tip of a neo-Hookean sheet," *The Quarterly Journal of Mechanics and Applied Mathematics*, vol. 51, no. 2, pp. 179–190, 1998.
- [43] G. Xotta, G. Mazzucco, V. A. Salomoni, C. E. Majorana, and K. J. Willam, "Composite behavior of concrete materials under high temperatures," *International Journal of Solids and Structures*, vol. 64, pp. 86–99, 2015.
- [44] F. M. de Sciarra and M. Salerno, "On thermodynamic functions in thermoelasticity without energy dissipation," *European Journal of Mechanics-A/Solids*, vol. 46, pp. 84–95, 2014.
- [45] R. Barretta, L. Feo, and R. Luciano, "Torsion of functionally graded nonlocal viscoelastic circular nanobeams," *Composites Part B: Engineering*, vol. 72, pp. 217–222, 2015.
- [46] L. Dezi, G. Menditto, and A. M. Tarantino, "Homogeneous structures subjected to repeated structural system changes," *Journal of Engineering Mechanics*, vol. 116, no. 8, pp. 1723–1732, 1990.
- [47] L. Dezi and A. M. Tarantino, "Time-dependent analysis of concrete structures with a variable structural system," *ACI Materials Journal*, vol. 88, no. 3, pp. 320–324, 1991.
- [48] L. Dezi, G. Menditto, and A. M. Tarantino, "Viscoelastic heterogeneous structures with variable structural system," *Journal of Engineering Mechanics*, vol. 119, no. 2, pp. 238–250, 1993.

Research Article

Euler-Bernoulli Nanobeam Welded to a Compressible Semi-Infinite Substrate

Pietro Di Maida¹ and Federico Oyedeji Falope²

¹*Department of Sciences and Methods for Engineering (DISMI), University of Modena and Reggio Emilia, Via Amendola 2, 42122 Reggio Emilia, Italy*

²*Department of Engineering Enzo Ferrari (DIEF), University of Modena and Reggio Emilia, Via P. Vivarelli 10, Int 27, 41125 Modena, Italy*

Correspondence should be addressed to Pietro Di Maida; pietro.dimaida@unimore.it

Received 23 December 2015; Accepted 5 October 2016

Academic Editor: Julius Kaplunov

Copyright © 2016 P. Di Maida and F. O. Falope. This is an open access article distributed under the Creative Commons Attribution License, which permits unrestricted use, distribution, and reproduction in any medium, provided the original work is properly cited.

The contact problem of an Euler-Bernoulli nanobeam of finite length bonded to a homogeneous elastic half plane is studied in the present work. Both the beam and the half plane are assumed to display a linear elastic behaviour under infinitesimal strains. The analysis is performed under plane strain condition. Owing to the bending stiffness of the beam, shear and peeling stresses arise at the interface between the beam and the substrate within the contact region. The investigation allows evaluating the role played by the Poisson ratio of the half plane (and, in turn, its compressibility) on the beam-substrate mechanical interaction. Different symmetric and skew-symmetric loading conditions for the beam are considered, with particular emphasis to concentrated transversal and horizontal forces and couples acting at its edges. It is found that the Poisson ratio of the half plane affects the behaviour of the interfacial stress field, particularly at the beam edges, where the shear and peel stresses are singular.

1. Introduction

The mechanical interaction between bars, strips, rings, thin films, and so forth and an elastic substrate has been widely investigated because of its great importance in many practical engineering tasks. As an example, in the framework of civil engineering, the load transfer between FRP sheets (or other reinforcing elements like discrete fibres [1, 2]) applied to existing concrete structures is often performed by modeling the reinforcing stiffeners as 2D membranes [3–6] welded to half plane (for the equilibrium configurations of cylindrical and cubic bodies [2]). By following such an approach, retrofitted concrete structures [7], elastic foundations [8–10], rigid road pavements [11], and retrofitted masonry elements [12, 13] have been studied (for the behaviour of high performance concrete based on fly ash, see [14]).

In microelectronics, various NEMS and MEMS involve thin films and coatings [5, 15–17] (examples about numerical studies performed on thin films can be found in [6, 18]), and the stress concentrations arising in the neighbourhood of

geometric discontinuities and/or across bimaterial interfaces provide useful information about the risk of occurrence of fracture phenomena [19, 20] in such devices and, in turn, about their stability in time [21, 22].

In mechanical engineering, the film-substrate contact mechanics is relevant in order to study the mechanical response of thermal barriers and protective alloys typically involved in a variety of mechanical devices, like blades of centrifugal pump impellers, components of compressors, gas turbines, and so forth. In most of these examples, the problem can be studied by neglecting the bending stiffness of the covering; namely, the coating is modeled like a membrane element. However, in a wide class of mechanical systems, the flexural behaviour of the covers can not be neglected without introducing rough approximations. As an example, the flexural behaviour must be taken into account to properly study beams [23] and multilayer systems [24]. As an example, foundations of buildings are often characterized by high values of flexural rigidity and, typically, they are simulated as beams or plates resting on an elastic support [8, 9].

Similarly, the mechanical behaviour of MEMS or NEMS based on coatings characterized by small length-to-thickness ratio must be studied by taking into account the bending stiffness of the layers.

The contact problem of an Euler-Bernoulli beam perfectly bonded to an elastic half plane has been performed in [23]. These authors carried out their investigation by considering an incompressible half plane (i.e., by considering $\nu_s = 0.5$, where ν_s is the Poisson ratio of the substrate), thus finding a nonoscillatory behaviour of the interfacial stress field. This allowed the authors to straightforwardly express the unknown peel and shear stresses as infinite series of Chebyshev polynomials having square-root singularities at the edges of the beam.

Studying the singular nature of the stress and strain fields in such contact problems is an important topic [6, 25] in order to assess if such systems are resistant or prone to delamination, interfacial crack propagation, and other damage phenomena [5, 26–28].

In the present work, the effect induced by the Poisson ratio of the half plane on the beam-half plane mechanical interaction has been studied. The oscillatory index characterizing the interfacial stress field is found to depend on the Poisson ratio of the half plane only. The strain compatibility condition leads to a system of two integral equations, which is reduced to algebraic systems by expanding the interfacial stresses in series of orthogonal Jacobi polynomials having complex index. In the present investigation, both the beam and the half plane have been assumed homogeneous bodies displaying linear elastic behaviour. However, the analysis can be extended to nonhomogeneous bodies by following the approach performed in [29–31]. The time dependence can be taken into account also (for a general approach concerning the nonlocal behaviour of functionally graded materials see, e.g., [32, 33]).

The paper is organized as follows. The formulation of the problem is given in Section 2. The main results are presented and discussed in Section 3. Finally, conclusions are reported in Section 4.

2. Formulation of the Problem

The problem of Euler-Bernoulli nanobeams bonded to an isotropic elastic half plane is formulated in the present section. The reference system is centred at the middle span of the beam, as shown in Figure 1. Perfect adhesion between the half plane and beam is assumed. Both the axial and flexural stiffness of the beam are taken into account. The beam and the underlying half plane have an isotropic constitutive law, characterized by the following elastic constants E_s , E_b , ν_s , and ν_b denoting the Young moduli and the Poisson ratio, respectively (the subscript i , with $i = b, s$ stands for beam or semi-infinite substrate, resp.). Furthermore, h , and $2a$ denote the height and the total length of the beam, respectively, whereas A and J indicate the area and the moment of inertia of the beam cross section.

The shear and peeling stresses, $\tau(y)$ and $q(y)$, respectively (Figure 2), which arise along the contact region, represent the unknown of the problem. In the following, the apex prime ($'$)

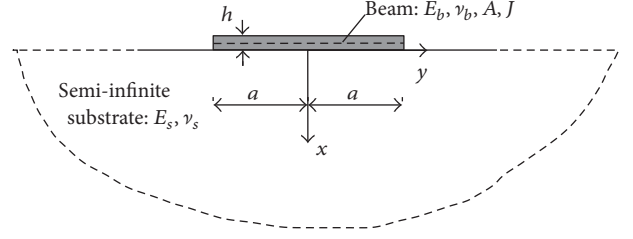


FIGURE 1: Semi-infinite substrate and beam geometry.

denotes the derivative with respect to the spatial coordinate y .

By considering the symmetric as well as skew-symmetric loading cases reported in Figure 2, the balance condition of the beam along $y \in [-a, +a]$ leads to

$$\begin{aligned} N(y) &= N^* + \int_y^a \tau(t) dt, \\ T(y) &= -T^* + \int_y^a q(t) dt, \\ M(y) &= M^* + T^*(a - y) + \frac{h}{2} \int_y^a \tau(t) dt \\ &\quad + \int_y^a q(t)(y - t) dt, \end{aligned} \quad (1)$$

where N , T , and M are the internal axial force, shear force, and bending moment of the beam, respectively, whereas N^* , T^* , and M^* are the corresponding external concentrated loads acting at the beam edges. By using the equilibrium conditions (1) and the isotropic elastic constitutive law, the axial strain ε_y^b , and the slope φ^b , take the expressions

$$\begin{aligned} \varepsilon_y^b(y) &= \frac{N^*}{E_b A} + \frac{1}{E_b h} \int_y^a \tau(t) dt + \frac{h}{2E_b J} \left\{ M^* \right. \\ &\quad \left. + T^*(a - y) + \int_y^a \left[\frac{h}{2} \tau(t) + q(t)(y - t) \right] dt \right\}, \\ \varphi^b(y) &= \frac{1}{E_b J_b} \left\{ y M^* + T^* \left(y - \frac{y^2}{2} \right) \right. \\ &\quad \left. + \frac{h}{2} \left[y \int_y^a \tau(t) dt + \int_0^y t \tau(t) dt \right] \right. \\ &\quad \left. - \frac{1}{2} \left[\int_0^a t^2 q(t) dt - \int_y^a (t - y)^2 q(t) dt \right] \right\} + \tilde{\varphi}, \end{aligned} \quad (2)$$

where $\tilde{\varphi}$ is an unknown integration constant. Concerning the semi-infinite substrate, the longitudinal strain and slope at the contact region are known in closed form [34] as

$$\begin{aligned} \varepsilon_y^s(y) &= \frac{2(1 - \nu_s^2)}{E_s \pi} \int_{-a}^{+a} \frac{\tau(t)}{y - t} dt \\ &\quad + \frac{(1 - 2\nu_s)(1 + \nu_s)}{E_s} q(y), \end{aligned}$$

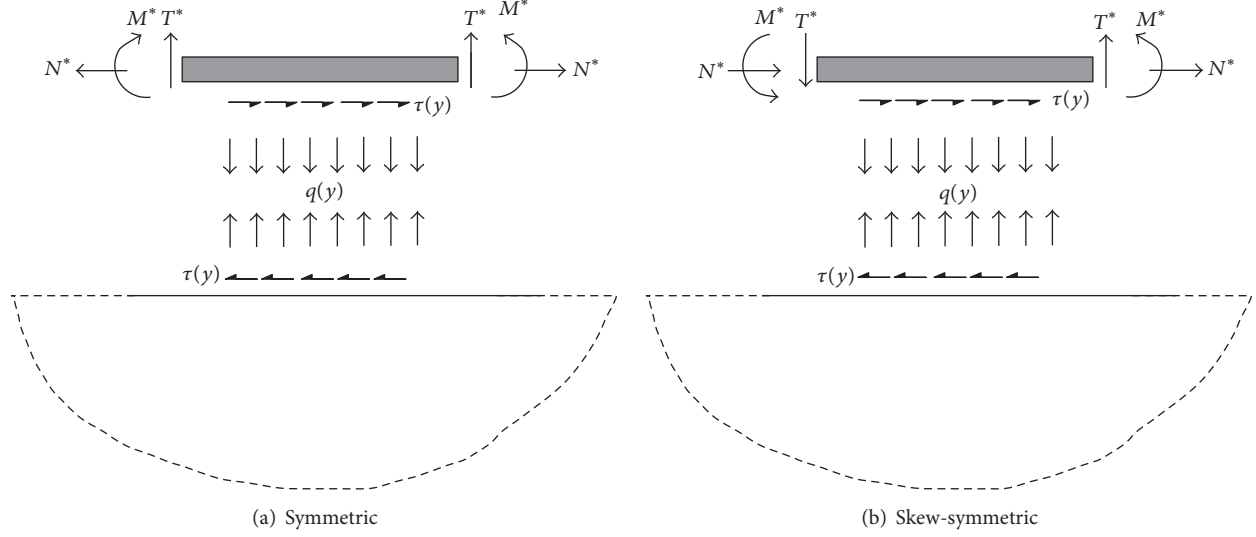


FIGURE 2: Mechanical interaction between the beam and the substrate for symmetric and skew-symmetric loading cases.

$$\begin{aligned} \varphi^s(y) = & -\frac{(1-2\nu_s)(1+\nu_s)}{E_s} \tau(y) \\ & + \frac{(1-\nu_s^2)}{E_s \pi} \int_{-a}^{+a} \frac{q(t)}{y-t} dt. \end{aligned} \quad (3)$$

Thus, the unknowns of the problem are the stress distributions $\tau(y)$ and $q(y)$ at the interface within the contact region.

The interfacial shear and peeling stresses can be straightforwardly expanded in series of Jacobi orthogonal polynomials,

$$\begin{aligned} \tau(y) &= E_s (a+y)^p (a-y)^p \sum_{n=0}^{\infty} C_n P_n^{(p,p)}\left(\frac{y}{a}\right), \\ q(y) &= E_s (a+y)^p (a-y)^p \sum_{n=0}^{\infty} D_n P_n^{(p,p)}\left(\frac{y}{a}\right), \end{aligned} \quad (4)$$

where $P_n^{(p,p)}(y/a)$ represents the Jacobi polynomial of order n (see Appendix) and p is the order of the singularity of the stress field at the beam edges, namely, at $y = \pm a$. Indeed, as shown by [23],

$$p = -\frac{1}{2} + \frac{i\epsilon}{2\pi}, \quad (5)$$

with $\epsilon = \log(3-4\nu_s)$ or $\epsilon = \log(3-\nu_s)/(1+\nu_s)$ for a plane strain or plane stress state, respectively.

The problem is governed by the following compatibility equations between the beam and the substrate:

$$\begin{aligned} \varepsilon_y^b(y) &= \varepsilon_y^s(y), \\ \varphi_y^b(y) &= \varphi_y^s(y). \end{aligned} \quad (6)$$

By introducing (2)–(4) into (6) and truncating series (4) to the first N elements, the imposition of the compatibility

conditions at $N+1$ collocation points y_k over the contact region allows reducing the system of singular integral equations (6) into a linear algebraic system for the unknown C_n and D_n . The collocation points y_k , with $k = 1, 2, \dots, N+1$, have been set as the roots of the Chebyshev polynomial of first kind of order $N+1$,

$$y_k = \cos\left[\frac{\pi k}{2(N+1)}\right]. \quad (7)$$

Once the coefficients C_n and D_n are found, the strain and displacement fields can be determined and, in turn, the internal forces in the beam can be assessed. The displacement components along the substrate surface [34] take the form

$$\begin{aligned} u^s(y) &= \frac{(1-2\nu_s)(1+\nu_s)}{2E_s} \left[\int_{-a}^y q(t) dt - \int_y^{+a} q(t) dt \right] \\ &\quad - \frac{2(1-\nu_s^2)}{\pi E_s} \int_{-a}^a \tau(t) \ln|y-t| dt \\ v^s(y) &= \frac{(1-2\nu_s)(1+\nu_s)}{2E_s} \left[\int_{-a}^y \tau(t) dt - \int_y^{+a} \tau(t) dt \right] \\ &\quad - \frac{2(1-\nu_s^2)}{\pi E_s} \int_{-a}^a q(t) \ln|y-t| dt, \end{aligned} \quad (8)$$

where u and v represent the longitudinal and transversal displacement. The displacement field of the beam reads

$$\begin{aligned} u^b(y) &= \bar{u} + \frac{N^*}{E_b A} y + \left(\frac{1}{E_b A} + \frac{h^2}{4E_b J} \right) \left[y \int_y^a \tau(t) dt \right. \\ &\quad \left. + \int_0^y t \tau(t) dt \right] + \frac{h}{4E_b J} \left[2M^* y + T^* (2ay - y^2) \right. \\ &\quad \left. + \int_y^a q(t) (y-t)^2 dt - \int_0^a t^2 q(t) dt \right], \end{aligned}$$

$$\begin{aligned}
v^b(y) = & \frac{1}{2E_b J} \left\{ -M^* y^2 - \frac{T^*}{3} (3ay^2 - y^3) \right. \\
& - h \left[\int_0^y t(y-t) \tau(t) dt \right] \\
& - h \left[\frac{y^2}{2} \int_y^a \tau(t) dt + \frac{1}{2} \int_0^y t^2 \tau(t) dt \right] \\
& + y \int_0^a t^2 q(t) dt - \int_y^a q(t) \left(yt^2 + \frac{y^3}{3} - y^2 t \right) dt \\
& \left. - \int_0^y \frac{q(t)}{3} dt \right\} + \bar{v} - \bar{\varphi} y.
\end{aligned} \tag{9}$$

All the integrals involved in the above expressions can be evaluated in closed form (see Appendix).

The strength of the interfacial stresses at the beam ends can be assessed through the peeling and shear stress intensity factors K_I and K_{II} :

$$\begin{aligned}
K_I(\pm a) &= \lim_{y \rightarrow \pm a} \frac{q(y)}{(a \mp y)^p} \\
&= \pm 2^p E_s a^p \sum_{n=0,2,\dots}^N D_n P_n^{(p,p)}(\pm 1), \\
K_{II}(\pm a) &= \lim_{y \rightarrow \pm a} \frac{\tau(y)}{(a \mp y)^p} \\
&= \pm 2^p E_s a^p \sum_{n=1,3,\dots}^N C_n P_n^{(p,p)}(\pm 1).
\end{aligned} \tag{10}$$

3. Results and Discussion

The behaviour of the beam-substrate system under the symmetric and skew-symmetric loading conditions reported in Figures 2(a) and 2(b) has been investigated. The series expansions (4) have been truncated to 13 terms and the compatibility conditions (6) have been imposed at 14 collocation points within the contact region. Referred to the dimensionless spatial coordinate $\xi = y/a$, Figures 3–5 show the dimensionless shear and peeling stress distributions due to different symmetric or skew-symmetric loading cases.

For the beam loaded with two axial forces acting at the film edges, the shear stress (Figure 3) shows a monotonic trend over the entire contact region. Conversely, the behaviour displayed by the peeling tractions is not monotonic as they change sign in the neighbourhood of the film edge.

For the case of shear forces acting at the beam edges, the shear contact stresses are reported in Figure 4. As shown, the results are almost invariant with respect to the Poisson ratio of the substrate, with particular reference to the peeling stress. The interfacial shear stress displays a nonmonotonic trend, in particular for the loading case of two skew-symmetric shear forces, except for $\nu_s = 0.5$, namely, for an incompressible half plane, as found by [23]. The loading case of two symmetric

couples acting at the beam edges induce an almost linear trend for the shear stress (Figure 5) in the region closer to the middle of the beam for any value assumed by the Poisson ratio of the half plane. Conversely, when two skew-symmetric couples act at the beam ends, the shear stress decreases as the Poisson ratio increases. Also for the loading cases of two end couples, the Poisson ratio affects the shear stress more than the peel tractions.

The trend exhibited by the peeling distribution on the contact surface allows satisfying the balance of momentum induced by shear stress along contact region and the external load acting on the beam.

4. Conclusions

The contact problem of an Euler-Bernoulli nanobeam perfectly welded to a homogeneous elastic half plane has been addressed in the present work. The problem has been solved by expressing the unknown shear and peel interfacial stresses as infinite series of Jacobi orthogonal polynomials. The compatibility condition between the strains of the beam and those of the underlying half plane leads to a system of two Fredholm integral equations with Cauchy kernel. The complex singular behaviour of such stresses has been handled by assuming properly the singularity of the stress field at the beam edges. This allows reducing the singular integral equations into a linear system of algebraic equations, which has been solved for the unknown coefficients of the interfacial stress field. The shear and peel stresses have been evaluated for different values of the Poisson ratio for the half plane, thus finding the effect played by this elastic parameter on the beam-substrate mechanical interaction. In particular, it has been shown that the Poisson ratio of the half plane affects mostly the shear stress distribution than the behaviour of the peel tractions. For both symmetric or skew-symmetric couples or shear forces acting at the beam edges Poisson ratio does not affect significantly the mechanical response of the system.

The analysis allows properly assessing the stress concentrations at the edges of the beam (note that high stress levels can increase the time-dependent effects, as shown in [35–37] for concrete frames), an important task in many engineering problems involving beams and plates bonded to an elastic support. For example, the obtained results can be used to properly design FRP stiffeners applied to concrete structures that are prone to various damaging phenomena (see, e.g., [38]). It should be noted that the case of a thermal variation ΔT (thermal variations can sensibly affect the mechanical behaviour of structural elements, as shown in [39, 40]) acting on the beam (for the effect produced by thermal loads on concrete structures, see, e.g., [38]) can be studied as the loading case of two symmetric axial end forces N by assuming

$$N = [(1 + \nu_b) \alpha_b - (1 + \nu_s) \alpha_s] EA \Delta T, \tag{11}$$

where α denotes the coefficient of thermal expansion. Note also that the contact mechanics of a nonhomogeneous composite beam with random composition and microstructure should be investigated by following the approach reported in [41, 42].

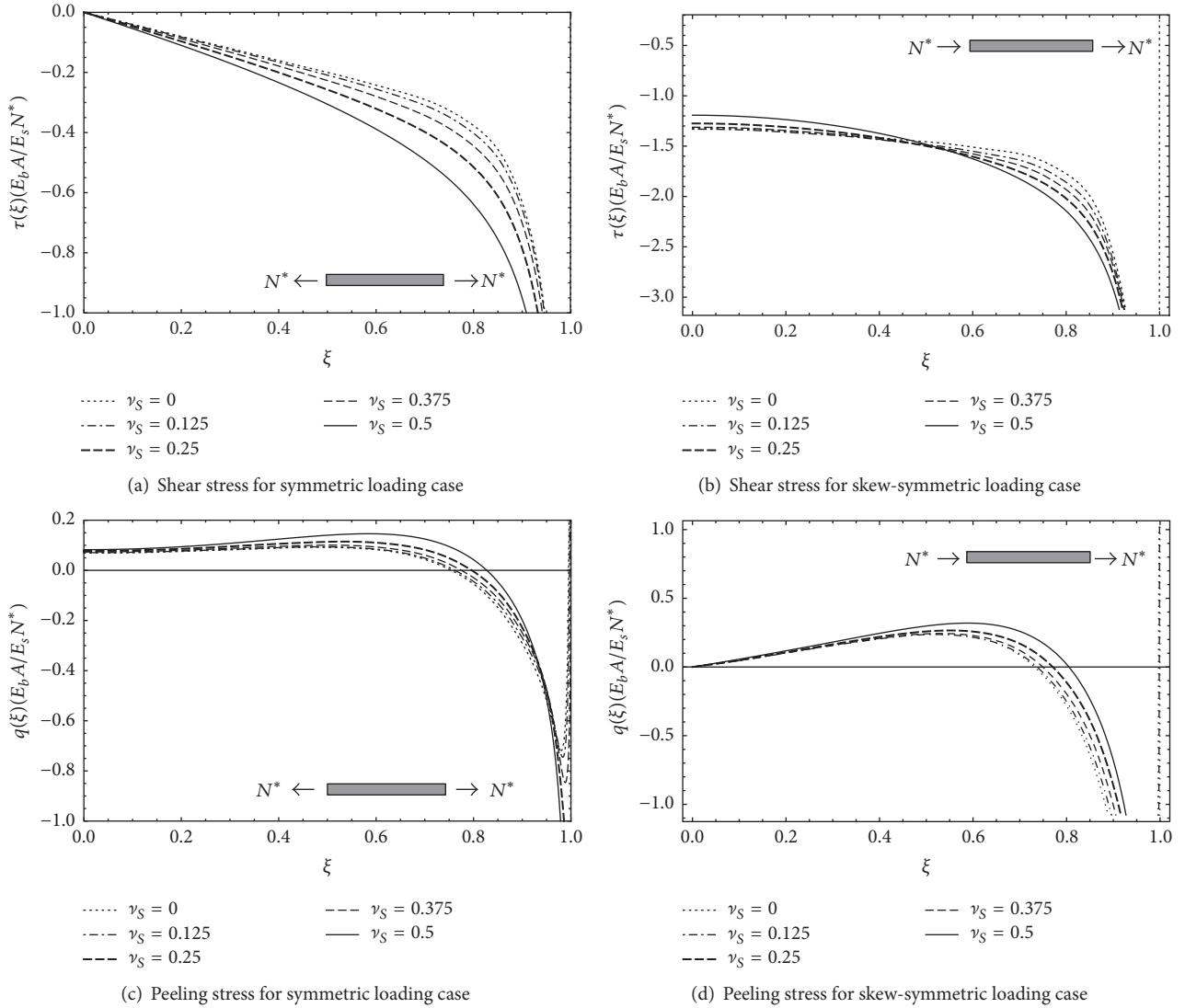


FIGURE 3: Dimensionless mechanical interactions of the beam subjected to axial forces acting at the edges.

Appendix

Jacobi Polynomials

The Jacobi polynomial $P_n^{(\alpha, \beta)}(t)$ of order n is defined as [43]

$$P_n^{(\alpha, \beta)}(t) = \frac{\Gamma(\alpha + n + 1)}{n! \Gamma(\alpha + \beta + n + 1)} \cdot \sum_{m=0}^n \binom{n}{m} \frac{\Gamma(\alpha + \beta + n + m + 1)}{\Gamma(\alpha + m + 1)} \left(\frac{t-1}{2}\right)^m, \quad (\text{A.1})$$

where Γ is the Euler gamma function. In the special case of $\alpha = \beta$ equal to 0 or 1/2 the Jacobi polynomials reduce to the Legendre or Chebyshev polynomials, respectively. Another

possible definition of the Jacobi polynomials is provided by Rodrigues' formula,

$$P_n^{(\alpha, \beta)}(t) = \frac{(-1)^n}{2^n n!} (1-t)^{-\alpha} \cdot (1+t)^{-\beta} \frac{d^n}{dt^n} \left[(1-t)^\alpha (1+t)^\beta (1-t^2)^n \right]. \quad (\text{A.2})$$

or, equivalently [44],

$$P_n^{(\alpha, \beta)}(t) = \frac{(\alpha + 1)_n}{n!} {}_2F_1\left(-n, 1 + \alpha + \beta + n; \alpha + 1; \frac{1-t}{2}\right), \quad (\text{A.3})$$

where ${}_2F_1$ represents the hypergeometric function for $|t| < 1$. The orthogonal properties of Jacobi polynomials over $[-1, +1]$ domain provide the following identities used in

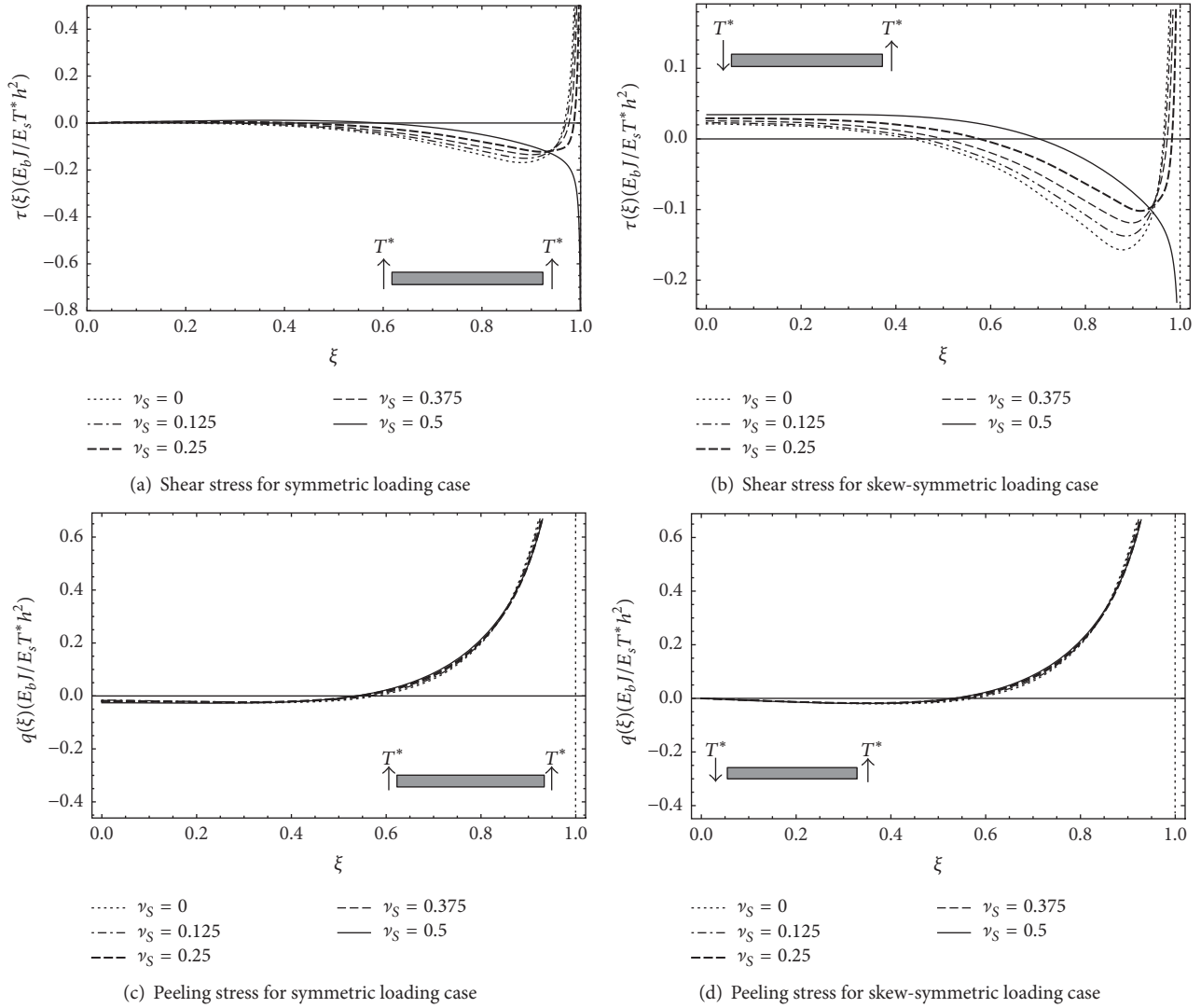


FIGURE 4: Dimensionless mechanical interactions of the beam subjected to shear forces acting at the edges.

Section 2 to evaluate in closed form the integrals involved in the compatibility equations [45]:

$$\int_{-1}^{+1} (1+t)^p (1-t)^p P_n^{(p,p)}(t) P_m^{(p,p)}(t) dt$$

$$= \frac{2^{2p+1} \Gamma^2(p+n+1) \delta_{nm}}{n! (2p+1+2n) \Gamma(2p+1+n)},$$

$$\int_{-1}^{+1} (1+t)^p (1-t)^p P_n^{(p,p)}(t) dt$$

$$= \sqrt{\pi} \frac{\Gamma(p+1)}{\Gamma(p+(3/2))} \delta_{n0},$$

$$\int_{-1}^{+1} t (1+t)^p (1-t)^p P_n^{(p,p)}(t) dt$$

$$= \sqrt{\pi} \frac{\Gamma(p+2)}{\Gamma 2(p+(5/2))} \delta_{n0},$$

$$\int_{-1}^r (1+t)^p (1-t)^p P_n^{(p,p)}(t) dt$$

$$- \int_r^{+1} (1+t)^p (1-t)^p P_n^{(p,p)}(t) dt$$

$$= \begin{cases} 2t_2 F_1\left(\frac{1}{2}, -p, \frac{3}{2}, r^2\right), & \text{for } n=0 \\ -\frac{(1-r^2)^{p+1}}{n} P_{n-1}^{(p+1,p+1)}(r), & \text{for } n=1, 2, \dots, \end{cases}$$

(A.4)

where δ_{nm} represents the Kronecker delta.

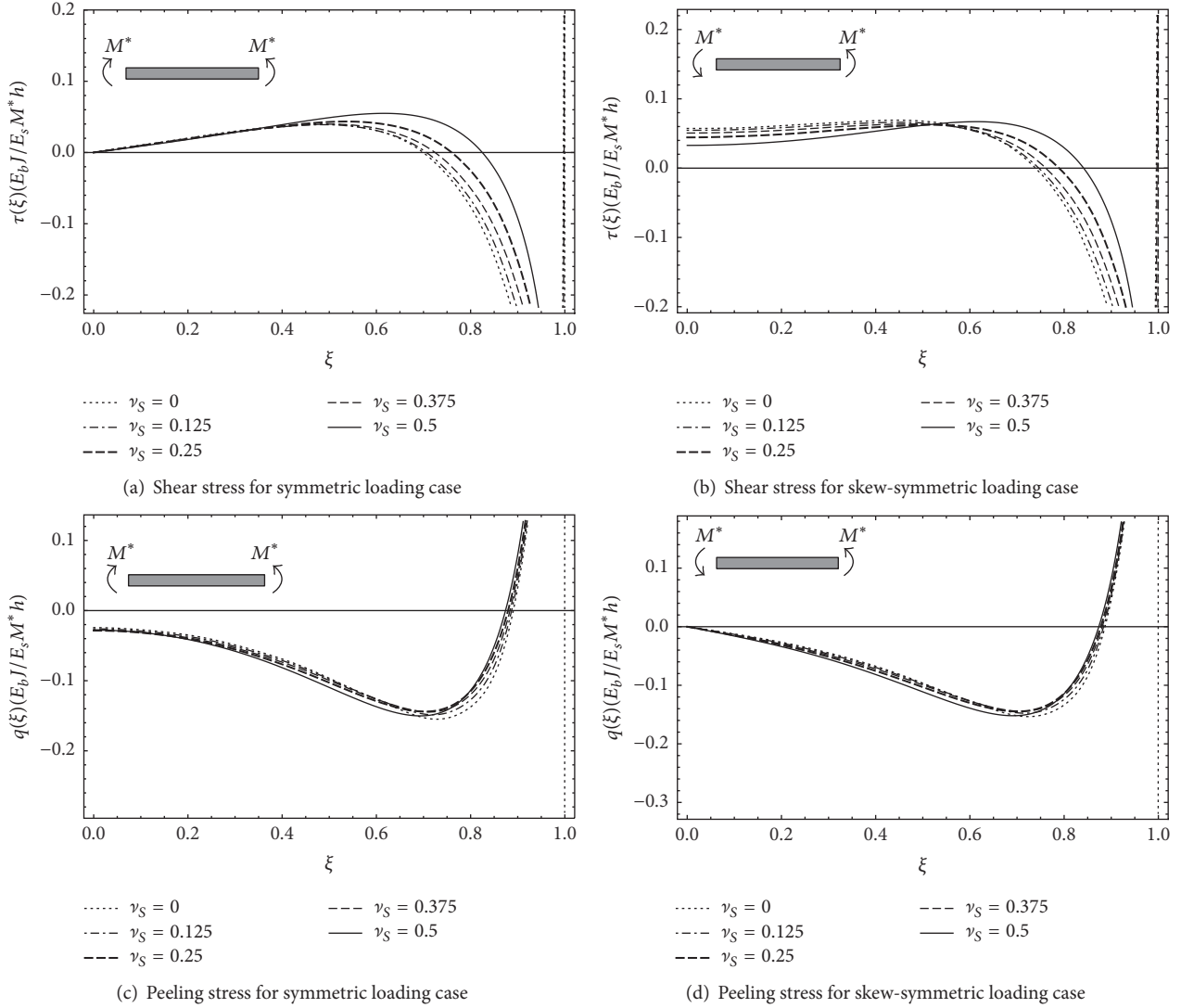


FIGURE 5: Dimensionless mechanical interactions of the beam subjected to couples acting at the edges.

$$\int_{-1}^r (1+t)^p (1-t)^p P_n^{(p,p)}(t) dt = \begin{cases} \frac{\sqrt{\pi}\Gamma(1+p)}{2\Gamma((3/2)+p)} - r {}_2F_1\left(\frac{1}{2}, -p, \frac{3}{2}, r^2\right), & \text{for } n=0 \\ \frac{1}{2n} P_{n-1}^{(p+1,p+1)}(r) (1+r)^{p+1} (1-r)^{p+1}, & \text{for } n=1, 2, \dots \end{cases}$$

$$\int_r^{+1} (1+t)^p (1-t)^p P_n^{(p,p)}(t) dt \tag{A.5}$$

$$= \begin{cases} \frac{\sqrt{\pi}\Gamma(1+p)}{2\Gamma((3/2)+p)} - r {}_2F_1\left(\frac{1}{2}, -p, \frac{3}{2}, r^2\right), & \text{for } n=0 \\ \frac{1}{2n} \left[\frac{1-(-1)^n}{2} P_{n-1}^{(p+1,p+1)}(0) - P_{n-1}^{(p+1,p+1)}(r) (1-r)^{p+1} (1-r)^{p+1} \right], & \text{for } n=1, 2, \dots \end{cases}$$

Competing Interests

The authors declare that they have no competing interests.

References

- [1] P. Bisegna and R. Luciano, "Bounds on the overall properties of composites with debonded frictionless interfaces," *Mechanics of Materials*, vol. 28, no. 1–4, pp. 23–32, 1998.
- [2] A. M. Tarantino, "Homogeneous equilibrium configurations of a hyperelastic compressible cube under equitriaxial dead-load tractions," *Journal of Elasticity. The Physical and Mathematical Science of Solids*, vol. 92, no. 3, pp. 227–254, 2008.
- [3] N. K. Arutiunian, "Contact problem for a half-plane with elastic reinforcement," *Journal of Applied Mathematics and Mechanics*, vol. 32, no. 4, pp. 652–665, 1968.
- [4] F. Erdogan and G. D. Gupta, "The problem of an elastic stiffener bonded to a Half Plane," *Journal of Applied Mechanics*, vol. 38, no. 4, pp. 937–941, 1971.
- [5] L. Lanzoni, "Analysis of stress singularities in thin coatings bonded to a semi-infinite elastic substrate," *International Journal of Solids and Structures*, vol. 48, no. 13, pp. 1915–1926, 2011.
- [6] N. Tullini, A. Tralli, and L. Lanzoni, "Intefacial shear stress analysis of bar and thin film bonded to 2D elastic substrate using a coupled FE-BIE method," *Finite Elements in Analysis and Design*, vol. 55, pp. 42–51, 2012.
- [7] D. D. Oehlers and R. Seracino, *Design of FRP and Steel Plated RC Structures*, Elsevier, 2004.
- [8] A. Nobili, "Variational approach to beams resting on two-parameter tensionless elastic foundations," *Journal of Applied Mechanics, Transactions ASME*, vol. 79, no. 2, Article ID 021010, 2012.
- [9] A. Nobili, E. Radi, and L. Lanzoni, "A cracked infinite Kirchhoff plate supported by a two-parameter elastic foundation," *Journal of the European Ceramic Society*, vol. 34, no. 11, pp. 2737–2744, 2014.
- [10] V. Salomoni, G. Mazzuocco, C. Pellegrino, and C. E. Majorana, "Threedimensional modeling of bond behaviour between concrete and FRP reinforcement," *Engineering Computation*, vol. 28, no. 1, pp. 5–29, 2011.
- [11] A. Nobili, L. Lanzoni, and A. M. Tarantino, "Experimental investigation and monitoring of a polypropylene-based fiber reinforced concrete road pavement," *Construction and Building Materials*, vol. 47, pp. 888–895, 2013.
- [12] A. Caporale, L. Feo, R. Luciano, and R. Penna, "Numerical collapse load of multi-span masonry arch structures with FRP reinforcement," *Composites Part B: Engineering*, vol. 54, no. 1, pp. 71–84, 2013.
- [13] A. Caporale and R. Luciano, "Limit analysis of masonry arches with finite compressive strength and externally bonded reinforcement," *Composites Part B: Engineering*, vol. 43, no. 8, pp. 3131–3145, 2012.
- [14] G. Dinelli, G. Belz, C. E. Majorana, and B. A. Schrefler, "Experimental investigation on the use of fly ash for lightweight precast structural elements," *Materials and Structures*, vol. 29, no. 194, pp. 632–638, 1996.
- [15] L. B. Freund and S. Suresh, *Thin Film Materials. Stress, Defect Formation and Surface Evolution*, Cambridge University Press, Cambridge, UK, 2004.
- [16] L. Lanzoni and E. Radi, "Thermally induced deformations in a partially coated elastic layer," *International Journal of Solids and Structures*, vol. 46, no. 6, pp. 1402–1412, 2009.
- [17] V. Guidi, L. Lanzoni, A. Mazzolari, G. Martinelli, and A. Tralli, "Design of a crystalline undulator based on patterning by tensile Si_3N_4 strips on a Si crystal," *Applied Physics Letters*, vol. 90, no. 11, Article ID 114107, 2007.
- [18] J. F. Luo, Y. J. Liu, and E. J. Berger, "Analysis of two-dimensional thin structures (from micro- To nano-scales) using the boundary element method," *Computational Mechanics*, vol. 22, no. 5, pp. 404–412, 1998.
- [19] A. M. Tarantino, "Nonlinear fracture mechanics for an elastic Bell material," *The Quarterly Journal of Mechanics and Applied Mathematics*, vol. 50, no. 3, pp. 435–456, 1997.
- [20] A. M. Tarantino, "On extreme thinning at the notch-tip of a Neo-Hookean sheet," *The Quarterly Journal of Mechanics and Applied Mathematics*, vol. 51, no. 2, pp. 179–190, 1998.
- [21] M. Ohring, *The Materials Science of Thin Films*, Academic Press, 1992.
- [22] Y. L. Shen, *Constrained Deformation of Materials. Devices, Heteroge-Neous Structures and Thermo-Mechanical Modeling*, Springer, 2010.
- [23] T. W. Shield and K. S. Kim, "Beam theory models for thin film segments cohesively bonded to an elastic half space," *International Journal of Solids and Structures*, vol. 29, no. 9, pp. 1085–1103, 1992.
- [24] H. Djabella and R. D. Arnell, "Two-dimensional finite-element analysis of elastic stresses in double-layer systems under combined surface normal and tangential loads," *Thin Solid Films*, vol. 226, no. 1, pp. 65–73, 1993.
- [25] A. M. Tarantino, "The singular wedge problem in the nonlinear elastostatic plane stress theory," *Quarterly of Applied Mathematics*, vol. 57, no. 3, pp. 433–451, 1999.
- [26] A. M. Tarantino, "Equilibrium paths of a hyperelastic body under progressive damage," *Journal of Elasticity*, vol. 114, no. 2, pp. 225–250, 2014.
- [27] A. M. Tarantino, "On the finite motions generated by a mode I propagating crack," *Journal of Elasticity*, vol. 57, no. 2, pp. 85–103, 1999.
- [28] A. M. Tarantino, "Crack propagation in finite elastodynamics," *Mathematics and Mechanics of Solids*, vol. 10, no. 6, pp. 577–601, 2005.
- [29] A. Apuzzo, R. Barretta, and R. Luciano, "Some analytical solutions of functionally graded Kirchhoff plates," *Composites Part B: Engineering*, vol. 68, pp. 266–269, 2015.
- [30] R. Barretta, L. Feo, and R. Luciano, "Some closed-form solutions of functionally graded beams undergoing nonuniform torsion," *Composite Structures*, vol. 123, pp. 132–136, 2015.
- [31] R. Barretta, L. Feo, R. Luciano, and F. Marotti de Sciarra, "Variational formulations for functionally graded nonlocal Bernoulli-Euler nanobeams," *Composite Structures*, vol. 129, pp. 80–89, 2015.
- [32] R. Luciano and J. R. Willis, "Non-local constitutive equations for functionally graded materials," *Mechanics of Materials*, vol. 36, no. 12, pp. 1195–1206, 2004.
- [33] R. Barretta, L. Feo, R. Luciano, and F. Marotti de Sciarra, "A gradient Eringen model for functionally graded nanorods," *Composite Structures*, vol. 131, pp. 1124–1131, 2015.
- [34] K. L. Johnson, *Contact Mechanics*, Cambridge University Press, London, UK, 1985.
- [35] L. Dezi, G. Menditto, and A. M. Tarantino, "Homogeneous structures subjected to repeated structural system changes," *ASCE Journal of Engineering Mechanics*, vol. 116, no. 8, pp. 1723–1732, 1990.

- [36] L. Dezi, G. Menditto, and A. M. Tarantino, "Viscoelastic heterogeneous structures with variable structural system," *Journal of Engineering Mechanics*, vol. 119, no. 2, pp. 238–250, 1993.
- [37] L. Dezi and A. Tarantino, "Time dependent analysis of concrete structures with variable structural system," *ACI Materials Journal*, vol. 88, no. 3, pp. 320–324, 1991.
- [38] V. A. Salomoni, C. E. Majorana, B. Pomaro, G. Xotta, and F. Gramigna, "Macroscale and mesoscale analysis of concrete as a multiphase material for biological shields against nuclear radiation," *International Journal for Numerical and Analytical Methods in Geomechanics*, vol. 38, no. 5, pp. 518–535, 2014.
- [39] G. Xotta, G. Mazzucco, V. A. Salomoni, C. E. Majorana, and K. J. Willam, "Composite behavior of concrete materials under high temperatures," *International Journal of Solids and Structures*, vol. 64, pp. 86–99, 2015.
- [40] V. A. Salomoni, C. E. Majorana, G. M. Giannuzzi, and A. Miliozzi, "Thermal-fluid flow within innovative heat storage concrete systems for solar power plants," *International Journal of Numerical Methods for Heat and Fluid Flow*, vol. 18, no. 7-8, pp. 969–999, 2008.
- [41] F. Greco and R. Luciano, "A theoretical and numerical stability analysis for composite micro-structures by using homogenization theory," *Composites Part B: Engineering*, vol. 42, no. 3, pp. 382–401, 2011.
- [42] R. Luciano and J. R. Willis, "Hashin-Shtrikman based FE analysis of the elastic behaviour of finite random composite bodies," *International Journal of Fracture*, vol. 137, no. 1, pp. 261–273, 2006.
- [43] J. C. Mason and D. C. Handscomb, *Chebyshev Polynomials*, Chapman & Hall/CRC, Boca Raton, Fla, USA, 2003.
- [44] M. Abramowitz and I. A. Stegun, *Handbook of Mathematical Functions: With Formulas, Graphs and Mathematical Tables*, Dover Publications, New York, NY, USA, 1972.
- [45] I. S. Gradshteyn and I. M. Ryzhik, *Table of Integrals, Series, and Products*, Academic Press, Cambridge, Mass, USA, 7th edition, 2007.

Research Article

Initiation of Failure for Masonry Subject to In-Plane Loads through Micromechanics

V. P. Berardi

Department of Civil Engineering, University of Salerno, Via Ponte don Melillo, 84084 Fisciano, Italy

Correspondence should be addressed to V. P. Berardi; berardi@unisa.it

Received 17 December 2015; Accepted 5 October 2016

Academic Editor: Theodoros C. Rousakis

Copyright © 2016 V. P. Berardi. This is an open access article distributed under the Creative Commons Attribution License, which permits unrestricted use, distribution, and reproduction in any medium, provided the original work is properly cited.

A micromechanical procedure is used in order to evaluate the initiation of damage and failure of masonry with in-plane loads. Masonry material is viewed as a composite with periodic microstructure and, therefore, a unit cell with suitable boundary conditions is assumed as a representative volume element of the masonry. The finite element method is used to determine the average stress on the unit cell corresponding to a given average strain prescribed on the unit cell. Finally, critical curves representing the initiation of damage and failure in both clay brick masonry and adobe masonry are provided.

1. Introduction

Materials used in civil engineering such as cement concrete [1–4] and masonry are subject to deterioration; moreover, constructions built in the past need to carry increasing seismic horizontal as well as vertical loads, leading to the need for strengthening interventions. Fibre reinforced plastics (FRP), polymeric nets embedded in the plaster, and other more classical materials and techniques are effectively used to strengthen existing structures [5–8]. More complex techniques require the insertion of seismic isolation bearings made of rubber, usually modelled as a hyperelastic material [9–16]. New materials are being tested for civil engineering applications; recently, carbon nanotubes (CNTs) are being used in various research works in order to improve the mechanical properties of cement mortar (usable also in strengthening existing structures); therefore many authors are investigating the behaviour of structures at nanoscale with nonlocal material models [17–21].

Numerical methods for determining the structural response of unreinforced and reinforced masonry constructions, such as arches, wall, and dome, are available in the literature [22–27]. It is important to have available methods for estimating not only the structural response but also the material behaviour. To this end, micromechanics and homogenization methods have been applied to the masonry

material. In this work, a micromechanical procedure is used in order to evaluate the initiation of damage and failure of masonry panels with in-plane loads following the approach developed in [28–30].

2. Micromechanical Analysis and Material Model

The masonry material is composed of two constituents: the brick and the mortar. These constituents have different mechanical properties and the resulting masonry material can be viewed as a composite so that classical techniques based on micromechanics and homogenization are used in order to determine the local and overall response of the masonry material. The overall mechanical properties of the composite are derived from the geometric and mechanical properties of the constituents, the microstructure of the composite, and so forth. Such information is contained in a reference volume element (RVE), which is statistically representative of the masonry under consideration. The following analyses are performed on the representative volume element. Instead of modelling the masonry as a random composite material (see, e.g., [31–36]), it is assumed that the constituents are arranged in a periodic way [37–45] and a unit cell is adopted as the representative volume element. The

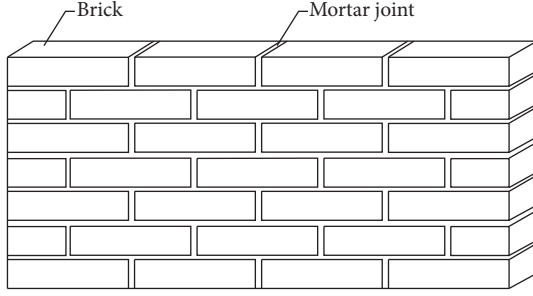


FIGURE 1: A masonry wall.

masonry considered in this work is shown in Figure 1, where a wall is depicted. The aim is to determine the strength of the masonry when it is subjected to in-plane loads.

The wall in Figure 1 is a three-dimensional structure whose three-dimensional unit cell is shown in Figure 2(a), where $2a_1$, $2a_2$, and $2a_3$ are the dimensions of the unit cell along the x_1 -, x_2 -, and x_3 -axes of the coordinate system with origin in the centre of the unit cell.

In micromechanical and homogenization analyses of periodic microstructure, the three-dimensional unit cell is subjected to the following periodic boundary conditions:

$$\begin{aligned}
 u_i(a_1, x_2, x_3) - u_i(-a_1, x_2, x_3) &= 2E_{i1}a_1 \\
 \forall x_2 \in [-a_2, a_2], \forall x_3 \in [-a_3, a_3], \\
 u_i(x_1, a_2, x_3) - u_i(x_1, -a_2, x_3) &= 2E_{i2}a_2 \\
 \forall x_1 \in [-a_1, a_1], \forall x_3 \in [-a_3, a_3], \\
 u_i(x_1, x_2, a_3) - u_i(x_1, x_2, -a_3) &= 2E_{i3}a_3 \\
 \forall x_1 \in [-a_1, a_1], \forall x_2 \in [-a_2, a_2],
 \end{aligned} \tag{1}$$

where u_i is the displacement along the x_i -axis and E_{ij} are the components of the average strain prescribed to the unit cell. Together with (1), the following constraint must be imposed in order to avoid the rigid-body translations:

$$\mathbf{u}(\mathbf{x}^*) = \mathbf{0}, \tag{2}$$

where \mathbf{x}^* is the position vector of the centre of the unit cell. Since the in-plane behaviour must be investigated, the plane unit cell shown in Figure 2(b) can be used as representative volume element for a two-dimensional (2D) analysis. In the homogenization analysis, the boundary conditions prescribed to the plane unit cell are

$$\begin{aligned}
 u_i(a_1, x_2) - u_i(-a_1, x_2) &= 2E_{i1}a_1 \quad \forall x_2 \in [-a_2, a_2], \\
 u_i(x_1, a_2) - u_i(x_1, -a_2) &= 2E_{i2}a_2 \quad \forall x_1 \in [-a_1, a_1].
 \end{aligned} \tag{3}$$

The average stress in the unit cell is denoted by Σ , whereas the local stress in a point of the constituent of the unit cell is the microstress σ and, for simplicity, will be called stress in the following. The constituents (brick and mortar) are considered linear elastic before their damage and failure. The bond between the constituents is considered perfect. It is

assumed that the plane unit cell and the constituents are subject to a plane stress state. Therefore, the principal stress perpendicular to the plane unit cell is equal to zero whereas the principal stresses parallel to the plane of the unit cell can be different from zero. The failure in a point of a constituent occurs when one of the following three failure criteria is satisfied.

First Criterion. If the two principal stresses parallel to the plane of the unit cell are nonnegative the failure occurs when the maximum principal stress in a point is equal to the tensile strength of the constituent.

Second Criterion. If the two principal stresses parallel to the plane of the unit cell are nonpositive the failure occurs when the following equation is satisfied:

$$CJ_2 + (1 - C)I_1 + CI_2 = 1, \tag{4}$$

where $C = 1.6$,

$$\begin{aligned}
 J_2 &= \frac{1}{f_c^2} (\sigma_2 - \sigma_3)^2, \\
 I_1 &= \frac{1}{f_c} (\sigma_2 + \sigma_3), \\
 I_2 &= \frac{\sigma_2 \sigma_3}{f_c^2},
 \end{aligned} \tag{5}$$

where σ_2 and σ_3 are the two nonpositive principal stresses parallel to the plane of the unit cell and f_c is the compressive strength of the material of the constituent.

Third Criterion. When a principal stress σ_1 parallel to the plane of the unit cell is nonnegative and the other principal stress σ_3 parallel to the plane of the unit cell is nonpositive, the failure occurs when the following equation is satisfied:

$$\frac{\sigma_1}{f_t} + \frac{\sigma_3}{f_c} = 1, \tag{6}$$

where f_t is the tensile strength of the material of the constituent.

Next, the average strain \mathbf{E} (which is a tensor with components E_{ij}) is imposed on the plane unit cell by means of the conditions (2) and (3). Then, the average stress Σ corresponding to the prescribed average strain \mathbf{E} is evaluated and the critical curves of the masonry are determined with a finite element homogenization technique. The critical curves may be plotted in the plane defined by Σ_{11} - and Σ_{22} -axes or in the plane defined by Σ_{11} - and Σ_{12} -axes. There are two kinds of critical curves: a generic critical curve may be related to the brick or to the mortar. The generic point of the critical curve related to a constituent represents the average stresses corresponding to the initiation of failure of that constituent. Specifically, the initiation of failure of a constituent is evaluated by prescribing a linear load path $\mathbf{E} = \lambda \mathbf{E}^0$, where \mathbf{E}^0 is a constant tensor, which does not vary in the loading process, and the scalar λ is an increasing loading positive parameter. Considering both constituents linear

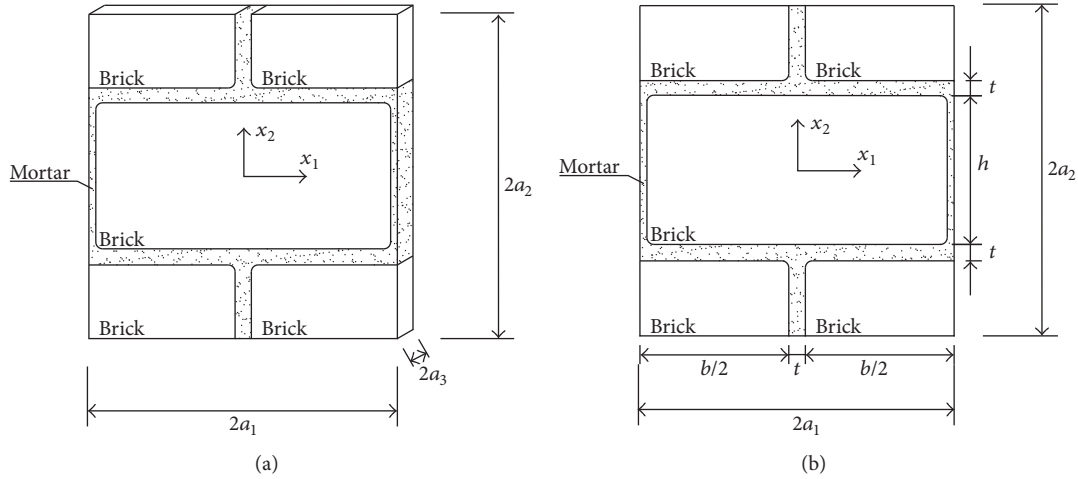


FIGURE 2: (a) Three-dimensional unit cell; (b) plane unit cell.

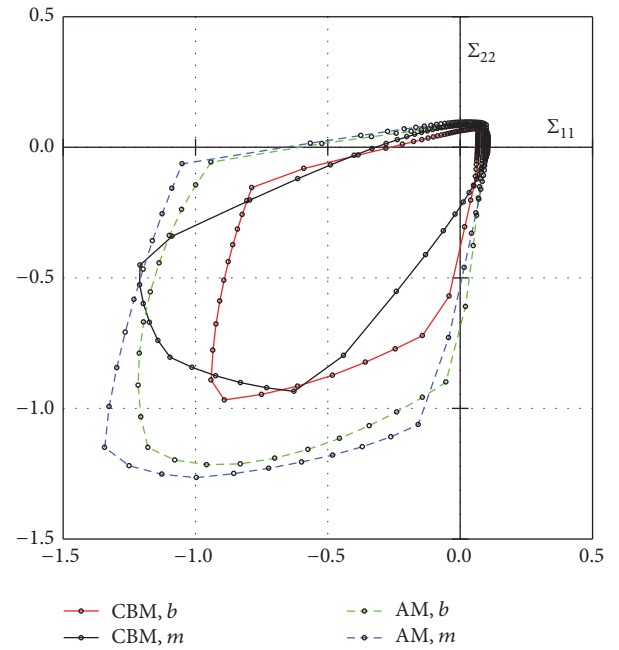
elastic, there exists a value $\lambda^{cr,i}$ such that the microstresses in a constituent i ($i = \text{brick or mortar}$) of the unit cell subject to the average strain $\mathbf{E} = \lambda^{cr,i} \mathbf{E}^0$ satisfy some of the above-mentioned criteria in the same constituent i , whereas failure criteria are not satisfied in the same constituent i when the unit cell is subject to $\mathbf{E} = \lambda \mathbf{E}^0$ for $0 \leq \lambda < \lambda^{cr,i}$. The average stress of the unit cell subject to the average strain $\mathbf{E} = \lambda^{cr,i} \mathbf{E}^0$ is denoted by $\Sigma^{cr,i}$. In the plane defined by Σ_{11} - and Σ_{22} -axes, the components $(\Sigma_{11}^{cr,i}, \Sigma_{22}^{cr,i})$ of $\Sigma^{cr,i}$ define a closed curve which represents the masonry critical curve related to the initiation of failure of the constituent i . An analogous critical curve can be plotted in the plane defined by Σ_{11} - and Σ_{12} -axes.

3. Numerical Examples

If the constituents have the same mechanical properties and the bond between the brick and the mortar is perfect, the masonry behaves like a homogeneous material and the homogenization procedure is not required. Critical cases occur when the mechanical properties of one constituent are significantly different from the mechanical properties of the other constituents. For example, in adobe masonry (AM), bricks and mortar have similar elastic properties, whereas in some kinds of clay brick masonry (CBM) Young's modulus of the brick may be significantly different from Young's modulus of the mortar. The masonry critical curves are very sensitive to the ratio E_b/E_m , where E_b and E_m are Young's moduli of the brick and the mortar, respectively. This is shown in Figure 3, where the masonry critical curve related to the initiation of failure of the constituent i is denoted by "b" for $i = \text{brick}$ and by "m" for $i = \text{mortar}$ in the legend of the figure.

The critical curves in Figure 3 are obtained by prescribing the following average strain:

$$\mathbf{E} = \begin{bmatrix} E_{11} & E_{12} \\ E_{21} & E_{22} \end{bmatrix} = \lambda \begin{bmatrix} \cos \varphi & 0 \\ 0 & \sin \varphi \end{bmatrix} \quad \text{for } \varphi \in [0, 2\pi]. \quad (7)$$


 FIGURE 3: CBM and AM critical curves, in the Σ_{11} - Σ_{22} plane, related to the initiation of failure of brick and mortar.

In this section, the mechanical properties of the constituents of CBM are $\nu_b = 0.23$, $\nu_m = 0.15$, $E_b = 10E_m = 10000$ MPa, $f_{cb} = 10f_{tb} = 1$ MPa, $f_{cm} = f_{cb}$, and $f_{tm} = f_{tb}$; the mechanical properties of the constituents of AM are $\nu_b = \nu_m = 0.15$, $E_b = 2E_m = 100$ MPa, $f_{cb} = 10f_{tb} = 1$ MPa, $f_{cm} = f_{cb}$, and $f_{tm} = f_{tb}$. In this work, ν_b and ν_m are Poisson's ratios of the brick and the mortar, respectively, f_{tb} and f_{tm} are the tensile strengths of the brick and the mortar, and f_{cb} and f_{cm} are the compressive strengths of the brick and the mortar. Both CBM and AM have the following geometric properties: $b = 400$ mm (width of the bricks), $h = 100$ mm (height of the bricks), $t = 10$ mm (thickness of mortar joints), and

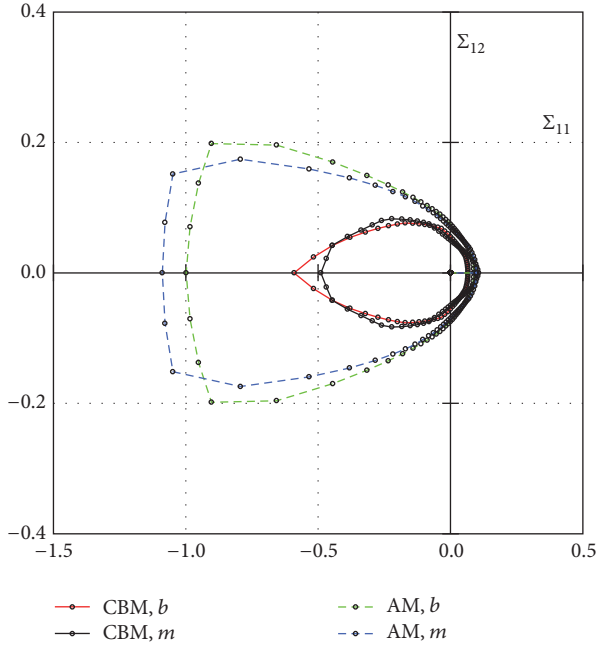


FIGURE 4: CBM and AM critical curves, in the Σ_{11} - Σ_{12} plane, related to the initiation of failure of brick and mortar.

$\rho = h/40$ (each brick corner was approximated as arc of circle with radius ρ).

In Figure 3, two different values of the ratio $c = E_b/E_m$ are considered: $c = 10$ for the CBM critical curves and $c = 2$ for the AM critical curves. Greater values of c determine greater concentration of the local stress and, as a consequence, smaller critical areas (the critical area is the area bounded by the critical curve related to the initiation of failure of a constituent). A similar behaviour is observed in Figure 4, where the critical curves are obtained by prescribing the following average strain:

$$\mathbf{E} = \begin{bmatrix} E_{11} & E_{12} \\ E_{21} & E_{22} \end{bmatrix} = \lambda \begin{bmatrix} \cos \varphi & \sin \varphi \\ \sin \varphi & 0 \end{bmatrix} \quad \text{for } \varphi \in [0, 2\pi]. \quad (8)$$

The contrast c between the masonry constituents also influences the deformed shape of the unit cell and the distribution of local stress in the unit cell, as shown in Figures 5 and 6, where the local stress σ_{12} on the deformed unit cell subject to the average strain (8) with $\varphi = \pi/2$ and $\lambda = 1$ is plotted for CBM ($c = 10$) and AM ($c = 2$), respectively.

4. Conclusions

In this work, masonry is viewed as a composite constituted of two components (namely, brick and mortar) so that classical techniques based on micromechanics and homogenization are used in order to determine the local and overall response of the masonry material. The critical curves of the masonry are determined with a finite element homogenization technique. The generic point of the critical curve related to a constituent represents the average stresses corresponding to the initiation of failure of that constituent. The numerical

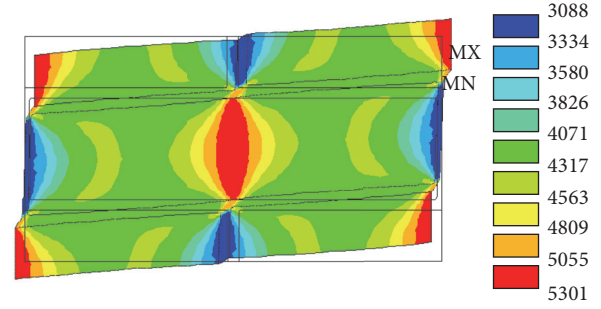


FIGURE 5: Local stress σ_{12} on the deformed CBM unit cell subject to a pure shear average strain $E_{12} = E_{21} = 1$.

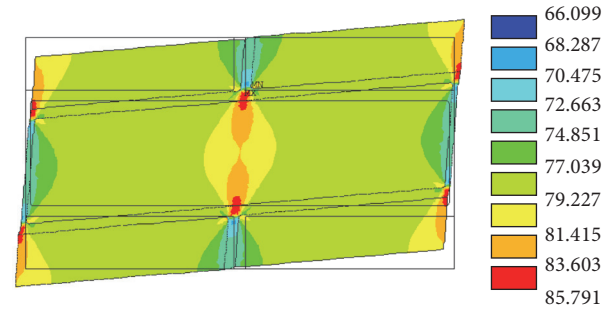


FIGURE 6: Local stress σ_{12} on the deformed AM unit cell subject to a pure shear average strain $E_{12} = E_{21} = 1$.

analyses show that the critical curves are sensitive to the contrast $c = E_b/E_m$ between brick and mortar: greater contrast involves earlier initiation of damage in the constituents.

Competing Interests

There are no competing interests related to this paper.

References

- [1] A. Caporale, L. Feo, and R. Luciano, "Damage mechanics of cement concrete modeled as a four-phase composite," *Composites Part B: Engineering*, vol. 65, pp. 124–130, 2014.
- [2] A. Caporale and R. Luciano, "A micromechanical four-phase model to predict the compressive failure surface of cement concrete," *Frattura ed Integrità Strutturale*, vol. 8, no. 29, pp. 19–27, 2014.
- [3] G. Dinelli, G. Belz, C. E. Majorana, and B. A. Schrefler, "Experimental investigation on the use of fly ash for lightweight precast structural elements," *Materials and Structures*, vol. 29, no. 10, pp. 632–638, 1996.
- [4] G. Xotta, G. Mazzucco, V. A. Salomoni, C. E. Majorana, and K. J. Willam, "Composite behavior of concrete materials under high temperatures," *International Journal of Solids and Structures*, vol. 64, pp. 86–99, 2015.
- [5] A. D'Ambrisi, F. Focacci, and R. Luciano, "Experimental investigation on flexural behavior of timber beams repaired with CFRP plates," *Composite Structures*, vol. 108, no. 1, pp. 720–728, 2014.
- [6] A. D'Ambrisi, F. Focacci, R. Luciano, V. Alecci, and M. De Stefano, "Carbon-FRCM materials for structural upgrade of

- masonry arch road bridges,” *Composites Part B: Engineering*, vol. 75, no. 3373, pp. 355–366, 2015.
- [7] A. D’Ambrisi, M. Mezzi, and A. Caporale, “Experimental investigation on polymeric net-RCM reinforced masonry panels,” *Composite Structures*, vol. 105, pp. 207–215, 2013.
- [8] V. Salomoni, G. Mazzucco, C. Pellegrino, and C. Majorana, “Three-dimensional modelling of bond behaviour between concrete and FRP reinforcement,” *Engineering Computations*, vol. 28, no. 1, pp. 5–29, 2011.
- [9] A. M. Tarantino, “The singular equilibrium field at the notch-tip of a compressible material in finite elastostatics,” *Zeitschrift für Angewandte Mathematik und Physik*, vol. 48, no. 3, pp. 370–388, 1997.
- [10] A. M. Tarantino, “On extreme thinning at the notch tip of a neo-Hookean sheet,” *The Quarterly Journal of Mechanics and Applied Mathematics*, vol. 51, no. 2, pp. 179–190, 1998.
- [11] A. M. Tarantino, “On the finite motions generated by a mode I propagating crack,” *Journal of Elasticity. The Physical and Mathematical Science of Solids*, vol. 57, no. 2, pp. 85–103 (2000), 1999.
- [12] A. M. Tarantino, “Asymmetric equilibrium configurations of symmetrically loaded isotropic square membranes,” *Journal of Elasticity*, vol. 69, no. 1–3, pp. 73–97, 2002.
- [13] A. M. Tarantino, “Asymmetric equilibrium configurations of hyperelastic cylindrical bodies under symmetric dead loads,” *Quarterly of Applied Mathematics*, vol. 64, no. 4, pp. 605–615, 2006.
- [14] A. M. Tarantino and A. Nobili, “Constitutive branching analysis of cylindrical bodies under in-plane equibiaxial dead-load tractions,” *International Journal of Non-Linear Mechanics*, vol. 41, no. 8, pp. 958–968, 2006.
- [15] A. M. Tarantino, “Homogeneous equilibrium configurations of a hyperelastic compressible cube under equitriaxial dead-load tractions,” *Journal of Elasticity. The Physical and Mathematical Science of Solids*, vol. 92, no. 3, pp. 227–254, 2008.
- [16] L. Lanzoni and A. M. Tarantino, “Damaged hyperelastic membranes,” *International Journal of Non-Linear Mechanics*, vol. 60, pp. 9–22, 2014.
- [17] A. Apuzzo, R. Barretta, and R. Luciano, “Some analytical solutions of functionally graded Kirchhoff plates,” *Composites Part B: Engineering*, vol. 68, pp. 266–269, 2015.
- [18] R. Barretta, L. Feo, and R. Luciano, “Torsion of functionally graded nonlocal viscoelastic circular nanobeams,” *Composites Part B: Engineering*, vol. 72, pp. 217–222, 2015.
- [19] R. Barretta, L. Feo, R. Luciano, and F. Marotti de Sciarra, “A gradient Eringen model for functionally graded nanorods,” *Composite Structures*, vol. 131, pp. 1124–1131, 2015.
- [20] R. Barretta, L. Feo, R. Luciano, and F. Marotti de Sciarra, “Variational formulations for functionally graded nonlocal Bernoulli-Euler nanobeams,” *Composite Structures*, vol. 129, pp. 80–89, 2015.
- [21] R. Barretta, R. Luciano, and F. Marotti De Sciarra, “A fully gradient model for Euler-Bernoulli nanobeams,” *Mathematical Problems in Engineering*, vol. 2015, Article ID 495095, 8 pages, 2015.
- [22] A. Caporale, R. Luciano, and L. Rosati, “Limit analysis of masonry arches with externally bonded FRP reinforcements,” *Computer Methods in Applied Mechanics and Engineering*, vol. 196, no. 1–3, pp. 247–260, 2006.
- [23] A. Caporale, L. Feo, and R. Luciano, “Limit analysis of FRP strengthened masonry arches via nonlinear and linear programming,” *Composites Part B: Engineering*, vol. 43, no. 2, pp. 439–446, 2012.
- [24] A. Caporale and R. Luciano, “Limit analysis of masonry arches with finite compressive strength and externally bonded reinforcement,” *Composites Part B: Engineering*, vol. 43, no. 8, pp. 3131–3145, 2012.
- [25] A. Caporale, L. Feo, R. Luciano, and R. Penna, “Numerical collapse load of multi-span masonry arch structures with FRP reinforcement,” *Composites Part B: Engineering*, vol. 54, no. 1, pp. 71–84, 2013.
- [26] A. D’Ambrisi, F. Focacci, and A. Caporale, “Strengthening of masonry-unreinforced concrete railway bridges with PBO-FRCM materials,” *Composite Structures*, vol. 102, pp. 193–204, 2013.
- [27] A. Caporale, L. Feo, D. Hui, and R. Luciano, “Debonding of FRP in multi-span masonry arch structures via limit analysis,” *Composite Structures*, vol. 108, no. 1, pp. 856–865, 2014.
- [28] A. Caporale, F. Parisi, D. Asprone, R. Luciano, and A. Prota, “Critical surfaces for adobe masonry: micromechanical approach,” *Composites Part B: Engineering*, vol. 56, pp. 790–796, 2014.
- [29] A. Caporale, F. Parisi, D. Asprone, R. Luciano, and A. Prota, “Micromechanical analysis of adobe masonry as two-component composite: influence of bond and loading schemes,” *Composite Structures*, vol. 112, no. 1, pp. 254–263, 2014.
- [30] A. Caporale, F. Parisi, D. Asprone, R. Luciano, and A. Prota, “Comparative micromechanical assessment of adobe and clay brick masonry assemblages based on experimental data sets,” *Composite Structures*, vol. 120, pp. 208–220, 2015.
- [31] R. Luciano and J. R. Willis, “Bounds on non-local effective relations for random composites loaded by configuration-dependent body force,” *Journal of the Mechanics and Physics of Solids*, vol. 48, no. 9, pp. 1827–1849, 2000.
- [32] R. Luciano and J. R. Willis, “Non-local effective relations for fibre-reinforced composites loaded by configuration-dependent body forces,” *Journal of the Mechanics and Physics of Solids*, vol. 49, no. 11, pp. 2705–2717, 2001.
- [33] R. Luciano and J. R. Willis, “Non-local constitutive response of a random laminate subjected to configuration-dependent body force,” *Journal of the Mechanics and Physics of Solids*, vol. 49, no. 2, pp. 431–444, 2001.
- [34] R. Luciano and J. R. Willis, “Boundary-layer corrections for stress and strain fields in randomly heterogeneous materials,” *Journal of the Mechanics and Physics of Solids*, vol. 51, no. 6, pp. 1075–1088, 2003.
- [35] R. Luciano and J. R. Willis, “FE analysis of stress and strain fields in finite random composite bodies,” *Journal of the Mechanics and Physics of Solids*, vol. 53, no. 7, pp. 1505–1522, 2005.
- [36] R. Luciano and J. R. Willis, “Hashin-Shtrikman based FE analysis of the elastic behaviour of finite random composite bodies,” *International Journal of Fracture*, vol. 137, no. 1–4, pp. 261–273, 2006.
- [37] A. Caporale, R. Luciano, and E. Sacco, “Micromechanical analysis of interfacial debonding in unidirectional fiber-reinforced composites,” *Computers and Structures*, vol. 84, no. 31–32, pp. 2200–2211, 2006.
- [38] A. Caporale and R. Luciano, “Micromechanical analysis of periodic composites by prescribing the average stress,” *Annals of Solid and Structural Mechanics*, vol. 1, no. 3, pp. 117–137, 2010.

- [39] A. Caporale, R. Luciano, and R. Penna, "Fourier series expansion in non-orthogonal coordinate system for the homogenization of linear viscoelastic periodic composites," *Composites Part B: Engineering*, vol. 54, no. 1, pp. 241–245, 2013.
- [40] A. Caporale, L. Feo, and R. Luciano, "Eigenstrain and Fourier series for evaluation of elastic local fields and effective properties of periodic composites," *Composites Part B: Engineering*, vol. 81, pp. 251–258, 2015.
- [41] F. Greco and R. Luciano, "A theoretical and numerical stability analysis for composite micro-structures by using homogenization theory," *Composites Part B: Engineering*, vol. 42, no. 3, pp. 382–401, 2011.
- [42] G. Cricri and R. Luciano, "Homogenised properties of composite materials in large deformations," *Composite Structures*, vol. 103, pp. 9–17, 2013.
- [43] D. Bruno, F. Greco, R. Luciano, and P. Nevone Blasi, "Nonlinear homogenized properties of defected composite materials," *Computers and Structures*, vol. 134, pp. 102–111, 2014.
- [44] L. Feo, F. Greco, L. Leonetti, and R. Luciano, "Mixed-mode fracture in lightweight aggregate concrete by using a moving mesh approach within a multiscale framework," *Composite Structures*, vol. 123, pp. 88–97, 2015.
- [45] F. Greco, L. Leonetti, and R. Luciano, "A multiscale model for the numerical simulation of the anchor bolt pull-out test in lightweight aggregate concrete," *Construction and Building Materials*, vol. 95, no. 6986, pp. 860–874, 2015.

Research Article

Modelling a Coupled Thermoelctromechanical Behaviour of Contact Elements via Fractal Surfaces

G. Mazzucco,¹ F. Moro,² and M. Guarnieri²

¹Department of Civil, Environmental and Architectural Engineering, University of Padova, Via F. Marzolo, 9, 35131 Padova, Italy

²Department of Industrial Engineering, University of Padova, Via Gradenigo 6/A, 35131 Padova, Italy

Correspondence should be addressed to G. Mazzucco; gianluca.mazzucco@dicea.unipd.it

Received 24 December 2015; Accepted 5 May 2016

Academic Editor: Franco Ramírez

Copyright © 2016 G. Mazzucco et al. This is an open access article distributed under the Creative Commons Attribution License, which permits unrestricted use, distribution, and reproduction in any medium, provided the original work is properly cited.

A three-dimensional coupled thermoelctromechanical model for electrical connectors is here proposed to evaluate local stress and temperature distributions around the contact area of electric connectors under different applied loads. A micromechanical numerical model has been developed by merging together the contact theory approach, which makes use of the so-called roughness parameters obtained from experimental measurements on real contact surfaces, with the topology description of the rough surface via the theory of fractal geometry. Particularly, the variation of asperities has been evaluated via the Weierstrass-Mandelbrot function. In this way the micromechanical model allowed for an upgraded contact algorithm in terms of effective contact area and thermal and electrical contact conductivities. Such an algorithm is subsequently implemented to construct a global model for performing transient thermoelctromechanical analyses without the need of simulating roughness asperities of contact surfaces, so reducing the computational cost. A comparison between numerical and analytical results shows that the adopted procedure is suitable to simulate the transient thermoelctromechanical response of electric connectors.

1. Introduction

Several engineering applications involve connections where the electrical contact relies on a relatively weak pressure, able to ensure a partial adhesion between two elements. The real contact surfaces are not flat but include many asperities [1]; contacts occur in a number n_c of small surfaces named *a-spots*, so that the effective contact area A_c is much smaller than the apparent, macroscopic, contact one A_a (Figure 1). The effective contact area can also be reduced due, for example, to natural oxidation and the presence of other superficial contaminant films, that can be present in the contact zone. A direct consequence of the fact that the electrical contact is established only through these *a-spots* is that contact resistivity increases, producing the constriction resistance. The total contact resistance can be generally estimated by means of a statistical approach linking the microscopic contact physics to the meso-scale modelling [2–4]; with this approach the total constriction resistance is defined as a function of parameters such as surface roughness, material hardness, normal pressure p_c , and temperature T .

Numerical simulations of electrical contacts can be conducted in agreement with the contact theory [5] which, in general, is able to evaluate only the apparent contact area A_c , possibly overestimating the electrical and the thermal connection; for example, in [6, 7] the electromechanical contact has been evaluated by considering a micro-macro approach where A_c has been statistically defined.

To improve the knowledge of the effective interconnection between two bodies in contact, a micromechanical numerical model is here developed to simulate the irregular contact surface. Micromechanical models require a homogenized material response which takes into account microstructural heterogeneity [8]. Analytical models of composite structures at nanoscale can be found in [9–14].

More specifically, in the present work the micromechanical model is characterized by means of three-dimensional contact surfaces obtained via the fractal theory [15, 16] which makes use of roughness parameters resulting from experimental measurements on real contact surfaces to simulate the surface asperities (Figure 2).

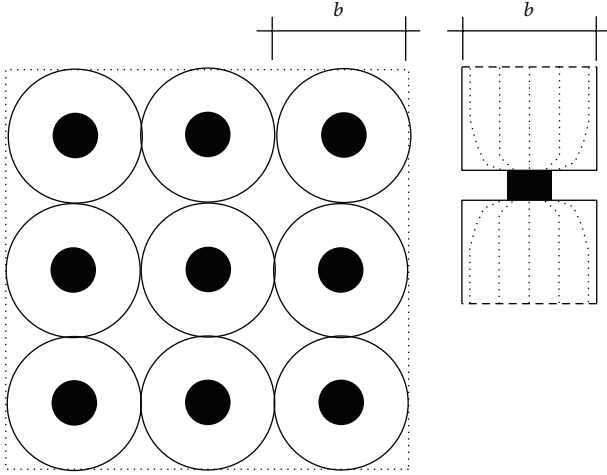


FIGURE 1: Schematic view of a -spot area.

Asperities heights, peaks distribution, and so forth are dependent on the contact surface preparation and the load history; in fact residual strains under elastoplastic cycles can modify the contact surfaces. The fractal theory has been followed to represent the initial asperities for a virgin material and to evaluate the effective electrical contact area; the material is modelled to behave elastoplastically and able to undergo large strains.

Previous three-dimensional models have been developed [17] to evaluate the global effects in terms of stress and temperature distributions around the contact area; the analyses were supported by experimental tests to retrieve the thermo-electromechanical characteristics of interest.

Here an analytical-numerical comparison is additionally carried out to validate this procedure, considering a classic case of a cylinder and a hemisphere in contact under different compression loads.

Such problems may undergo instability [18–20], which would require a local investigation of the stress field in large strains [21–24]; nevertheless this topic is not addressed in the present micro-macro approach, under the assumption that the compressive load does not generate buckling.

2. The Analytical Model

On the macroscopic scale two contact elements pressed together apparently touch each other on area A_a that, due to surface roughness, is much larger than area A_c of effective mechanical contact. In fact, on such a scale contact occurs between the asperities of the two surfaces in a number n_c of small surfaces per macro-unit area, named a -spots, which both increase with the applied contact force P [25]. Current density lines are forced to pass through a -spots, causing a local increase in resistance R_c . For a single circular a -spot of radius a_c and sufficiently thick elements, R_c is analytically known. A more complex question is determining the total constriction resistance corresponding to A_a and given by many a -spots whose number and radius depend on the

compressive load P , the surface roughness, and the material properties.

A statistical approach that allows linking the macroscopic model needed for numerical simulation with the physics of microscopic contacts is extensively presented in [2–4] and it has been taken as reference for the present work. The statistical characterization of the surface roughness is considered as representative quantities: the mean plane between peaks and valleys of the asperities, the mean absolute asperity slope m , and the root mean square (RMS) of the surface roughness σ_r , whereas the contact between the two surfaces is expressed by the mean plane distance Y . As long as relatively weak contact forces are considered, m and σ_r can be assumed to be constant, so that only Y varies with the applied load P .

When the load increases, the asperities in contact are crushed and the mean distance Y between two bodies decreases (Figure 3). We define d_{\max} as the maximum mean distance between the two bodies ($Y = d_{\max}$ when the two bodies are in contact but the external load is equal to 0). If the external load is applied, the mean distance d is evaluated by

$$Y = d_{\max} - \frac{P}{K_{\text{spot}}}, \quad (1)$$

where K_{spot} is the spot stiffness in the contact surface. The spot stiffness is evaluated in [4, 17] via the relationship

$$K_{\text{spot}} = \frac{c_1}{2} \left(\frac{2}{\sqrt{\pi}} \right)^{1+c_2} \left(\frac{4\sigma_r}{m} \right)^{c_2}, \quad (2)$$

where c_1, c_2 are two material parameters.

Starting from these conditions, the following expression is derived for the a -spot mean radius, their number, and the total contact surface

$$\begin{aligned} a_c &= \sqrt{\frac{8}{\pi}} \frac{\sigma_r}{m} \exp\left(\frac{Y^2}{2\sigma_r^2}\right) \operatorname{erfc}\left(\frac{Y}{\sqrt{2}\sigma_r}\right), \\ n_c &= \frac{1}{16} \left(\frac{m}{\sigma_r}\right)^2 \frac{A_a}{\operatorname{erfc}\left(Y/\sqrt{2}\sigma_r\right) \exp\left(Y^2/\sigma_r^2\right)}, \\ A_c &= n_c \pi a_c^2 = \frac{1}{2} \operatorname{erfc}\left(\frac{Y}{\sqrt{2}\sigma_r}\right) A_a. \end{aligned} \quad (3)$$

In order to relate Y to P , in agreement with most of the available literature, a plastic deformation of the asperities has been assumed, because a -spots are very small so that weak forces can produce very high local pressures over them, highly exceeding the yield limit [3, 4]. However it must also be noted that hypothesis of elastic deformations is even reported in literature, considering that asperities may behave plastically at first but when the a -spots enlarge enough, loads are elastically supported. As far as the linear assumption is accepted, the plastic condition allows expressing the contact force as $P = A_c H_c$, with H_c the contact micro-hardness, whereas A_a is related to the macroscopic apparent pressure $p_c = P/A_a$, so that

$$p_c = \frac{H_c}{2} \operatorname{erfc}\left(\frac{d}{\sqrt{2}\sigma_r}\right). \quad (4)$$

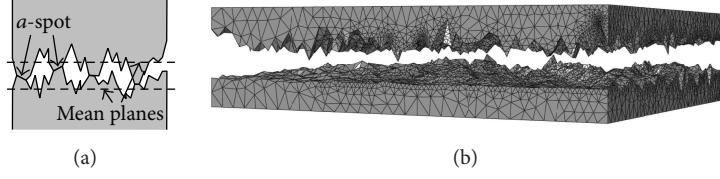


FIGURE 2: (a) Effective contact area; (b) typical fractal surface.

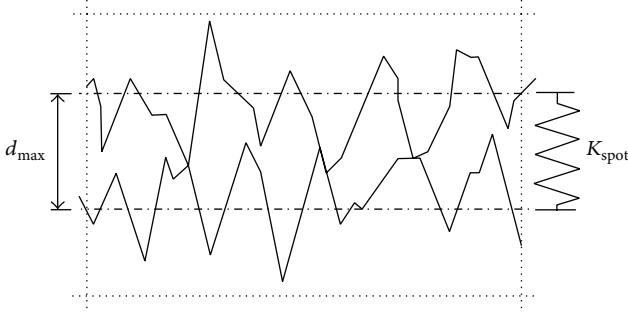


FIGURE 3: Connection between two contact surfaces.

Considering the Vickers hardness test, H_c can be found starting by a Vickers micro-hardness measure H_v

$$H_v = c_1 d_v^2, \quad (5)$$

where d_v is the mean indentation diagonal; that is, in a similar way

$$\begin{aligned} H_c &= c_1 d_c^2, \\ d_c &= \sqrt{2\pi} a_c. \end{aligned} \quad (6)$$

Considering the plurality of a -spots and the proximity among them, each current tube can expand far from its contact point to a radius b (Figure 1). The total contact resistance R_c can be defined as the inverse of the contact conductance $R_c = 1/h_c$ that can be evaluated as

$$h_c = 1.25 k_c \left(\frac{m}{\sigma_r} \right) \left(\frac{A_c}{A_a} \right)^{0.95} \quad (7)$$

in which k_c is the electrical conductivity.

Moreover, as the contact surfaces generally present some level of oxidation and often also stray deposits of insulating substances, a film resistance has been added to the constriction resistance from (7). As it strongly depends on the level of cleanness of the surfaces and on the used metal, values taken from literature have been considered.

3. The Thermoelctromechanical Model

Under an electrical flux, bodies' configurations are subjected to modifications caused by electrical energy dissipation. Correspondingly, a coupled thermoelctromechanical model has been accounted for.

The electric field is governed by Maxwell's equation

$$\int_{\Gamma} \mathbf{J} \cdot \mathbf{n} d\Gamma = \int_{\Omega} r_c d\Omega, \quad (8)$$

where Γ is the surface area, Ω is the volume, \mathbf{J} is the electrical current density vector (per unit area), and r_c is the internal volumetric current source (per unit volume).

\mathbf{J} can be defined via Ohm's law by considering the current density as a function of the electrical conductivity matrix $\boldsymbol{\sigma}^E = \boldsymbol{\sigma}^E(T)$, with T being temperature, and the gradient of the electrical potential \mathbf{E}^E

$$\mathbf{J} = \boldsymbol{\sigma}^E \cdot \mathbf{E}^E = -\boldsymbol{\sigma}^E \cdot \frac{\partial \varphi}{\partial \mathbf{x}}, \quad (9)$$

where \mathbf{x} is the position vector in the current configuration and φ is the electrical potential. The thermal energy generated by the electrical current can be defined by Joule's law that evaluates the dissipated electrical energy P_E as

$$P_E = \mathbf{E}^E \cdot \mathbf{J}. \quad (10)$$

The energy released in the form of internal heat is

$$r = \eta P_E, \quad (11)$$

where r is the heat energy generated during dissipation and η is the energy conversion factor.

Thermal variations within a body involve a new mechanical configuration. The stiffness matrix for a coupled thermoelctromechanical model results as

$$\begin{bmatrix} \mathbf{k}_{mm} & \mathbf{k}_{mT} & \mathbf{0} \\ \mathbf{k}_{Tm} & \mathbf{k}_{TT} & \mathbf{k}_{T\varphi} \\ \mathbf{0} & \mathbf{k}_{\varphi T} & \mathbf{k}_{\varphi\varphi} \end{bmatrix}, \quad (12)$$

where \mathbf{k}_{mm} , \mathbf{k}_{TT} , $\mathbf{k}_{\varphi\varphi}$ are the mechanical, thermal, and electrical parts, respectively, whereas \mathbf{k}_{mT} , \mathbf{k}_{Tm} , $\mathbf{k}_{\varphi T}$, $\mathbf{k}_{T\varphi}$ are the coupling terms.

At present the piezoelectric behaviour is not considered and the constitutive relation can be defined as

$$\mathbf{T} = \mathbf{C}(\mathbf{X}, T) : \mathbf{E}^e(\mathbf{X}, T) = \mathbf{C}(\mathbf{X}, T) : (\mathbf{E} - \mathbf{E}^T), \quad (13)$$

where the stress tensor \mathbf{T} is dependent on the logarithmic elastic strain \mathbf{E}^e , obtained by subtracting the thermal strain tensor \mathbf{E}^T to total logarithmic strain \mathbf{E} , and the constitutive tensor \mathbf{C} . Considering an elastoplastic material, the constitutive tensor \mathbf{C} is dependent on both the position vector in the reference configuration \mathbf{X} and temperature T .

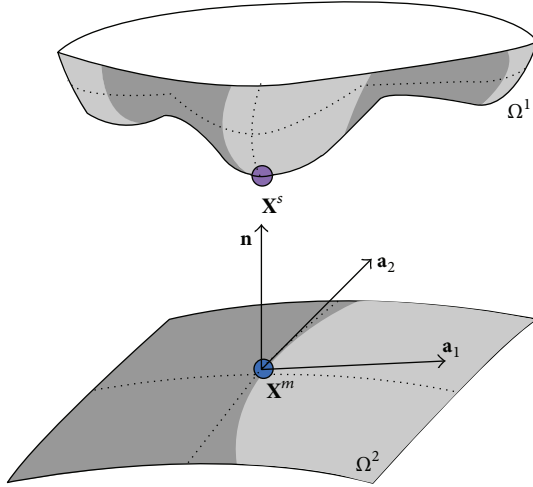


FIGURE 4: Contact scheme.

4. The Contact Algorithm

In order to simulate the thermoelectric interconnection when two bodies are touching, the contact theory has been applied [5].

Considering two bodies, Ω^1 and Ω^2 (Figure 4), for example, representative of connection components, two surfaces can be identified, Γ^1 (with $\Gamma^1 \in \Omega^1$, named *slave*) and Γ^2 (with $\Gamma^2 \in \Omega^2$ named *master*), where contact is possible. The *closed contact* condition is achieved and the two bodies are in contact if the contact surface $\Gamma^c = \Gamma^1 \cap \Gamma^2 \neq \emptyset$.

Contact is defined when the fundamental conditions are set:

- (i) Nonpenetration conditions:

$$\begin{aligned} (\mathbf{u}^m - \mathbf{u}^s) \cdot \mathbf{n} + g &\geq 0 \quad \text{on } \Gamma^c \\ g &= (\bar{\mathbf{X}}^m - \mathbf{X}^s) \cdot \mathbf{n} \quad \text{on } \Gamma^c, \end{aligned} \quad (14)$$

where \mathbf{u}^i (with i equal to m , master, and s , slave) are the displacement vectors, \mathbf{X}^i are the position vectors in the reference configuration, g is the gap function (the distance between two points in contact), and \mathbf{n} is the normal vector (Figure 4).

- (ii) Action-reaction conditions:

$$\mathbf{t}^m + \mathbf{t}^s = 0 \quad \text{on } \Gamma^c, \quad (15)$$

where \mathbf{t}^i are the stress vectors.

- (iii) Kuhn-Tucker conditions:

$$\begin{aligned} g &\geq 0, \\ p_c &\leq 0, \\ p_c \cdot g &= 0, \end{aligned} \quad (16)$$

on Γ^c ,

where p_c is the normal pressure: $p_c = \mathbf{t} \cdot \mathbf{n}$.

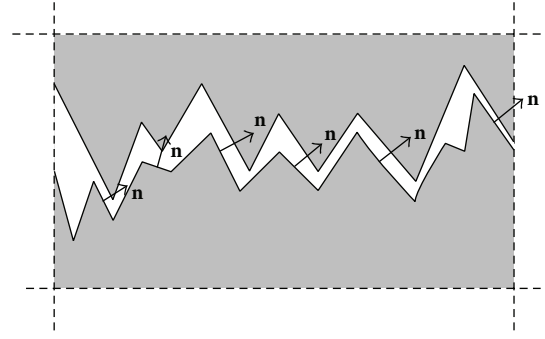


FIGURE 5: Normal contact definition in the fractal surface.

Generally, friction effects between two bodies in contact are dependent on the roughness of the contact surface; in our case, if one considers the adopted material asperity model, friction is a direct consequence of the model itself and it comes from the transversal asperity connections, so that a normal condition only has been considered (Figure 5).

The normal contact is characterized by a normal pressure, defined based on the penalty method; that is,

$$p_c = k_n \cdot g_n^\alpha, \quad (17)$$

where g_n is the gap function along the normal direction and k_n is the penalty coefficient.

In the developed three-dimensional numerical model here presented, characterized by tetrahedral elements, master and slave surfaces have been defined on the contact faces of the elements (Figure 6). The closed contact condition has been considered in the *contact pair*, defined through a slave node and a master point. On these surfaces only the gap function g is evaluated.

The master point \mathbf{x}^m in a contact pair is chosen as the point with the minimum distance from the slave node \mathbf{x}^s (*minimal distance rule*); generally it does not coincide with a master *node* but with a generic point belonging to surface Γ^2 .

The minimum distance between slave nodes and master points can be defined by considering that the master point is obtained by the orthogonal projection of the slave node onto the master surface (see Figure 7), where the normal direction \mathbf{n} is defined by

$$\mathbf{n} = \frac{\mathbf{a}_1 \times \mathbf{a}_2}{\|\mathbf{a}_1 \times \mathbf{a}_2\|} \quad (18)$$

and \mathbf{a}_i are the tangent vectors to the master surface in \mathbf{x}^m (Figure 4) [26].

A “*master element*” is characterized by the elements faces, and the tangent vector at a generic point \mathbf{x}^m can be consequently defined taking into account the shape functions derivatives in the master element. A master point can generally be represented by referring to two different reference systems: a global reference system (g.r.s.), $\mathbf{x}^m = \mathbf{x}^m(x_1, x_2, x_3)$, and a local curvilinear reference system (l.r.s.) belonging to the master surface, $\mathbf{x}^m = \mathbf{x}^m(\xi) = \mathbf{x}^m(\xi_1, \xi_2)$. The shape

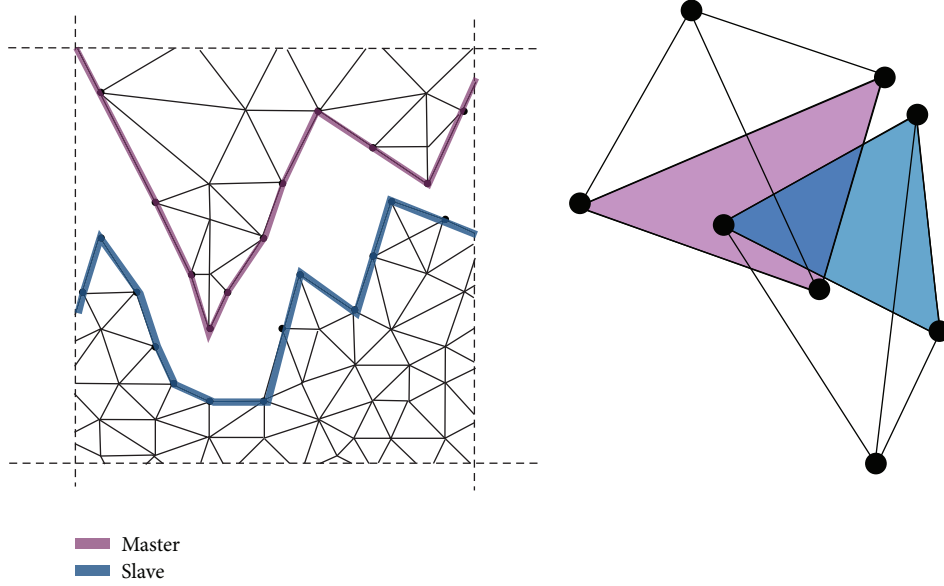


FIGURE 6: Master and slave surfaces in finite elements.

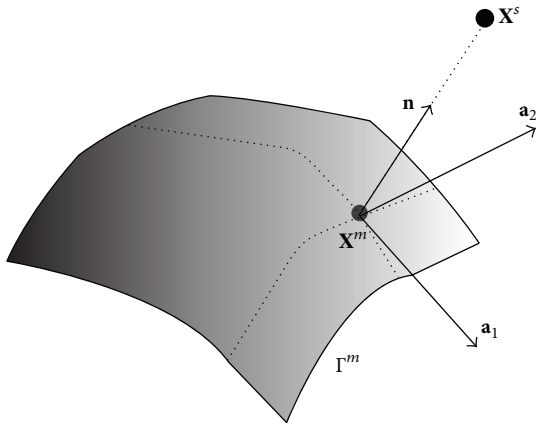


FIGURE 7: Definition of the normal direction in a point and location of a master point.

functions of a master element related to point \mathbf{x}^m can be defined as

$$\begin{aligned}
 x_1^m &= \sum_{i=1}^n N_i(\xi_1, \xi_2) x_1^i, \\
 x_2^m &= \sum_{i=1}^n N_i(\xi_1, \xi_2) x_2^i, \\
 x_3^m &= \sum_{i=1}^n N_i(\xi_1, \xi_2) x_3^i
 \end{aligned} \tag{19}$$

in which n is the number of element nodes, N_i is the shape function for node i , and $\mathbf{x}^i = (x_1^i, x_2^i, x_3^i)$ are the coordinates of the master element nodes referred to as the g.r.s.

5. Thermoelectromechanical Conditions

The contact surfaces shown before must additionally transfer thermal and electrical potential fluxes.

The heat flux per unit area q defined between a contact pair has been assumed as

$$q = h(T^m, T^s, p_c)(T^m - T^s), \tag{20}$$

where the thermal conductivity h is dependent on the temperature T^i (with i equal to m , master, and s , slave) and the normal contact pressure p_c .

The electric flux density J has been defined as

$$J = h_c(T^{\text{avg}}, p_c)(\varphi^m - \varphi^s) = h_c \Delta\varphi \tag{21}$$

with $\Delta\varphi$ being the electric potential between master and slave surfaces and h_c the gap of electrical conductance or electrical conductivity in the contact zone, which is dependent on the average temperature in the contact zone $T^{\text{avg}} = T^m - T^s$ and on the normal pressure p_c .

By assuming that the effective contact area A_c can be represented as a circular area, the contact resistance R_c can be obtained following Yovanovich's resistance relation [3, 4] and considering that, in general, the contact size is much larger than the mean free path of electrons; correspondingly the contact resistance can be obtained as

$$R_c = \frac{\rho^m + \rho^s}{2D}, \tag{22}$$

where ρ^i is the resistivity of the contact surface i and D is the contact diameter. Experimental tests have been conducted on samples in aluminium alloy with assumed resistivity equal to $3.4 \cdot 10^{-8} \Omega\text{m}$ [27]. A thermoelectrical conductance due to the interstitial gas layers [16] has been here neglected.

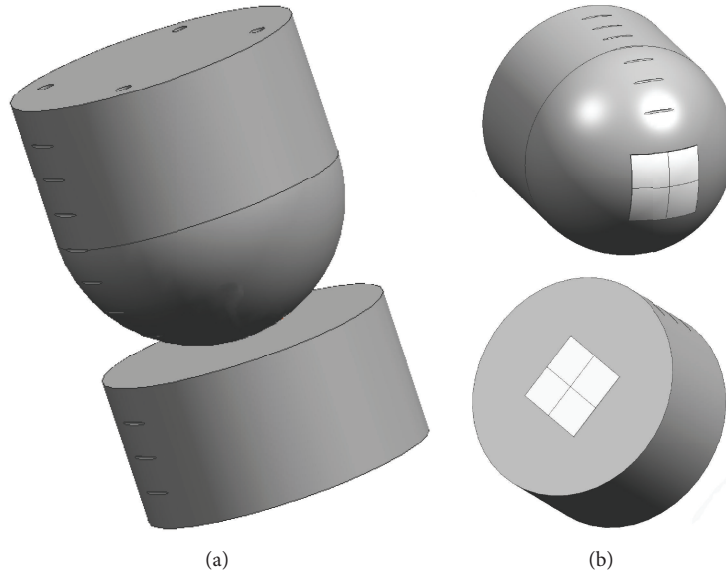


FIGURE 8: Sample of electrical contact (a); roughness surface test zone (b).

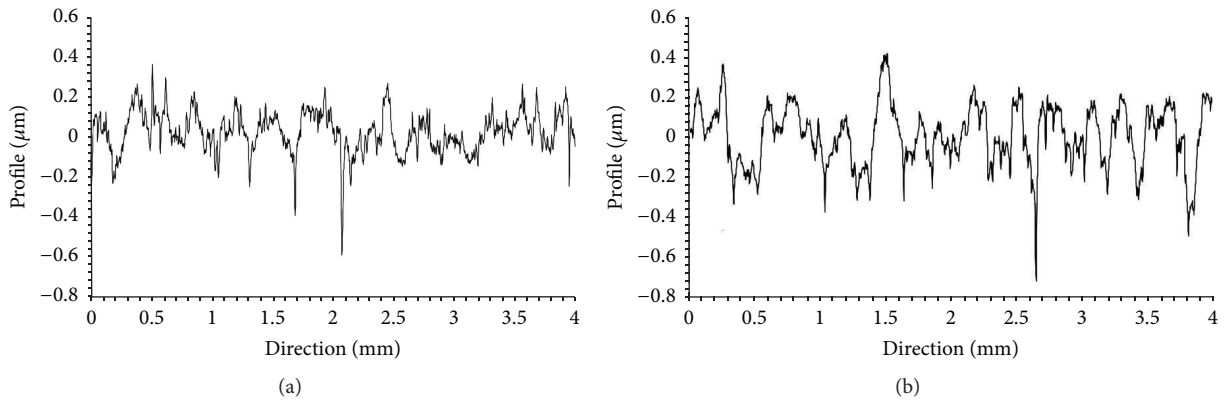


FIGURE 9: Typical roughness profiles in two different positions.

6. Roughness Tests

To evaluate the electrical resistance between two contact bodies under different compression load levels, experimental tests have been conducted with an aluminium cylinder and a hemisphere (Figure 8(a)). In this simplified case the apparent contact surface A_a remains circular and can be also analytically estimated. The effective contact area, that is, the zone where the thermoelectric connections are defined, is dependent on contact surface asperities; the surface roughness in the contact area has consequently been characterized.

For each contact surface of cylinders and hemispheres, 20 roughness profiles have been evaluated, in 20 different positions (the measurements have been taken in the neighbourhood of the contact zone between the cylinder and the hemisphere).

Profile lengths are equal to 4.0 mm considering a cut-off length of 0.8 mm. The sampling measures have been taken every $2 \mu\text{m}$.

Typical examples of roughness profiles evaluated in different positions of the sample are shown in Figure 9.

The RMS surface roughness σ_r in the contact zone has been defined as

$$\sigma_r = \frac{1}{2} \sqrt{\sigma_{r,1}^2 + \sigma_{r,2}^2}, \quad (23)$$

where $\sigma_{r,i}$ is the RMS value in the contact surface i . The RMS for the two contact surfaces has been obtained based on the roughness tests, reaching an average value of $\sigma_r = 0.105 \mu\text{m}$. The mean absolute asperity slope \bar{m} has been evaluated equal to 13%.

7. The Fractal Surface

The roughness parameters obtained via the roughness tests are dependent on the resolution of available measuring

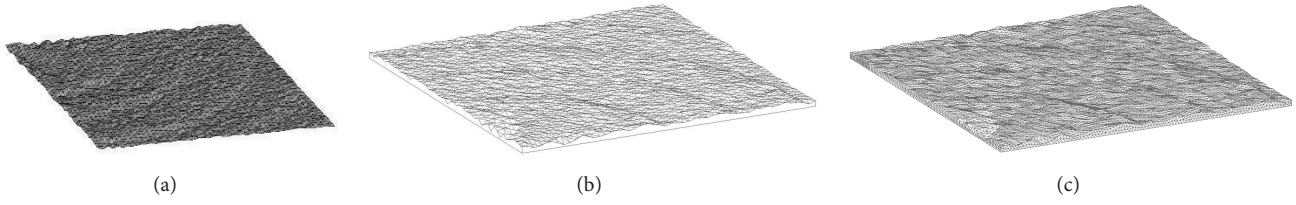


FIGURE 10: Example of a generated fractal surface (a); solid geometry (b); mesh of the numerical model (c).

instruments because of the multiscale character of the roughness and its nonstationary features. The fractal theory can be adopted [27] to evaluate the invariant roughness parameters for all scale levels.

At this purpose the numerical representations of the effective contact area have been conducted in agreement with the fractal approach. A micromechanical model has been developed to evaluate where the thermoelectrical connection

occurs, taking into account the material asperity in the contact surface.

So, starting from the theory of the fractal geometry, the topology description of the rough surface has been possible. The asperity height $z(x, y)$ in a plane (x, y) has been calculated with the modified Weierstrass-Mandelbrot (WM) function [16]

$$z(x, y) = L \left(\frac{G}{L} \right)^{D-2} \left(\frac{\ln \gamma}{M} \right)^{1/2} \sum_{m=1}^M \left\{ \sum_{n=0}^N \gamma^{n(D-3)} \left[\cos \varphi_{m,n} - \cos \left(\frac{2\pi \gamma^n (x^2 + y^2)^{0.5}}{L} \cos \left(\tan^{-1} \left(\frac{y}{x} \right) - \frac{\pi m}{M} \right) + \varphi_{m,n} \right) \right] \right\}, \quad (24)$$

where the mechanical characteristics are L , sample length, G , fractal roughness, D , fractal dimension; considering a two-dimensional surface, the limits of parameter D are $2 < D < 3$. D represents the extent of space occupied by the rough surface; γ is the scaling parameter (equal to 1.5); M is the number of superimposed ridges used in constructing the surface profile; n is a frequency index; and $\varphi_{m,n}$ is a random phase with interval $[0-2\pi]$.

The only unknown variables in (24) are G and D , which can be experimentally estimated.

7.1. Fractal Surface Generation. To define the fractal surface two different codes have been developed: the first written in C++ language is able to define the WM coefficients after reading different 1D roughness profiles experimentally obtained, with roughness surface tests at different positions in the same area of the analysed contact surface. This code evaluates the surface conditions with different parameters such as maximum and minimum height peak present in the profiles, average height of asperities, profile slope, and asperity density distribution.

These surface characteristics are necessary to obtain an equivalent fractal surface developed via a second code, written in Fortran 90, where the three-dimensional WM surface (Figure 10) is defined.

After adopting such a method for generating a fractal surface, a solid geometry has been then defined and afterwards a numerical model has been created (Figures 10(b) and 10(c)). The irregular surface has been meshed via a triangular discretization.

As shown in (24), the fractal surface can be defined provided that a “random phase” parameter, representative of an independent random variable, is known. Hence, a specific Fortran function has been called to generate randomly a phase parameter as shown in Box 1.

8. Mechanical Characteristics

An aluminium alloy has been tested. The mechanical characteristics in terms of elastic modulus E and yield stress have been obtained at room temperature via tensile tests. A thermal variation of such parameters has been accounted for in agreement with Eurocode 9 prescriptions [28]. When temperature increases, the elastic modulus and yield stress decrease (Figure 11(a)).

For the sake of simplicity, a bilinear temperature-dependent elastoplastic relation has been assumed for the numerical analyses (Figure 11(b)).

The hardness parameters have been experimentally defined by considering the Vickers measure; namely, a value $H_v = 315$ MPa at room temperature was obtained for the tested alloy.

9. Numerical Analyses

Two different models have been carried out in the following: a micromechanical model, to evaluate the effective contact area between two contact surfaces (and consequently upgrading

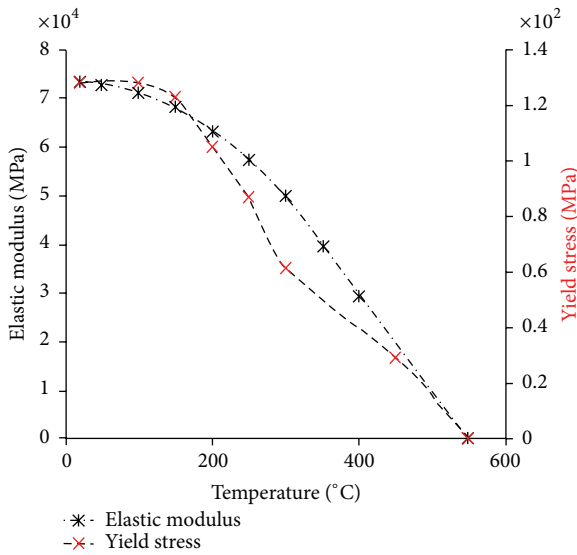
```

Real * 8 function randomPhase()
implicit none
real * 8      :: phi
real * 8, parameter :: pi = 3.141592653589793d0
call RANDOM_SEED()
call RANDOM_NUMBER(phi)
randomPhase = abs(2.d0 * pi * phi)

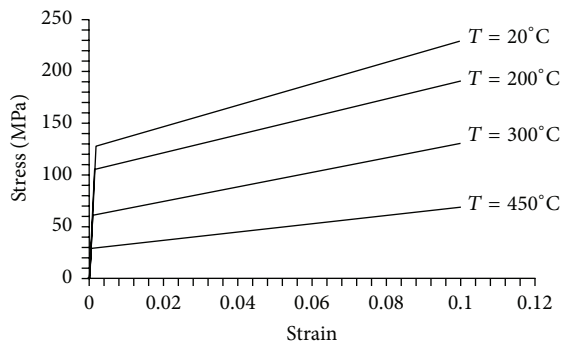
return
end function randomPhase

```

Box 1: Random phase function in Fortran 90.



(a)



(b)

FIGURE 11: Mechanical characteristics versus temperature (a); stress-strain relation at different temperatures (b).

the contact algorithm), and a global model where the thermoelectromechanical characteristics have been modified in agreement with the micromechanical results.

9.1. The Micromechanical Model. To evaluate the effective contact zone, where the real electrothermomechanical connections are established, fractal interfaces associated with the contact algorithm have been considered. In the real contact

surfaces the irregular asperities generate stress concentrations that can be estimated through the fractal surfaces themselves.

The WM equation used to generate the roughness surface considers a random phase parameter that allows the creation of different fractal surfaces with the same mechanical characteristics (derived by experimental tests). The contact surfaces used in the numerical models have been built by taking an average value of 10 different surfaces obtained via the WM equation to simulate the cylinder contact surface and 10 for the hemispheric one. The maximum in-plane extension of the fractal surface has been assumed $1.0 \times 1.0 \text{ mm}^2$ and the average asperity height is equal to about $0.2 \mu\text{m}$.

The independent variables G and D have been calculated by taking into account that maximum, minimum, and average asperity heights must be the same, when comparing fractal surfaces and experimental measurements.

The micro-model of the cylinder in contact with the hemisphere consists of 123610 nodes and 513833 tetrahedral elements; circular macro asperities have been created to simulate the effective contact surface, by means of surface preparation techniques.

During compression of the two electrical joint surfaces, the different asperity heights come into contact at different times and the effective contact area depends on the external load as shown in Figure 12.

Figures 12(b) and 12(c) show that contact occurs first in the circular macro asperities and, subsequently, contact involves the internal part of the surface. As shown in Figure 13(a), the joint stiffness increases when surface asperities enter into contact but stiffness decreases at higher temperatures. The relation in terms of contact stiffness, temperature, and gap function has been used to evaluate the mechanical penalty coefficient in the global model.

When two asperities are touching, the transferred mechanical stress rapidly increases above the yield stress (Figure 13(b)).

As already stated, when compression occurs, at the contact surface the effective contact area A_c changes with temperature, but as reported also in [27], the relation between the applied load and the effective contact area results to be linear, with decreasing slope at increasing temperatures (see Figure 14). At thermal melting point (about 550°C) the curve becomes almost horizontal.

If the effective contact area is equal to zero the two surfaces are not in contact and the contact resistance R_c is infinite. In agreement with (22), R_c decreases as A_c increases (Figure 15(a)).

As evidenced in Figure 14, by varying normal pressure and temperature, the effective contact area A_c changes, which allows obtaining R_c law in terms of pressure and temperature variations (Figure 15(b)).

Hence, the contact algorithm adopted in the macro scale model has been modified in light of the thermoelectromechanical relations coming from the micromechanical model just illustrated. In the global one, roughness contact surfaces have not been represented to reduce the computational cost, and the contact area itself gives the apparent contact area A_a related to the pair, once the effective contact area A_c

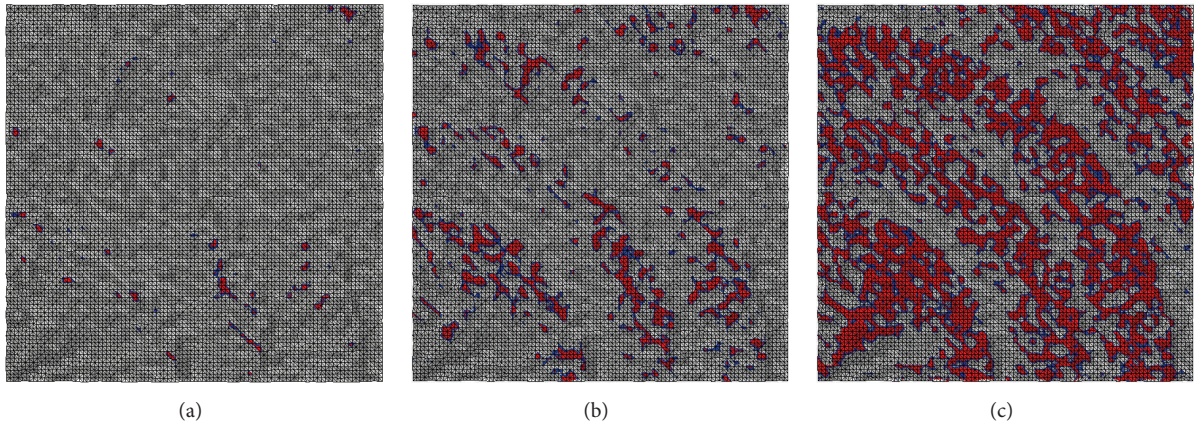


FIGURE 12: Effective contact surface at 79% of the applied load (a); at 89% of the applied load (b); at 100% of the applied load (c).

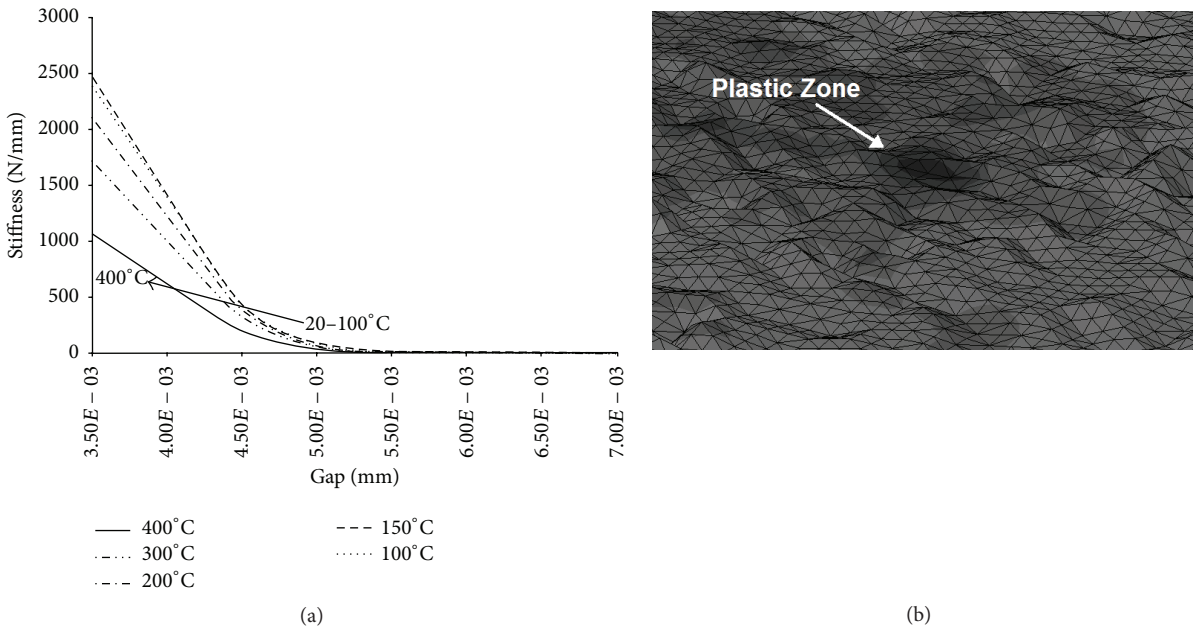


FIGURE 13: Contact stiffening at different temperatures (a); Von Mises stress during contact closure.

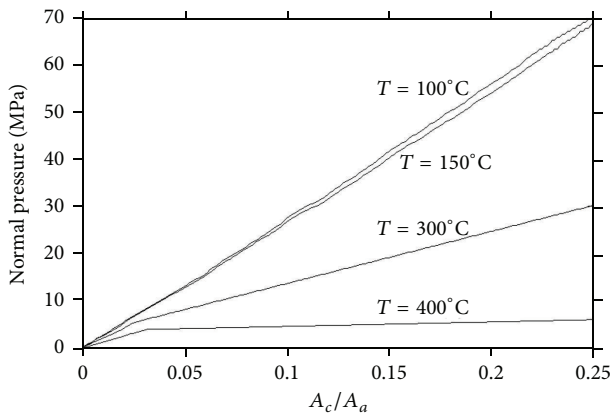


FIGURE 14: Normal pressure versus a -dimensional contact area.

is evaluated following the relationship shown in Figure 16. Consequently, the contact resistance R_c has been defined for each contact pair.

9.2. Global Model and Comparison of the Results. The global model has been carried out as illustrated in Guarnieri et al. [29], where a hemisphere and a cylinder are put in contact at different compressive load levels and different electrical potentials. These types of shapes ensure a closed solution for the analytical approach, because the resulting contact surface is always circular. The contact characteristics have been compared considering the analytical formulation and the previously described fractal characterization.

The schematic view of contact between the two surfaces is shown in Figure 8, where the maximum diameter for the

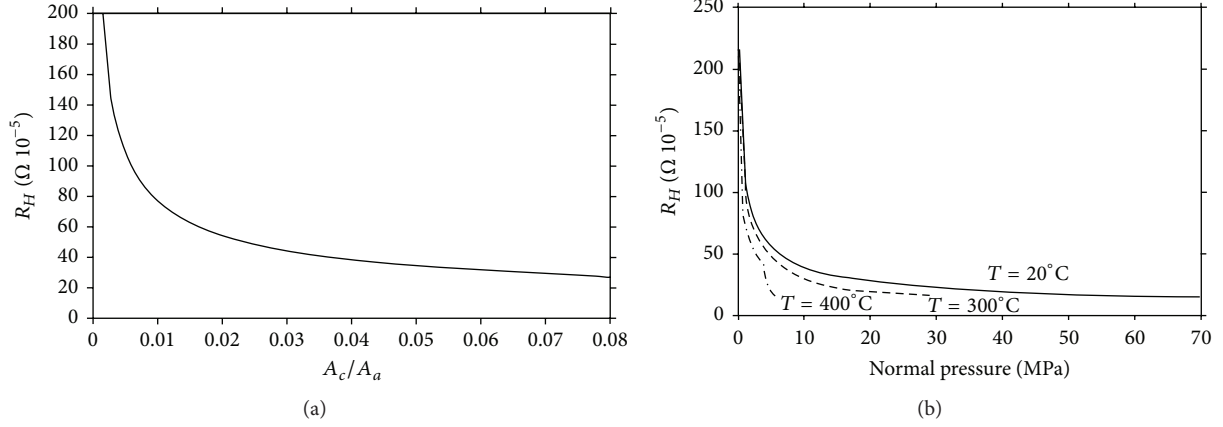


FIGURE 15: Contact resistance R_c versus a -dimensional contact area (a); R_c versus normal pressure (b).

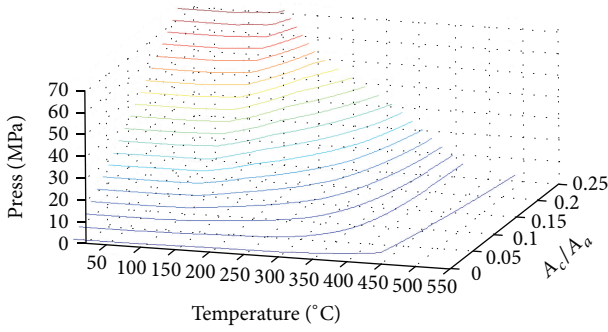


FIGURE 16: Relation between temperature, contact area, and normal pressure.

samples d is assumed to be equal to 90 mm and the material is conceived to behave thermoelastoplastically.

A current density $J = 1.0 \text{ A/mm}^2$ is applied to the hemisphere after the load application, at an initial temperature of 20°C .

The three-dimensional numerical model consists of 730000 tetrahedral elements (Figure 17(a)) and linear shape functions. Due to symmetry, only 1/4 of the geometry has been considered.

After the application of the compressive load, the sphere touches the cylinder in the contact zone and the contact pressure increases following the elastoplastic relationship. A permanent indentation occurs if the elastic field is exceeded as shown in Figure 17(b) [30].

The geometric configuration of the sample allowed for obtaining a circular apparent contact surface at different load levels (see Figure 18), which is proved in the following to correspond to that analytically evaluated [1].

In the contact algorithm the electrical conductance h_{ci} at the contact pair i has been obtained via the apparent contact area $A_{a,i}$ and the effective contact area $A_{c,i}$, based on Yovanovich's formulation [2, 4]

$$h_{ci} = 1.25k_c \frac{m}{\sigma} \left(\frac{A_{c,i}}{A_{a,i}} \right)^{0.95}, \quad (25)$$

where k_c is the average electrical conductance of the two bodies in contact

$$\frac{1}{k_c} = 2 \left(\frac{1}{k_{c,m}} + \frac{1}{k_{c,s}} \right). \quad (26)$$

A_{ci} has been calculated, via the micromechanical models, as a function of contact pressure and temperature. In the analytical and numerical models k_c has been assumed to be equal to $2.9 \times 10^4 \text{ S/mm}$. Similarly, the thermal conductance has been evaluated and the thermal conductivity h has been assumed to be equal to $0.237 \text{ W/(K}\cdot\text{mm)}$. This assumption allowed evaluating the variation of the electrical and the thermal conductance at different contact positions, under different contact pressures.

Analytical and numerical results have been compared by considering the contact surface at 20°C .

A comparison in terms of real contact area A_c and h_v is reported in Table 1 and in Figure 19.

As shown, the numerical and the analytic results for A_c are pretty similar at different load levels, which confirms that fractal surfaces are good to evaluate the real contact surface in these types of problems.

A slight discrepancy is encountered in the first load steps: such difference can be explained by the fact that the analytical method is based on a statistical approach and the correspondent results are averaged, whereas the fractal approach takes into account the effective contact area found through the micromechanical model during the overall compressive load histories; that is, the analytical method is not able to locally catch the real contact area at low load values. Indeed, the deviation between the results gradually decreases when the load increases, due to the fact that the contact spots defined by the fractal model are comparable to those obtained via the statistical approach. In fact, the resulting contact areas must finally coincide, getting closer to the real one.

According to the micromechanical model, the real contact area A_c is consequently a function dependent on load and temperature, $A_c = A_c(P, T)$. This allows evaluating the

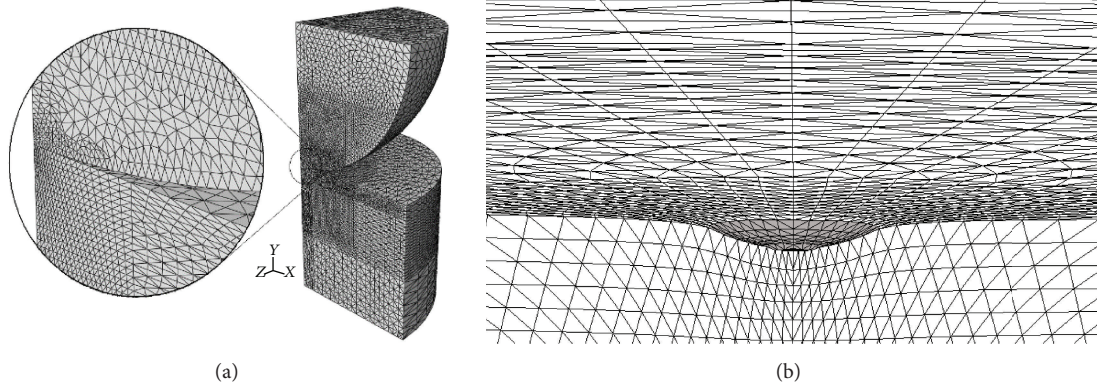


FIGURE 17: Three-dimensional model of the electric connector (a); sphere indentation (b).

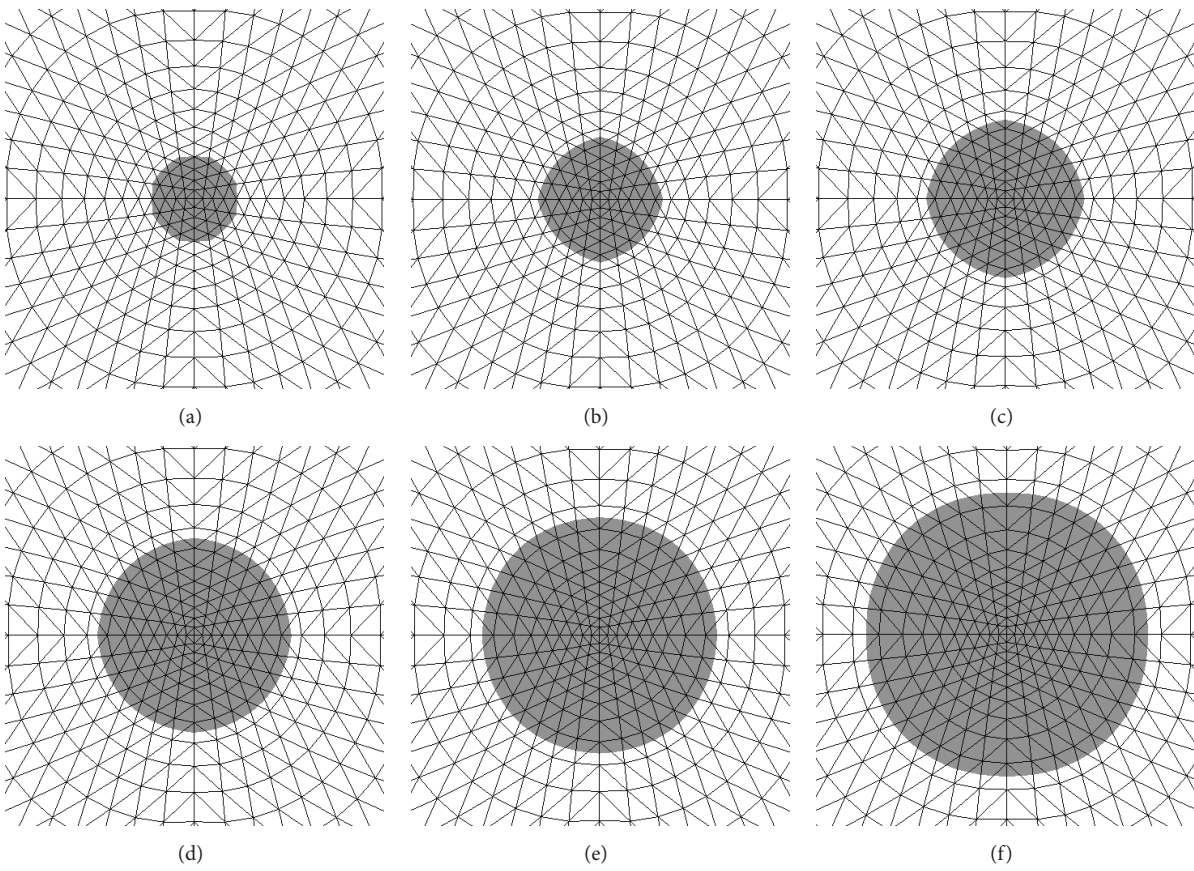


FIGURE 18: Apparent contact surface at different load levels (at room temperature $T = 20^\circ\text{C}$): 2% (a); 11.6% (b); 18.4% (c); 35% (d); 56% (e); 100% (f).

TABLE 1: Comparison between analytical and numerical results.

% load	A_a (mm ²)	$A_{c,\text{analytical}}$ (mm ²)	$A_{c,\text{fractal}}$ (mm ²)	P (MPa)	$h_{c,\text{analytical}}$ (S/mm ²)	$h_{c,\text{fractal}}$ (S/mm ²)
0.00E + 00	0.00E + 00	0.00E + 00	0.00E + 00	0.00E + 00	0.00E + 00	0.00E + 00
1.00E - 02	1.26E - 01	1.02E - 02	1.27E - 03	5.06E + 01	3.98E + 03	5.48E + 02
1.00E - 01	2.89E - 01	2.63E - 02	1.24E - 02	2.20E + 02	4.44E + 03	2.17E + 03
2.50E - 01	5.15E - 01	4.97E - 02	4.02E - 02	3.09E + 02	4.69E + 03	3.83E + 03
4.00E - 01	8.49E - 01	8.14E - 02	7.65E - 02	3.00E + 02	4.69E + 03	4.39E + 03
5.50E - 01	1.32E + 00	1.24E - 01	1.17E - 01	2.64E + 02	4.69E + 03	4.39E + 03
7.50E - 01	1.99E + 00	1.81E - 01	1.84E - 01	2.40E + 02	4.69E + 03	4.50E + 03
1.00E + 00	2.90E + 00	2.64E - 01	2.74E - 01	2.20E + 02	4.69E + 03	4.60E + 03

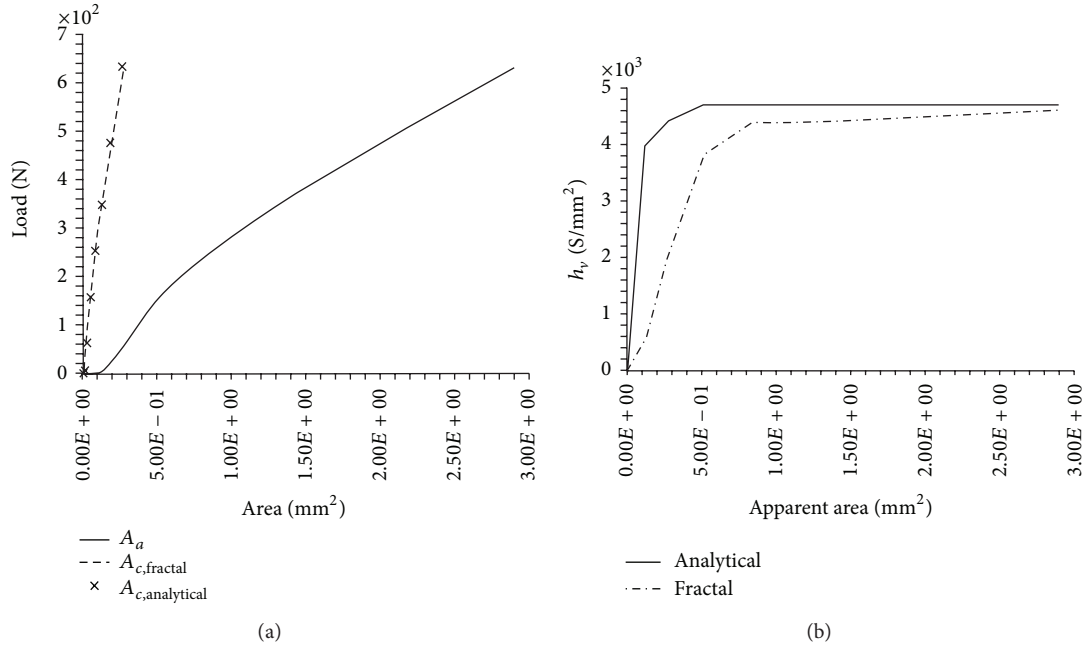


FIGURE 19: Apparent and real contact area at different load levels (20°C) (a); comparison between analytical and numerical electrical conductivities (b).

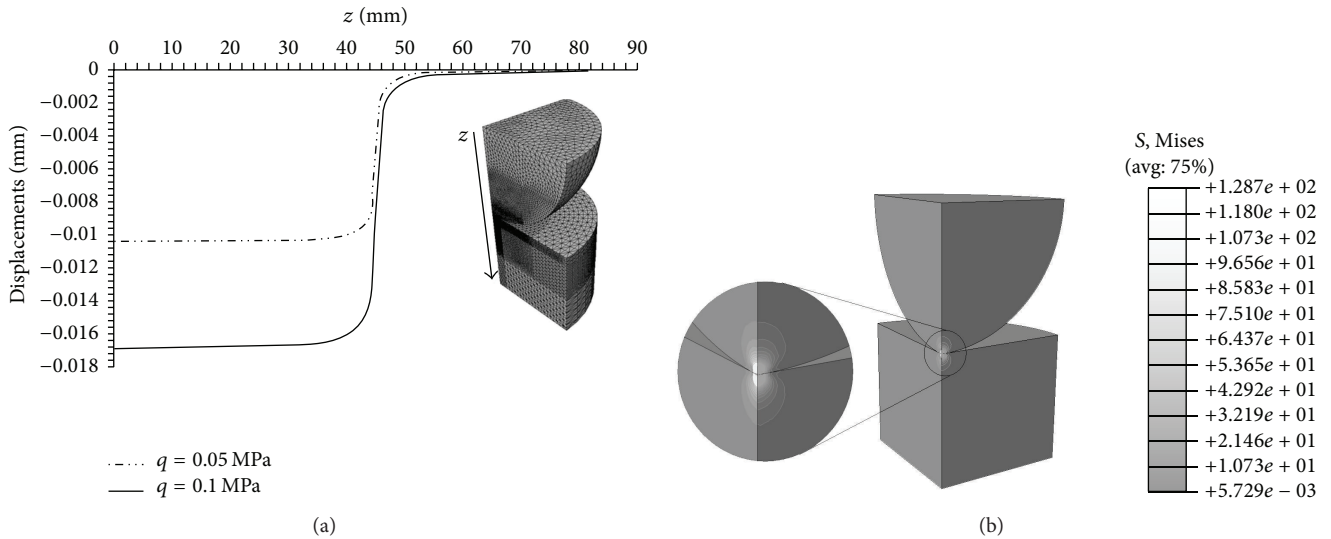


FIGURE 20: Vertical displacements versus position at different loads levels (a); Von Mises stress (b).

interaction between two bodies during an electrical connection, by taking into account the different thermal deformations at different positions of the contact zone during transient load scenarios.

The global model is also able to evaluate the displacement variations and the stress fields (Figures 20(a) and 20(b)) when an electrical current is applied at different compressive loads.

The contact discontinuity generates a sudden deviation in terms of electrical potential and temperature (Figure 21); when the contact area increases, at higher loads, the peak of

temperature and electrical potential decreases, being locally higher than the thermal and the electrical contact conductivities.

10. Conclusions

A three-dimensional coupled thermoelectromechanical model for electrical connectors has been here proposed to evaluate local stress and temperature distributions around the contact area of the connectors under different applied loads.

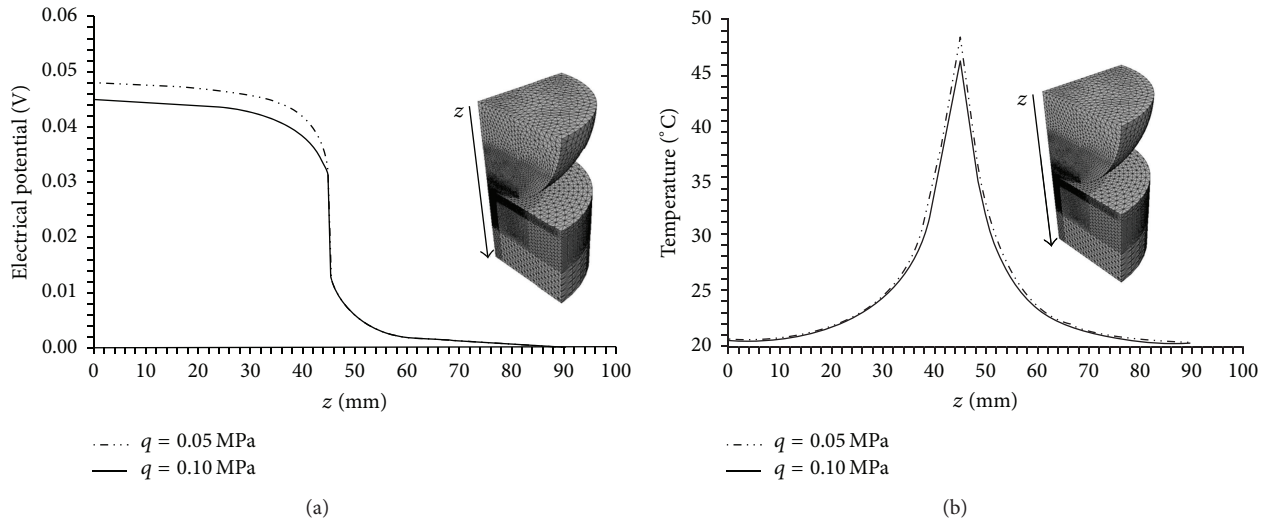


FIGURE 21: Comparison between electrical potential versus position at different loads levels (a); comparison between temperature versus position at different loads levels (b).

The electrical resistance arising in the contact area varies with the effective contact area A_c , where thermal and electrical contacts are established. It can be assumed that A_c depends on the surface roughness and the contact pressure.

A micromechanical numerical model has been developed by merging together the contact theory approach [5], which makes use of roughness parameters obtained from experimental measurements on real contact surfaces, with the topology description of the rough surface via the theory of fractal geometry. Particularly, the asperities variation has been evaluated via the Weierstrass-Mandelbrot function [16].

In this way the micromechanical model has allowed for obtaining an upgraded contact algorithm in terms of effective contact area A_c , as well as thermal and electrical contact conductivities, qualifying a small region of the total contact zone.

Such an algorithm has been subsequently implemented in a global model for performing transient thermoelectromechanical analyses without the need of simulating roughness asperities of contact surfaces, so reducing the computational costs.

A comparison between numerical and analytical results proved that the adopted procedure is suitable to simulate the transient thermoelectromechanical response of electric connectors.

Nomenclature

\mathbf{a}_i : Tangent vector along i direction
 A_a : Apparent contact area
 A_c : Effective/real contact area
 a_c : a -spot radius
 b : Contact point radius
 \mathbf{C} : Constitutive tensor
 c_i : Material parameters ($i = 1, 2$)
 d : Sample diameter
 D : Fractal dimension

d_{\max} : Maximum mean distance between two bodies
 d_v : Mean indentation diagonal
 \mathbf{E} : Total logarithmic strain
 \mathbf{E}^E : Electrical potential gradient
 \mathbf{E}^e : Elastic logarithmic strain
 \mathbf{E}^T : Thermal logarithmic strain
 g : Gap function
 G : Fractal roughness
 g_n : Gap function along normal direction
 h : Thermal conductivity
 h_c : Electrical contact conductance
 H_c : Contact microhardness
 H_v : Vickers microhardness
 J : Current density
 \mathbf{J} : Electrical current density
 \mathbf{k}_{ij} : Stiffness matrix parameters
 k_n : Penalty coefficient
 L : Sample length
 m : Mean asperity slope
 M : Number of superimposed ridges used in constructing the surface profile
 \mathbf{n} : Normal vector
 N_i : Shape function
 n_c : Numbers of a -spots
 P : Compressive load
 p_c : Contact pressure
 P_E : Dissipated energy
 q : Heat flux per unit area
 r : Heat energy release
 r_c : Internal volumetric current source
 R_c : Contact resistance
 T : Temperature
 \mathbf{T} : Stress tensor
 \mathbf{t} : Contact stress vector
 \mathbf{u} : Displacement vector
 \mathbf{x} : Position vector in actual configuration

\mathbf{X} : Position vector in reference configuration
 Y : Mean plane distance
 z : Asperity height
 γ : Scaling parameter
 Γ : Surface area
 η : Energy conversion factor
 ξ_i : Curvilinear coordinates
 ρ : Resistivity in the contact surface
 σ_g : Gap electrical conductance
 σ_r : RMS (root mean square)
 σ^E : Electrical conductivity matrix
 φ : Electrical potential gradient
 \emptyset : Random phase
 Ω : Volume.

Competing Interests

The authors declare that they have no competing interests.

References

- [1] R. Holm, *Electric Contacts—Theory and Application*, Springer, New York, NY, USA, 2000.
- [2] F. H. Milanez, M. M. Yovanovich, and J. R. Culham, “Effect of surface asperity truncation on thermal contact conductance,” *IEEE Transactions on Components and Packaging Technologies*, vol. 26, no. 1, pp. 48–54, 2003.
- [3] S. Song and M. Yovanovich, “Explicit relative contact pressure expression—dependence upon surface roughness parameters and Vickers microhardness coefficients,” in *Proceedings of the 25th AIAA Aerospace Sciences Meeting*, Reno, Nev, USA, 1987.
- [4] S. Song and M. M. Yovanovich, “Relative contact pressure: dependence on surface roughness and Vickers microhardness,” *Journal of Thermophysics and Heat Transfer*, vol. 2, no. 1, pp. 43–47, 1988.
- [5] P. Wriggers, *Computational Contact Mechanics*, Springer, Berlin, Germany, 2006.
- [6] D. P. Boso, G. Zavarise, and B. A. Schrefler, “A formulation for electrostatic-mechanical contact and its numerical solution,” *International Journal for Numerical Methods in Engineering*, vol. 64, no. 3, pp. 382–400, 2005.
- [7] F. Moro, P. Alotto, F. Freschi, and M. Guarnieri, “A cell method formulation of 3-D electrothermomechanical contact problems with mortar discretization,” *IEEE Transactions on Magnetics*, vol. 48, no. 2, pp. 503–506, 2012.
- [8] F. Greco and R. Luciano, “A theoretical and numerical stability analysis for composite micro-structures by using homogenization theory,” *Composites Part B: Engineering*, vol. 42, no. 3, pp. 382–401, 2011.
- [9] R. Barretta, R. Luciano, and F. M. de Sciarra, “A fully gradient model for Euler-Bernoulli nanobeams,” *Mathematical Problems in Engineering*, vol. 2015, Article ID 495095, 8 pages, 2015.
- [10] A. Apuzzo, R. Barretta, and R. Luciano, “Some analytical solutions of functionally graded Kirchhoff plates,” *Composites Part B: Engineering*, vol. 68, pp. 266–269, 2015.
- [11] R. Barretta and R. Luciano, “Analogies between Kirchhoff plates and functionally graded Saint-Venant beams under torsion,” *Continuum Mechanics and Thermodynamics*, vol. 27, no. 3, pp. 499–505, 2015.
- [12] R. Barretta, L. Feo, and R. Luciano, “Torsion of functionally graded nonlocal viscoelastic circular nanobeams,” *Composites Part B: Engineering*, vol. 72, pp. 217–222, 2015.
- [13] R. Barretta, L. Feo, R. Luciano, and F. Marotti de Sciarra, “An Eringen-like model for Timoshenko nanobeams,” *Composite Structures*, vol. 139, pp. 104–110, 2016.
- [14] R. Barretta, L. Feo, and R. Luciano, “Some closed-form solutions of functionally graded beams undergoing nonuniform torsion,” *Composite Structures*, vol. 123, pp. 132–136, 2015.
- [15] L. Kogut and K. Komvopoulos, “Electrical contact resistance theory for conductive rough surfaces,” *Journal of Applied Physics*, vol. 94, no. 5, pp. 3153–3162, 2003.
- [16] W. Yan and K. Komvopoulos, “Contact analysis of elastic-plastic fractal surfaces,” *Journal of Applied Physics*, vol. 84, no. 7, pp. 3617–3624, 1998.
- [17] M. Guarnieri, C. Majorana, G. Mazzucco, and F. Moro, “Numerical simulation and experimental validation of a coupled mechanical-thermal-electrical contact model,” in *Proceedings of the 14th Biennial IEEE Conference on Electromagnetic Field Computation (CEFC ’10)*, 1 pages, Chicago, Ill, USA, May 2010.
- [18] A. M. Tarantino, “Asymmetric equilibrium configurations of hyperelastic cylindrical bodies under symmetric dead loads,” *Quarterly of Applied Mathematics*, vol. 64, no. 4, pp. 605–615, 2006.
- [19] A. M. Tarantino, “Homogeneous equilibrium configurations of a hyperelastic compressible cube under equitriaxial dead-load tractions,” *Journal of Elasticity*, vol. 92, no. 3, pp. 227–254, 2008.
- [20] L. Lanzoni and A. M. Tarantino, “Equilibrium configurations and stability of a damaged body under uniaxial tractions,” *Zeitschrift für Angewandte Mathematik und Physik*, vol. 66, no. 1, pp. 171–190, 2015.
- [21] A. M. Tarantino, “The singular wedge problem in the nonlinear elastostatic plane stress theory,” *Quarterly of Applied Mathematics*, vol. 57, no. 3, pp. 433–451, 1999.
- [22] A. M. Tarantino, “The singular equilibrium field at the notch-tip of a compressible material in finite elastostatics,” *Zeitschrift für Angewandte Mathematik und Physik*, vol. 48, no. 3, pp. 370–388, 1997.
- [23] A. M. Tarantino, “On extreme thinning at the notch tip of a neo-Hookean sheet,” *The Quarterly Journal of Mechanics and Applied Mathematics*, vol. 51, no. 2, pp. 179–190, 1998.
- [24] A. M. Tarantino and A. Nobili, “Finite homogeneous deformations of symmetrically loaded compressible membranes,” *Zeitschrift für Angewandte Mathematik und Physik*, vol. 58, no. 4, pp. 659–678, 2007.
- [25] P. G. Slade, *Electric Contacts: Principles and Applications*, Marcel Dekker, New York, NY, USA, 1999.
- [26] G. Mazzucco, V. A. Salomoni, and C. E. Majorana, “Three-dimensional contact-damage coupled modelling of FRP reinforcements—simulation of delamination and long-term processes,” *Computers and Structures*, vol. 110–111, pp. 15–31, 2012.
- [27] M. Braunovic, N. K. Myshkin, and V. V. Konchits, *Electrical Contacts: Fundamentals, Applications and Technology*, CRC Press, Boca Raton, Fla, USA, 2007.
- [28] EN 1999 Eurocode 9, “Design of aluminium structures—part 1-2: general—structural fire design,” 2001.
- [29] M. Guarnieri, C. E. Majorana, G. Mazzucco, and F. Moro, “Coupled mechanical-electrical-thermal modeling of electric

contacts based on the cell method,” in *Proceedings of the COMPUMAG Conference*, Florianopolis, Brazil, November 2009.

- [30] Z. Song and K. Komvopoulos, “Elastic-plastic spherical indentation: deformation regimes, evolution of plasticity, and hardening effect,” *Mechanics of Materials*, vol. 61, pp. 91–100, 2013.

Research Article

Fire Spalling Prevention via Polypropylene Fibres: A Meso- and Macroscale Approach

G. Mazzucco and G. Xotta

*Department of Civil, Environmental and Architectural Engineering (DICEA), University of Padova,
Via F. Marzolo 9, 35131 Padova, Italy*

Correspondence should be addressed to G. Xotta; giovanna.xotta@dicea.unipd.it

Received 26 December 2015; Accepted 19 July 2016

Academic Editor: Julius Kaplunov

Copyright © 2016 G. Mazzucco and G. Xotta. This is an open access article distributed under the Creative Commons Attribution License, which permits unrestricted use, distribution, and reproduction in any medium, provided the original work is properly cited.

A deep understanding of concrete at the mesoscale level is essential for a better comprehension of several concrete phenomena, such as creep, damage, and spalling. The latter one specifically corresponds to the separation of pieces of concrete from the surface of a structural element when it is exposed to high and rapidly rising temperatures; for this phenomenon a mesoscopic approach is fundamental since aggregates performance and their thermal properties play a crucial role. To reduce the risk of spalling of a concrete material under fire condition, the inclusion of a low dosage of polypropylene fibres in the mix design of concrete is largely recognized. PP fibres in fact evaporate above certain temperatures, thus increasing the porosity and reducing the internal pressure in the material by an increase of the voids connectivity in the cement paste. In this work, the contribution of polypropylene fibres on concrete behaviour, if subjected to elevated thermal ranges, has been numerically investigated thanks to a coupled hygrothermomechanical finite element formulation. Numerical analyses at the macro- and mesoscale levels have been performed.

1. Introduction

In the last three decades, catastrophic fire events in concrete tunnels (such as the Danish Great Belt one, the Channel Tunnel, Mont Blanc, and Tauern tunnels) led to the development of new fire protection systems to increase the safety of the people as well as the strength of concrete structures under high temperatures.

One of the principal problems in concrete under fire exposure is spalling, corresponding to the ablation of concrete segments until collapse of the structure, when exposed to high and rapidly rising temperatures. This phenomenon is influenced by many factors but can be explained by taking into account two main contributions: a thermal stress, generated by a thermal gradient between the heated surface and the internal concrete zone, and the pore pressure increments in concrete that occurs when the internal water evaporates [1].

In order to prevent spalling, when concrete structures are subjected to elevated temperatures, the role of polypropylene

(PP) fibres into concrete mix design is largely recognized. These fibres are anisotropic monofilaments (diameter $d = 10 \div 100 \mu\text{m}$ and length $l = 3 \div 20 \text{mm}$) that are not able to increase the material stiffness, but under high temperatures the explosive spalling risk decreases if the volume content in the mix design is between 1 and 3 kg/m^3 of concrete.

Studies have proved that PP fibres reduce pore pressure into the cement paste, so decreasing the risk of explosive spalling. In fact, the fibres are in a solid state at room temperature but when it increases the state changes; melting phase starts at about 165°C and over 325°C the fibres vaporize and the connected voids channels increase the permeability and diffusivity [1, 2] into concrete. PP evaporation process terminates when temperature is over 475°C .

In this work, the complex mechanism of polypropylene contribution on concrete behaviour under thermal conditions will be numerically investigated through a 3D thermohygro-mechanical finite element code [3, 4], appropriately updated to take into account the effect of the polypropylene fibres if they are added in the mix

design [5]. Innovative concrete systems are investigated in [6, 7].

Numerical analyses at the macro- and mesoscale levels have been performed and validated considering experimental tests by literature. Recent theoretical and computational advances about composite structures also at nanoscale can be found in [8, 9].

To simulate spalling phenomenon, it is not possible to use a linear constitutive law of the material, as concrete has a brittle behaviour; numerically, the softening branch of the material can be described through several theories such as the fracture [10, 11] and damage [12, 13]. In this work, Mazars' damage law [14] with nonlocal correction has been adopted.

A mesoscopic approach has a remarkable importance for understanding specific concrete phenomena, such as spalling. Indeed, this representation is able to determine the effects of internal hyperstaticity due to the different mechanical characteristics, triggering stress concentrations that can lead to damage.

2. Concrete as a Multiphase Material

Although traditional engineering studies consider concrete as a homogeneous material, idealized as a continuum medium with average properties (macroscopic approach), concrete is a highly heterogeneous material and its composite behaviour is exceedingly complex.

On a macroscopic approach, most of the works proposed in literature assume phenomenological relationships based on macroscopic observations; even if this approach implies a series of simplifications, using continuum-type constitutive models, a satisfactory description of the basic features of the mechanical behaviour of concrete has been reached. Anyway, to obtain a deeper understanding of the macroscopic constitutive behaviour of concrete, it is necessary to adopt a lower scale of observation, that is, mesoscale.

A mesoscale approach will provide a more realistic description of concrete than the macroscale, influenced by the geometry and the properties of its multiple constituents. This could be expected, since the observed macroscopic behaviour is a direct consequence of the phenomena, which take place at the level of the material heterogeneities.

At this level, concrete becomes a mixture of cement paste with aggregates inclusions of various sizes. Aggregates generally occupy 60–80% of the volume of concrete and greatly influence its properties, mix proportion, and economy. Aggregates can be divided into two distinct categories: fine (often called sand) and coarse aggregates; the latter represents around 40–50% of concrete volume. However concrete is not just a two-phase composite; it has been found that the presence of grains in the cement paste causes a thin layer of matrix material surrounding each inclusion to be more porous than the bulk of the surrounding cement paste matrix. This layer is named interfacial transition zone (ITZ) and has relevant effects on the properties of concrete, being likely to act as the “weak link in the chain” when compared to the bulk cement paste and the aggregate particles [15, 16].

For the numerical simulations at the mesoscale mesoscopic continuum models have been adopted; each single composite constituent itself has been approached as a multiphase material, fully described and characterized via a coupled thermohygro-mechanical model.

Coarse aggregates have been simplified assuming spherical shapes, in order to eliminate possible stress concentrations generated by the angularities; they are distributed randomly in the concrete sample and have an elastic behaviour (they do not creep and do not damage).

The mortar matrix, comprehensive of the cement paste and of the fine aggregates, and the ITZ, whose thickness is strictly related to the diameter of each aggregate, are homogeneous materials; they can be subjected to creep and damage.

Finally PP fibres, having a size on the order of micrometer, are not explicitly represented in the mesoscale approach; their presence and effect have been taken into consideration updating the concrete formulation as explained in the subsequent section.

3. Theoretical Background

Concrete is considered as a multiphase system where the voids of the skeleton are partly filled with liquid and partly with a gas phase. The liquid phase consists of bound water and capillary water, while the gas phase, that is, moist air, is a mixture of dry air and water vapor and it is assumed to behave as an ideal gas.

When higher than standard temperatures are taken into account, several phenomena are considered within the code, dealing with concrete as a porous medium: heat conduction, vapor diffusion, and liquid water flow in the voids.

As regards the mechanical field, the model couples shrink, creep, and damage within the constitutive law of the material. For details, please refer to [17, 18].

In order to take into account the effect of PP fibres, concrete porosity formulation has been enriched and the micro-cracking that appears after PP fibres vaporization around the void channels has been considered [5].

3.1. PP Fibres Effect on Concrete Porosity. Total porosity at different temperatures and different dosages of fibres can be expressed as [5]

$$n = n_c + n_m + n_M + n_{a,ITZ} + n_{f,ITZ} + n_{relax} + n_{air} + n_f + n_{crack}, \quad (1)$$

where the capillary porosity n_c and the micro- and macroporosities n_m and n_M terms depend only on the mix design, while the rest of the equation is related to the PP fibres effect at different temperatures. Specifically, the porosity terms dependent on fibres mean the following: $n_{a,ITZ}$ is related to aggregates ITZ connected by fibres; $n_{f,ITZ}$ is due to ITZ formation around fibres; n_{relax} is related to voids variation due to PP fibres relaxation; n_{air} takes into account micro air bubbles connection and consequent porosity increment; n_f considers void channels formation, at high temperatures,

after fibres evaporation; and finally n_{crack} is the porosity increment to the microthermal cracks.

Applying this porosity formulation to the hygrothermo-mechanical FE code, the hydraulic diffusivity C will vary accordingly.

Following Bazant's formulation [19], C is so expressed:

$$C_1(T) = C_0 \left[0.3 + \left(\frac{13}{t_e} \right)^{0.5} \right] \frac{T}{T_0} \cdot e^{(Q/RT_0 - Q/RT)} \left[\alpha_0 + \frac{1 - \alpha_0}{1 + ((1 - h) / (1 - h_c))^{n_h}} \right], \quad (2)$$

where C_0 is the diffusivity part, dependent on the physics characteristics related to the w/c ratio.

The PP fibres employed in the concrete material at elevated temperatures, increasing the porosity and the connections between the material voids and not affecting the chemical reactions in the matrix, can be taken into account modifying only the term C_0 :

$$C_0(n) = \gamma \exp^{(\beta n)}, \quad (3)$$

where γ and β are constitutive parameters.

3.2. Microcracking Related to PP Fibres. An aspect that has to be considered, when determining the concrete diffusivity containing PP fibres, is the microcracking that appears around the void channels once the fibres evaporate [20]. The cracks, being a mechanical response of the cement paste due to a local stiffness variation, cause a void increment, so reducing the internal concrete pressure after the peak and causing a variation in hydraulic diffusivity.

For the determination of the microthermal cracks, a formulation that considers a damage variable dependent only on temperature has been developed [21]:

$$d_{mc} = \begin{cases} 0 & \text{if } T \leq T_m, \\ 1 - \frac{\alpha(\Delta T)}{\alpha_0} & \text{if } T_m < T \leq T_M, \\ 1 & \text{if } T > T_M, \end{cases} \quad (4)$$

where T_m and T_M are the minimum and maximum temperatures when microcracks occur and α_0 is the initial thermal expansion. The $\alpha(\Delta T)$ term is the linear variation of the thermal expansion during heating and $\Delta T = T - T_m$ is the thermal variation when microcrack takes place:

$$\alpha(\Delta T) = \alpha_0 (1 - h_\alpha \Delta T), \quad (5)$$

where h_α is the tangent modulus of the damaged curve $h_\alpha = 1/(T_M - T_m)$.

The hygrometric diffusivity C_0 has been modified to take into account the microcrack contribution as follows:

$$C_{0,mc} = C_0 + \Delta C_{0,mc} = C_0 + d_{mc} C_{mc}, \quad (6)$$

where C_{mc} can be found experimentally.

3.3. Visco-Elasto-Damaged Formulation. The skeleton of the concrete material has been represented as a viscoelastic material coupled with Mazars' damage formulation [3].

Following a FE formulation the stress-strain relation can be so expressed:

$$\boldsymbol{\sigma}(t) = (1 - d) \int_0^t \mathbf{B}^{-1} R(t, t') d\boldsymbol{\varepsilon}(t'), \quad (7)$$

where t is the analysis time, t' is the relaxation time, $\boldsymbol{\sigma}$, $\boldsymbol{\varepsilon}$ are the stress and strain tensors, respectively, d is the scalar damage parameter, \mathbf{B} is the derivative shape function operator, and R is the relaxation function, dual to the compliance or creep function, in accordance with the Maxwell-Chain model:

$$R(t, t') = \sum_{\mu=1}^N E_\mu e^{[\gamma(t') - \gamma(t)]}, \quad (8)$$

where E_μ represents the μ th elastic modulus of the Maxwell unit and γ is the reduction time parameter.

The damage variable d is evaluated following Mazars' formulation [14], where the load function is assumed as follows:

$$f = \varepsilon_{\text{eq}} - k, \quad (9)$$

where k is an internal variable $k(t) = \max[\varepsilon_{\text{eq}}(t)]$ and ε_{eq} is the equivalent strain:

$$\varepsilon_{\text{eq}} = \sqrt{\langle \boldsymbol{\varepsilon} \rangle : \langle \boldsymbol{\varepsilon} \rangle}. \quad (10)$$

The damage law is an exponential function, subdivided in a compression and in a traction part:

$$d = \alpha_t d_t + \alpha_c d_c = \alpha_t \left\{ 1 - \frac{(1 - A_t) k_0}{\varepsilon_{\text{eq}}} - A_t e^{[-B_t(\varepsilon_{\text{eq}} - k_0)]} \right\} + \alpha_c \left\{ 1 - \frac{(1 - A_c) k_0}{\varepsilon_{\text{eq}}} - A_c e^{[-B_c(\varepsilon_{\text{eq}} - k_0)]} \right\}, \quad (11)$$

where A_i , B_i (with $i = c, t$), and k_0 are the material parameters; α_i are the coupled coefficients.

4. Numerical Models

4.1. 3D Numerical Analyses at the Macro- and Mesolevel without PP Fibres Inclusions. Before investigating the effect of polypropylene fibres, the behaviour of a base cell of concrete, without addition of PP fibres, modelled at the macro- and mesolevel and subjected only to a heating rate has been presented in this subsection.

A representation of the concrete at the mesolevel will allow us to determine the effects of internal hyperstaticities due to the different characteristics of the individual phases, which are due to concentrations of stresses and strains during the heating process of the material and that can lead to

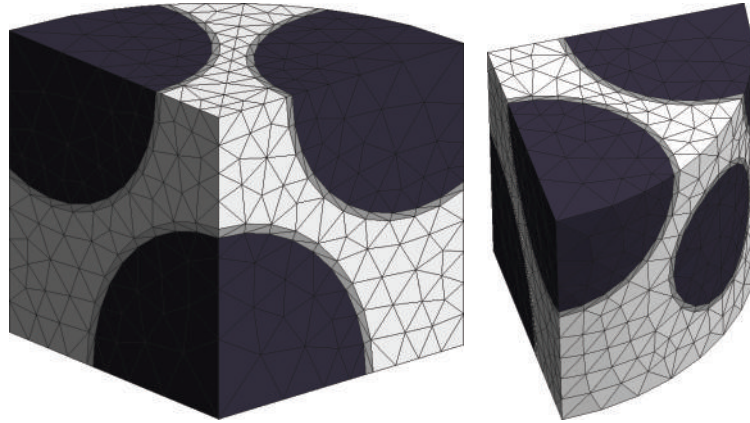


FIGURE 1: Base cell at the mesolevel.

a mechanical damage. Such concentrations are not visible by using macroscopic models.

Details of the cell adopted in the analyses are visible in Figure 1; symmetry conditions have been assumed to simplify the numerical model.

A cylindrical cell of radius equal to 10 mm has been considered. As regards the cell at the mesolevel, it contains approximately a 40% of coarse aggregates with an average diameter equal to 1.2 cm, assumed spherical in order to eliminate any possible stress concentration due to angularities, and a thin layer of ITZ whose thickness is closely related to the diameter of the inclusions. The discretization adopted here consists of 1402 nodes and 6708 linear tetrahedral elements.

The hygrothermomechanical properties of the various components have been properly assumed based on literature data as follows.

Material Parameters

Matrix

- E [MPa]: (2.5000e + 04) elastic modulus.
- ν : (2.0000e - 01) Poisson's coefficient.
- ρ [T/mm³]: (2.7000e - 09) material density.
- k [W/(mm°C)]: (1.3700e - 03) thermal conductivity.
- c [J/(T°C)]: (8.8000e + 05) specific heat.
- α_0 : (2.5000e - 02) coeff. Bazant formulation.
- n_{Diff} : (6.0000e + 00) exponent in diffusivity equation (Bazant formulation).
- C_0 : (1.1350e - 01) initial diffusivity.
- T_0 [°C]: (2.0000e + 01) room temperature.
- Age [day]: (9.5000e + 01) concrete age.
- n_0 : (7.5000e - 02) initial porosity in the concrete.
- d_a : (2.0000e + 00) aggregate diameter (average).

Aggregates

- E [MPa]: (6.0000e + 04) elastic modulus.

ν : (1.5000e - 01) Poisson's coefficient.

ρ [T/mm³]: (1.8000e - 09) material density.

k [W/(mm°C)]: (1.3700e - 03) thermal conductivity.

c [J/(T°C)]: (8.8000e + 05) specific heat.

In the performed analysis, the sample was subjected to a linear thermal ramp applied on the outer surface, which starts from a room temperature of 20°C, up to 300°C in 1000 sec, and then is kept constant.

Mechanical damage triggering for the macro- and mesoscale models is shown in Figure 2.

As can be noted, while at the macroscale damage interests at the beginning the external ring and then enters in the sample, at the mesolevel its evolution is driven by aggregates distribution and ITZ. Indeed, damage initially triggers within ITZ (being the weakest zone due to its properties), and then it will spread inside this layer and finally will involve the cement paste. Damage concentrations are located where the distance between two different aggregates are minimal and the stress concentrations are maximal.

In the next section, a model including fibres will be presented and damage evolution comparisons will be discussed.

4.2. Numerical Analyses Considering the Effect of PP Fibres

4.2.1. Macroscopic Numerical Models. At first, the numerical model has been validated at the macroscale level referring to the experimental tests of Phan [22], where a concrete sample of size 100 × 100 × 200 mm has been heated with a thermal ramp of 5°C/min, reaching a maximum temperature of 600°C. The concrete sample has been coated with insulating material on all sides except the face that will be subjected to heating, to reproduce the behaviour that would have a wall if subjected to a fire. A dosage of 1.5 kg/m³ of PP fibres has been added to the mix design (fibres length equal to 13 mm, with a diameter of 0.1 mm).

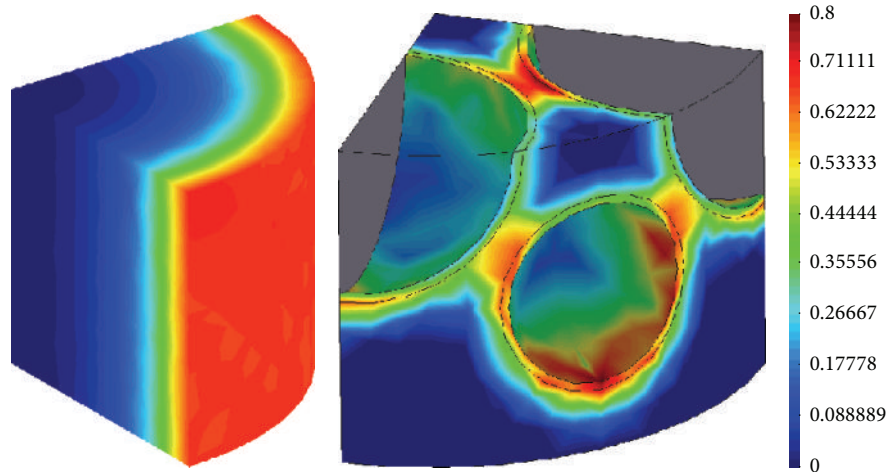


FIGURE 2: Damage triggering at the macro- and mesoscale level.

Materials parameters for concrete and PP fibres are summarized as follows.

Properties of Concrete and PP Fibres

Concrete

E [MPa]: $(4.0000e + 04)$ elastic modulus.
 ν : $(2.0000e - 01)$ Poisson's coefficient.
 ρ [T/mm^3]: $(2.4000e - 09)$ material density.
 k [$W/(\text{mm}^\circ\text{C})$]: $(1.3700e - 03)$ thermal conductivity.
 c [$J/(T^\circ\text{C})$]: $(8.8000e + 05)$ specific heat.
 T_0 [$^\circ\text{C}$]: $(2.0000e + 01)$ room temperature.
 Age [day]: $(2.8000e + 01)$ concrete age.

PP Fibres

V [mm^3]: $(1585.6237e + 03)$ volume.
 d [mm]: $(1.0000e - 01)$ mean diameter.
 L [mm]: $(1.3000e + 01)$ mean length.
 ITZ [mm]: $(1.7000e - 02)$ ITZ thickness.
 B : $(1.0000e - 03)$ relaxation coefficient of PP fibres.

The specimen did not show spalling phenomenon. Pore pressure data, measured at 25 and 50 mm from the heated surface, were collected; the temperature was also measured, in addition to the data of the heated surface and the temperature of the furnace.

The results reported in Figure 3 show a good agreement between the experimental and numerical results in terms of pore pressure as a function of time at a distance of 25 mm from the heat source. An abrupt drop of the pressure after the peak can be noticed, due to the fusion of the fibres and to microcracking, which increase the porosity and consequently the diffusivity of water vapor in the specimen.

This set of macrolevel analyses did not capture the real local behaviour related to the presence of aggregates, that is,

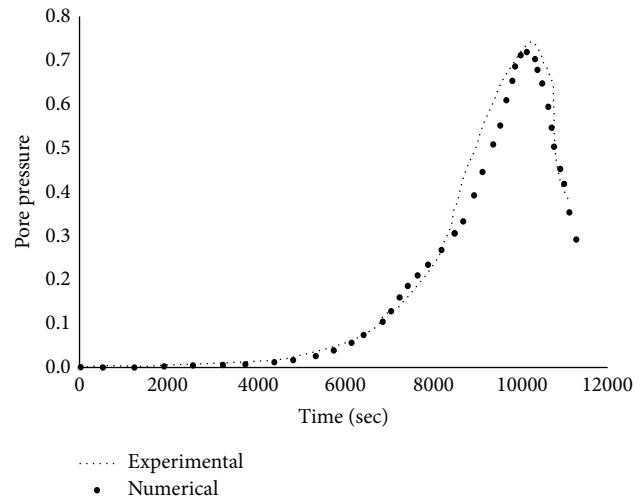


FIGURE 3: Pore pressure temporal evolution; numerical and experimental comparison at 25 mm of depth from the heat source.

stress concentrations, but they did correctly assess the mean value of the pore pressure into the sample at different time steps, although the obtained hygral and thermal distributions were uniform.

4.2.2. Mesoscopic Numerical Models. In this example, a cylindrical concrete sample with a diameter $D = 100$ mm and a height $H = 200$ mm (Figure 4(a)) has been subjected to a fire condition. A three-dimensional model has been carried out in a mesoscale approach where an aggregate random distribution, in agreement with the curve reported in Figure 4(b), has been taken into account.

The concrete mix design in volume is composed of water for a 16%, inerts for a 72%, and cement for a 12%. The inerts have been subdivided as follows: 53% is sand and 47% is gravel.

Only the coarse aggregates have been explicitly represented in the mesoscale model as spheres having different

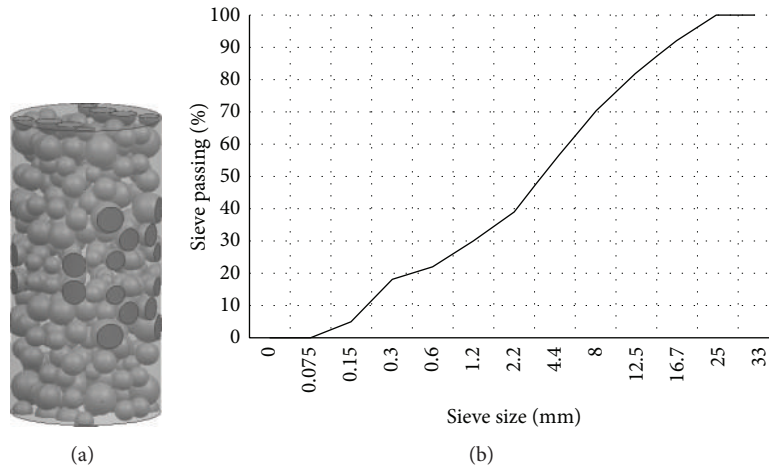


FIGURE 4: Sample model (a); aggregates distribution (b).

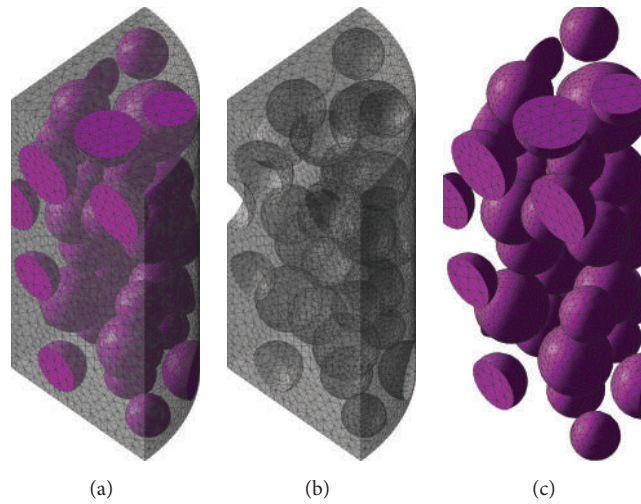


FIGURE 5: Numerical model: matrix and aggregates (a); matrix (b); aggregates (c).

diameters between 3 and 25 mm. Sand and fine aggregates have been taken into account into the cement matrix. The hygral, thermal, and mechanical characteristic for the cement matrix and the coarse aggregates are reported in material parameters. In this example, the ITZ interface between the matrix and the aggregates is neglected.

Two different concrete samples have been evaluated, with and without PP fibres in the matrix. In the first model, the addition of 0.3 kg/m^3 of fibres with a length $L_f = 19.0 \text{ mm}$ has been considered, while in the second model the same concrete without PP fibres has been represented.

In a mesoscale approach, the porosity formulation has to be modified as coarse aggregates have been explicitly represented.

So, porosity in the cement matrix is evaluated as follows:

$$n = n_c + n_m + n_M + n_{\text{air}} + n_{f,\text{ITZ}} + n_{\text{relax}} + n_f \quad (12)$$

with an initial porosity $n_c + n_m + n_M = 0.075$.

Coarse aggregates are considered with a constant small porosity $n = 0.0001$.

In order to simplify the numerical analyses, symmetry conditions have been assumed (Figure 5), obtaining a numerical model composed of 17600 nodes and 91300 tetrahedral elements with linear shape functions and five degrees of freedom (displacements along the three directions, humidity, and temperature).

A random aggregates distribution in the sample, according to the mix design grading curve of Figure 4(b), has been realized following [23, 24]. Numerically, a continuous mesh discretization has been realized, where no numerical contact condition has been considered at the interface between matrix and aggregates.

Mechanical boundary conditions have been set on the symmetry surfaces and a slow thermal heating curve has been applied on the external surfaces of the cylindrical sample (see Figure 6). No mechanical loads have been considered in this numerical example.

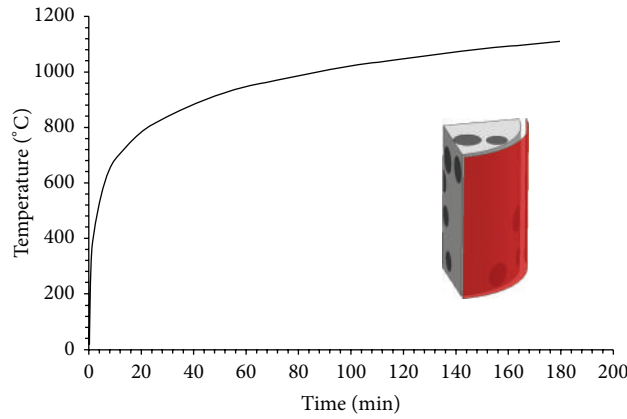


FIGURE 6: Heating curve.

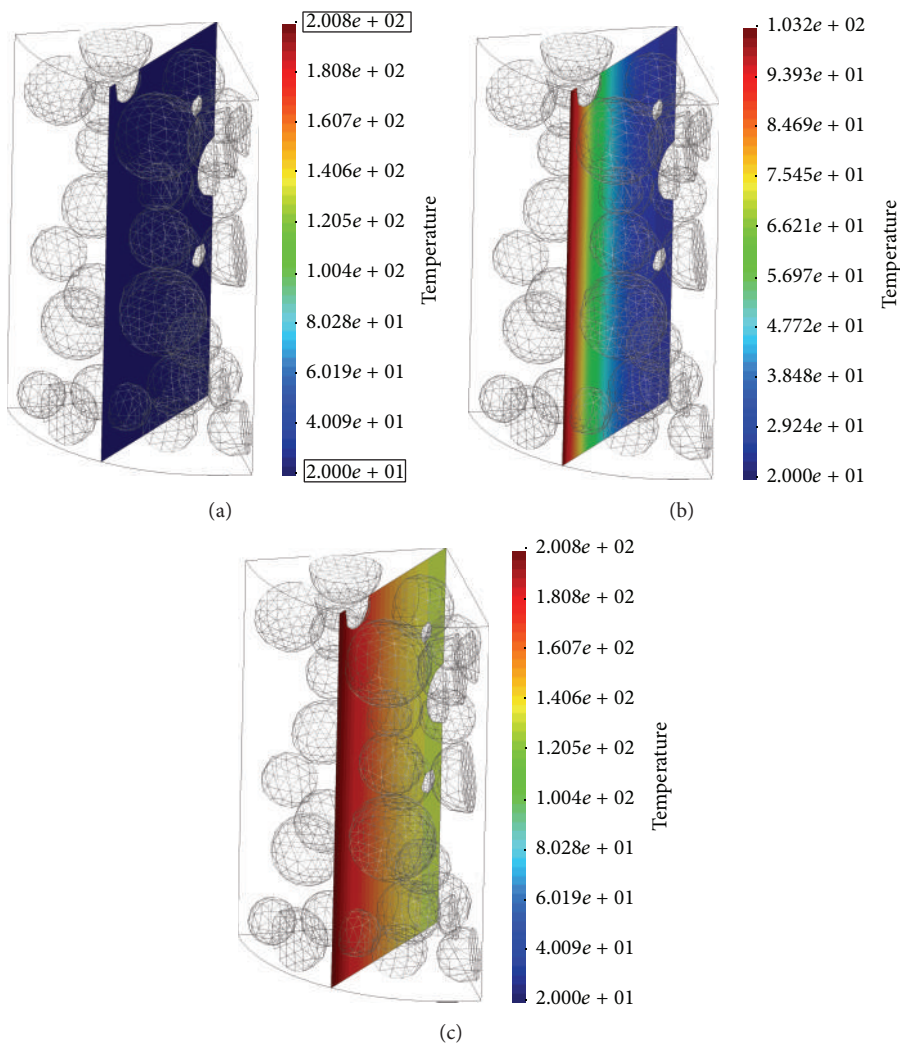


FIGURE 7: Temperature variation inside the sample at 0.0 min (a); 8.0 min (b); 25.0 min (c) after the start of the analysis.

Considering the same thermal conductivity and specific heat for the cement matrix and the aggregates, the thermal distribution inside the sample during the analysis is not affected by the different components, as visible in Figure 7.

As regards the hygral evolution, different results are obtained (Figure 8). The humidity reduction caused by thermal field is influenced by the aggregates distribution, being considered with a low porosity.

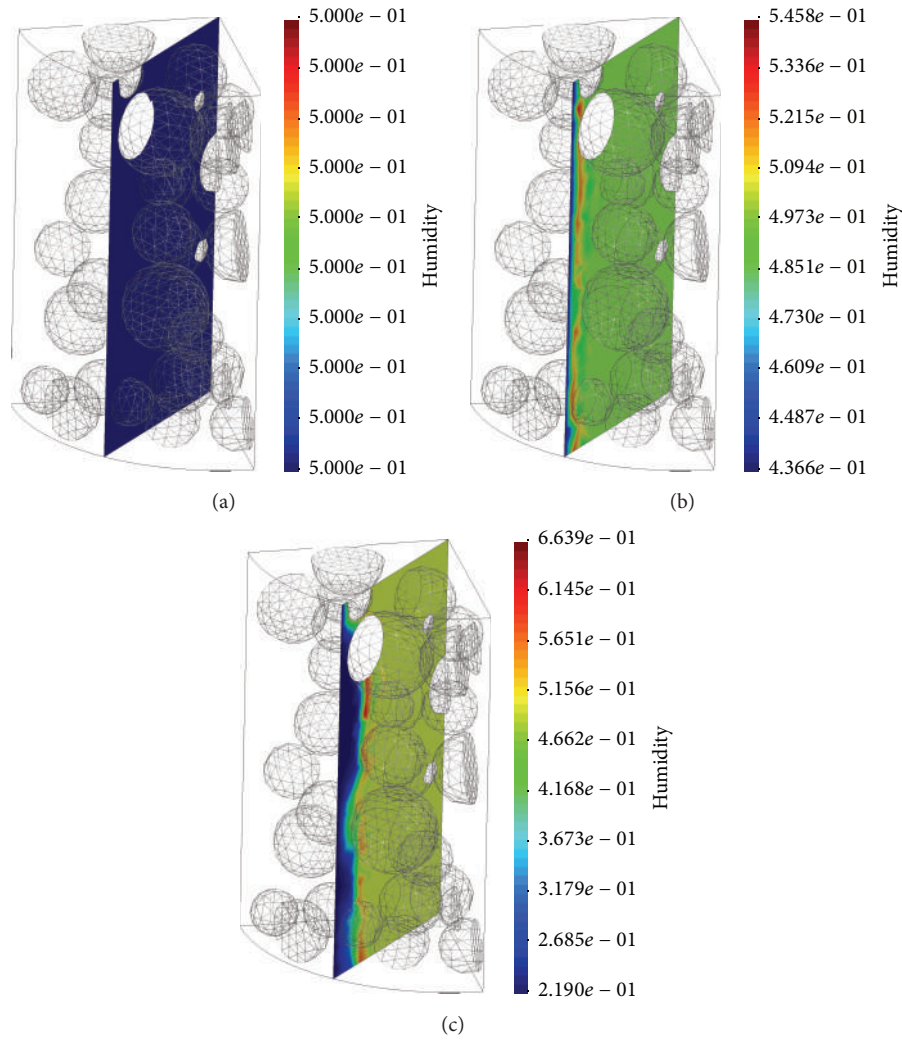


FIGURE 8: Humidity variation inside the sample at 0.0 min (a); 8.0 min (b); 25.0 min (c) after the start of the analysis.

Moisture clog is the humidity increment that occurs in the internal part of the sample due to the fact that the temperature pushes water inward during thermal heating, as visible in Figure 9. This effect causes a consequent water pressure increment which, together with the thermal gradient, is one of the spalling causes.

Considering the presence of PP fibres into the concrete mixing there will be a porosity increase, so reducing the water pressure and consequently the spalling risk.

Around the grains of the concrete sample, a lower humidity reduction can be noticed (Figure 10(a)), as well as higher water pressure results if compared to other zones where the distance between the aggregates is bigger (Figure 10(b)).

The small humidity variations around the aggregates can be associated to the initial conditions assumed for the sample. The analysis starts considering that the hygrothermal conditions of the aggregates and the matrix are in equilibrium with the environment (50% of humidity and 20°C of temperature have been assumed). The hydraulic diffusivity in the inert has been assumed very low, causing a slow water release during the analysis that will maintain humidity

of the cement matrix, so increasing also the internal water pressure.

The water pressure p_{gw} has been evaluated in agreement with [25]

$$p_{gw} = p_{gws}h, \quad (13)$$

where p_{gws} is the water vapor saturation pressure, obtained following the Clausius-Clapeyron relation as a function of the molar mass M_w ; the evaporation enthalpy ΔH_{gw} ; and the gas constant R :

$$p_{gws} = p_{gws0} \frac{M_w \Delta H_{gw}}{R} \left(\frac{1}{T} - \frac{1}{T_0} \right), \quad (14)$$

where T_0 is the room temperature and p_{gws0} is the initial water pressure (see [18]).

In Figure 11, the water pressure variation inside the two samples (with and without PP fibres) has been reported, where an internal pressure reduction is visible if polypropylene fibres have been added in the concrete mixing.

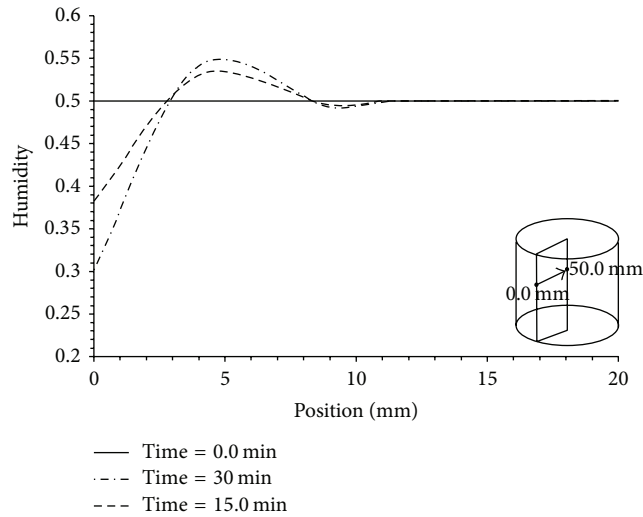


FIGURE 9: Humidity versus radial position.

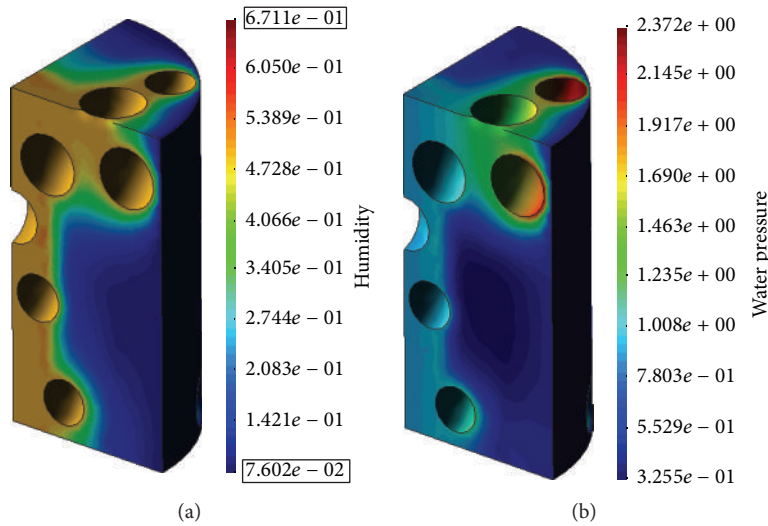


FIGURE 10: Humidity (a) and water pressure (b) distribution in the sample after 40 min of the analysis.

In the sequence shown in Figure 11, the water pressure is approximately the same in the sample with and without fibres before PP melting point (Figures 11(a), 11(d), 11(b), and 11(e)). This result can be explained considering that the variation of the initial porosity (porosity at room temperature) in the matrix having PP fibres, due to the increment of micro air bubbles trapped in the paste, in the ITZ around fibres, is not very high and therefore the hygrothermic diffusivity does not change too much. Exceeding the melting temperature for PP fibres (that occurs between 165°C and 200°C), the diffusivity in the paste increases, so reducing the water pressure. Diffusivity increases again when temperature gets over 325°C, that is, the polypropylene vaporization point.

The water pressure reduction in the sample with PP fibres can be seen also in Figure 12, where at different times a decrease of p_{gw} is visible in the sample containing polypropylene; this is related to the porosity increment caused by the presence of fibres.

The analyses presented in this subsection, differently from the macroscopic ones reported in Section 4.2.1, did allow seeing humidity and temperature concentrations due to the barrier effect related to the explicit representation of aggregates; that is, accurate evaluations of the local effects in terms of humidity, temperature, and pore pressure.

5. Conclusions

In this work, the complex mechanism of polypropylene fibres contribution on concrete behaviour at elevated temperatures has been investigated; an additive decomposition of porosity law has been carried out to evaluate the PP effects that occur during thermal evolution.

Three-dimensional hygrothermomechanical finite element models have been performed and validated considering experimental tests by literature to evaluate the diffusivity

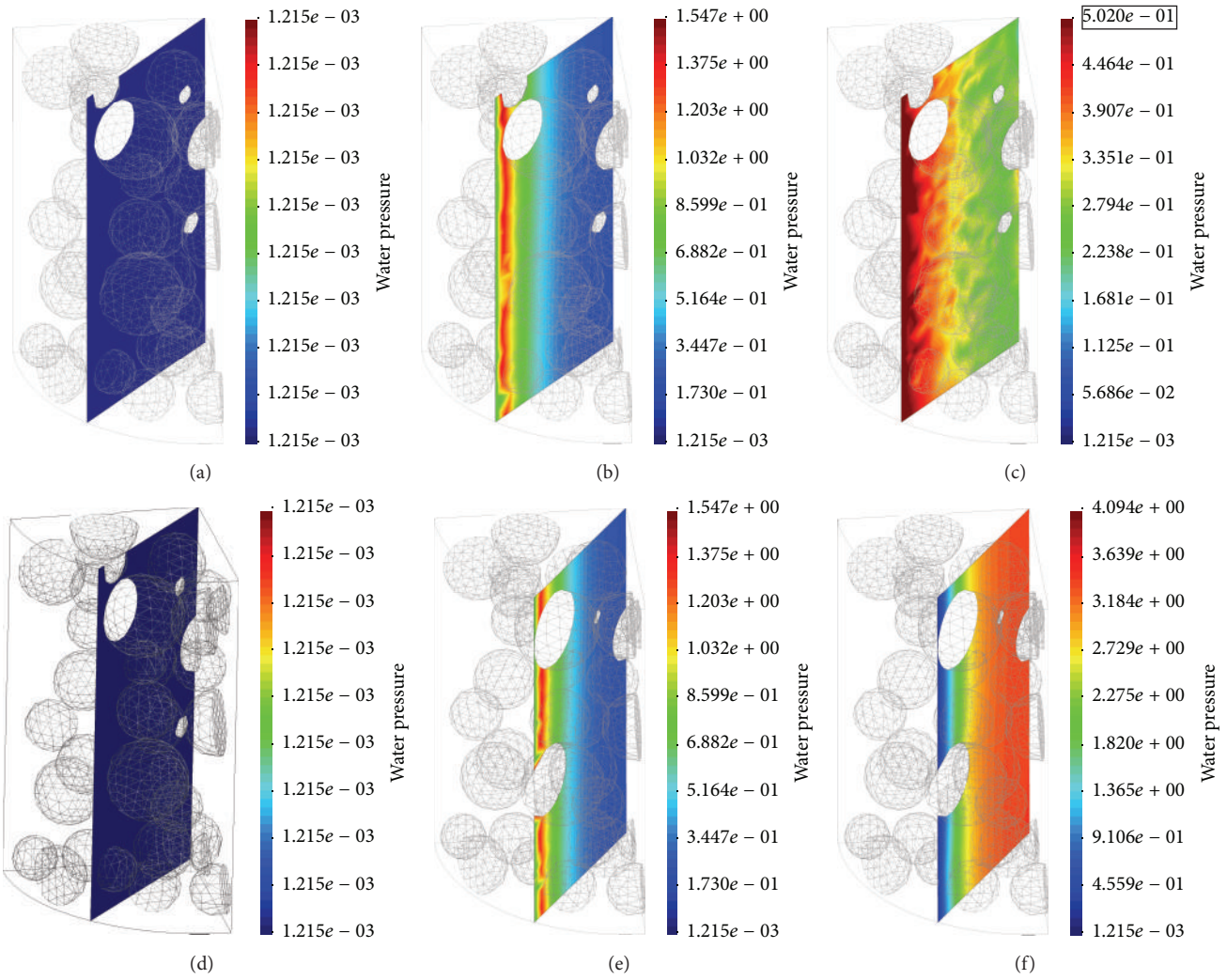


FIGURE 11: Water pressure distribution inside the sample at different temperatures for the two samples, with and without PP fibres: at 20°C with PP (a); at 200°C with PP (b); at 350°C with PP (c); at 20°C without PP (d); at 200°C without PP (e); at 350°C without PP (f).

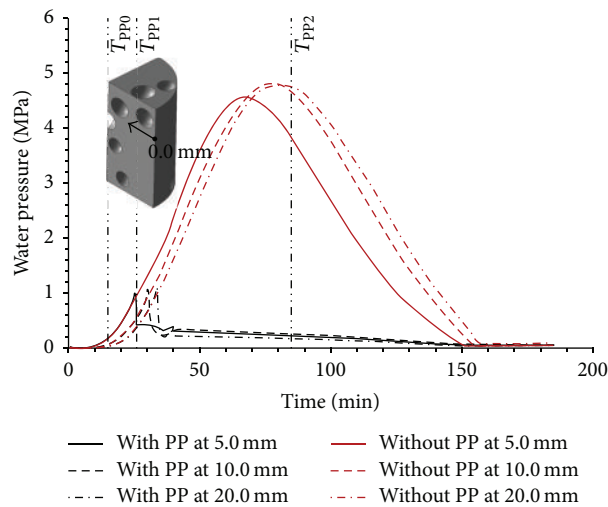


FIGURE 12: Water pressure versus time at different sample positions with and without PP fibres.

variations in concrete, with and without fibres addition. As could be noted, the porosity variation law is able to evaluate the reduction of internal pressure in the concrete material when PP fibres are added to the mix design.

Macro- and mesoscale numerical analyses have been carried out; the latter has provided a more realistic description of concrete than the macroscale analysis, as the mesoscale analysis is influenced by the geometry and the properties of multiple constituents of concrete.

Competing Interests

The authors declare that they have no competing interests.

References

- [1] G. A. Khoury and B. Willoughby, "Polypropylene fibres in heated concrete. Part 1: molecular structure and materials behaviour," *Magazine of Concrete Research*, vol. 60, no. 2, pp. 125–136, 2008.
- [2] C.-G. Han, Y.-S. Hwang, S.-H. Yang, and N. Gowripalan, "Performance of spalling resistance of high performance concrete with polypropylene fiber contents and lateral confinement," *Cement and Concrete Research*, vol. 35, no. 9, pp. 1747–1753, 2005.
- [3] G. Xotta, V. A. Salomoni, and C. E. Majorana, "Thermo-hygro-mechanical meso-scale analysis of concrete as a viscoelastic-damaged material," *Engineering Computations*, vol. 30, no. 5, Article ID 17090567, pp. 728–750, 2013.
- [4] C. E. Majorana, V. Salomoni, and B. A. Schrefler, "Hygrothermal and mechanical model of concrete at high temperature," *Materials and Structures*, vol. 31, no. 210, pp. 378–386, 1998.
- [5] G. Mazzucco, C. E. Majorana, and V. A. Salomoni, "Numerical simulation of polypropylene fibres in concrete materials under fire conditions," *Computers & Structures*, vol. 154, pp. 17–28, 2015.
- [6] R. Barretta, R. Luciano, and J. R. Willis, "On torsion of random composite beams," *Composite Structures*, vol. 132, pp. 915–922, 2015.
- [7] R. Barretta, R. Luciano, and F. M. de Sciarra, "A fully gradient model for Euler-Bernoulli nanobeams," *Mathematical Problems in Engineering*, vol. 2015, Article ID 495095, 8 pages, 2015.
- [8] R. Barretta, L. Feo, R. Luciano, and F. Marotti de Sciarra, "A gradient Eringen model for functionally graded nanorods," *Composite Structures*, vol. 131, pp. 1124–1131, 2015.
- [9] F. Greco and R. Luciano, "A theoretical and numerical stability analysis for composite micro-structures by using homogenization theory," *Composites Part B: Engineering*, vol. 42, no. 3, pp. 382–401, 2011.
- [10] Z. P. Bažant, M. R. Tabbara, M. T. Kazemi, and G. Pyaudier-Cabot, "Random particle model for fracture of aggregate or fiber composites," *Journal of Engineering Mechanics*, vol. 116, no. 8, pp. 1686–1705, 1990.
- [11] S. Eckardt, S. Hafner, and C. Könke, "Simulation of the fracture behaviour of concrete using continuum damage models at the mesoscale," in *Proceedings of the European Congress on Computational Methods in Applied Sciences and Engineering (ECCOMAS '04)*, Jyväskylä, Finland, July 2004.
- [12] D. Krajcinovic, "Distributed damage theory of beams in pure bending," *Journal of Applied Mechanics*, vol. 46, no. 3, pp. 592–596, 1979.
- [13] L. Lanzoni and A. M. Tarantino, "Damaged hyperelastic membranes," *International Journal of Non-Linear Mechanics*, vol. 60, pp. 9–22, 2014.
- [14] J. Mazars and G. Pyaudier-Cabot, "Continuum damage theory—application to concrete," *Journal of Engineering Mechanics*, vol. 115, no. 2, pp. 345–365, 1989.
- [15] G. Xotta, G. Mazzucco, V. A. Salomoni, C. E. Majorana, and K. J. Willam, "Composite behavior of concrete materials under high temperatures," *International Journal of Solids and Structures*, vol. 64, pp. 86–99, 2015.
- [16] Z. Sun, E. J. Garboczi, and S. P. Shah, "Modeling the elastic properties of concrete composites: experiment, differential effective medium theory, and numerical simulation," *Cement and Concrete Composites*, vol. 29, no. 1, pp. 22–38, 2007.
- [17] P. Baggio, C. E. Majorana, and B. A. Schrefler, "Thermo-hygro-mechanical analysis of concrete," *International Journal for Numerical Methods in Fluids*, vol. 20, no. 6, pp. 573–595, 1995.
- [18] D. Gawin, C. E. Majorana, and B. A. Schrefler, "Numerical analysis of hygro-thermal behaviour and damage of concrete at high temperature," *Mechanics of Cohesive-Frictional Materials*, vol. 4, no. 1, pp. 37–74, 1999.
- [19] Z. P. Bažant and L. N. Najjar, "Nonlinear water diffusion in nonsaturated concrete," *Matériaux et Construction*, vol. 5, no. 1, pp. 3–20, 1972.
- [20] C. Rossino, F. L. Monte, S. Cangiano, R. Felicetti, and P. G. Gambarova, "Concrete spalling sensitivity versus microstructure: preliminary results on the effect of polypropylene fibres," in *Proceedings of the MATEC Web of Conferences*, vol. 6, EDP Sciences, Paris, France, September 2013.
- [21] K. Willam, I. Rhee, and Y. Xi, "Thermal degradation of heterogeneous concrete materials," *Journal of Materials in Civil Engineering*, vol. 17, no. 3, pp. 276–285, 2005.
- [22] L. T. Phan, "Pore pressure and explosive spalling in concrete," *Materials and Structures*, vol. 41, no. 10, pp. 1623–1632, 2008.
- [23] G. Mazzucco, G. Xotta, B. Pomaro, C. E. Majorana, F. Faleschini, and C. Pellegrino, "Mesoscale modelling of concrete with recycled aggregates," in *Proceedings of the 10th International Conference on Mechanics and Physics of Creep, Shrinkage, and Durability of Concrete and Concrete Structures (CONCREEP '15)*, pp. 853–863, Vienna, Austria, September 2015.
- [24] S. Torquato, *Random Heterogeneous Materials: Microstructure and Macroscopic Properties*, vol. 16, Springer Science & Business Media, Berlin, Germany, 2013.
- [25] R. W. Lewis and B. A. Schrefler, *The Finite Element Method in the Static and Dynamic Deformation and Consolidation of Porous Media*, John Wiley & Sons, 2nd edition, 1998.

Review Article

A Review on Radiation Damage in Concrete for Nuclear Facilities: From Experiments to Modeling

Beatrice Pomaro

Department of Civil, Environmental and Architectural Engineering, University of Padova, via F. Marzolo 9, 35131 Padova, Italy

Correspondence should be addressed to Beatrice Pomaro; beatrice.pomaro@dicea.unipd.it

Received 24 December 2015; Accepted 19 July 2016

Academic Editor: Anna Pandolfi

Copyright © 2016 Beatrice Pomaro. This is an open access article distributed under the Creative Commons Attribution License, which permits unrestricted use, distribution, and reproduction in any medium, provided the original work is properly cited.

Concrete is a relatively cheap material and easy to be cast into variously shaped structures. Its good shielding properties against neutrons and gamma-rays, due to its intrinsic water content and relatively high-density, respectively, make it the most widely used material for radiation shielding also. Concrete is so chosen as biological barrier in nuclear reactors and other nuclear facilities where neutron sources are hosted. Theoretical formulas are available in nuclear engineering manuals for the optimum thickness of shielding for radioprotection purposes; however they are restricted to one-dimensional problems; besides the basic empirical constants do not consider radiation damage effects, while its long-term performance is crucial for the safe operation of such facilities. To understand the behaviour of concrete properties, it is necessary to examine concrete strength and stiffness, water behavior, volume change of cement paste, and aggregate under irradiated conditions. Radiation damage process is not well understood yet and there is not a unified approach to the practical and predictive assessment of irradiated concrete, which combines both physics and structural mechanics issues. This paper provides a collection of the most distinguished contributions on this topic in the past 50 years. At present a remarkable renewed interest in the subject is shown.

1. Introduction

Despite the increasing interest in renewable energy, nuclear power still has an important role in the energy supply worldwide. Almost 12% of world's electricity is generated by nuclear power plants; nuclear energy is used by 30 countries in the world, for total 439 units, 64 new ones being under design. Europe depends on nuclear power for more than one-quarter of its electricity; in fact almost 30% of electricity demand is satisfied this way; 40% comes from fossil fuel and the remaining from renewables. 131 nuclear power reactors were operating in 2014 in Europe and nuclear plant construction is currently underway in three EU member states: Finland, France, and Slovakia [1].

Understanding the conditions that lead to concrete deterioration is object of a new attention worldwide in matter of nuclear plants. In USA many plants have already had a life extension from 40 to 60 years and serious consideration is now being given to a further extension to 80 years. In fact according to the Atomic Energy Act of 1954 and the Nuclear Regulatory Commission regulations the operating licenses

for commercial power reactors are issued for 40 years and can be renewed for additional 20 years with no limit to the number of renewals.

Japan has now entered the period of safety management of nuclear plants; 20 nuclear power plants in Japan have undergone an examination called *Plant Life Management* by the Japanese government to determine their ability to carry on continuous operation. So in this country work is in progress to improve a quantitative evaluation method based on the time-dependent performance of structures and their components in relation to the deterioration mechanism, which could serve as a maintenance program to extend the operational period of up to 20 years in the near future.

Most of the EU's operational nuclear plants were built in the 1970s and 1980s and were designed to last for around 40 years; therefore they are due to retire by the 2020s unless they get extensions [2]. Some of the oldest reactors are in Belgium, two of which just reached age 40, and 10 extra years has been recently approved for them until 2025 [3]; France is the EU's nuclear leader, its 58 reactors producing nearly three-quarters of the country's electricity; this country also is considering

whether to extend their lifespan to 50 years in 2018 or 2019 [4].

Nuclear reactors, however, are not the only structural type undergoing nuclear radiation damage which must address durability considerations.

For instance, radioisotopes are extensively used in medicine; in over 10,000 hospitals worldwide radiotherapy is the way in which some medical conditions are treated, using radiation to weaken or destroy particular targeted cells; these facilities as well require the design of bunker-type rooms, able to sustain photon and neutron radiation.

This paper is aimed at picturing out state of the art of the most relevant contributions from the late 1950s up to now on the topic of radiation damage of concrete employed for nuclear shielding, from the phenomenological evidences to the modeling aspects.

Many contemporary authors agree that the technical information necessary for determining an appropriate threshold value of nuclear radiation in assessing the soundness of concrete structures under irradiation conditions is poor, especially in regard to concrete durability evaluation. Consequently, further experimental tests are needed. On the other hand, from the first studies some advancements on the interaction between concrete and neutrons or gamma-rays have been made, which would now need implementation in predictive models of concrete deterioration and validation against representative laboratory tests to evaluate the related rate effects.

The understanding of radiation effects on concrete was largely based on Hilsdorf and coauthors' curves compiled in 1978 [5] up to a few years ago, when the need to develop comprehensive safety evaluation systems for aging nuclear power plants has become a compelling issue.

Fujiwara et al. [6] have recently conducted an irradiation test on concrete specimens simulating the exercise scenario of a boiling water reactor in Japan (maximum temperature 65°C; maximum neutron fluence 12×10^{18} n/cm² ($E > 0.1$ MeV)) by far consistently with a 60-year operation. With this work they confirmed that, within the range of radiation doses adopted in the study, radiation exposure did not significantly affect the basic long-term material characteristics; on the other hand the tendency pictured in [5] in terms of the decrease of concrete compressive strength in response to rise in neutron fluence was not detected, due to some critical observations supported also by [7–9].

In fact, despite the big effort in compiling a first data base of experimental results on irradiated concrete, the applicability of the reference values by Hilsdorf and coauthors to the soundness evaluation of concrete in light-water reactors is questioned in [8], basically in reason of some inconsistency of the experimental conditions with the real irradiation conditions (namely, Portland cement for the concrete mix; irradiation from fast neutron spectrum ($E > 0.1$ MeV); temperature field less than 65°C); in particular the experimental database in [5] is said to show wide scattering due to different choices on measured properties (bending strength instead of compressive strength or bending tension strength instead of splitting tension strength), binder type of concrete, specimen

size (even dimensions of 8–15 mm), temperature of concrete (100°C or higher up to 550°C), and neutron spectrum (slow or fast neutrons or not available spectrum).

The work by Field et al. [10] very recently expanded the data collection provided in [5] with those coming from later experimental campaigns on neutron-irradiated concrete and mortars; it provides a complete up to date database to start from to investigate the key variables associated with radiation-induced degradation in concrete structures. Effects on concrete in terms of compressive and tensile strength, modulus of elasticity, weight loss, and volumetric change are here plotted and classified under the applied laboratory conditions. It is here pointed out for a wider data collection that the effects of some important parameters such as the neutron fluence magnitude at which concrete deterioration becomes significant, the neutron fluence energy cutoff associated with the threshold fluence level, and the effect of high concrete temperature during irradiation, to mention a few, cannot be readily separated out and clearly evaluated from the existing data.

2. Phenomenological Aspects on Irradiated Concrete

Radiation on shielding materials is known to affect them deep in their chemical structure. In metals radiation leads to the displacements of atoms from their equilibrium lattice sites, causing lattice defects, which are responsible for an increase of hardness but also embrittlement, and so loss of ductility [11–13]. In polymers the formation of additional cross-links is due to the surplus energy brought by radiation [14]. In geomaterials, like concrete, nuclear radiation leads to the break of atomic bonds, which is supposed to explain the decay in the mechanical properties envisaged in exposed concrete [15, 16] as it will be illustrated in the following.

The first comprehensive collection of published experimental data on the effects of nuclear radiation on the properties of concrete dates back to Hilsdorf et al. [5] and Kaplan [17], with the recent observations on the first work already mentioned in the previous section. It stands out that up to integrated neutron fluence of the order of 10^{19} n/cm² the effects of the irradiation are relatively small, while higher fluence may have detrimental effects on concrete compressive and tensile strength and modulus of elasticity.

In particular, distinguishing between fast or slow neutrons, Gray [18] found that for fast neutron fluence between 7×10^{18} and 3×10^{19} n/cm² the modulus of irradiated concrete was between 10% and 20% less than that of nonirradiated unheated concrete. Alexander [19] reported similar reductions in values of elastic modulus for slow neutron fluence of about 2×10^{19} n/cm². Negligible changes in mechanical properties and weight/volume were found for fast neutrons with $E > 1$ MeV at a fluence of 3×10^{18} n/cm² by Stoces et al. [20].

There is also evidence that concrete hardens under irradiation [21, 22]: from these studies the interference of penetrating ionizing radiation with the process of setting of cement paste has been found in the form of increased compressive

and tensile strength, especially at the very beginning of the hardening period.

Almost in all the cases in which samples were tested to investigate the effects of neutron radiation, the concrete samples were also exposed to secondary gamma radiation, produced by nuclear reactions. Not many tests are in literature on the effects of gamma radiation alone without the simultaneous exposure to neutron radiation. Alexander [19] reports that for gamma radiation doses of about 10^{10} rad there is no reduction in the compressive strength of concrete, when compared with the strength of companion specimens which have been neither irradiated nor heated; there is, however, evidence of reductions between 25% and 60% in compressive strength for doses exceeding 10^{11} rad [23]. In this last test campaign the specimens were immersed in demineralized water in order to shield them against neutrons and study the effect of gamma radiation alone, but demineralized water was found to contribute to deteriorating concrete and after several years of exposure the surface of the irradiated samples was partially destroyed.

Soo and Milian [24] found that a loss in the compressive strength could occur at gamma doses that are much less than the threshold dose of 2×10^8 Gy (2×10^{10} rad). They postulated that the loss of strength could be connected with the radiolysis of the water of hydration in the cement as well as pore water. A loss of hydrogen and oxygen radiolytic species during irradiation would decrease the level of cement hydration and thus the strength of the cement.

The experimental campaign in [25] on concrete under gamma irradiation allowed concluding that the interaction with the shielding material leads to lowering both its strength and its porosity. The mechanism is explained to happen as a series of chemical reactions within the material, starting from the radiolysis of water and ending with the formation of calcite (CaCO_3); crystallites of calcite grow into pores, decreasing their size and destroying the tobermorite gel, a calcium silicate hydrate mineral responsible for concrete strength, by their crystallization pressure.

Another experimental study was conducted by Vodák et al. [26] to investigate further on the porosity variation in cement paste under gamma irradiation and under natural carbonation.

The radiolytic process seems to be confirmed by more recent studies [27], taking advantage of X-ray diffraction and scanning electron microscopy methods. The absorption of gamma radiation is found to induce the amorphization of cement hydrates and finally cause their decomposition. Moreover, bubbles were envisaged after irradiation exposure, which must be the effect of separation of the chemically bonded water, and numerous cracks in the cement matrix were also observed.

The presence of calcium is pointed out as a major cause for the progression of radiolysis; in fact the withdrawal of calcium under gamma-rays is responsible for the formation of $\text{CaO}_2 \cdot 8\text{H}_2\text{O}$, a highly insoluble phase which forms at the expense of portlandite and ettringite, leading to their elimination in case of very high radiation doses [28].

The basic mechanisms controlling the radiolysis in cementitious matrices are reviewed in the specific context

of gamma irradiation in [29]. Two main outcomes result from water radiolysis: (i) buildup of internal gas overpressure (mainly hydrogen and oxygen) that may lead to cracking and/or explosive gas mixture when hydrogen gas is mixed with atmospheric oxygen in fraction of 4% and (ii) corrosion of steel bars in the long-term due to the attack by oxidizing products at the steel-concrete interface [30].

Thermal expansion coefficient, thermal conductivity, and shielding properties appear to be little affected by radiation. As for the coefficient of thermal expansion, Hilsdorf et al. [5] and Granata and Montagnini [21] indicate that for neutron fluence less than 5×10^{19} n/cm² there is no significant difference between the coefficient of thermal expansion of neutron-irradiated concrete samples and the coefficient of nonirradiated samples subjected to high temperature. Also, radiation energy is converted to heat when absorbed by a shield. The heat generated by irradiation can reach quite high temperatures, depending on the shielding material used and the configuration of the shielding structure. Hilsdorf et al. [5] found that temperatures even of the order of 250°C developed in some of the investigations he summarized, which is high enough to generate considerable damage in shielding materials.

An extensive study on the effect of elevated temperature exposure on properties and shielding effectiveness is reported in [31].

As for creep experiments under irradiation, limited reference data exist: [18, 32] for neutron and gamma irradiation, respectively. In particular the internal gas pressures resulting from water hydrolysis under gamma irradiation seem to affect concrete shrinkage and creep in some measure.

2.1. Physical Interpretation of the Experimental Results.

Because the shielding properties of concrete are found to be driven mainly by the selection of the aggregates in the concrete mix; the choice must be taken in reason of the different attenuation mechanisms characterizing the specific particles to be addressed: gamma-rays or neutrons [17, 33–35].

Gamma-rays are attenuated by interactions at the level of the electrons of the atoms composing the shielding medium; in particular they show having a negligible effect on the solid materials composed of ionic and metallic bonds, but they can break anisotropic chemical bonds such as covalent bonds. Typically, siliceous materials are subject to gamma-rays degradation because the Si-O bond is a covalent bond. At this purpose concrete to be used as a gamma-ray shielding material should be designed to maximize the density of electrons within it. Practically, high-density iron ore aggregates are chosen at this purpose. This is the case of barytes, ferrophosphorus, magnetite, and hematite.

Instead, neutrons interact with nuclei of atoms leading to change in the lattice spacing within the material during these collision events. Therefore, neutrons have a more significant effect on dense and well-crystallized materials than on randomly structured materials with high porosity. In concrete, aggregates (coarse and fine aggregates) are in a crystallized phase, while cement paste is an amorphous phase; therefore neutron radiation causes more distortion and damage to

the internal structure of aggregates than to that of cement paste. Moreover neutron attenuation is more effective when fast neutrons are made to collide with lightweight atoms (typically hydrogen) so hydrous aggregates are to be preferred for neutron shielding; hydrous aggregates are in fact capable of increasing the fixed-water content of concrete or retaining their water of crystallization at high temperatures. This is the case of serpentine, limonite, goethite, and bauxite.

In some cases the enrichment of minerals with certain elements, such as boron, is considered to enhance the thermal neutron attenuation of concrete and cut down secondary gamma-rays production. Boron-containing aggregates include colemanite, borocalcite, and ferroboration.

The specific effect of radiation-induced damage of aggregates is of primary interest in recent research, in view of the durability assessment of old nuclear structures.

Kelly et al. [36] and Elleuch et al. [37] emphasize the predominant role of the aggregate in the development of neutron irradiation-induced swelling and the potential creation or aggravation of damage in the surrounding paste.

Vanelstraete and Laermans [38] have shown that fast neutrons cause displacement cascades in quartz resulting in disordered regions of the crystal. For sufficiently high doses, damage regions overlap, reducing long-range ordering and resulting in amorphization of the SiO_2 phase. The loss of ordering is observed as a reduction of density and increase in swelling of the quartz phase. Complete amorphization is supposed to be reached at a neutron dose greater than $2 \times 10^{20} \text{ n/cm}^2$.

The effect of nuclear irradiation, bot neutrons, and gamma-rays on quartz was studied extensively by [39]. Crystalline quartz or α -quartz, with specific gravity of about 2.65 is found to convert to distorted amorphous quartz with specific gravity of 2.27 under a fluence of 10^{20} n/cm^2 for fast neutrons with an energy level $>0.1 \text{ MeV}$ and under a dose of 10^{12} Gy for beta- and gamma-rays.

Maruyama et al. [8] confirm that an expansion of siliceous aggregate takes place due to neutron collisions. Atom alignments are deformed and a part of the energy imparted by neutron collision remains as a kind of strain energy causing permanent distortion. Also, denser siliceous aggregates have a larger risk of expansion due to neutron irradiation.

Because the atomic structure of some aggregates can be converted from crystalline structure to distorted amorphous structure with an increase in volume and a decrease in weight, the loss of concrete mechanical properties is conceived to be definitely correlated with radiation-induced aggregate swelling in [10].

The antagonist effect of neutrons and gamma-rays in radiation damage must be considered: the crystalline lattice structure present in the aggregates is much more affected by neutrons than the more vitreous lattice structure of the cement paste, which is much more attacked by gamma-rays.

At this purpose, many authors [5, 17, 18, 40, 41] state that different types of aggregates lead to concrete with different resistance against neutron radiation. Concrete made with flint aggregate shows considerably larger volume changes than concrete made with limestone aggregates; the phenomenon can be explained, once more, by the weakness of

covalent bonds in quartz aggregates with respect to the ionic bonds in calcareous aggregates.

On the other hand, the cement paste undergoes shrinkage due to (i) the radiolysis process under gamma radiation, as illustrated above, and (ii) the evaporation of pore water under radiation heat.

So the mismatch in the volumetric change of concrete components (expansion in aggregates and shrinkage of the mortar) may cause damage at the interface between the two phases.

The uneven shrinkage properties of aggregates and cement paste may lead to loss of concrete compressive strength. While the overall volume growth of the composite compromises the tensile strength, this last is shown to decay on average of 62% and 47%, respectively, for flint and limestone aggregates in the range of 2×10^{19} – $4 \times 10^{19} \text{ n/cm}^2$ [17]. According to [21] a neutron fluence of less than 10^{19} n/cm^2 does not lead to a volume increase of the irradiated samples; rather in this range the volume change of irradiated samples is the expected shrinkage due to temperature exposure of the specimens.

The conversion of crystalline quartz into distorted quartz has a twofold detrimental consequence: (i) microcracking due to differential volume change in the composite and (ii) higher reactivity to certain aggressive chemicals, for example, calcium hydroxide responsible in concrete of alkali-silica reactions (ASR) [42, 43]. Both of these effects are detrimental to the long-term performance of irradiated concrete.

2.2. Radiation-Induced Effects on ASR. The alkali-silica reaction evolves in concrete as follows: OH^- ions present in the alkaline solution in the micropores of concrete react with SiO_2 in aggregates to perform the scission of the Si-O bonds and the subsequent expansion of the aggregates by hydration of SiO_2 . The consumption of OH^- ions due to hydrolysis leads to the dissolution of Ca^{2+} ions into the solution. The Ca^{2+} ions then react with hydrated SiO_2 gels (ASR gel) to generate calcium silicate. Rigid calcium silicate shells typically form on the surfaces of the aggregates as the reaction by-product is generated. The alkaline solution can penetrate into the aggregates through the calcium silicate shells and dissolve SiO_2 groups. Since the rigid shells prevent the deformation of the aggregates, the expansion pressure generated by the penetration of the solution is accumulated in the aggregates under the confining pressure of the silicate shells, thus leading to cracks and the final expansion of the aggregates.

ASR may be accelerated both by lattice defects in SiO_2 minerals from neutrons irradiation and by the preexistence of cracks in the aggregates.

The experiments by Ichikawa and Koizumi [39], Ichikawa and Kimura [44], and Ichikawa and Miura [45] prove that nuclear radiation significantly increases the reactivity of silica-rich aggregates to alkalis; the decrease of the resistance to nuclear radiation with increasing the content of SiO_2 in aggregates strongly indicates that the deterioration is due to the acceleration of ASR in concrete, according to the authors.

In particular the work in [39] shows that nuclear irradiation may change the ASR expansion potential of aggregates, which is driven by the stiffness of the ASR gel and contributes

to the free expansion capability of the aggregate in determining the extent of damage due to ASR. In fact when the ASR gel is soft and its stiffness is low, it is able to permeate into the surrounding porous cement paste; therefore the swelling pressure is not high and the cracking potential is low. In that case a large amount of ASR gel formation may not create severe damage and cracking in concrete. On the other hand, when the ASR gel is stiff, a small amount of ASR can generate significant damage [35]. The stiffness of ASR gel depends mainly on its chemical composition, such as the ratio of Na_2O to SiO_2 . Struble and Diamond [46] conducted a study to investigate the swelling pressure of ASR in terms of ASR chemical composition.

Though not specifically addressing ASR, the work by Vodák et al. [25] indicates that irradiation generates a succession of chemical reactions, leading to a decrease in the size of pore space and hence inhibiting concrete to absorb some of the ASR gel produced prior to expansion.

Saouma and Hariri-Ardebili [47] critically reviewed existing available literature on ASR and they conclude that radiation effects on concrete degradation are minimal for the first 40-year operation of a nuclear power plant; however they agree with [6] that a structural life extension to 60–100 years may prove problematic, though the data to fully support this concern are insufficient. The work is contextualized to Seabrook site, the first reported nuclear plant in the USA known to possibly suffer from ASR, which saw in 2010 its operating license extended from 2030 to 2050. The work is aimed at developing an aging management program for old nuclear plants; it expresses the concern of overreliance on surface crack observation and structural component testing and at the same time it encourages the development of reliable Finite Element Method (FEM) based simulations to address the long-term assessment of such structures.

Graves et al. [48] offer a comprehensive evaluation of potential aging-related degradation modes for light-water reactor materials and components. Here ASR is pointed out as one of the high-ranked causes of damage that can potentially affect in the long-term the concrete containment of nuclear plants, together with creep of the posttensioned system and irradiation of concrete itself, which, as shown, may accelerate ASR.

3. Particle Transport Simulations for Nuclear Radiation Problems

The description of all the possible interactions between a radiation particle and the absorber medium is the topic of the so-called *transport theory*, a special branch of statistical mechanics.

Accurate calculations of particle transport are needed, nowadays more than in the past, for many reasons.

(i) The necessity to develop theoretical models of radiation transport also for particle energies above 20 MeV: attenuation coefficients, such as neutron cross sections, need to be evaluated for such energies, while complete libraries are available for a representative set of nuclides up to 20 MeV [49]. Neutrons are known to be easily transported over many energy decades, from the hundreds of MeV down to the meV

range; therefore the knowledge of the cross section over the whole energy range is a concern.

Many new facilities, working at high energy, have been recently built or are planned, in order to perform experiments in this sense, to calibrate and validate predictive theoretical models.

(ii) The need to accurately describe the proton- and neutron-induced interaction mechanisms: a number of new applications in the last fifteen years are devoted to the production of intense neutron fluxes by protons impinging on a thick target of a heavy element (mercury, lead, uranium, etc.) for the purposes of point (i), thus producing a cascade of nuclear reactions, known as *spallation reactions*, which involve protons, neutrons, nuclear fragments (alpha-particles, tritium, and deuterium), and secondary gamma-rays.

(iii) The assistance in the design of accelerator-driven systems, which are conceived as nowadays solution to the problem of the transmutation, a possible mechanism for reducing the volume and hazard of the radioactive waste (spent fuel) in nuclear power reactors: accelerator-driven systems consist of a reactor coupled with a high-intensity proton accelerator impinging on a high-density target. The spallation reactions taking place in the target result in high neutron fluxes here and in the surrounding core, which requires accurate evaluation, for shielding design purposes and for the radiological protection assessment (e.g., thermomechanical assessment and study of the activation of components and materials).

(iv) Similarly, the assistance in the design of other nuclear facilities, such as new-generation reactors (generation IV): the concept with these next-generation reactors is to use different coolants (sodium-, gas-, or liquid-metal cooling system) and to consider recycling of the fuel, in order to both reach higher power (improved efficiency) and minimize the waste production. For these systems a radiation damage assessment of the materials subject to the intense neutron fluxes (fuel cladding, vessel, and cooling system) is mandatory for fulfilling safety requirements [50].

(v) The scientific knowledge of the biological effects of radiation, to study particle transport for biomedical purposes: Monte Carlo simulations of neutron transport in human tissues have been conducted in recent years, due to the difficulty in carrying out experiments, in order to determine the tissue-specific weighting factors at different energies, which are useful for the assessment of the effective dose of exposed subjects.

Two approaches are possible to quantify the main variable in transport theory, the radiation flux density, throughout a certain domain: the deterministic approach given by the solution of the Boltzmann transport equation and the statistical approach given by Monte Carlo simulations.

As for the first method, an exact solution is possible only in few cases [51, 52], but not for complex geometries; consequently much effort has been done in the development of approximations to the transport equation, both numerically and analytically. In this second case the diffusion theory and the two-group theory are worth mentioning.

Numerically speaking, the solution of the Boltzmann equation requires (i) energy discretization of the neutron spectrum into discrete energy intervals based on a multi-group formalism; (ii) angular discretization of the angular direction of the radiation flux; (iii) space discretization or mesh, according to FEM formulation.

As regards the second methods, some software programs [53–57] are under continuous upgrade by their developers to solve radiation transport problems via the Monte Carlo technique.

3.1. Modeling Approaches for Irradiated Concrete. When addressing the specific issues involving irradiated concrete, especially with regard to its durability, ad hoc numerical methods must be defined to catch all the complex coupled mechanisms illustrated above, which might be used in conjunction with radiation transport calculations.

In the following some recent distinguishing models of radiation-related issues concerning concrete are reviewed.

Radiation-induced volumetric expansion is identified as a predominant source of cracking in the cement paste of pressurized water reactors in [58]. Based on an extensive literature review on postirradiation experimental data, the authors here developed a 2D micromechanical formulation accounting for the radiation-induced swelling of aggregates, which uses upscaling techniques to address the macroscopic scale starting from the material scale (aggregates and cement paste), that is, homogenization theory applied to random media. Mechanical properties of concrete vary at varying neutron fluence; no gamma-rays effects are considered nor thermohydraulic mechanisms in concrete.

In a companion study Giorla et al. [59] proposed a 2D FEM model of concrete at the mesoscale, where aggregates are supposed to be elastic and subject to thermal and radiation-induced swelling while the cement matrix is viscoelastic and it undergoes damage, drying shrinkage, and thermal expansion. Therefore this model embodies thermohydraulic aspects, though they are not coupled with the mechanical field because actually thermal expansion, radiation-induced volumetric expansion, and shrinkage result in imposed deformations. In particular here radiation-induced volumetric expansion is a predominant cause of the development and propagation of damage around the aggregate and surroundings.

In [60] a combined use of a thermohydraulic FEM model with a Monte Carlo code is suggested to analyse radiation damage on a real nuclear facility under its design operational life. Damage is here made to depend on the neutron fluence based on Hilsdorf and coauthors' data [5], with all the limitations discussed in Section 1; the model does not account for a specific radiation-induced volumetric expansion but it allows catching the thermal aspect of the phenomenon related to the energy deposition due to radiation attenuation together with its implications on the hydraulic field.

A chemomechanical approach to model aggregate dissolution and product precipitation in a microstructural reaction-transport environment has been used in [61] to simulate near-surface degradation of Portland cement paste

in contact with a sodium sulfate solution. With this tool microstructural changes due to new solids in a confined-growth condition are responsible for localized stress and damage in a coupled way.

So far, then, in both the theoretical and the numerical field no fully coupled radiothermohydraulic models have been accomplished yet to simulate the deterioration mechanism of irradiated concrete, though an approach in this sense has been proposed in [7], where the mismatch in the volume changes between cement paste and aggregate is pointed out as the main cause of cracking. For the sake of completeness, the proposed model nowadays could take also advantage of the recent advances on microscopic modeling in the field of fracture mechanics and crack propagation [62–66]. Recent theoretical studies and benchmark examples of engineering interest at the nanoscale can be found in [67–69], also in the context of thermoelasticity and viscoelasticity [70].

3.2. Modeling Approaches for ASR. Though not always addressing radiation-induced effects specifically, a considerable interest in modeling ASR for concrete durability investigations is found in literature. The effort in the past years up to now was spent on the development of both: macroscopic models and micro-/mesoscopic models.

The first are aimed at investigating the overall structural behavior of entire concrete elements in their real context, while the latter look at the phenomenon at a material scale, often coupling the mechanical field with the chemical reactions involved in the ASR gel production.

The work by Ulm et al. [71] belongs to the first kind of approach. They developed a chemothermomechanical model in the framework of Biot's theory, where the concrete is conceived as a two-phase material including the expansive gel and the homogenized concrete skeleton. Here the volumetric expansion of the gel is evaluated as a function of the reaction kinetics, which is influenced by temperature.

Saouma and Perotti [72] proposed a chemothermomechanical model based on two main assumptions: the volumetric expansion of the gel and its redistribution in relation of weights depending on the stress tensor.

In [73] a chemoelastic damage model, validated on the basis of the accelerated multiaxial experimental tests on small specimens, is formulated to simulate the mechanical effects of ASR in large dams.

As for the applications focusing on a lower scale, various analytical models based on empirical equations were developed to explain ASR at the mesoscale of concrete: Bazant and Steffens [74] proposed that the chemical reaction kinetics is related to the diffusion process of the reactants, leading to subsequent fracture in the characteristic unit cell of the concrete, modeled with one spherical glass particle; Multon et al. [75] developed a microscopic chemomechanical model based on damage theory in order to assess the decrease of stiffness of the mortar due to cracking caused by ASR and to quantify the related expansion. The diffusion and the fixation of alkalis are here assessed with the mass balance equation and by defining a threshold alkalis concentration, above which the formation of the gel is meant to start.

An analytical model, for which a numerical solution is provided, is studied in [76]. The formulation is based on the description of the transport and reaction of alkalis and calcium ions within a relative elementary volume, particularly taking into account the influence of the reactive aggregate size grading on ASR evolution.

Comby-Peyrot et al. [77] introduced a 3D mesoscopic FEM model of concrete as a biphasic medium with coarse aggregates randomly embedded in the cement matrix. Damage in the cement matrix is caused by the phenomenon of isotropic dilation of the reactive aggregates, specifically induced by ASR.

Dunant and Scrivener [78] developed a 2D mesoscale extended finite element (XFEM) model which defines the geometry of the gel swelling by updating the enrichment function. A specific damage parameter accounts for triggering of the fracture in the aggregates, due to growing gel pockets in them.

Alnaggar et al. [79] proposed a mesoscale formulation of ASR deterioration in concrete specimens via the Lattice Discrete Particle Model (LDPM), in a chemothermomechanical way, including nonuniform expansions, expansion transfer, and heterogeneous cracking.

In [80] 3D micro-CT scans of the microscale hardened cement paste are used to calibrate a coupled chemothermohydro-mechanical FEM model in which the gel is assumed to be produced in the micropores of the paste and it exerts uniform pressure on the neighborhood. The expansion coefficient of the gel at the microscale was obtained through a two-step homogenization approach, thus enabling correlating microscale damage and macroscale failure.

These references are not exhaustive; however, a comprehensive review of modeling of ASR in concrete is provided in [81, 82].

4. Conclusions

Concerns over aged nuclear power stations are mounting in several countries today. This is the primary reason for a renewed interest in radiation damage assessment of biological concrete shields in such facilities.

The behavior of irradiated concrete has reached up to date commonly accepted explanations. Particularly, cement paste and aggregates are known to behave differently under radiation exposure conditions: cement paste shrinks under drying conditions, the decrease in volume being only partially covered by the thermal expansion due to high temperatures arisen by associated radiation heat. Shrinkage of the cement paste is mostly explained by water hydrolysis and water evaporation occurring under gamma-ray irradiation. On the other hand, aggregates expand due to accumulation of defects in their crystal structures generated mainly by neutron collisions. This uneven volume expansion between cement matrix and aggregates is pointed out as the primary cause of damage in irradiated cementitious materials, to date, based on the available experimental studies. Much of the research related to this topic was conducted from the 1960s to the 1970s in support of the development of prestressed concrete reactor

vessels for high temperature reactors and radioactive waste storage facilities.

The need for long-term predictions of concrete shielding of old reactors has enhanced the effort towards the modeling of the related deterioration mechanisms, both theoretically and numerically. The most relevant features which allow fully addressing the whole complex physical process are here summarized and the recent achievements in matter of irradiated concrete modeling are reviewed.

In this framework further research is recommended aimed at consolidating the new outstanding micro-/mesomechanical models in order to (i) fill the knowledge gaps from past experiments and (ii) possibly allow the integration of radiation-induced effects into the chemothermohydro-mechanical aspects of the problem in a coupled way.

Competing Interests

The author declares no competing interests.

References

- [1] <http://world-nuclear.org/info/Facts-and-Figures/World-Nuclear-Power-Reactors-and-Uranium-Requirements/>.
- [2] <http://www.carbonbrief.org/the-trouble-with-europes-ageing-nuclear-power-plants>.
- [3] <https://euobserver.com/beyond-brussels/129795>.
- [4] <http://uk.reuters.com/article/us-europe-nuclear-power-insight-idUKKBN0GH05U20140818>.
- [5] H. K. Hilsdorf, J. Kropp, and H. J. Koch, "The effects of nuclear radiation on the mechanical properties of concrete," in *Proceedings of the Douglas McHenry International Symposium on Concrete and Concrete Structures*, ACI SP 55-10, pp. 223–251, American Concrete Institute, Mexico City, Mexico, 1978.
- [6] K. Fujiwara, M. Ito, M. Sasanuma et al., "Experimental study of the effect of radiation exposure to concrete," in *Proceedings of the 20th International Conference on Structural Mechanics in Reactor Technology (SMIRT '09)*, paper 1891, SMIRT20-Division I, Espoo, Finland, 2009.
- [7] I. Maruyama, O. Kontani, A. Ishizawa, M. Takizawa, and O. Sato, "Development of system for evaluating concrete strength deterioration due to radiation and resultant heat," IAEA-CN-194-093, Topic: 3-6 Non-metallic material Ageing Management, 2012.
- [8] I. Maruyama, O. Kontani, S. Sawada, O. Sato, G. Igarashi, and M. Takizawa, "Evaluation of irradiation effects on concrete structure-background and preparation of neutron irradiation test," in *Proceedings of the ASME Power Conference (POWER '13)*, no. 98114, 9 pages, ASME, Boston, Mass, USA, August 2013.
- [9] O. Kontani, S. Sawada, I. Maruyama, M. Takizawa, and O. Sato, "Evaluation of irradiation effects on concrete structure—gamma-ray irradiation tests on cement paste," in *Proceedings of the ASME 2013 Power Conference (POWER '13)*, no. 98099, ASME, Boston, Mass, USA, August 2013.
- [10] K. G. Field, I. Remec, and Y. Le Pape, "Radiation effects in concrete for nuclear power plants—part I: quantification of radiation exposure and radiation effects," *Nuclear Engineering and Design*, vol. 282, pp. 126–143, 2015.
- [11] D. S. Billington, "Radiation damage in reactor materials," in *Proceedings of the International Conference on the Peaceful Uses*

- of *Atomic Energy*, vol. 7 of *Nuclear Chemistry and Effects of Irradiation*, pp. 421–432, United Nations, Geneva, Switzerland, 1955.
- [12] F. E. Faris, “The effect of irradiation on structural materials,” in *Proceedings of the International Conference on the Peaceful Uses of Atomic Energy*, vol. 7 of *Nuclear Chemistry and Effects of Irradiation*, pp. 484–489, United Nations, Geneva, Switzerland, August 1955.
- [13] S. T. Konobeevsky, N. F. Pravdyuk, and V. I. Kutaitsev, “The effect of irradiation on the structure and properties of structural materials,” in *Proceedings of the International Conference on the Peaceful Uses of Atomic Energy*, vol. 7 of *Nuclear Chemistry and Effects of Irradiation*, pp. 479–483, United Nations, Geneva, Switzerland, August 1955.
- [14] A. Holmes-Siedle and L. Adams, *Handbook of Radiation Effects*, Oxford University Press, New York, NY, USA, 2002.
- [15] B. T. Price, C. C. Horton, and K. T. Spinney, *Radiation Shielding*, Pergamon Press, London, UK, 1957.
- [16] R. G. Jaeger, *Engineering Compendium on Radiation Shielding*, vol. 2, Springer, Berlin, Germany, 1970.
- [17] M. F. Kaplan, *Concrete Radiation Shielding: Nuclear Physics, Concrete Properties, Design, and Construction*, John Wiley & Sons, New York, NY, USA, 1989.
- [18] B. S. Gray, “The effect of reactor radiation on cements and concrete,” in *Proceedings of the Conference on Prestressed Concrete Pressure Vessels*, pp. 17–39, Commission of European Communities, Luxembourg City, Luxembourg, 1972.
- [19] S. C. Alexander, *Effects of Irradiation on Concrete: Final Results*, Atomic Energy Research Establishment, United Kingdom Atomic Energy Authority, Harwell, UK, 1963.
- [20] B. Stoces, P. Otopal, V. Juricka, and J. Gabriel, “Effect of radiation on the mechanical properties of concrete,” Tech. Rep. UJV-2390.R,T, Translated from the Czech, 1970.
- [21] S. Granata and A. Montagnini, “Studies on behavior of concretes under irradiation,” in *Concrete for Nuclear Reactors*, vol. 2 of *Special Publication SP-34*, pp. 1163–1172, American Concrete Institute, 1972.
- [22] B. Nowakowski, “Influence of penetrating ionizing radiation on the curing of grouts and cement mortars,” *Building Science*, vol. 7, no. 4, pp. 271–276, 1972.
- [23] J. F. Sommers, “Gamma radiation damage of structural concrete immersed in water,” *Health Physics*, vol. 16, no. 4, pp. 503–508, 1969.
- [24] P. Soo and L. M. Milian, “The effect of gamma radiation on the strength of Portland cement mortars,” *Journal of Materials Science Letters*, vol. 20, no. 14, pp. 1345–1348, 2001.
- [25] F. Vodák, K. Trtík, V. Sopko, O. Kapičková, and P. Demo, “Effect of γ -irradiation on strength of concrete for nuclear-safety structures,” *Cement and Concrete Research*, vol. 35, no. 7, pp. 1447–1451, 2005.
- [26] F. Vodák, V. Vydra, K. Trtík, and O. Kapičková, “Effect of γ -irradiation on properties of hardened cement paste,” *Materials and Structures*, vol. 44, no. 1, pp. 101–107, 2011.
- [27] A. Lowińska-Kluge and P. Piszora, “Effect of gamma irradiation on cement composites observed with XRD and SEM methods in the range of radiation dose 0–1409 MGy,” *Acta Physica Polonica A*, vol. 114, no. 2, pp. 399–411, 2008.
- [28] P. Bouniol and A. Aspart, “Disappearance of oxygen in concrete under irradiation: the role of peroxides in radiolysis,” *Cement and Concrete Research*, vol. 28, no. 11, pp. 1669–1681, 1998.
- [29] P. Bouniol and E. Bjergbakke, “A comprehensive model to describe radiolytic processes in cement medium,” *Journal of Nuclear Materials*, vol. 372, no. 1, pp. 1–15, 2008.
- [30] P. Bouniol, B. Muzeau, and V. Dauvois, “Experimental evidence of the influence of iron on pore water radiolysis in cement-based materials,” *Journal of Nuclear Materials*, vol. 437, no. 1–3, pp. 208–215, 2013.
- [31] D. J. Naus, “A compilation of elevated temperature concrete material property data and information for use in assessments of nuclear power plant reinforced concrete structures,” Tech. Rep. NUREG/CR-7031 ORNL/TM-2009/175, US Nuclear Regulatory Commission, Oak Ridge National Laboratory, 2010.
- [32] D. McDowall, “The effects of gamma radiation on the creep properties of concrete,” in *Proceedings of the Information Exchange Meeting on “Results of Concrete Irradiation Programs”*, EUR 4751 f-e, pp. 55–69, Commission des Communautés Européennes, Brussels, Belgium, 1971.
- [33] T. Rockwell, *Reactor Shielding Design Manual*, McGraw-Hill, New York, NY, USA, 1956.
- [34] A. N. Komarovskii, *Shielding Materials for Nuclear Reactors*, Pergamon Press, London, UK, 1961.
- [35] K. William, Y. Xi, and D. Naus, “A review of the effects of radiation on microstructure and properties of concretes used in nuclear power plants,” Tech. Rep. NUREG/CR-7171 ORNL/TM-2013/263, US Nuclear Regulatory Commission, Oak Ridge National Laboratory, 2013.
- [36] B. Kelly, J. Brocklehurst, D. Mottershead, and S. McNearney, “The effects of reactor radiation on concrete,” in *Proceedings of the 2nd Information Meeting on Prestressed Concrete and Reactor Pressure Vessels and Their Thermal Isolation*, EUR-4531, pp. 237–265, Commission des Communautés Européennes, Brussels, Belgium, 1969.
- [37] M. F. Elleuch, F. Dubois, and J. Rappeneau, “Effects of neutron radiation on special concretes and their components,” in *ACI Special Publication SP-34: Concrete for Nuclear Reactors*, Paper SP34-51, pp. 1071–1108, 1972.
- [38] A. Vanelstraete and C. Laermans, “Tunneling states in neutron-irradiated quartz: measurements of the ultrasonic attenuation and velocity change,” *Physical Review B*, vol. 42, no. 9, pp. 5842–5854, 1990.
- [39] T. Ichikawa and H. Koizumi, “Possibility of radiation-induced degradation of concrete by alkali-silica reaction of aggregates,” *Journal of Nuclear Science and Technology*, vol. 39, no. 8, pp. 880–884, 2002.
- [40] D. Campbell-Allen, E. W. E. Low, and H. Roper, “An investigation on the effect of elevated temperatures on concrete for reactor vessels,” *Nuclear Structural Engineering*, vol. 2, no. 4, pp. 382–388, 1965.
- [41] D. J. Naus, “Primer on durability of nuclear power plant reinforced concrete structures: a review of pertinent factors,” Tech. Rep. NUREG/CR-6927 ORNL/TM-2006/529, US Nuclear Regulatory Commission, Oak Ridge National Laboratory, 2007.
- [42] A. F. Cohen, “Low-temperature thermal conductivity in neutron irradiated vitreous silica,” *Journal of Applied Physics*, vol. 29, no. 3, pp. 591–593, 1958.
- [43] L. W. Hobbs and M. R. Pascucci, “Radiolysis and defect structure in electron-irradiated α -quartz,” *Journal de Physique Colloques*, vol. 41, no. 7, pp. 237–242, 1979.
- [44] T. Ichikawa and T. Kimura, “Effect of nuclear radiation on alkali-silica reaction of concrete,” *Journal of Nuclear Science and Technology*, vol. 44, no. 10, pp. 1281–1284, 2007.

- [45] T. Ichikawa and M. Miura, "Modified model of alkali-silica reaction," *Cement and Concrete Research*, vol. 37, no. 9, pp. 1291–1297, 2007.
- [46] L. Struble and S. Diamond, "Unstable swelling behaviour of alkali silica gels," *Cement and Concrete Research*, vol. 11, no. 4, pp. 611–617, 1981.
- [47] V. E. Saouma and M. A. Hariri-Ardebili, "A proposed aging management program for alkali silica reactions in a nuclear power plant," *Nuclear Engineering and Design*, vol. 277, pp. 248–264, 2014.
- [48] H. Graves, Y. Le Pape, D. Naus et al., "Expanded materials degradation assessment (EMDA), 4: aging of concrete," Tech. Rep. NUREG/CR-7153, ORNL/TM-2011/545, US Nuclear Regulatory Commission, Oak Ridge National Laboratory, 2013.
- [49] P. Vaz, "Neutron transport simulation (selected topics)," *Radiation Physics and Chemistry*, vol. 78, no. 10, pp. 829–842, 2009.
- [50] A. Alemberti, "Verso i reattori di IV generazione," in *Proceedings of the Workshop: IV Generation Nuclear Reactors: Which Issues for Metals?* AIM (Italian Association of Metallurgy) with Ansaldo Nucleare and IENI (National Council for Research, Institute for Energy and Interphases), Genova, Italy, February 2011, (Italian).
- [51] J. R. Harrison, *Nuclear Reactor Shielding*, Temple Press, London, UK, 1958.
- [52] J. K. Shultis and R. E. Faw, *Radiation Shielding*, Prentice Hall, New York, NY, USA, 1996.
- [53] D. B. Pelowitz, Ed., "MCNPX user's manual, version 2.7.0", Tech. Rep. LA-CP-11-0438, Los Alamos National Laboratory, 2011.
- [54] D. B. Pelowitz, J. W. Durkee, J. S. Elson et al., "MCNPX 2.7.0 extensions," Tech. Rep. LA-UR-11-02295, Los Alamos National Laboratory, 2011.
- [55] S. Agostinelli, "Geant4—a simulation toolkit," *Nuclear Instruments and Methods in Physics Research Section A: Accelerators, Spectrometers, Detectors and Associated Equipment*, vol. 506, no. 3, pp. 250–303, 2003.
- [56] J. Allison, K. Amako, J. Apostolakis et al., "Geant4 developments and applications," *IEEE Transactions on Nuclear Science*, vol. 53, no. 1, pp. 270–278, 2006.
- [57] A. Ferrari, P. R. Sala, A. Fass, J. Ranft, and A. Fassò, "FLUKA: a multi-particle transport code," Tech. Rep. CERN-2005-10, INFN/TC.05/11, SLAC-R-773, 2011.
- [58] Y. Le Pape, K. G. Field, and I. Remec, "Radiation effects in concrete for nuclear power plants, part II: perspective from micromechanical modeling," *Nuclear Engineering and Design*, vol. 282, pp. 144–157, 2015.
- [59] A. Giorla, M. Vaitová, Y. Le Pape, and P. Štemberk, "Mesoscale modeling of irradiated concrete in test reactor," *Nuclear Engineering and Design*, vol. 295, pp. 59–73, 2015.
- [60] B. Pomaro, V. A. Salomoni, F. Gramegna, G. Prete, and C. E. Majorana, "Radiation damage evaluation on concrete shielding for nuclear physics experiments," *Annals of Solid and Structural Mechanics*, vol. 2, no. 2–4, pp. 123–142, 2011.
- [61] P. Feng, E. J. Garboczi, C. Miao, and J. W. Bullard, "Microstructural origins of cement paste degradation by external sulfate attack," *Construction and Building Materials*, vol. 96, pp. 391–403, 2015.
- [62] A. M. Tarantino, "The singular equilibrium field at the notch-tip of a compressible material in finite elastostatics," *Journal of Applied Mathematics and Physics*, vol. 48, no. 3, pp. 370–388, 1997.
- [63] A. M. Tarantino, "On extreme thinning at the notch tip of a neo-Hookean sheet," *The Quarterly Journal of Mechanics and Applied Mathematics*, vol. 51, no. 2, pp. 179–190, 1998.
- [64] A. M. Tarantino, "On the finite motions generated by a mode I propagating crack," *Journal of Elasticity*, vol. 57, no. 2, pp. 85–103, 1999.
- [65] A. M. Tarantino, "Crack propagation in finite elastodynamics," *Mathematics and Mechanics of Solids*, vol. 10, no. 6, pp. 577–601, 2005.
- [66] A. Caporale, L. Feo, and R. Luciano, "Damage mechanics of cement concrete modeled as a four-phase composite," *Composites Part B: Engineering*, vol. 65, pp. 124–130, 2014.
- [67] R. Barretta, L. Feo, R. Luciano, and F. Marotti de Sciarra, "An Eringen-like model for Timoshenko nanobeams," *Composite Structures*, vol. 139, pp. 104–110, 2016.
- [68] R. Barretta, L. Feo, R. Luciano, and F. Marotti de Sciarra, "A gradient Eringen model for functionally graded nanorods," *Composite Structures*, vol. 131, pp. 1124–1131, 2015.
- [69] R. Barretta, L. Feo, R. Luciano, and F. Marotti de Sciarra, "Variational formulations for functionally graded nonlocal Bernoulli-Euler nanobeams," *Composite Structures*, vol. 129, pp. 80–89, 2015.
- [70] R. Barretta, L. Feo, and R. Luciano, "Torsion of functionally graded nonlocal viscoelastic circular nanobeams," *Composites Part B: Engineering*, vol. 72, pp. 217–222, 2015.
- [71] F.-J. Ulm, O. Coussy, L. Kefei, and C. Larive, "Thermo-chemo-mechanics of ASR expansion in concrete structures," *Journal of Engineering Mechanics*, vol. 126, no. 3, pp. 233–242, 2000.
- [72] V. Saouma and L. Perotti, "Constitutive model for alkali-aggregate reactions," *ACI Materials Journal*, vol. 103, no. 3, pp. 194–202, 2006.
- [73] C. Comi, R. Fedele, and U. Perego, "A chemo-thermo-damage model for the analysis of concrete dams affected by alkali-silica reaction," *Mechanics of Materials*, vol. 41, no. 3, pp. 210–230, 2009.
- [74] Z. P. Bazant and A. Steffens, "Mathematical model for kinetics of alkali-silica reaction in concrete," *Cement and Concrete Research*, vol. 30, no. 3, pp. 419–428, 2000.
- [75] S. Multon, A. Sellier, and M. Cyr, "Chemo-mechanical modeling for prediction of alkali silica reaction (ASR) expansion," *Cement and Concrete Research*, vol. 39, no. 6, pp. 490–500, 2009.
- [76] S. Poyet, A. Sellier, B. Capra et al., "Chemical modelling of alkali silica reaction: influence of the reactive aggregate size distribution," *Materials and Structures*, vol. 40, no. 2, pp. 229–239, 2007.
- [77] I. Comby-Peyrot, F. Bernard, P.-O. Bouchard, F. Bay, and E. Garcia-Diaz, "Development and validation of a 3D computational tool to describe concrete behaviour at mesoscale. Application to the alkali-silica reaction," *Computational Materials Science*, vol. 46, no. 4, pp. 1163–1177, 2009.
- [78] C. F. Dunant and K. L. Scrivener, "Micro-mechanical modelling of alkali-silica-reaction-induced degradation using the AMIE framework," *Cement and Concrete Research*, vol. 40, no. 4, pp. 517–525, 2010.
- [79] M. Alnaggar, G. Cusatis, and G. Di Luzio, "A discrete model for alkali-silica-reaction in concrete," in *Proceedings of the 8th International Conference on Fracture Mechanics of Concrete and Concrete Structures (FraMCoS '12)*, J. G. M. Van Mier, G. Ruiz, C. Andrade, R. C. Yu, and X. X. Zhang, Eds., 2012.

- [80] T. Wu, I. Temizer, and P. Wriggers, "Multiscale hydro-thermo-chemo-mechanical coupling: Application to alkali-silica reaction," *Computational Materials Science*, vol. 84, pp. 381–395, 2014.
- [81] J. W. Pan, Y. T. Feng, J. T. Wang, Q. C. Sun, C. H. Zhang, and D. R. J. Owen, "Modeling of alkali-silica reaction in concrete: a review," *Frontiers of Structural and Civil Engineering*, vol. 6, no. 1, pp. 1–18, 2012.
- [82] L. F. M. Sanchez, S. Multon, A. Sellier, M. Cyr, B. Fournier, and M. Jolin, "Comparative study of a chemo-mechanical modeling for alkali silica reaction (ASR) with experimental evidences," *Construction and Building Materials*, vol. 72, pp. 301–315, 2014.

Research Article

Some Aspects of Structural Modeling of Damage Accumulation and Fracture Processes in Metal Structures at Low Temperature

Valeriy Lepov, Albert Grigoriev, Valentina Achikasova, and Kyunna Lepova

V. P. Larionov's Institute of Physical-Technical Problems of the North, SB RAS, Yakutsk 677980, Russia

Correspondence should be addressed to Valeriy Lepov; lepov@iptpn.ysn.ru

Received 4 December 2015; Accepted 1 June 2016

Academic Editor: Theodoros C. Rousakis

Copyright © 2016 Valeriy Lepov et al. This is an open access article distributed under the Creative Commons Attribution License, which permits unrestricted use, distribution, and reproduction in any medium, provided the original work is properly cited.

The problem of brittle fracture of structures at low temperature conditions connected to damage accumulation and ductile-brittle transition in metals. The data for locomotive tire contact impact fatigue and spalling are presented. The results of experimental testing showed the impact toughness drop at low temperature. The internal friction method was applied to revealing of the mechanism of dislocation microstructure changes during the low temperature ductile-brittle transition. It has been shown for the first time that the transition is not connected to interatomic interactions but stipulated by thermofluctuation on nucleus such as microcracks and by their further growth and coalescence. From now on, the proposed mechanism would be used for theoretical and numerical modeling of damage accumulation and fracture in materials.

1. Introduction

It is well known that during the low temperature climate operation the catastrophic breakdown of structure and machine elements often occurred. In that case the plasticity properties fall and the character of fracture changes from ductile to brittle [1, 2]. The significant loss of safety and economic efficiency occurred in the operation of railway equipment in extremely low climatic temperatures conditions [3, 4]. This leads to growth of energy and resource intensity of transportation. Special actuality of this problem is considering the construction of new rail lines and increase of cargo turnover. The most important units of railway equipment are tire and rail. Their durability and reliability significantly affect operating costs, and destruction is unacceptable because they pose a clear threat to traffic safety. The railroad located on territory of the Republic of Sakha (Yakutia) in Siberia (Russia) is distinguished by low climatic temperatures and acutely continental climate [5]. The period of subzero extends about 210 days and the minimum of temperature reaches 60°C below zero. The difference of the average temperature achieves 70°C and more per season.

The diversity of the phenomenon of ductile-brittle transition is reflected by the factors affecting the type of fracture:

both internal and external. Thus the chemical composition and the structure of the material reflect the physical nature of the phenomenon, and the loading rate, temperature, type of stress-strain state, and the size of the structure define the mechanical nature, respectively. It should be noted that the structural mechanism of the process occurring in the range of ductile-brittle transition therefore still remains undetermined. Nevertheless the existence of the phenomenon is well studied by optical and electronic metallography. Image in Figure 1 demonstrated the boundary of ductile (on upper-right part) and brittle (on bottom-left part) mechanism of fracture.

The next step will be the multiscale modeling of damage accumulation and fracture. It should include the growth and coalescence mechanism of ductile pores and brittle small cracks and use the data of microstructure evolution on nano- and microscales also [6]. The stress and strain distribution partially accords with the thermodynamically consistent theory of elastoplasticity coupled with nonlocal damage in the strain space which was used [7, 8]. The coupling of critical level of damage and strain invariants ratio [9] defines the crack opening conditions and coalescence with the main crack [10].

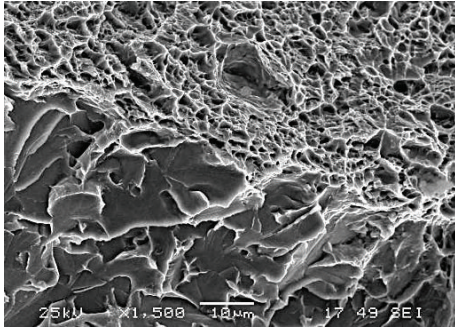


FIGURE 1: Microstructural image demonstrated the low temperature ductile-brittle transition in structural steel 09G2.

TABLE 1: Chemical composition of steel, mass%.

Element	C	Si	Mn	P	S
Content	0,6	0,33	0,83	0,02	0,02

2. Materials and Methods

The locomotive tires are exposed to influence of various loadings during operation. Material of the wheel of this locomotive element is merged in the complex stress state. So the internal and superficial defects are developed and damage plastic deformation and difficult tension take place.

2.1. Materials. The chemical composition of the locomotive tear bandage steel is shown in Table 1 and meets the requirements of the standard for such material [3].

The results of standard tension test for this steel do not have a great gap fixed for mechanical properties (as yielding, breaking point, and tensile strain) at room and low temperature (see Table 2). The deformation curves are shown in Figure 2; and numbers 1–4 indicate samples.

But because the bandage of locomotive tire is operated not only in a wide range of working temperatures, in static and dynamic loading too the principle is to study the impact toughness of the material of the band, as positive (20°C) and below freezing (−20, −40, and −60°C) also. Table 3 shows the results of impact test of bandage steel and average values for three or five samples.

These values have been approximated by splines for further application (see Figure 3) [4].

2.2. Experimental Methods. The method of internal friction is one of the most sensitive methods in the study of the fine structure of metals and alloys. Measurement of internal friction runs in a wide range of frequencies. Measurement in the ductile-brittle transition of materials with BCC lattice is conveniently carried out at low frequencies (of the order of a few hertz), because the internal friction is sensitive to various disturbances and alterations of the structure at the level of crystal lattice and therefore is often used by researchers to examine the actual defect structure of crystals. In the present work, measurements of internal friction held by the method of free torsional vibrations widely used for dynamic mechanical analysis of metallic materials [11, 12].

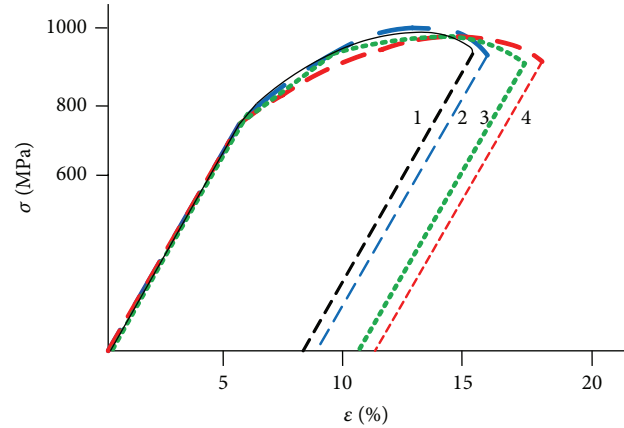


FIGURE 2: The deformation curves for tensile test.

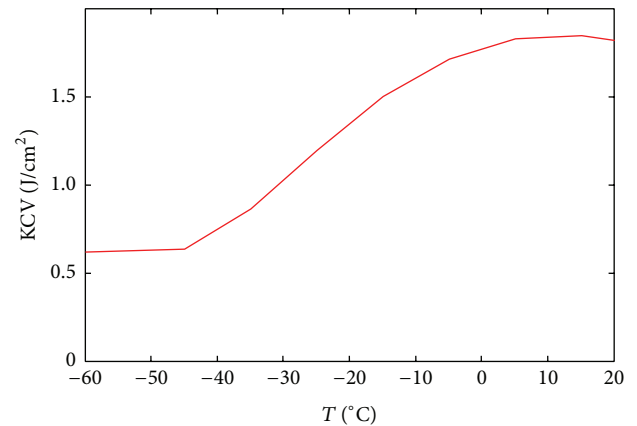


FIGURE 3: Approximation curve for impact toughness.

TABLE 2: Results of standard tensile test.

$T, ^\circ\text{C}$	σ_T	σ_B	δ
Room	708,97	1067,77	10,61
	686,12	1012,94	10,14
	705,40	1030,90	10,09
	690,16	1037,2	10,28
−50	747,61	1035,3	8,64
	769,85	1135,21	8,93
	749,77	1029,49	8,33
	755,74	1066,67	8,63

The reverse torsion pendulum has been used as the implementation of internal friction method. The lower end of test sample in the experiment has the form of a wire and was fixed stationary one. The upper end was rigidly connected to the inertial detail, suspended on torsion bars. The system was excited by torsional vibration. After removal of the driving force, the pendulum did damped oscillations. Main parameters of oscillations were measured (only the change of vibration amplitude, i.e., the number of oscillations here) to allow the calculation of the viscoelastic characteristics of the material sample [13].

TABLE 3: Results of test for impact toughness KCV.

$T, ^\circ\text{C}$	20	-20	-40	-60
	2,29			0,70
KCV, J/cm ²	1,75	1,33	0,71	0,58
	1,69	1,37	0,54	0,74
	1,72	1,38	0,96	0,51
	1,64			0,67
Average	1,82	1,36	0,73	0,62

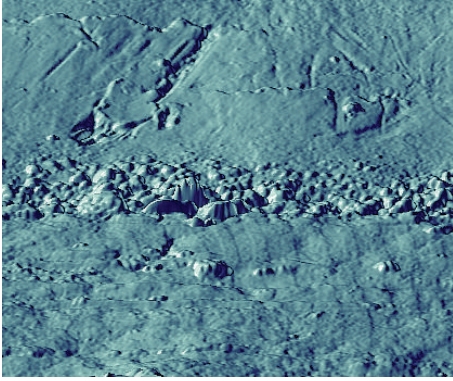


FIGURE 4: STM-image of the steel probe deformation surface with grain boundary.

As the test material, in this case structural steel 09G2 was selected. The test material has BCC lattice, which is characterized by low temperature ductile-brittle transition. Investigated wire samples have a diameter of 1 mm and working length 10 cm. The relative deformation of the order of 10^{-5} has been defined at the frequency of oscillation of pendulum about 1 Hz.

The important advantage of combined structural models should be mentioned also. It is the ability to find a way of experimental data obtained for one of the kinds of loading and behavior of the material, to the other, and combine experimental data related to various kinds of stress state and external influence.

The source data for the models are the sizes and quantitative characteristics of the distribution of defects at different structural levels obtained on the basis of scanning probe and optical microscopy and fractography, characterized by the fractal dimension, and it changes in the damage accumulation process.

Structural level in this case means the area of the extent to which the prevailing is certain defect structures (e.g., vacancy, dislocation, dislocation cluster, crack, micropore, strip shift, and nonmetallic inclusion). Structural levels sometimes could match the scale. Figure 4 presents the deformation surface image of low-alloyed steel plane probe near the rupture [14]. The image was obtained by STM and has $5 \times 5 \mu\text{m}$ size. Just through the middle of the image a grain boundary passes with some structural defects around (small cracks, slip bends, and twins).

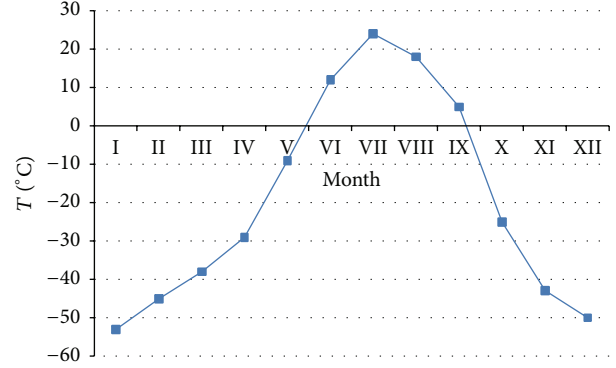


FIGURE 5: Minimal average month temperatures per five years in Tommot city.

3. Results and Discussion

The modeling of damage accumulation processes should consider the complex effects of high-cycle fatigue and low-cycle impact loading. The impact toughness as shown in Table 3 greatly depends on the test temperature. So the overall damage Ψ could differentiate for high-cycle fatigue damage Ψ_F and low-cycle impact damage Ψ_L [9]:

$$\Psi = \Psi_F + \Psi_L = \frac{1}{N} \sum_{i=1}^N \Psi_{Fi} + \frac{1}{K} \sum_{k=1}^K \Psi_{Lk}, \quad (1)$$

where Ψ_{Fi} is damage during fatigue i -cycle, Ψ_{Lk} is damage during impact k -cycle, N, K are appropriate cycles value. For operation at low temperatures the fatigue damage of tire has reduced but the impact damage significantly grown.

In Figure 5 the time-average temperature on railroad track section near Tommot city has been shown. The appropriate toughness KCV could be found according to curve in Figure 3. The damage has been calculated taking into account the associated flow rule and J -integral dependence as [4]

$$\Psi_L = \sum_{j=1}^K \left[\left(1 - \frac{\text{KCV}_j}{\text{KCV}_0} \right)^m \right], \quad (2)$$

where $\text{KCV}_0, \text{KCV}_j$ are impact toughness at room temperature and in j -damage condition accordingly and $m \sim 0,25, \dots, 0,3$ is depending of material and stress state factor. The derivation of this empirical formula is based on connection between the stress intensity factor and J -integral, on the one hand, and proportion between values of stress intensity factor and impact toughness KCV, established experimentally for the high-strength steels, on the other hand [15, 16].

The mechanism of dislocation movement on microscale could be established by an internal friction measurement. Also the internal friction is one of the main methods for determination of energy dissipation localization in low temperature ductile-brittle transition [12]. The experiment by pendular oscillator for wire samples of structured low-alloyed steel 09G2 (content is about 0,1% carbon and 2% manganese) was carried out. The measurements of temperature dependence for internal friction of both tempered and

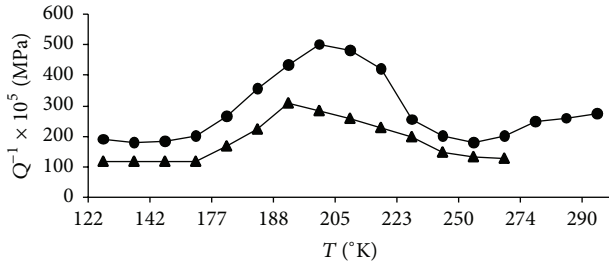


FIGURE 6: Temperature curve of internal friction of the testing steel.

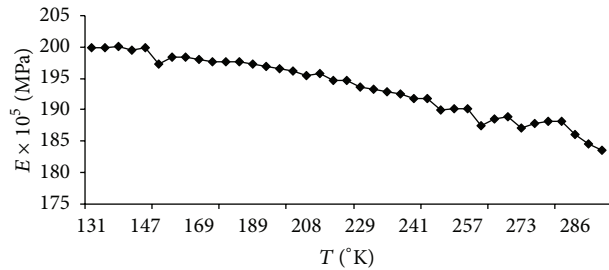


FIGURE 7: Temperature dependence of Young's modulus for testing steel.

annealed samples of the test material in the temperature range 100–300 K have been used. Concerning the interpretation of internal friction data the magnitude was determined by the next equation [11]:

$$Q^{-1} = \frac{\ln K}{\pi} \frac{1}{n}, \quad (3)$$

where Q^{-1} is the inverse mechanical quality factor, n is the number of oscillations within the reduction of the amplitudes of the oscillations, and K is a number indicating how many times the initial amplitude decreases for n oscillations.

On the temperature curve of internal friction of the investigated steel is observed a maximum in the range of 160–240 K (see Figure 6). Maximum of the curve for the tempered sample is higher than that of the annealed sample. The maximum of activation energy is calculated at the frequency shift and achieved a value of 0,2 eV. The interval of existence of this maximum steel 09G2 coincides with the interval of existence of ductile-brittle transition under impact toughness test.

During the experiment a temperature dependence of Young's modulus by resonance method has been investigated. The natural frequencies of a sample of steel 09G2 has been also determinate. The temperature dependence of the modulus of elasticity represents a monotonously increasing with decreasing temperature, a linear relationship in the range of ductile-brittle transition (see Figure 7).

Analytical possibilities of the method of internal friction allow obtaining the necessary information to study the early stages of damage in the area of ductile-brittle transition. The local changes in the submicroscopic structure of material occur in conditions of microstrains. Methods of mechanical spectroscopy allow evaluating the stages of development of the degradation processes and accumulation of the damage

of deformed low-carbon steels [4]. There are a number of dislocation mechanisms responsible for low temperature inelastic scattering energy in various metals and alloys with BCC lattice. It can be thermal or geometric kinks in the motion of dislocations, interaction of dislocations with point defects, and the change in the density of mobile dislocations [11–13].

Stochastic model of crack growth and fracture in multiphase heterogeneous material is based on the mechanism triggered by stresses opening small cracks or pores on particles or ruptures of material [7–10, 14, 15].

Further viscoplastic growth and mutual coalescence of defects provide the crack propagation. Figure 8 showed the Web-oriented visualization examples of crack growth on microdefects. Algorithm has been realized by modern version of Java script language [16, 17]. Modification of the model can be connected with application to a wide range of phenomena, for example, the accumulation of damage in porous media, materials with multiple phase transitions, including evaporation, melting, and freezing, and the second-order phase transition [18–21].

4. Summary

The new criterion and approach of damage estimation for locomotive tire in extreme uncertainty conditions are offered. It is revealed that the lifetime of tire is significantly sensitive to impact strength at low temperature during operation.

Monotonic temperature dependence of Young's modulus in the range of ductile-brittle transition leads to confirming hypothesis about the dislocation and phonon mechanism of the phenomenon. Selection of the structural level occurs according to the classical Hamilton principle of stationary action or least action. In this case the rupture of atomic bonds occurs on athermal thermofluctuation mechanism in the inelastic scattering of phonons and under the action of tensile stresses, which can be appropriately modeled numerically. It should be noted that the revealing mechanism of internal friction of nano- and microcrystalline steels and alloys makes possible the building of theoretical and numerical models of the damage accumulation and fracture of the materials with a variable temperature-dependent structure.

So the new visualization possibilities of programming of damage accumulation and fracture processes presented in this paper too. The possibility of crack growth under the low-cycling and dynamic load and in cases of complex loading is examined.

5. Conclusions

This paper aims at experimental verification aspects of multiscale structural Web-oriented modeling of damage accumulation and fracture of heterogeneous materials. In very cold climate conditions the low temperature ductile-brittle transition in BCC-steel and alloys has a great significance. In such a practical problem like the strength of locomotive tire, for example, it is important to take into account the distribution of minimal temperature per calendar year and experimental dependence of impact toughness to reveal the

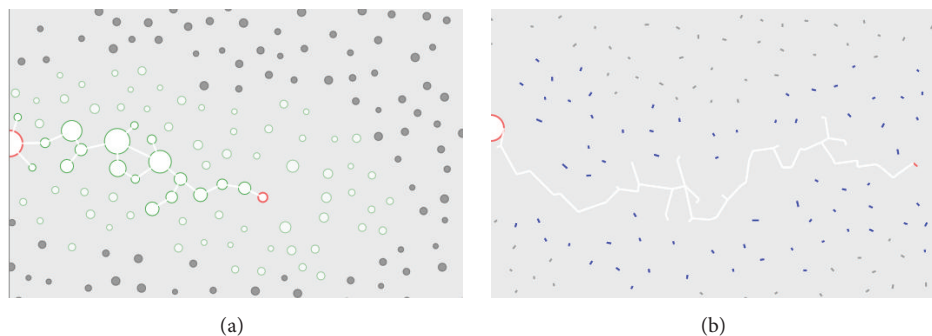


FIGURE 8: Java script visualization examples of crack growth on (a) micropores and (b) small cracks.

ductile-brittle transition range. The dislocation mechanism of such transition was showed by the amount of dissipation energy during the internal friction test. Then for modeling of the damage accumulation process and pores growth and crack branching it is necessary to bring the nonlocal viscoelastic approach the thermodynamically consistent theory of elastoplasticity. For the Web-oriented visualization rendition the plane and stochastic approximation of crack distribution in multiscale structure has been used. The next step should be the connection between the modeling of material and prediction of real structure lifetime. Besides the transport this approach is highly desired in potentially dangerous industrial objects such as electricity and thermal power plants.

Competing Interests

The authors declare that they have no competing interests.

Acknowledgments

This research has been partially supported by Russian Foundation for Basic Research (Project 15-41-05010) and Federal Agency of Scientific Organization of Ministry of Science and Education of Russian Federation.

References

- [1] A. Y. Krasovskii, "Ductile-to-brittle transition temperature as a measure of the crack resistance of steels," *Strength of Materials*, vol. 17, no. 10, pp. 1439–1446, 1985.
- [2] V. I. Trefilov, Ed., *Strain Hardening and Fracture of Polycrystalline Metal*, Naukova dumka, Kiev, Ukraine, 1989 (Russian).
- [3] A. V. Grigoriev and V. V. Lepov, "The mechanism of damage accumulation and fracture of railroad wheel material in condition of the North," *Vestnik Severo-Vostochnogo Federal'nogo Universiteta*, vol. 9, no. 1, pp. 79–85, 2012.
- [4] A. V. Grigoriev and V. V. Lepov, "Assessment of the service life of rail equipment operating in extreme conditions of the North," *Zavodskaja Laboratorija. Diagnostika Materialov*, vol. 81, no. 12, pp. 42–48, 2015 (Russian).
- [5] M. Weller, "Characterization of high purity bcc metals by mechanical spectroscopy," *Le Journal de Physique IV*, vol. 5, pp. C7-199–C7-204, 1995.
- [6] V. Lepov, A. Ivanova, V. Achikasova, and K. Lepova, "Modeling of the damage accumulation and fracture: structural-statistical aspects," *Key Engineering Materials*, vol. 345-346, pp. 809–812, 2007.
- [7] F. Marotti De Sciarra, "Hardening plasticity with nonlocal strain damage," *International Journal of Plasticity*, vol. 34, pp. 114–138, 2012.
- [8] F. M. Marotti de Sciarra, "A nonlocal model with strain-based damage," *International Journal of Solids and Structures*, vol. 46, no. 22-23, pp. 4107–4122, 2009.
- [9] V. Lyakhovskiy, Y. Hamiel, and Y. Ben-Zion, "A non-local viscoelastic damage model and dynamic fracturing," *Journal of the Mechanics and Physics of Solids*, vol. 59, no. 9, pp. 1752–1776, 2011.
- [10] V. Lepov and A. Loginov, "Non-Markovian evolution approach to structural modeling of material fracture," *World Journal of Engineering*, vol. 9, no. 3, pp. 207–212, 2012.
- [11] Y. Kogo, Y. Iijima, N. Igata, and K. Ota, "Internal friction of carbon-carbon composites at elevated temperatures," *Journal of Alloys and Compounds*, vol. 355, no. 1-2, pp. 148–153, 2003.
- [12] V. Lepov, V. Achikasova, A. Ivanova, and K. Lepova, "Low-temperature ductile-brittle transition in metals: the micro-mechanics and modeling," in *Proceedings of the 23rd Annual International Conference on Composites or Nano Engineering*, Chengdu, China, 2015.
- [13] M. S. Blunter and Y. V. Piguzov, Eds., *The Method of Internal Friction in Physical Metallurgy Studies*, Metallurgija, Moscow, Russia, 1991 (Russian).
- [14] V. V. Lepov, A. M. Ivanov, B. A. Loginov et al., "The mechanism of nanostructured steel fracture at low temperatures," *Nanotechnologies in Russia*, vol. 3, no. 11-12, pp. 734–742, 2008.
- [15] S. A. Golovin and S. A. Pushkar, *Microplasticity and Fatigue of the Metals*, Metallurgija, Moscow, Russia, 1980 (Russian).
- [16] K. B. Broberg, "Computer demonstration of crack growth," *International Journal of Fracture*, vol. 42, no. 3, pp. 277–285, 1990.
- [17] E. A. Arkhangel'skaya, V. V. Lepov, and V. P. Larionov, "The role of defects in the development of delayed fracture of a damaged medium under the effect of hydrogen," *Materialovedenie*, vol. 8, pp. 7–10, 2003.
- [18] C. A. Reddy, "Strengthening mechanisms and fracture behavior of 7072Al/Al₂O₃ metal matrix composites," *International Journal of Engineering Science and Technology*, vol. 3, no. 7, pp. 6090–60100, 2011.
- [19] S. Nasrazadani and A. Raman, "The application of infrared spectroscopy to the study of rust systems-II. Study of cation

deficiency in magnetite (Fe_3O_4) produced during its transformation to maghemite ($\gamma\text{-Fe}_2\text{O}_3$) and hematite ($\alpha\text{-Fe}_2\text{O}_3$),” *Corrosion Science*, vol. 34, no. 8, pp. 1355–1365, 1993.

- [20] D. M. Levin, A. N. Chukanov, and A. A. Yakovenko, “The application of mechanical spectroscopy to the study of substructural degradation and the initial stages of fracture of steels,” *Izvestija of Tula’s State Univerity, Natural Sciences*, vol. 18, pp. 1625–1626, 2013.
- [21] N. Shahidzadeh-Bonn, P. Vié, X. Chateau, J.-N. Roux, and D. Bonn, “Delayed fracture in porous media,” *Physical Review Letters*, vol. 95, no. 17, Article ID 175501, 4 pages, 2005.